Imperial College London

Understanding Molecular Origin of Efficient and Stable Organic Photoconversion Devices

Chiara Labanti

Centre for Doctoral Training in Plastic Electronics

Department of Physics, Imperial College London

A thesis submitted to Imperial College London for the degree of Doctor of Philosophy

Academic Year 2022/2023

"Come to me, all you who labour and are overburdened, and I will give you rest.
Shoulder my yoke and learn from me, for I am gentle and humble in heart,
and you will find rest for your souls.
Yes, my yoke is easy and my burden light."
Matthew 11:28.30

Acknowledgements

While the final safe harbour is at last in sight, I would like to acknowledge the Centre for Doctoral Training in Plastic Electronics, the Centre for Processable Electronics, and the whole Imperial College community for giving me the opportunity to embark in this long journey.

This PhD would not have been possible without my supervisor, Prof Ji-Seon Kim, all the time spent to refine my work and digging out its scientific relevance, all the opportunities I received to learn cutting-edge research, use the most advanced equipment, and travel around the world to explore the scientific community.

I also acknowledge all the main contributors to the research presented here, especially Dr Artem Bakulin, Prof James Durrant, Prof Yun-Hee Kim, and all the team at Samsung Advanced Institute of Technology, for the fruitful collaborations and for introducing me to other techniques and aspects of organic electronics.

Thank you to all my companions who reminded me where the destination was throughout the storms, the stalls, the deviations, when the ship got bogged down or was spinning around itself. Thank you to Katie (wisest sea guide), Ella, Yi-Chun, Joel, Matyas, Amber, James, Saurav, Katia, Emily, Song Yi, Charlie, Lei, Vick, Ying, Tianhao. Thank you for your kindness and positive energy you gave me every day in the office, lab, and our numerous trips. Thanks to the most experienced sailor Gihan who patiently helped me to mend the sails and tidy up the ropes after any mishap in the lab.

Outside this small crew, I am grateful to all the collaborators, academics, researchers, and students, who interacted with me in these years and helped me to put my work and aspirations in a bigger picture for my scientific life and my future directions. Sorry if the space is limited for including all the many names.

And finally, all my thankfulness to my family, my most solid harbour during this challenging expedition, who never ceased to accompany me from the other side of the Channel even when it was not possible to get back to the base for many many

months. Thank you for reminding me why I sailed out and why it is worth enduring towards a shiny landing place. Thanks to my faithful friends more or less far, to Chiara and Cesare in particular.
And thank you to my father, my ever glowing lighthouse, to whom this work is dedicated.

Declaration

Except where specific reference is made, this work is original, has been conducted by me, and has not already been submitted either wholly or in part to satisfy any degree requirement at this or any other university.

Chiara Labanti, June 2023

The copyright of this thesis rests with the author. Unless otherwise indicated, its contents are licensed under a Creative Commons Attribution-Non Commercial 4.0 International Licence (CC BY-NC).
Under this licence, you may copy and redistribute the material in any medium or format. You may also create and distribute modified versions of the work. This is on the condition that: you credit the author and do not use it, or any derivative works, for a commercial purpose.
When reusing or sharing this work, ensure you make the licence terms clear to others by naming the licence and linking to the licence text. Where a work has been adapted, you should indicate that the work has been changed and describe those changes. Please seek permission from the copyright holder for uses of this work that are not included in this licence or permitted under UK Copyright Law.

Abstract

Organic semiconductors (OSCs) are sparking great interest for their potential to substitute inorganic-based technologies (*e.g.*, silicon) in optoelectronic device applications. In recent years, both organic photovoltaics (OPVs) and organic photodetectors (OPDs) have reported dramatic and steady progress in performances, with additional attractive characteristics of lightweight, colour-tunability/transparency, mechanical flexibility, and low-cost fabrication. However, for organic optoelectronics to be ready for the market as a reliable alternative to silicon counterparts, further performance and lifetime increase is required. This involves, for example, improving photodetection speed and reducing dark currents in OPDs, and suppressing OPV photodegradation mechanisms. In this thesis, both design of OSC molecular structure and engineering of device active layer are utilised as powerful tools to improve efficiency of photon-to-electron conversion processes in OPVs and OPDs and to extend operational lifetimes, in both solution-processed and vacuum-evaporated devices. Firstly, the effect of different modifications in OSC chemical structures is analysed, including heteroatom substitution and end-group engineering in non-fullerene acceptors, and geometry control in small-molecule donors. By detailed investigation of molecular physics combining energetic (by air photoemission spectroscopy) and structural (by Raman spectroscopy) characterisation, the role of these modifications on device performance is pinpointed. In particular, backbone rigidity and fine-tuning of charge delocalisation along the molecule are found essential to suppress chemical and morphological degradation during OPV operations, while

the adoption of different donor conformations (twisted *vs.* planar) determines trap-state distribution and photodetection speed in OPDs. Secondly, OPD active layer characteristics are engineered by fabrication parameter tuning, taking into account factors like donor:acceptor ratio and thickness. Here, it is found that high content of donor polymer is crucial to suppress dark current and ensure fast photodetection by morphology and energetic optimisation, while thickness increase in evaporated blends can control molecular orientation and packing order, which is particularly promising in fullerene-free OPDs.

Contents

1. Introduction 19
1.1 Motivation and Aims 19
1.2 Outline 20
1.3 Declaration of Work 22

2. Background 23
2.1 Introduction to Organic Semiconductors 23
2.2 Organic Photoconversion Devices 30
2.2.1 Organic Photovoltaics: Principle of Operations 30
2.2.2 Organic Photodetectors: Principle of Operations 33
2.3 Materials Choice for Photoconversion Devices 38
2.3.1 Families of Nonfullerene Acceptors 39
2.3.2 Optoelectronic Properties of High-Performance Nonfullerene Acceptors 41
2.3.3 Choice of Donor Materials 42
2.4 Efficiency Challenges 42
2.4.1 Morphology Optimisation 44
2.4.2 Enhancing Charge Generation 45
2.4.3 Control of Voltage Loss 47
2.5 Stability Challenges 48
2.5.1 Chemical Stability 49
2.5.2 Morphological Stability 50

3. Methods 54
3.1 Sample and Device Fabrication 54
3.2 Raman Spectroscopy 55
3.2.1 Fundamentals of Raman Spectroscopy 55
3.2.2 Raman Spectroscopy in Organic Semiconductors 59
3.2.3 Raman Experimental Details 61

3.3 Energetics . . . 61
3.3.1 Air Photoemission Spectroscopy . . . 61
3.3.2 Kelvin Probe and Surface Photovoltage . . . 62
3.3.3 Energetics Experimental Details . . . 63
3.4 Absorption Spectroscopy . . . 64
3.5 Photoluminescence and Transient Photoluminescence . . . 65
3.6 Atomic Force Microscopy . . . 66
3.7 Computational Methods (Density Functional Theory) . . . 66
3.8 Electrical Characterisation . . . 67
3.9 Supporting Methods . . . 69
3.9.1 Transient Absorption Spectroscopy . . . 69
3.9.2 Transient Photovoltage and Charge Extraction . . . 70
3.9.3 Grazing Incidence X-ray Spectroscopy . . . 70

4. Improving Stability in Bulk Heterojunction Organic Photovoltaics via Selenium-Substituted Nonfullerene Acceptors . . . 71
4.1 Introduction . . . 72
4.2 Results and Discussion . . . 74
4.2.1 Device Performances and Operational Stability . . . 74
4.2.2 Optoelectronic and Morphological Characterisation . . . 77
4.2.3 Investigation of Photostability and Degradation Mechanisms . 81
4.3 Conclusion . . . 90
4.4 Experimental Section . . . 90

5. Light-Intensity-Dependent Photoresponse Time of Organic Photodetectors and its Molecular Origin . . . 93
5.1 Introduction . . . 93
5.2 Results and Discussion . . . 95
5.2.1 Twisted (NP-SA) and Planar (MPTA) Donor Molecules . . . 95
5.2.2 Responsivity and J–V Characteristics . . . 96
5.2.3 High-Light Device Response Time Governed by Shallow Traps 97
5.2.4 Low-Light Device Response Time Governed by Deep Traps . . 98
5.2.5 Molecular-Structure-Dependent Intermolecular Coupling . . . 100
5.2.6 Molecular Origins of Shallow and Deep Traps . . . 105
5.3 Conclusion . . . 109
5.4 Experimental Section . . . 110

6. Nonfullerene Acceptor Dilution as a Facile Strategy for Device Optimisation towards High-Efficiency Solution-Processed Bulk Heterojunction Or-

ganic Photodetectors . . . 113
6.1 Introduction . . . 114
6.2 Results and Discussion . . . 116
6.2.1 Impact of Acceptor Dilution on Optoelectronic Properties . . 116
6.2.2 Impact of Acceptor Dilution on Photodetector Performance . . 117
6.2.3 The Origin of Blend-Ratio-Dependent OPD Performance: the Nature of Electronic Species . . . 121
6.2.4 The Origin of Blend-Ratio-Dependent OPD Performance: Energetic Landscape upon Acceptor Dilution . . . 134
6.3 Conclusion . . . 136
6.4 Experimental Section . . . 138

7. Efficient Nonfullerene-Based Organic Photodetectors Enabled by Reduced Deep Traps with Highly Intermixed Evaporated Bulk Heterojunction Systems 139
7.1 Introduction . . . 140
7.2 Results and Discussion . . . 142
7.2.1 Thickness-Dependent Optoelectronic Properties . . . 142
7.2.2 Organic Photodetector Performance . . . 147
7.2.3 Exploring the Origin of Device Performance . . . 149
7.2.4 Photophysics in Fullerene *versus* Nonfullerene-Based OPDs . . 151
7.3 Conclusion . . . 157
7.4 Experimental Section . . . 158

8. Conclusion and Further Work . . . 160
8.1 Conclusion . . . 160
8.2 Further Work . . . 162

9. List of Publications . . . 164

Bibliography . . . 166

Appendix 198

A. Full Chemical Names . . . 199

B. Nonfullerene Acceptors: a Short Review of Molecular Design . . . 208

C. Improving Stability in Bulk Heterojunction Organic Photovoltaics via Selenium-Substituted Nonfullerene Acceptors - Supporting Material . . . 213

D. Light-Intensity-Dependent Photoresponse Time of Organic Photodetectors and its Molecular Origin - Supporting Material 220

E. Nonfullerene Acceptor Dilution as a Facile Strategy for Device Optimisation towards High-Efficiency Solution-Processed Bulk Heterojunction Organic Photodetectors - Supporting Material 222

List of Figures

2.1 Illustration of atomic orbital hybridisation, in the case of sp^2 hybridisation 24
2.2 Molecular singlet states in orbital and state representations 25
2.3 Schematic of the steps involved in photon-to-electron conversion in a donor/acceptor system 27
2.4 Potential energy diagram describing the transfer of an electron from molecule A to B, as a function of the normal-mode coordinate Q . . . 29
2.5 *J-V* curve of a typical BHJ solar cell 31
2.6 Illustration of recombination loss in OSCs 32
2.7 Equivalent electric circuit representing ideal and non-ideal solar cells . 32
2.8 Schematics of a typical OPD device, with energy level diagram and J-V characterisation in dark and under light 34
2.9 Molecular structures of some of the most commonly-used OPV materials, including fullerene derivatives, donor polymers, and NFAs . . 40
2.10 Comparison of state-of-the-art OPD figures of merit with inorganic counterparts, depending on spectral range of photodetection 43
2.11 Examples of morphology optimisation in OPV and OPD systems . . . 45
2.12 Evolution of PV parameters during light exposure (1 Sun by white LED) for BHJ devices using different ITIC derivatives or PCBM, in combination with PBDB-T donor polymer 51
2.13 Schematic of photoinduced morphology reorganisation in fullerene *vs.* NFA-based BHJ systems 52

3.1 Schematics of the energy transitions involved in elastic (Rayleigh) and inelastic (Stokes and anti-Stokes) scattering of light 56
3.2 Wavelength-dependent Raman study on DPPB-3Se polymer 59
3.3 Schematic illustration of photoemission process from a metallic sample 63
3.4 Schematic of Kelvin probe operating and measurement principles . . 64

3.5 Spectrum of the LED light source used for device lifetime testing and film degradation, with and without inclusion of IR component 68

4.1 Molecular structure of selenated NFA molecules, with PV characterisation of PBDB-T:NFA solar cells 74
4.2 Evolution of photovoltaic parameters under continuous light exposure (white LED) of PBDB-T:NFA devices 76
4.3 UV-Vis absorption spectra of pristine NFAs and PBDB-T and of PBDB-T:NFA blends treated by thermal annealing 77
4.4 UV-Vis absorption spectra of different selenated NFA blends with PBDB-T 78
4.5 EQE spectra of PBDB-T:NFA devices 79
4.6 Photoluminescence and transient absorption characterisation of selenated NFA systems 80
4.7 Investigation of photodegradation mechanisms in PBDB-T:NFA systems, including absorption, Raman, and photoluminescence characterisation 81
4.8 AFM maps of fresh and light-aged PBDB-T:NFA blends 83
4.9 GIWAXS 2D maps for neat and blended SeOutMe, with schematics of crystalline structure 84
4.10 Results of DFT simulations for the different NFA single molecules . . 86
4.11 HOMO and LUMO distributions for DFT energy-optimised structures of different NFAs 88
4.12 Energetics analysis for selenated NFA films, including tail-state characterisation and comparison with DFT-simulated energy levels 89

5.1 Molecular structure of small molecule donors 96
5.2 OPD device characteristics at high-light intensity 97
5.3 Low-light illumination photocurrent transients 99
5.4 Optical and molecular structural properties 101
5.5 Steady-state PL and TCSPC analysis for NP-SA and MPTA films . . 101
5.6 AFM maps of neat donor films and respective blends with C_{60} on quartz substrate 102
5.7 PL quenching analysis in NP-SA:C_{60} and MPTA:C_{60} devices 103
5.8 DFT simulation of MPTA Raman spectra for different twisting angles between the donor and the acceptor unit 104
5.9 Characterisation of MPTA-C_{60} adduct 105
5.10 Energetic analysis of NP-SA:C_{60} and MPTA:C_{60} blends 106

5.11 DFT simulated HOMO levels for NP-SA and MPTA for the near-equilibrium configurations 20° around the possible isomeric forms . . 107
5.12 DFT calculations for NP-SA compared with the Se-substituted version of MPTA 108
5.13 Density of states from photoemission spectra of neat and blended NP-SA and MPTA 109
5.14 Device structure and energetic diagram of donor:C_{60} OPDs 111

6.1 Optical properties of PM6:Y6 blends with different D/A blend ratios 117
6.2 Absolute absorbance and PL of PM6:Y6 blends with different D/A blend ratios 117
6.3 Device characterisation for PM6:Y6 active layer with increasing donor content 118
6.4 Photovoltaic parameters for PM6:Y6 devices with different BHJ blend ratios 119
6.5 EQE spectra for PM6:Y6 devices with different blend ratios at increasing reverse bias 120
6.6 Normalised EQE spectra for PM6:Y6 devices with different blend ratios at increasing reverse bias 122
6.7 Bias-dependent PL analysis for balanced and diluted PM6:Y6-based devices 124
6.8 Electric characterisation under reverse bias of PM6:Y6 devices with different blend ratios 125
6.9 Transient photocurrent decay for PM6:Y6 devices with different blend ratios at increasing reverse bias 126
6.10 Transient photocurrent under red LED (633 nm) excitation for PM6:Y6 devices with different blend ratios at increasing reverse bias 127
6.11 Normalised transient photocurrent decay for PM6:Y6 devices with different blend ratios under reverse bias 129
6.12 τ_{fall} of transient photocurrent for PM6:Y6 devices with different blend ratios 130
6.13 Electron and hole mobility analysis in PM6:Y6 systems 131
6.14 Transient absorption spectroscopy for PM6:Y6 BHJs with different blend ratios 133
6.15 Transient PL for balanced and diluted PM6:Y6 blends 134
6.16 Energetic analysis and schematics of BHJ photophysical mechanisms 136

7.1 Thickness-dependent optoelectronic properties of MPTA:Cl_6-SubPc films . . . 143
7.2 Grazing-incidence X-ray diffraction profiles in the out-of-plane direction for neat and blended MPTA films . . . 144
7.3 AFM maps of MPTA:Cl_6-SubPc BHJ films . . . 145
7.4 Thickness-dependent optoelectronics and morphology of neat MPTA and Cl_6-SubPc films . . . 145
7.5 Photoluminescence spectra of neat MPTA films of different thicknesses 146
7.6 Density of trap states for MPTA:Cl_6-SubPc BHJs of different thicknesses . . . 147
7.7 Thickness-dependent OPD characterisation of MPTA:Cl_6-SubPc-based devices . . . 147
7.8 Bias-dependent EQE spectra of MPTA:Cl_6-SubPc BHJ devices with different active layer thicknesses . . . 149
7.9 Photoluminescence emission analysis in MPTA:Cl_6-SubPc BHJ . . . 150
7.10 Absolute bias-dependent PL spectra of thin and thick MPTA:Cl_6-SubPc BHJ devices . . . 151
7.11 Comparison of photophysics in MPTA:Cl_6-SubPc and MPTA:C_{60} BHJ systems . . . 152
7.12 Schematics of the energy diagram in MPTA:Cl_6-SubPc and MPTA:C_{60} devices . . . 153
7.13 TAS spectra for MPTA:C_{60} and MPTA:Cl_6-SubPc BHJs . . . 154
7.14 Bias-dependent EQE and absolute PL for MPTA:C_{60} and MPTA:Cl_6-SubPc-based devices . . . 154
7.15 Comparison of trap state impact on device performance in MPTA:C_{60} and MPTA:Cl_6-SubPc OPDs . . . 155
7.16 Density of trap states for MPTA:C_{60} and MPTA:Cl_6-SubPc devices (60 nm), quantified by charge extraction analysis. . . . 157

C.1 Absorption spectra of fresh and aged PBDB-T:NFA blends exposed to white LED light source . . . 214
C.2 Raman spectra of fresh and aged PBDB-T:NFA blend films . . . 215
C.3 Assignment of Raman modes of PBDB-T . . . 215
C.4 Assignment of the NFA Raman modes, comparing experimental data with DFT simulations . . . 216
C.5 DFT-simulated Raman spectra of the four NFAs with different core-end dihedral . . . 217
C.6 Raman spectra of fresh and light-aged neat NFAs . . . 218

C.7 PL spectra of fresh and light-aged PBDB-T:NFA blends 219

D.1 Comparison of experimental and DFT simulated Raman spectra for NP-SA and MPTA 220

E.1 Temperature-dependent PL analysis for PM6:Y6 BHJs 223
E.2 Energetic characterisation of PM6:Y6 BHJ thin films with different blend ratios 224

List of Tables

4.1 Champion and average photovoltaic parameters for ∼15 devices and T_{50} lifetime for PBDB-T:NFA solar cells 75
4.2 Summary of PL quenching for the different NFA blends with respect to the neat donor and acceptor components 78
4.3 Summary of the lattice parameters, angles, and crystalline structure symmetry for neat and blended SeOutMe 85

7.1 Summary of lamellar and π-π stacking distances in neat and blended MPTA films 144

C.1 Description of PBDB-T Raman modes 213
C.2 Description of NFA Raman modes 213

D.1 Detailed assignment of Raman vibrational modes of NP-SA and MPTA 221

Frequently Used Abbreviations

Abbreviation	**Description**
OSC	Organic semiconductor
OPV	Organic photovoltaic
OPD	Organic photodetector
HOMO	Highest occupied molecular orbital
LUMO	Lowest unoccupied molecular orbital
BHJ	Bulk heterojunction
FMO	Frontier molecular orbital
V_{OC}	Open-circuit voltage
J_{SC}	Short-circuit current
FF	Fill factor
PCE	Power conversion efficiency
E_{g}	Energy bandgap
PL	Photoluminescence
SPV	Surface photovoltage
CT	Charge transfer
DOS	Density of states
NIR	Near infrared
ICT	Intramolecular charge transfer
ESP	Electrostatic potential distribution
FWHM	Full width at half maximum

1 | Introduction

1.1 Motivation and Aims

As we approach the first quarter of the 21st century, it is by now clear how this historical period is full of challenges and opportunities. A nearly-eight-billion-sized fast-growing population and its expanding urbanisation generate a dramatic increase in energy consumption,[1,2] with a predicted 44% rise in demand by 2030.[3] This is widely covered by use of carbon-intensive power sources, such as coal and natural gas, which result in catastrophic increase in atmospheric levels of CO_2 and other pollutants,[2] with disruption of climate patterns, ecosystems, and biodiversity throughout the planet.[4] In particular, there is general consensus in the scientific community that a threshold of 1.5°C global temperature increase should not be overcome, lest we bring the consequences of anthropogenic climate change beyond the point of no return. For this, drastic curtailing of fossil fuels consumption should take place, with at least 80% reduction of the current levels necessary to keep up with international targets.[2,5]

At the same time, population and economic growth is also accompanied by unprecedented technological development, with the rise of globalisation and interconnection via IT advances. In particular, the emergence of the Internet of things, with over 40 billion devices connected by 2023, shows great potential not only for higher production efficiency in Industry 4.0, but also for sustainability (*e.g.*, smart cities, smart homes) and welfare (*e.g.*, e-health).[6]

To enjoy "the best of both worlds", with smart technologies powered by efficient and clean energy, photovoltaic (PV) power generation stands out as a great alternative to traditional non-renewable sources, and it could in principle fuel all humanity activities,[7] provided suitable infrastructures for energy storage and distribution. However, although recent progress in economy of scale made PV price-wise competitive, with a cost of 56 USD/MWh for utility-level compared to over 70 USD/MWh for gas and coal, traditional silicon-based solar modules require expen-

sive, energy-intensive fabrication[8] relying on a complex supply chain, subject to geopolitical instability and price fluctuations.[9]

In this context, organic electronics, using carbon-based semiconductors, represent a great promise to achieve efficient photoconversion, not only for cost-effective, easily processable organic photovoltaics (OPVs), but also for low-power-consumption, colour-tunable sensors (organic photodetectors, OPDs), with extensive opportunities for integration on flexible and biological substrates. In recent years, OPVs have raised from proof-of-concept devices with negligible performances to impressive power conversion efficiencies >18%[10–12] and even >20% for tandem solar cells,[13] while figures of merit of OPDs are now rivalling inorganic-based counterparts, especially in infrared detection.[14] Applications of organic electronics have already demonstrated the market potential of the field, spanning from colourful solar windows in public buildings[15,16] to energy sources for portable devices powered by indoor light (OPVs),[17] from sensors for automatic driving cars to noninvasive point-of-care diagnostics (OPDs).[18]

However, several challenges still remain to make OPVs and OPDs a viable alternative to silicon-based technologies. In particular, issues like OPV operational stability and large-area fabrication, and OPD limits for high-frequency detection, need to be tackled for taking full advantage of organic electronics potential.

In this thesis, some of these challenges will be investigated in the perspective of optimising materials design towards high-efficiency and long-lived organic photoconversion devices. Exploring different routes of molecular engineering and strategies for device architecture, guidelines for optimal materials selection and fabrication parameters will be proposed, demonstrating performance and lifetime improvements in OPV and OPD applications.

1.2 Outline

This thesis is divided into chapters, each focusing on a different aspect of the work presented. Below, a brief overview of the content of each chapter is given.

Chapter 2 lays out the fundamentals of organic semiconductor physics, with specific emphasis on working principles and candidate materials in OPV and OPD applications.

Chapter 3 introduces the experimental techniques and computational methods used for materials and device characterisation, and what information can be extracted by each of them.

The work presented in the main chapters (Chapter 4-Chapter 7) takes into consideration the role of different parameters of molecular design and device active layer engineering, and how they can be tailored to optimise the photon-to-electron conversion physics.

Chapter 4 investigates the effect of core selenium substitution and end-group modification on the photostability of nonfullerene acceptor-based OPVs. By systematic characterisation of light-induced degradation mechanisms, the role of molecular rigidification, charge delocalisation along the acceptor backbone, and intermolecular interactions is discussed. This allows formulation of molecular design guidelines towards highly-stable OPVs.

Chapter 5 studies the role of molecular conformation of small-molecule donors for evaporated bulk-heterojunction OPDs, comparing a twisted (NP-SA) and a fully planar (MPTA) structure. By analysis of light-intensity-dependent device photophysics, the origin of different trap state distributions and their impact on photodetector performance are traced back to donor molecular conformation. This work highlights how selection of OPD candidate materials should be carried out depending on the targeted device operating conditions.

In terms of device active layer engineering, Chapter 6 presents a blend-ratio dependent study of state-of-the-art blends, focusing on highly diluted Y6 bulk heterojunctions with high PM6 content. Here, it is shown that polymer-rich devices are greatly promising for OPD applications, with excellent figures of merit under moderate reverse bias. In particular, the influence of blend ratio on charge generation, charge transfer, and transport is analysed, and guidelines for synergistic optimisation of different OPD figures of merit are outlined.

Chapter 7 analyses the role of active layer thickness and acceptor choice in evaporated OPDs, where the planar MPTA donor is paired to either C_{60} or to the sublimable NFA Cl_6-SubPc. It is found that the thickness-dependent intermolecular interactions in MPTA and the mixing with the relatively big and 3D-structured NFA molecule can be successfully harnessed to tune solid-state packing. Upon thickness increase, this results in a finely intermixed BHJ architecture, with systematic MPTA orientation, leading to excellent OPD performance. In particular, the substitution of C_{60} with a NFA alternative proves to be highly successful to suppress deep-trap formation pathways in MPTA, fixing the poor efficiency under low light observed in Chapter 5.

Finally, Chapter 8 summarises the main conclusions of the work presented, and outlines the future research needed to expand the findings of this thesis and to

tackle the remaining challenges towards high-efficiency and stable photoconversion devices.

1.3 Declaration of Work

The work introduced in Chapter 4 was published in *ACS Nano* in 2021, with myself as first author.[19] The initial results were employed to fulfill the requirements for my MRes in Plastic Electronics, completed in 2019. The materials utilised in the study were synthesised in the group of Prof Yun-Hi Kim at Gyeongsang National University (Jinju, Korea). All device fabrication and most of materials characterisation was carried out directly by me. Collaborations with Dr Sooncheol Kwon (Gwangju Institute of Science and Technology, Korea) and Rhea Kumar (Imperial College London, Department of Chemistry) provided the GIWAXS and transient absorption data, respectively. The content of this chapter is adapted with permission from *ACS Nano* 2021, 15, 4, 7700–7712. Copyright 2021 American Chemical Society.

The results presented in Chapter 5 were published in *Nature Communications* in 2022, with me as lead co-author.[20] All devices and thin films were fabricated by collaborators at Samsung Advanced Institute of Technology (Suwon, Korea). Transient optoelectronic measurements (transient photovoltage and charge extraction) were carried out by Dr Jiaying Wu at Imperial College London (Department of Chemistry), while I was directly in charge of all other thin-film and device measurements and molecule simulations. Raman spectra were collected and analysed together with Dr Saurav Limbu.

The data in Chapter 6 are relative to device and thin films fully fabricated by myself. All materials characterisation was carried out by me directly, while collaboration with Dr Yifan Dong (Imperial College London, Department of Chemistry) provided the transient absorption data.

For Chapter 7, devices and thin films were provided by collaborators at Samsung Advanced Institute of Technology (Suwon, Korea). Most of sample analysis was carried out by me, in close collaboration with Dr Song Yi Park for photoemission spectroscopy and device electrical characterisation. Transient absorption was provided by Dr Yifan Dong and charge extraction and capacitance analysis by Dr Aniket Rana (Imperial College London, Department of Chemistry). Grazing incidence X-ray diffraction characterisation was carried out at the Department of Materials, Imperial College London, by Dr Andrey Berenov.

2 | Background

The molecules and different electronic devices covered in this thesis are based on the class of materials known as *organic semiconductors* (OSCs). Structured on carbon and other typically light atoms (mostly H, N, O, F, and S), OSCs show specific characteristics of electronic conduction and interaction with light, whose description requires physical models distinguished from those used for traditional inorganic semiconductors. In particular, the investigation of OSCs is not only interesting for scientific research beyond the well-established science of inorganic counterparts, but also highly relevant for potential technological development. In fact, the "special" properties of OSCs include attractive characteristics to incorporate in optoelectronic devices, such as lightweight, colour-tunability, mechanical flexibility, and biocompatibility, which represent a great promise for next-generation photovoltaics (OPVs), photodetectors (OPDs), and transistors, while organic LEDs are already a solid reality in the market. Numerous textbooks and review articles cover different aspects of OSC science,[21–25] while current frontier research is active in tackling some unsolved questions on the fundamental light-induced processes in OSCs and continuous performance improvement in OSC-based devices.[26–31]

In this chapter, an overview of chemical design options, optoelectronic, transport, and morphological properties of this class of materials will be given, especially focusing on mechanisms of photocurrent generation and charge mobility in OSCs. Further on, the physics of OSC-based optoelectronic devices - namely, OPVs and OPDs - will be introduced, and the current available strategies to enhance performance and stability will be summarised. All the full chemical names of the materials mentioned hereby are available in Appendix A.

2.1 Introduction to Organic Semiconductors

The fundamental difference between organic and inorganic semiconductors[21] lays on the nature of the charges responsible for electric conduction. In typical inor-

ganic SCs such as Si, Ge, and GaAs, low bandgap E_g (0.5-1.5 eV) and high dielectric constant (*e.g.*, $\varepsilon_r \sim 12$ for Si and GaAs, $\varepsilon_r \sim 16$ for Ge) allow for the creation of a small density of free charges by thermal excitation at room temperature, where coulombic interaction between electron-hole (e-h) pairs can be neglected. This is also true for additional density of charge extrinsically introduced for device applications: in particular, the photogenerated e-h pairs created in inorganic solar cells and photodetectors upon illumination can be described as free charge carriers. Moreover, the crystalline nature of most inorganic SCs results in a continuum of energy levels separated by the E_g, described as a band structure, with excitation process promoting an electron from the valence to the conduction band, and mobility pathways are easily established in the highly ordered molecular lattice. Even for amorphous inorganic SCs, where localised electronic states are present within the bandgap, conductivity is high as carriers in tail states can be readily excited into high-mobility bands (*i.e.*, complementing band-to-band with hopping conductivity).[32] On the other side, OSCs

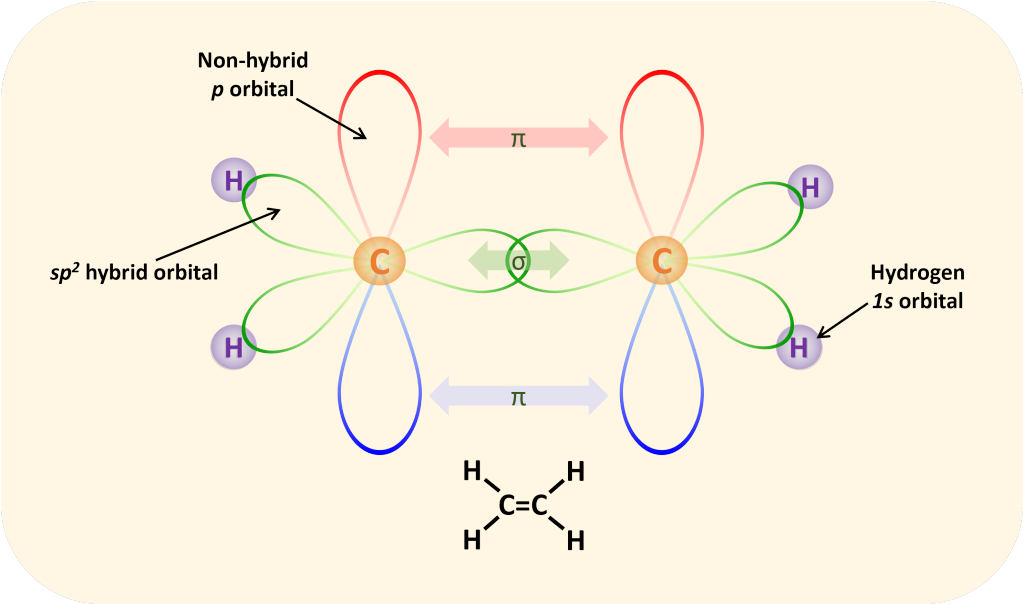


Fig. 2.1: Illustration of atomic orbital hybridisation, in the case of sp^2 hybridisation typically found in OSCs. For a carbon atom with four electrons in the *2s* and *2p* outer orbitals, the *2s* and two of the *p* orbitals assume an intermediate (*i.e.*, hybrid) character, therefore being called sp^2 orbitals. These can establish directional σ bonds, with the lobes aligned in a trigonal planar structure, while the remaining orbital retains its *p* character and forms a delocalised bond perpendicular to the plane, as illustrated here for an ethylene molecule. This π orbital is the fundamental chemical entity in OSCs, governing transport and packing properties of small-molecule and polymer materials.

are relatively large molecules based on light atoms bonded *via* hybridised orbitals (π-conjugation, see more details in Figure 2.1 schematics), where E_g is normally large (1.5-3 eV) and dielectric constant low ($\varepsilon_r \sim 3.5$). Therefore, charge density is

negligible at room temperature, and carriers can only be created by extrinsic processes such as separation of photogenerated e-h pairs, introduction of dopant species, or injection from the electrodes. Here, e-h coulombic interactions are strong, so that carriers are not free, but bound pairs known as *excitons*. Moreover, the solid-state packing of OSCs, held together by weak van der Waals interactions, is typically disordered, and discrete levels are maintained rather than bands, so that electron excitation and transport are determined by transitions between these energy levels.

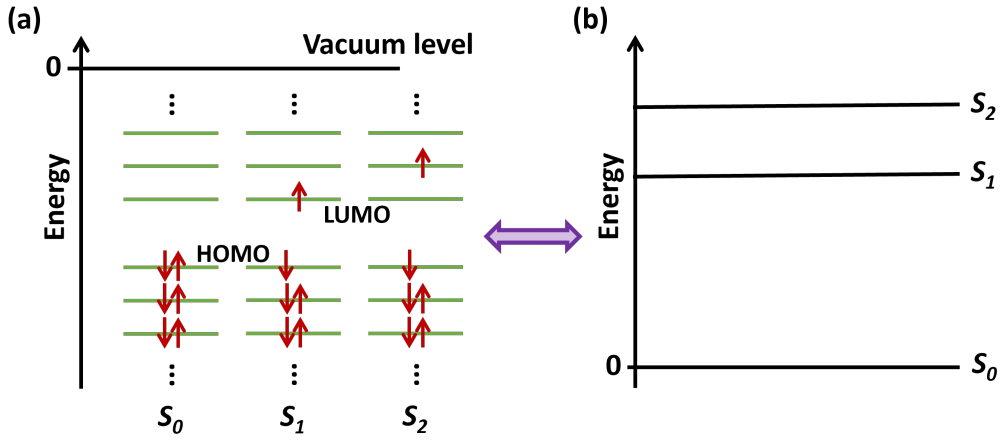


Fig. 2.2: Molecular singlet states in an orbital (a) and a state (b) representation. The former shows the energies of single-electron orbitals and their gradual filling with antiparallel spin electrons, while the latter presents the overall energy levels of the molecule in a specific electronic configuration. Note that the HOMO-LUMO difference only approximates the energy difference between S_0 and higher excited states, since it neglects any electron-electron interaction upon filling of different orbitals. In a rough approximation, the energy difference between S_0 and S_1 is lower than the HOMO-LUMO difference by the exciton binding energy, due to the stabilisation by coulombic attraction once the e-h pair is formed.

In particular, to understand the processes of light-induced charge generation in OSCs, on which both OPV and OPD operations are based, it is important to introduce a basic description of the molecular orbitals between which the transitions take place. As OSCs are molecular materials with atoms predominantly bound by hybridised C-C bonds, σ-orbitals and largely delocalised π-orbitals are formed by atomic orbital hybridisation. Based on this, overall molecular orbitals can be calculated by different models such as *linear combination of atomic orbitals* (LCAO), to describe the energetic states that charge carriers can occupy. In general, we refer to the *highest occupied* and the *lowest unoccupied molecular orbitals* (HOMO and LUMO, respectively), as the relevant energy levels between which photoexcitation occurs. In a simple picture (Figure 2.2a), this implies the promotion of an electron

from the HOMO of the molecule in the singlet ground state (S_0, with the HOMO occupied by two electrons with antiparallel spin), to the LUMO or higher levels depending on the energy of the incident photon. Therefore, the molecule passes to an excited singlet state (S_1, S_2, ...), since the electronic spin is preserved upon optical excitation. Note that in the case of charge injection this does not apply, and triplet states of the manifold T_n should also be considered.

This can be illustrated either in an orbital diagram description (Figure 2.2a), where single electrons are visualised in their respective energy levels, or in a state diagram description (Figure 2.2b), where the energies of the overall molecular states are indicated. Here, a *caveat* should be given about the exact energy position of the frontier molecular orbitals (FMOs), since the HOMO-LUMO and the ground-to-excited-state energy differences do not exactly match. Namely, the former ignores the interactions (electrostatic, exchange...) arising once the e-h pair is formed, especially the exciton binding energy of the coulombic e-h attraction. However, these expressions are normally used interchangeably in most OSC literature. For molecules with a net charge (*e.g.*, doping, charge injection...), the interactions with the surrounding environment and the coupling with local lattice distortion determines the creation of a *polaron*, which also stabilises the system energy so that polaron energy levels lie within the HOMO-LUMO gap.

Another distinction is between the HOMO/LUMO, whose difference determines the *optical bandgap* of the material, and the ionisation potential I_P/electron affinity E_A (respectively, the energy required/gained to remove/add an electron from/into a neutral molecule), whose difference determines the *electronic bandgap*.[21] In fact, the latter takes into account multi-electron correlation, and can be experimentally accessed by photoemission techniques.

Following photo-excitation, the different processes involved in photon-to-electron conversion in organic photoactive materials can be summarised as in Figure 2.3.[33] Incoming photons with energy higher than materials optical E_g (generally the lowest between the donor and the acceptor in a photoactive blend) excite the semiconductor from the ground state to the lowest-energy singlet state S_1, with excess energy typically released by thermalisation in the femtosecond timescale.[33] Excitons experience strong Coulomb attraction due to the low dielectric constant in disordered organic materials and tend to recombine, so that a donor-acceptor interface is required for effective exciton dissociation. This is generally provided by a bicontinuous interpenetrated network of an electron donor (D) and an electron acceptor (A) with respective domain size comparable with the typical exciton diffusion lengths of 5-15 nm.[34,35] This is the so-called bulk heterojunction (BHJ) approach, used in the most

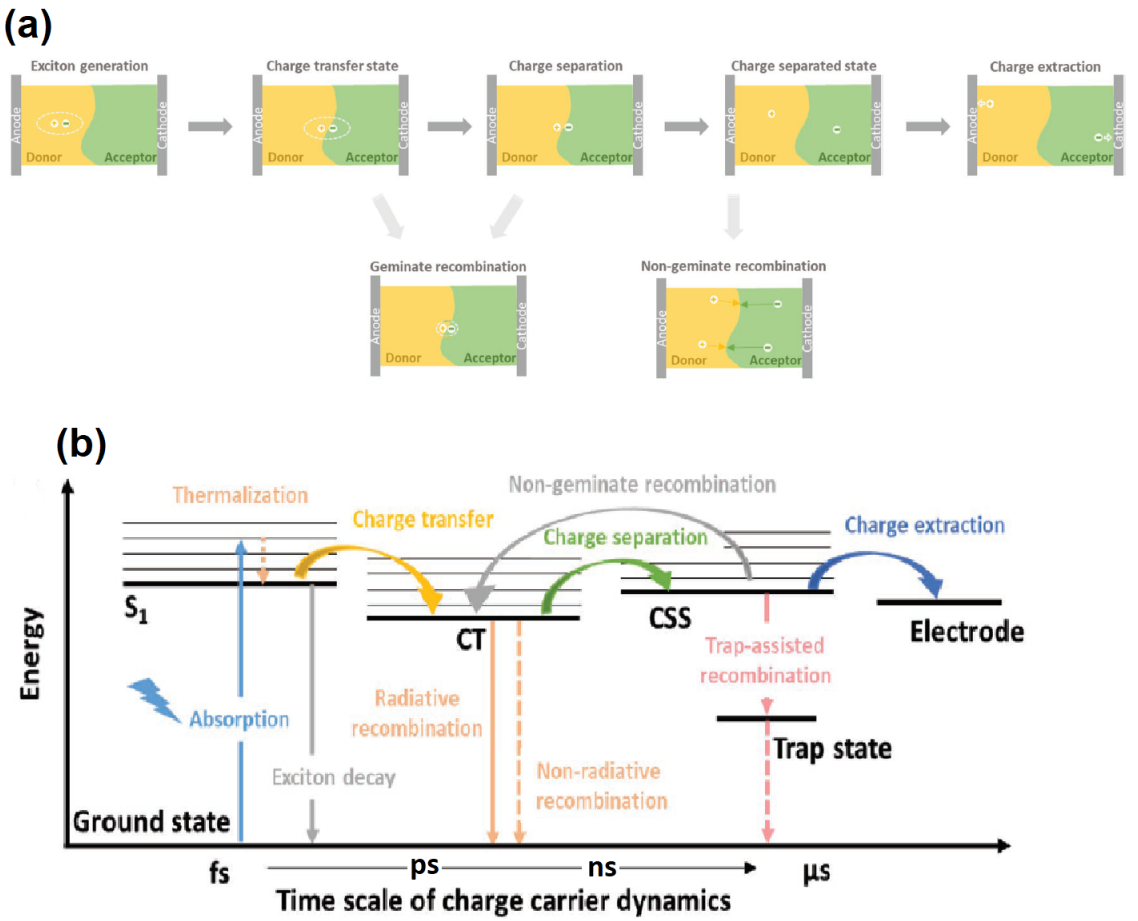


Fig. 2.3: Schematic of the steps involved in photon-to-electron conversion in a D/A system (a), with the Jablonsky diagram (b) illustrating the process from light absorption to charge extraction through the intermediate species and the timescale of each phase. Adapted from [33], with permission.

efficient OPV systems. However, bilayer architectures (*i.e.*, planar heterojunction, PHJ), or harnessing the intrinsic D-A structure of molecules (*e.g.*, for double-cable polymers or calamitic nonfullerene acceptors) are arising as valid alternatives.[36–38]

In the presence of a D/A structure, the exciton can diffuse to the interface and form a so-called CT state, a more loosely bound electron-hole pair over the D/A species with energy lower than S_1. If the CT state does not undergo geminate recombination (either radiative or non-radiative), it can split into fully separated electron and hole (charge separated state, CS), also known as electron and hole polarons referring to the electric charge coupled with the lattice distortion in analogy to crystalline inorganic semiconductors.[33] The process of CT and CS generation usually occurs in the pico to nanosecond timescale following excitation. However, more complex processes can make this picture more articulated, including the presence of triplet states as T_1 in the T_n manifold, where singlets can decay by intersystem

crossing (ISC) followed by triplet recombination or ISC of singlet CT into triplet CT with backtransfer to T_1.[35]

After the formation of a CS state, the charge carriers are driven by the materials energetics towards respective electrodes (*i.e.*, anode and cathode), but charges can also recombine by bimolecular recombination (*i.e.*, a type of non-geminate recombination where an electron and a hole originating from different excitons encounter and reform a bound CT state which then decays to S_0) or meet at a trap site (trap-assisted recombination), typically in the nano to microsecond timescale. Conversely, efficient transport ensures that electrons and holes can reach respective electrodes and be successfully extracted as electric current.

At this regard, it is worth mentioning the main concepts used to describe charge carrier transport in OSCs.[21] In particular, electronic transitions in π-conjugated materials are strongly coupled to molecular vibrational modes, so that mobile charges are accompanied by a continuous lattice distortion (*i.e.*, phonons) in their motion to form a so-called *polaron*. Therefore, electron-phonon coupling determines transport physics in these media, termed *hopping transport*, a series of non-coherent steps between localised sites.

A fundamental description of charge transport in organic semiconductors is laid out in the theoretical framework proposed by R.A. Marcus since the 1950s (Marcus theory),[39,40] with the approximation of weak coupling between neighbouring molecules A and B. In this case, localised polarons are transferred between adjacent molecules by thermally activated "jumps", which need to overcome the *reorganisation energy* λ. As schematised in Figure 2.4, this is the energy required for the geometry change in the two molecules (λ_{inner}) and in the surrounding environment (λ_{outer}) to accommodate the passage of an electron between A and B. λ_{outer} is important in solution, where solvation effects and inter-molecular displacement can significantly contribute, while λ_{inner} is predominant in typical solid-state films. In particular, $\lambda_{inner} = \lambda_A + \lambda_B$, including the energy associated with the geometrical distortion of A from its charged to neutral state, and of B from its neutral to charged state. The *polaron binding energy* E_{pol} is therefore defined as the energy difference between a molecule without and with the distortion associated with adding an electron. In the approximation of parabolic potential energies of neutral molecules and small distortions, the required energy for changing the geometry of A up to the activation of the electron transfer to B, E_{act}, corresponds to half the polaron binding energy and a quarter of the reorganisation energy $E_{act} = \frac{E_{pol}}{2} = \frac{\lambda}{4}$. In a classical description of nuclear mode statistics, it follows that the probability of the electron transfer from A and B, and therefore the *hopping rate* k_{ET}, are proportional to

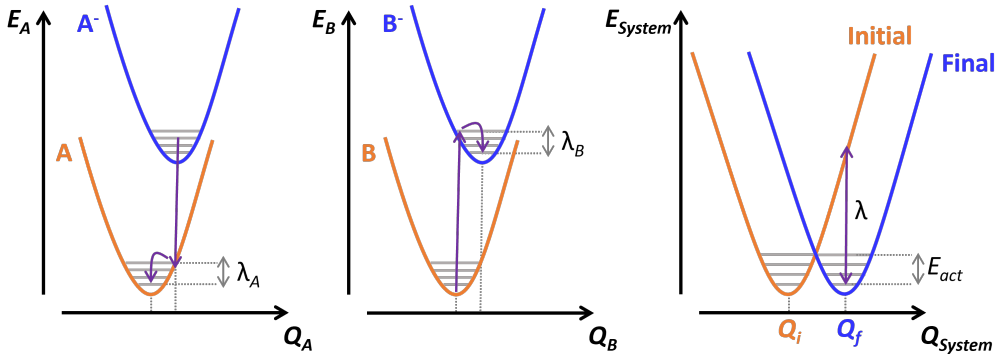


Fig. 2.4: Potential energy diagram describing the transfer to an electron from molecule A to B, as a function of the normal-mode coordinate Q. The reorganisation energies λ_A and λ_B, respectively, are required to distort A molecular geometry from the charged to the neutral state, and B geometry from neutral to charged. Overall, the process can be described in terms of system potential energy and generalised configuration coordinates (E_{System}, Q_{System}), being the charge on A in the initial state and on B in the final. For thermally-activated charge hopping, an energy $E_{act} = \lambda/4$ is required, with $\lambda = \lambda_{inner} + \lambda_{outer} = \lambda_A + \lambda_B + \lambda_{outer}$. This corresponds to the crossing point between the potential energy curves of initial and final states. Note that λ is the potential energy difference for the final state in initial and final Q_{System} configuration. The result can be derived from geometric considerations in the approximation of both parabolic potential energy surfaces with the same curvature.

$e^{-\frac{\lambda}{4k_BT}}$. Moreover, for weak coupling regimes, electronic coupling can be considered as a perturbation, so that, for phonon energies «k_BT,

$$k_{ET} = \frac{J^2}{\hbar}\sqrt{\frac{\pi}{\lambda k_B T}}e^{-\frac{\lambda}{4k_BT}}, \tag{2.1}$$

where J is the electronic transfer integral (electronic coupling), $\hbar$ the reduced Planck constant, k_B the Boltzmann constant, and T the temperature of the systems. Through Einstein relation ($D = \frac{k_BT}{q}\mu$, connecting diffusivity D and drift mobility μ) and the definition of diffusivity ($D = \frac{a^2 k_{ET}}{2}$, in one dimension), the charge mobility μ is therefore related to k_{ET} as

$$\mu = \frac{ea^2J^2}{6\hbar(k_BT)^{3/2}}\sqrt{\frac{\pi}{\lambda}}e^{-\frac{\lambda}{4k_BT}}, \tag{2.2}$$

with a being the distance between hopping sites and e the elementary charge.
This relation shows how k_{ET} and μ are affected by the physics parameters that ultimately depend on molecular structures and packing arrangement in OSC materials. In particular, high μ can be achieved in systems with strong electronic coupling J (critically related to precise orbital distribution, which can be controlled by molecu-

lar design) and low reorganisation energy λ. This can be effectively manipulated by both materials engineering (*e.g.*, planar, rigid molecules) and morphology control (*e.g.*, dielectric environment, packing structure), so that a rich toolbox is available from chemistry and physics to maximise the mobility in OSC systems.

2.2 Organic Photoconversion Devices

2.2.1 Organic Photovoltaics: Principle of Operations

A solar cell is an optoelectronic device converting the photon energy from the Sun or an artificial light source into electric current. As dictated by the nature of charge carriers and transport properties of organic semiconductors explained above, the typical OPV active layer is comprised of a BHJ with blended D and A materials, with charge separation occurring at their interface. To assess the performance of organic solar cells, the most accessible and direct characterisation is by J-V scan, where the extracted photocurrent density (J) is measured as a function of applied voltage (V). From here, typical figures of merit can be calculated. As shown in Figure 2.5, the short-circuit current density J_{SC} of a solar cell is the extracted photogenerated J when no voltage is applied to the device, and the open-circuit voltage V_{OC} is the applied voltage to stop current passing through the device. The most direct figure of the "usefulness" of a solar cell is provided by the output power density (also shown in Figure 2.5), simply the product $J \cdot V$ along the J-V curve. It can be noted that only for voltages $0 < V < V_{\mathrm{OC}}$ a positive power is delivered by the device, while at open-circuit and short-circuit conditions no power is generated. The maximum power point can be determined from the highest absolute value of power density P_{max}, with associated V_{max} and J_{max}, which is a typical condition chosen for OPV operations. The ratio between P_{max} and $J_{\mathrm{SC}} \cdot V_{\mathrm{OC}}$ provides a third important PV parameter known as fill factor (FF), quantifying the practically achievable power output of the cell with respect to the upper limit in the case of a perfectly square J-V characteristic:

$$FF = \frac{J_{max} V_{max}}{J_{SC} V_{OC}}. \tag{2.3}$$

These three parameters allow to express the power conversion efficiency (PCE) of a solar cell as

$$PCE = \frac{J_{SC} V_{OC} FF}{P_{in}}, \tag{2.4}$$

where P_{in} is the incident power density of the light source, typically set as 100 mW/cm^2 for a standard solar simulator test (AM1.5 G spectrum). Each PV parameter is related to different characteristics of the solar cell and can provide important

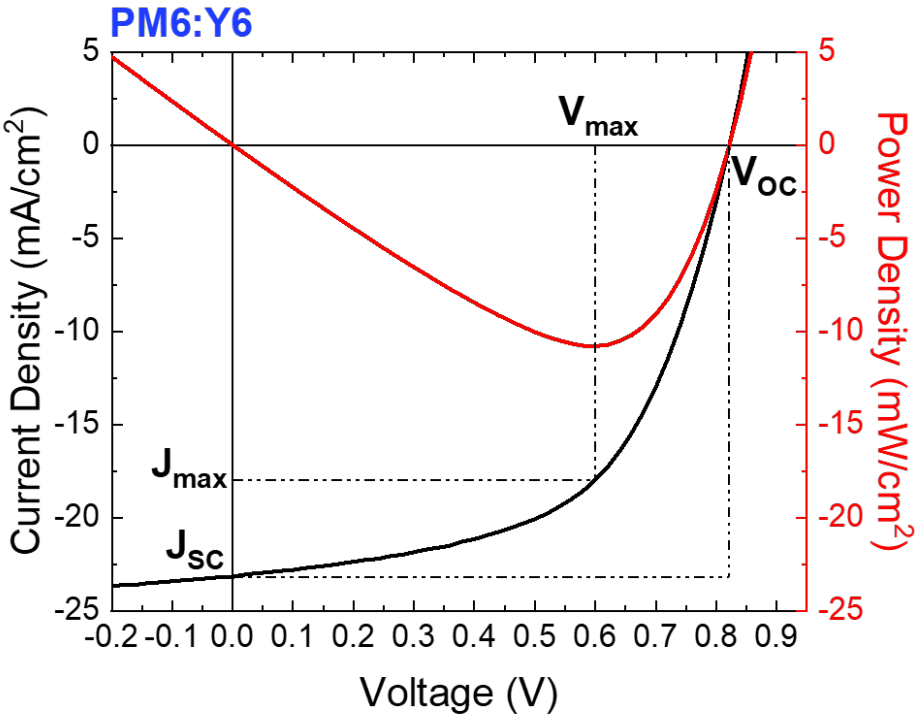


Fig. 2.5: J-V curve of a typical BHJ solar cell using PM6 and Y6 as donor and acceptor materials, respectively. The power density plot is also shown, allowing to locate the maximum power point at (V_{max},J_{max}) for FF calculation. Other photovoltaic parameters J_{SC} and V_{OC} are also indicated.

insights into device photophysics and loss mechanisms. For example, V_{OC} in BHJ OPVs is related to the energy offset between the HOMO of the donor material and the LUMO of the acceptor,[41,42] but it is also affected by the several pathways of voltage loss. In fact, an ideal solar cell described in the Shockley-Queisser (SQ) model[43] has a step-like absorption with 100% EQE above the bandgap and 0 below, and all the photogenerated carriers are collected with only above-bandgap radiative losses ΔV_{OC}^{SQ}.[28,44] In addition to the losses due to non-ideal absorption profile to match the light-source spectrum, additional voltage losses can be grouped into radiative due to below bandgap absorption $\Delta V_{OC}^{rad,belowgap}$ and non-radiative $\Delta V_{OC}^{non-rad}$, so that the overall losses are expressed as

$$\Delta V = \frac{E_g}{e} - V_{OC} = \frac{E_g}{e} - V_{OC}^{SQ} + \Delta V_{OC}^{rad,belowgap} + \Delta V_{OC}^{non-rad}, \tag{2.5}$$

where E_g is the bandgap of the photoactive blend (*i.e.*, the smallest between D and A), e the elementary charge, and $\frac{E_g}{e} - V_{OC}^{SQ} = \Delta V_{OC}^{SQ}$, as summarised in the schematics in Figure 2.6. In BHJ systems with small HOMO offsets - as the most recent based on low bandgap NFAs, where S_1 and CT states are close - $\Delta V_{OC}^{rad,belowgap}$

can be <100 meV, while $\Delta V_{OC}^{non-rad}$ dominate (typically 300-350 meV).[28,45]

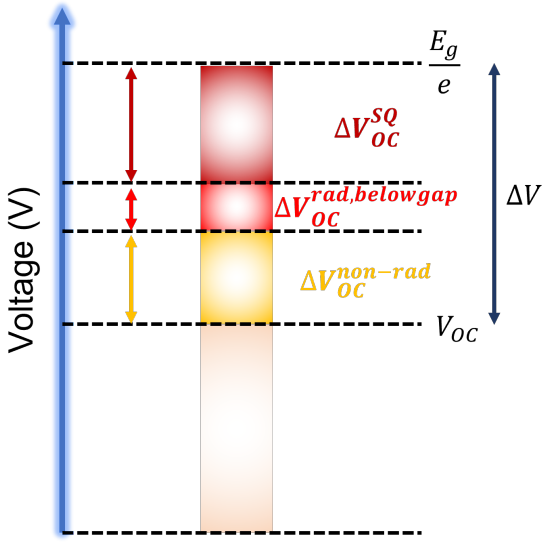


Fig. 2.6: Illustration of recombination loss fractions in OSCs, leading to an effective open-circuit voltage V_{OC} from a bandgap E_g of the photoactive system. Amount of losses due to different mechanisms are in scale of relative magnitude.

As for J_{SC}, this is largely limited by the absorption of the materials and the extraction efficiency, so that complementary D/A absorption profiles, thick active layers and optimised energy cascade with extraction layers and electrodes are essential to maximise this parameter.[46]

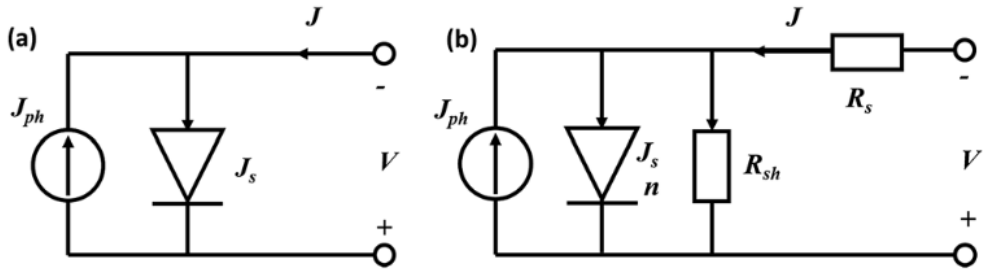


Fig. 2.7: Equivalent electric circuit representing an ideal solar cell (a), and with inclusion of lossy elements (b). From [34], with permission.

Lastly, the fill factor FF expresses how easily charge carriers can be extracted from the device in the presence of built-in potential and applied bias. In the ideal case, all the photogenerated current density J_{SC} is extracted for $0 < V < V_{OC}$, but in practice the solar cell behaviour is diodic and extraction depends on the applied voltage. This can be expressed in terms of equivalent circuit as illustrated in Figure 2.7, with the introduction of ideality factor n, series resistance R_s and shunt resistance R_{sh}. While an ideal solar cell can be schematised as an ideal diode

($n = 1$) with saturation current density J_s connected to a current generator (*e.g.*, by solar light) corresponding to a photocurrent density J_{ph}, a real solar cell is more precisely described as a non-ideal diode (n as a free parameter) connected to a resistance R_s in series and to another resistance R_{sh} in parallel. This allows to give an expression for the total current density J as

$$J = J_s[exp(\frac{e(V - JR_s)}{nk_BT}) - 1] + \frac{V - JR_s}{R_{sh}} - J_{ph}. \tag{2.6}$$

R_s and R_{sh} are thus the main factors affecting the FF in organic solar cells. In particular, R_s is contrasting charge extraction by internal resistance such as bulk resistance in the BHJ and contact resistance in the passage to transport layers and electrodes, while R_{sh} represents the leakage losses by pinholes, traps and cell edges. Therefore, to maximise FF both a low R_s and a high R_{sh} are needed, which can be achieved by careful device optimisation. Examples include selection of best interlayers for band alignment, tailoring of domain size and purity, control of packing orientation and distance, and engineering of vertical concentration gradients,[34] although universal strategies for high FF are still subject of current research in the OPV field.

2.2.2 Organic Photodetectors: Principle of Operations

Since their first appearance in the early 80s,[47] organic semiconductors for photodetecting applications have gained increasing momentum, and they have been successfully utilised in a wide range of applications. Thanks to several advantages over inorganic counterparts, OPDs are currently employed in a variety of fields spanning from imagers (such as full-colour,[48] NIR,[49] X-ray,[50,51] or bioimagers[52]) to biomedical applications (artificial eyes,[53] chemiluminescence,[54] pulse-oximetry[55,56]), from security devices to optical communications.[57,58] In particular, some of the characteristics making organic materials attractive candidates for photodetector fabrication are, similarly to solar cells, low production costs, facile device engineering, and useful mechanical properties such as stretchability and bendability.[14] The strong light absorption in OSCs (optical absorption coefficient $\sim 10^5$ cm^{-1} *vs.* $\sim 10^3$ cm^{-1} for Si) opens up possibilities for thin active layers.[59] Moreover, the tailorable optical and electronic properties of organics make them particularly suitable for OPDs, where the spectral detection range can be tuned without the need for colour filters.[14] However, due to the intrinsically different photophysics based on strongly bound e-h pairs and hopping transport, OPDs are still lagging behind inorganic counterparts in all performance metrics, especially when it comes to performance reproducibility

and consistency for device commercialisation.

In this paragraph, the operation mechanisms and figure of merits of OPDs will be introduced, and a brief review of the state of the art in OPD field will illustrate the current guidelines for materials design and device architecture for high performance devices.

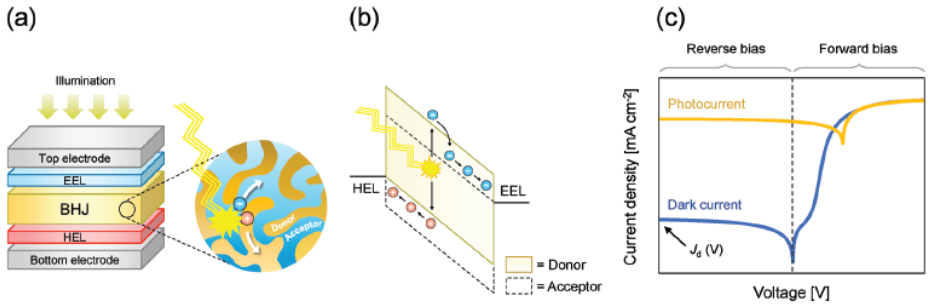


Fig. 2.8: (a) Schematics of a typical OPD device architecture, with the BHJ active layer sandwiched between hole/electron extraction layers (HEL/EEL) and respective electrodes. Large area of D/A interfaces is crucial for separation of electron-hole pairs, as shown in the inset. (b) OPD energetics diagram, with example of photogenerated carriers excited in the donor and separated by the D/A LUMO offset. (c) Typical *J*-*V* curves for an OPD device in dark and under illumination, with indication of the region of interest for the evaluation of performance metrics (J_d is evaluated in the reverse bias region). From [60], with permission.

The operational mechanisms of OPDs can be understood in analogy to OPVs. As schematised in Figure 2.8a for the case of a BHJ active layer, incoming photons are absorbed by semiconducting materials, with exciton generation followed by CT formation and dissociation at the D/A interface. However, the purpose of OPD devices is to generate an electrical signal in response to light stimulation, which is maximised under reverse electric field by increased band bending towards respective electrodes (Figure 2.8b). This corresponds to operating in the negative voltage portion of the *J*-*V* curve (Figure 2.8c), known as photoconductive mode,[60] where the signals detected with or without photoexcitation are respectively known as photocurrent and dark current densities (typically reported at a specified voltage).

In particular, OPDs aim at delivering photocurrent in response to a light input of desired wavelength, so that engineering of active materials is crucial in OPD design to maximise absorbance and charge generation within the target spectral range. Since OPDs operate under an applied reverse field and do not generate a net power output, specific figures of merit are required to assess their performances, which differ from the usual parameters used for photovoltaics.[60]

First and foremost, an efficient photon-to-electron conversion is desired, which

can be quantified in terms of **responsivity** R (expressed in A W^{-1}), defined as the ratio between the output photocurrent density J_{ph} and the incoming light intensity P_{in}:

$$R = \frac{J_{ph}}{P_{in}}. \tag{2.7}$$

Alternatively, **external quantum efficiency** (EQE) can be used - *i.e.*, the number of generated electrons per incident photon discriminated by wavelength:

$$EQE = R\frac{h\nu}{e}, \tag{2.8}$$

where h is the Plank constant, ν the incoming radiation frequency, and e the elementary charge. In microscopic terms, the process of photon-to-electron conversion can be expressed as EQE efficiency[59]

$$\eta_{EQE} = \eta_A \eta_{ED} \eta_{CT} \eta_{CC}, \tag{2.9}$$

where the final EQE is dictated by the efficiency of light absorption (η_A), exciton diffusion (η_{ED}), CT state dissociation (η_{CT}), and charge collection (η_{CC}). Depending on the OPD application, it may be preferred to achieve high EQE over the whole spectrum (broadband OPDs), or to narrow it down to a specific range for colour-selective photodetection, typically defined for a Gaussian-like EQE with FWHM lower than 100 nm. This can be realised by materials engineering or manipulation of device architecture, such as exploiting the microcavity effect in narrowband OPDs.[61] Since OPDs are generally operated in reverse bias, it is also crucial to assess the R trend with increasing electric field, and to identify the optimum balance between R and dark current depending on the applied voltage.

For practical applications in optoelectronics, another crucial figure of merit is the **photoresponse speed**, defined as the time required from light excitation to charge extraction to the electrodes. In particular, **rise** and **fall response times** (τ_{rise}, τ_{fall}) are measured between 10% and 90% of the normalised photogenerated signal, and **frequency response** is determined for an output reduction by -3 dB (also indicated as *cutoff frequency*, f_{-3dB}). Accurate analysis is usually performed by photocurrent transient characterisation with time-of-flight or small perturbation methods like impedance spectroscopy. Photoresponse times are generally in the μs timescale for organic-based systems, while rare examples in the sub-μs range are also found.[61–63] This is not reaching record performance of inorganic counterparts (*e.g.*, response times can be <1 ns in commercial Si and InGaAs PDs), but it is fast enough for imaging devices with standard interframe time of ms order. Due to the

low mobility of organic semiconductors, the carrier transient time τ_{tr} is typically considered the main contribution to the photoresponse time, whereas this should always be compared to the RC-time τ_{RC} due to the resistance R and the capacitance C of the circuit (affected by factors such as pixel area, thickness of all the layers in the device, and circuit configuration in measurement equipment). Where τ_{tr} is the dominant time constant, photoresponse speed is generally limited by the slowest between electron and hole mobility, which can be significantly affected by active layer design such as polymer:NFA solution-processed BHJ as opposed to co-evaporated small molecule systems. Other factors to take into account are the electric field[64,65] and the active layer thickness,[66] while temperature[67] and light intensity[68] indirectly affect mobilities *via* carrier density. Moreover, longer exciton diffusion lengths are crucial for fast photoresponse, and can be achieved by BHJ design and reduction of trap density.[69,70]

To quantify the sensitivity of photodetectors, a fundamental parameter is the **noise equivalent power** NEP, defined as the minimum signal power detectable above noise (*i.e.*, for which signal-to-noise ratio SNR is 1). This can be expressed in terms of R as

$$NEP = \frac{I_{noise}}{R\sqrt{B}}, \tag{2.10}$$

with I_{noise} the noise current and B the bandwidth of detection. The NEP reciprocal normalised by the device area A is the specific detectivity D^*, directly proportional to EQE through the noise spectral density S_n:[71]

$$D^* = \frac{R\sqrt{AB}}{I_{noise}} = \frac{e\lambda\sqrt{A}}{hc}\frac{EQE}{S_n}, \tag{2.11}$$

with λ the wavelength of incident light and c the speed of light. Its unit of measurement, cm $Hz^{1/2}$ W^{-1}, is often quoted as Jones in the photodetector community. For a detailed expression of D^*, all factors contributing to noise in the device should be taken into account. Typically, the main component of dark current fluctuations (*i.e.*, the noise due to processes other than photogeneration by the excitation source) is considered to be the shot noise I_{shot}, originated from the discrete nature of charges and depending on the dark current I_d flowing through the detector without any light stimulation ($I_{shot} = 2eI_dB$).[72] In this approximation

$$D^* \approx \frac{R\sqrt{AB}}{I_{shot}} = \frac{R\sqrt{A}}{\sqrt{2eI_d}} = \frac{R}{\sqrt{2eJ_d}}, \tag{2.12}$$

with J_d the **dark current density**. However, to avoid overestimation of D^*, other sources of noise should be also accounted for. These include thermal noise I_{th}, di-

rectly proportional to the device temperature T square root and inversely to the shunt resistance R_{sh} square root ($I_{th} = 2\sqrt{\frac{k_B T B}{R_{sh}}}$, with k_B the Boltzmann constant); the flicker noise $I_{1/f}$, with S_n inversely related to the frequency f of the signal; the generation-recombination noise I_{g-r}, expressed in terms of carrier lifetime τ with a Lorentzian spectrum $S_n = A\frac{\tau}{1+(2\pi f\tau)^2}$ (A is a constant depending on the variation of carriers in the device).[72,73] Since a precise estimation of the different I_{noise} components is practically challenging, reported D^* often take into account only I_{shot} and consider J_d constant at a specified reverse bias, with the *caveat* of its dependency on applied electric field.[60] Since the dark current is one of the most important parameters to determine OPD performances, negatively affecting SNR and D^*, the investigation of its origin is an intriguing topic of ongoing research in the OPD community. In particular, the mechanisms of dark injection from the contacts into the Gaussian DOS of the active layer HOMO/LUMO and the thermally-activated generation within the active layer are considered the dominant processes to tackle for J_d reduction.[60] However, recent studies report trap-assisted charge generation, dominated by mid-gap traps, as one of the determinant origins of J_d.[71,74] At present, strategies such as materials engineering for DOS narrowing and trap density reduction, and careful device architecture (*e.g.*, blocking layers,[75] bilayer structure in active layer[76,77]) allow to limit J_d to 10^{-9}-10^{-11} A cm^{-2},[78–81] with constant work to push these records further. This will be the specific subject of Chapter 5, where the control of shallow-trap DOS is achieved by conformational planarity in small-molecule donors for evaporated OPDs. In particular, this enhances device performance by both J_d reduction and increase in photodetection speed at relatively high light intensities.

Finally, the **linear dynamic range** (LDR) is also an important figure of merit to evaluate, defined as the light intensity range over which the photogenerated current is linearly proportional to the input light intensity. This is expressed in decibel as[82]

$$LDR = 20log\frac{P_{max}}{P_{min}}, \tag{2.13}$$

where P_{max} and P_{min} are respectively the maximum and minimum optical power generating linear electrical response. The lower limit of LDR is generally attributed to the NEP, while the maximum detectable signal is typically determined by resistive behaviour in the device, including series resistance from the electrodes and charge collection resistance for high carrier density under strong light intensity,[83–85] so that device architecture and balanced BHJ mobilities are important factors for extending LDR.

2.3 Materials Choice for Photoconversion Devices

At its initial stage, the OPV and OPD field was strongly dominated by fullerene acceptors (FAs), where the good electron transport properties, low-lying LUMO and well-established synthetic routes brought forward C_{60}- and C_{70}-based materials as the preferential candidates as electron acceptors. Although optical, electrical and morphological properties can be tuned in fullerene derivatives such as PCBM, ICMA and ICBA,[86] the available chemistry is quite limited, and FAs are all limited by a low light absorption in the visible and infrared, relatively strong V_{OC} losses, and morphological instability leading to poor device lifetime.[45,87]

These issues have been widely overcome by the advent of NFAs, which showcase an abundant list of advantages over FA counterparts.[31,87] Whereas the first NFAs were based on fused diimides with poor morphology and very low efficiencies, the skyrocketing advances in NFAs has started in the mid 2010s with the synthesis of fused-ring electron acceptors (FREA) based on A-D-A conjugated structure. In particular for OPVs, great chemical tunability gives broad opportunities to match FMO levels of donor materials, good visible and NIR absorption extends the coverage of solar spectrum for high current generation, and facile morphology control limits device degradation and improves lifetime.

Although for evaporated OPDs C_{60}-based materials are still largely utilised,[88,89] NFAs are emerging also in this field for their multiple benefits, including higher visible-NIR absorption, tunable energetics, and superior light and thermal stability.[90–92]

Matching with suitable donor materials, either polymer or small-molecule-based, is also key to desired performance of photoconversion devices, and their evolution has been parallel to the one of NFAs. The choice of D:A pairs is particularly relevant for spectrally selective OPDs, where the absorption range of BHJ components plays the crucial role.[59] For example, UV-light can be probed by large E_g materials reaching up to 280 nm,[93–95] which are relevant for biological, industrial, and aerospace applications. On the other side, conjugated polymers[96–102] or small molecule families such as phthalocyanines, porphyrins,[103] and squaraine dyes[104–106] are suitable for infrared OPDs, in high demand for optical communications, night vision, and environmental monitoring. Examples include the polymers LBPP-1,[107] with response up to 1200 nm, and TQ-T, extending over 1800 nm.[108] NIR applications can also benefit from the direct harvesting of interfacial CT states, as demonstrated in P3HT:PCBM OPDs detecting up to 950 nm.[109] However, low E_g materials tend to suffer from high leakage currents, and the use of injection barriers to bypass the problem can be detrimental to photocurrent.[110] Finally, the combination of

multiple organic materials can result in successful demonstrations of panchromatic OPDs for full-spectrum photodetection. Blends of low-E_g polymers and PCBM[111] achieve a $D^* > 10^{12}$ Jones between 300 and 1450 nm, while a conjugated polymer with DTBTT donor and thienoisoindigo acceptor units[101] shows a detection range extended from 300 to 1600 nm.

In this paragraph, a brief review on the advances in chemical design of NFAs and matching donor materials will be given, with a special emphasis on the critical molecular sites to act upon for NFA functionalisation and control of optoelectronic properties.[31,112]

2.3.1 Families of Nonfullerene Acceptors

Detailed discussion of historical development in NFA design, initially targeted for OPV applications, is given in Appendix B. Overall, the main NFA families can be summarised as follows, depending on the structural features of the π-conjugated backbone, with examples of chemical structures of common fullerenes, NFAs, and donor polymers illustrated in Figure 2.9. These NFA materials have been originally developed for OPV applications, but they are recently demonstrating great potential in OPD devices as well.

- **Rylene diimide NFAs**: At the beginning of NFA research, the fused aromatic structure of rylene diimides appeared promising thanks to the high electron mobility, facile chemical modification at different positions, high absorption coefficient, shallow LUMO, and good stability.[113–115] From initial fully-fused examples such as perylene diimide,[116–118] several derivatives have been synthesised to prevent excessive aggregation and enhance photocurrent generation, including *via* molecular functionalisation[119–122] or dimerisation,[123,124] approaching a 10% PCE with matching donor polymer.[125] However, further performance improvement is unlikely, primarily due to the challenging morphology control, as well as to the large bandgaps having limited compatibility with the state-of-the-art donor materials.
- **A-D-A calamitic NFAs**: Harnessing the intramolecular push-pull interactions between donor and acceptor building blocks alternating along the conjugated backbone is an effective route to reduce E_g and increase absorption coefficient, in the so-called *calamitic* NFAs. The first examples have been designed with an A-D-A structure,[126] where HOMO and LUMO levels can be easily tuned by functionalisation of respective units. Prototypical molecules in this family include ITIC,[127] comprised of an IDTT core and DCI end groups,

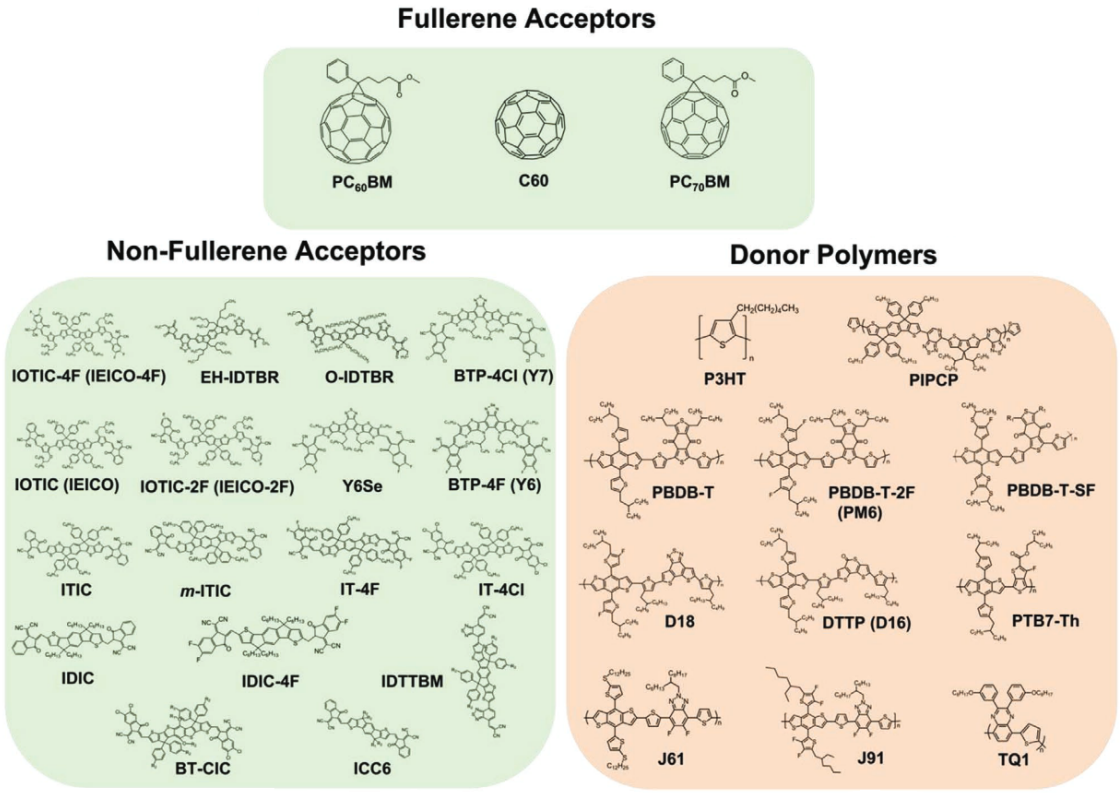


Fig. 2.9: Molecular structures of some of the most commonly OPV materials, including fullerene derivatives, donor polymers, and NFAs. Adapted from [35], with permission.

and O-IDTBR,[128] with an IDT core, BT spacers, and rhodanine end units. A-D-A acceptors are highly versatile in their molecular design, as all the elements of their chemical structure can be engineered to tune optoelectronic properties and self-assembly in solid state. For example, core extension can increase conjugation length and tune ICT,[129] end-group functionalisation shifts FMOs and regulates π-π stacking,[130–132] while nonconjugated side chain design (length, branching, alkyl *vs.* aromatic...) affects packing and charge mobility,[127,133–135] with demonstrations of PCEs approaching 15%.[132] The role of different core and end-group design rules in ITIC-derivatives for optimising efficiency and stability of OPVs will be investigated in Chapter 4, combining selenium substitution in the core and methylation of end groups.

- **A-DA′D-A calamitic NFAs**: Further ICT enhancement, increased absorption and photocurrent generation, and E_g towards the infrared region have been realised by replacing the central D unit with a DA′D moiety, where A′ indicates a further acceptor unit within the donor core.[136,137] In particular, this has been applied in the now dominating Y-family of NFAs,[138,139] breaking performance records with PCEs approaching the 20% threshold.[10–12] Also in

this case a plethora of molecular engineering routes is available, such as by fine-tuning of DA′D structure,[140–142] end-group halogenation,[143–146] and side-chain optimisation. This is particularly crucial in Y-series NFAs, where two pairs of nonconjugated side chains can be selected at different core positions (*i.e.*, β-position of outer thiophenes and central pyrrole). By combination of different side-chain characteristics, intermolecular spacing, crystalline formation, interactions with donor polymer, and molecular orientation can be controlled towards maximised charge generation and effective transport,[11,147–150] which is the current frontier towards record device performance.[11]

- **Other NFAs**: Other notable non-FREA NFA groups to mention are the sublimable small molecules of the phthalocyanine,[151] subphthalocyanine (SubPc),[152] and coronene[153] families. In particular, SubPc derivatives have shown wide energetic tunability to match a large choice of donors in OPD and OPV applications,[152,154] and the effective morphology control in SubPc-based BHJs will be the subject of Chapter 7.

2.3.2 Optoelectronic Properties of High-Performance Nonfullerene Acceptors

Overall, calamitic A-DA′D-A NFAs of the Y-family[136,137] are greatly promising for overcoming the 20% *PCE* threshold not only due to the extended absorbance and enhanced NIR harvesting, but also for the special characteristics of exciton diffusion and charge dissociation dynamics. This also holds a great potential for OPD applications, as illustrated in Chapter 6. Across multiple studies, several beneficial factors have been pinpointed in Y6 systems, such as a long exciton lifetime,[155] high electroluminescence quantum efficiency,[156] small reorganisation energy for electron-hole pair formation (λ_e,$\lambda_h \sim 80$ meV),[157] and barrierless CT-to-CS conversion[158] by interfacial band bending, caused by the sizeable quadrupole moment of A-DA′D-A NFAs.[159] All these characteristics are key to minimise radiative and non-radiative recombination and to maintain small voltage losses in devices. Moreover, charge generation and transport dynamics in Y-series also benefit from a peculiar packing motif, where intermolecular interactions are not only possible *via* end-group π-π stacking, but also through the core D′ unit, creating a 3D network for charge hopping.[157] In fact, the curved banana shape with high dipole moment and the A-DA′D-A structure enhance intermolecular interactions for strong electronic coupling ($J \sim 38$ meV in multiple lattice directions).[160] A complex and adaptable crystalline packing is formed even by spin-coating fabrication, including monoclinic and triclinic polymorphs,[157,160–162] where ambipolar transport with high mobility (μ_e and

$\mu_h \sim$ 2-5$\times 10^{-4}$ $cm^2V^{-1}s^{-1}$) is possible.[139,157,160,162]

2.3.3 Choice of Donor Materials

Concurrently, the fast advance of NFAs has only been possible thanks to the parallel evolution of matching donor polymers. For solution-processed devices, initial homopolymers such as P3HT[81,163] have been gradually replaced by D-A copolymers, and their optoelectronic and transport properties have been tuned through heteroatom substitution (*e.g.*, fluorination as in PM6), building block matching with NFAs (*e.g.*, D18), and side-chain engineering for packing control.[35,164–166] For both OPV and OPD applications, excellent photodetection has been achieved with DPP,[167,168] BDT,[127,169,170] and TQ units.[171,172] Overall, desirable characteristics for polymer design include: 1) suitable HOMO energetics[173] to maximise V_{OC}, reduce dark hole injection and enhance E_{CT}, all beneficial for low J_d;[174] 2) specific backbone units and side chains to tune packing order and orientation, such as short alkyl chains;[175,176] 3) additional functional groups to control vertical segregation towards relevant electrodes, such as EDOT side chains giving beneficial interaction with PEDOT:PSS interlayer for ultralow J_d;[173] 4) depending on the targeted applications (especially for OPDs), polymer E_g should be tuned to control spectral response, and suitable low E_g materials can be designed for IR OPDs (currently up to 1600-1800 nm[101,108]).

In the new frontier of ternary devices, the synergistic use of two donor polymers is successfully employed to balance packing order with effective D/A intermixing. For example, the combination of semi-crystalline PM6 with highly crystalline D18 perfectly optimises this trade-off, with PM7:D18:L8-BO OPVs showing a delicate double-fibril network where recombination and transport losses are minimised for a record PCE of 19.6%.[177]

For evaporated BHJs, especially utilised as OPDs, small-molecule donors need to be selected, typically based on dipolar D-A structures.[178–180] The importance of molecular design in these materials will be treated in Chapter 5, comparing twisted and planar donors for evaporated OPDs and how the geometric conformation affects shallow and deep trap formation and overall photodetection speed.

2.4 Efficiency Challenges

Although efficiency records for organic photoconversion devices are following rapidly with development of new NFAs, we are still far from unveiling their full

potential. As for OPVs, *PCE*s have not yet overcome the 20% barrier in single-junction devices, which is well within reach in the context of the Shockley-Queisser theory,[181,182] even taking into account the additional losses unavoidable for OSCs (*e.g.*, disorder at the absorption band edge). For this ambitious goal, the main challenges to face can be ascribed to morphology control, increase in absorption and charge generation and reduction of voltage losses, which are ultimately all interconnected and need to be synergistically addressed.[35]

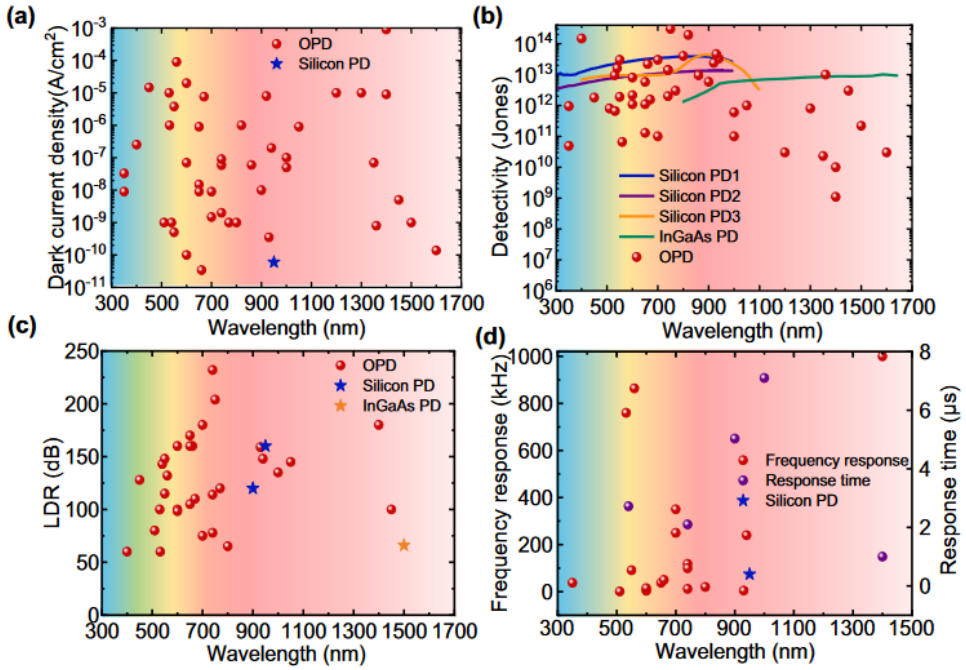


Fig. 2.10: Comparison of state-of-the-art OPD figures of merit with inorganic counterparts, depending on spectral range of photodetection. From [14], with permission.

As for OPDs, a comparison with their state-of-the-art performance with Si-based commercial devices shows the great promise of organic materials for next generation electronics, but also the challenges which still need to be tackled for full competitiveness.[14] As shown in Figure 2.10, only very few OPD examples exist with lower J_d than Si references ($\sim 10^{-10}$ A cm^{-2}),[81] with common values several orders of magnitude higher than Si-PDs. Although for OPDs a specific detectivity of $\sim 10^{12}$ Jones is considered high, record D^* above inorganic counterparts (*i.e.*, $\sim 10^{14}$ Jones) are occasionally reported,[183,184] while *LDR* is already rivalling Si and InGaAs PDs, exceeding 200 dB.[111,185] In terms of response speed, the challenge to achieve fast-response OPDs still remains, with state-of-the-art devices below Si performances, and most OPDs showing a τ_{rise}/τ_{fall} of several µs.[81] To further improve OPD figure of merits, similar challenges to those found in OPV field need to be tackled, including the optimisation of light absorption and charge generation, enhancement

in transport properties, and morphology control.

For both OPVs and OPDs, these key challenges can be addressed both by materials design and device engineering, although the requirements for optimum device performance differ for photovoltaics *vs.* photodetector operations.

2.4.1 Morphology Optimisation

Firstly, in terms of morphology optimisation in OPVs, it is well-known that BHJ formation requires a delicate trade-off between D/A interpenetration for high exciton yield, favourable crystalline packing and domain purity with continuous percolation pathways, and presence of amorphous phases at the D/A interface.[46,163,186] These were extremely hard to simultaneously achieve in FA OPVs due to the tendency to segregate,[187,188] dimerise,[189] or too finely intercalate[179] of small fullerene buckyballs. However, the effective intermolecular interactions in FREAs,[190] strong quadrupole moments,[158,159] and large dimensions[191] allow for a more favourable self-assembly in BHJ, reaching an optimised 3D structure without strict need of solvent additives or annealing treatments.[139,192] As identified in several works, morphological features to optimise include π-π stacking distance, crystalline order, domain size and purity, intermolecular orientation, 3D packing network, and interaction strength between D and A moieties.[35,46] For example, a predominant portion of high molecular weight (M_W) polymer has been shown desirable due to the closer D/A packing and stronger electronic coupling between donor and acceptor molecules, with increased rate of charge transfer.[193] Moreover, thermal annealing has been widely employed to tune phase separation and enhance packing order, leading to higher carrier mobility and increased photocurrent generation.[186,194] Molecular engineering on both NFAs and matched donors also strongly affects the BHJ structure, as demonstrated with fluorination as a way to improve π-π stacking order, charge transport, and photocurrent extraction.[195–197] More recently, record performances in OPVs have been demonstrated by accurate morphology control in ternary BHJ with two donor polymers, where a double-fibril network is formed to synergistically optimise exciton diffusion, CT separation, as well as transport (see Figure 2.11b).[177]

Morphology optimisation is also crucial for OPD performance, but the ideal domain size to achieve in BHJ is different from the OPV case. Optimum morphology can be analysed in terms of miscibility of the blend components using Flory-Huggins interaction parameters χ.[198–200] In OPDs for low-bias applications (*i.e.*, no gain mechanisms), medium χ values are preferential for suitable domain separation, although operation in reverse bias allows smaller domain size compared

to OPVs.[179] In fact, electric-field assistance ensures effective CT dissociation and charge extraction even at D/A large interfacial area, so that fine BHJ intermixing increases the photocurrent yield (see Figure 2.11c). Optimum BHJ morphology can be achieved by processing methods such as thermal and solvent vapour annealing or solvent additives.[201] For example, DIO processed OPDs show greatly suppressed J_d due to better D/A interfaces and improved transport,[202,203] while beneficial vertical segregation and smoother BHJ for higher mobility can be achieved by heating above the glass transition temperature.[204–206] Examples of different approaches for morphology optimisation are illustrates in Figure 2.11.

Morphology control in OPDs will be explored in the following of this thesis. In particular, Chapter 6 presents the advantages of a donor-rich BHJ to enhance transport and suppress J_d thanks to the interconnectivity and large bandgap of the polymer matrix. Furthermore, Chapter 7 shows how substituting a fullerene with an NFA in small-molecule evaporated OPDs can optimise BHJ formation towards elimination of morphological traps.

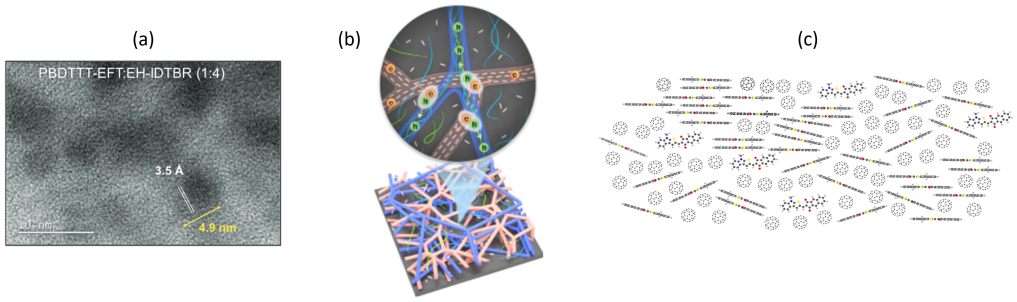


Fig. 2.11: Examples of morphology optimisation in OPV and OPD systems. (a) Polymer:NFA BHJ transmission electron microscopy images, showing domains of pure EH-IDTBR of ∼5 nm dimension, suitable for effective exciton dissociation in OPVs (adapted from [207], with permission). (b) Schematic depiction of a double-fibril network morphology formed in ternary D:D:A OPV blends (from [177], with permission). (c) Finely intermixed blend morphology in optimised small-molecule based OPDs, where domain segregation is only preserved at the nanoscale (see detailed discussion in Chapter 5).

2.4.2 Enhancing Charge Generation

Secondly, in terms of charge generation, the appearance of NFAs has completely changed the interpretation of the involved photophysical mechanisms. For large E_g FAs, it was held that the difference between singlet exciton energy (E_{S_1}, for the relevant photoexcited species) and the energy of the CT state (E_{CT}) drives charge dissociation, so that a minimum D/A HOMO difference is necessary for efficient photocurrent generation. Following CT state formation, a sufficient delocalisation

(*i.e.*, over 4 nm) should be reached to overcome coulombic capture and a CT binding energy of ≈500 meV.[208] Therefore, a driving force E_{S_1}-E_{CT} over 300 meV was considered a strong requirement for FAs, with severely compromised OPV efficiency for lower offsets.[209–211]

This paradigm has been completely transformed with the advent of NFAs, showing impressive charge generation efficiency even at ultra-low HOMO offsets (*i.e.*, <100 meV).[158,212] This is highly beneficial to reduce energy losses associated with charge generation, so that high V_{OC} and J_{SC} can be achieved at the same time. However, requirements for minimum HOMO offsets still hold, and an optimum ΔHOMO of 140 - 240 meV has been proposed from different studies.[155,195] An important *caveat* is about the experimental technique used for energy level characterisation, since ΔHOMO in NFA systems can appear less "ultra-low" if measured by photoemission techniques compared to cyclic voltammetry.[213] For example, Karuthedath *et al.*[159] suggest an ideal offset of 500 eV for maximized photovoltaic internal quantum efficiency (IQE_{PV}), using ultraviolet photoemission spectroscopy for HOMO measurements. Moreover, they argue that the strong NFA quadrupole moments induce interfacial band bending, creating a favourable cascade for CT-to-CS conversion, but a barrier for exciton-to-CT, so that the proposed minimum HOMO offset is required. This strong quadrupole moment of NFAs can tune the energy levels for the same material with varying molecular orientations. In a recent work, Fu *et al.*[214] explore these molecular-orientation dependent energetics in Y6 layers deposited from different solvents, showing a 200 meV offset between films with preferential face-on or edge-on orientation, which matches with energy level simulations for corresponding packing structures. This can open up new frontiers beyond the BHJ concept, such as bilayer or even single-component OPV and OPD devices,[190,215,216] where the ΔHOMO at differently-oriented grain boundaries in polycrystalline NFAs can provide the driving force for charge separation.

Although a low ΔHOMO is beneficial to minimise voltage losses,[217] this is at the expense of charge generation dynamics, slowing down hole transfer up to ∼10 ps,[195] which is also affected by the slow diffusion to D/A interface. Therefore, efficient charge generation requires an interplay of different characteristics in addition to minimum driving energy, and the fine optimisation of these is key to paving the way towards >20% PCE in OPVs and high D^* in OPDs. In particular, requirements include tuning of interfacial D/A electrostatics, close D/A packing for strong electronic coupling, large D/A contact area, low CT reorganisation energy, and the harnessing of further intermolecular excited states with low binding energy, all of which can be controlled by molecular design as well as morphology engineering.[35] In

addition, reducing energetic disorder and shallow trap presence is crucial for efficient and fast charge generation.[212,218] NFAs appear to be promising at this regard, with Urbach energies lower than 30 meV, so that geminate trap-induced CT recombination can be minimised.[142,219] Trap density reduction is also key to suppressed J_d and fast photoresponse in OPDs,[71,74] as discussed in Chapter 5. Finally, although Förster resonance energy transfer (FRET, *i.e.*, the transfer of a photon between two molecules by dipole-dipole coupling) has been recently studied as a common pathway for photon harvesting in low-E_g NFAs, it should be noted that this is not a desirable characteristic in record-breaking OPVs, since it is indication of sub-optimal BHJ structure.[193,195] In fact, FRET can be active over several nanometres, longer than the range of CT, so that it is typically involved when a too segregated morphology makes charge generation arduous.

2.4.3 Control of Voltage Loss

Finally, another crucial factor towards high-performance photoconversion devices is the minimisation of the voltage losses involved in charge generation, introduced in Subsection 2.2.1. This is not only essential to maintain high V_{OC} in OPVs, but also to suppress J_d in OPDs (detailed discussion in Chapter 6). Whereas radiative losses from geminate recombination can be limited to as low as 200 meV for high *PCE* OPVs, ample room is available for reduction of non-radiative losses $\Delta V_{OC}^{non-rad}$.[44,220] These are currently in the 200-550 meV range, and need to be pushed below 150 meV for approaching the benchmark of 20% *PCE*.[221,222]

In addition to small E_{S_1}-E_{CT} offsets, other requirements for low $\Delta V_{OC}^{non-rad}$ involve strong photoluminescence of S_1 state, long exciton lifetime,[155] and favourable D/A interfacial orientation.[223,224] Moreover, for ultra-low ΔHOMO systems, the hybridisation of S_1 and singlet ^{1}CT states by intensity borrowing can also be involved to further reduce $\Delta V_{OC}^{non-rad}$, which needs strong D/A electronic coupling.[225] Although overlooked in NFA OSCs, non-radiative recombination *via* triplet states should also be controlled, avoiding back transfer from triplet ^{3}CT and ^{1}T states.[226] For example, maximising exciton separation by optimum phase segregation (*i.e.*, with domain size close to exciton diffusion length) is a promising strategy, favouring CT dissociation over back transfer.[227]

A further challenge is about the reduction of non-geminate recombination losses after charge separation, so that efficient carrier extraction can be achieved. These can occur *via* bimolecular recombination of e-h pairs during transport to electrodes or by trap-assisted mechanisms (bulk or surface).[35] Disorder-related non-radiative

losses can be successfully controlled by NFA molecular engineering, with characteristics such as a planar, rigid backbone[212] or halogenation[228] reducing trap density in BHJs. However, bimolecular recombination remains high in state-of-the-art OPVs, and different routes have been explored to reduce it. Examples include fine-tuning of interfacial area and molecular packing by thermal annealing[186] or molecular design (*e.g.*, fluorination to improve π-π stacking),[229] towards an extraction time τ_{ex} two orders of magnitude faster than recombination time τ_{rec}.[195] Some effective core and end-group engineering routes will be given in Chapter 4, where selenium substitution in the central unit enhances molecular rigidity, and peripheral methylation tunes charge distribution along the backbone, for suppressed trap density and improved OPV performance. Efficient and balanced carrier transport is also crucial for suppressing recombination losses, and recent research has been devoted to pushing NFA and polymer mobilities towards the 10^{-3} $cm^2V^{-1}s^{-1}$ range. Here, similar strategies to trap reduction can be utilised, such as packing enhancement, molecular rigidity/planarity, and fluorination, with finely interpenetrated BHJ also beneficial for optimum transport.[35] Finally, reduction of voltage loss can be also achieved by careful tuning of D:A blending ratio, as explored in the donor-rich OPDs presented in Chapter 6.

As discussed in this section, the areas to work on for approaching theoretical records in OPV and OPD performances have been clearly identified. However, details of loss mechanisms and practical strategies to tackle them are the subject of ongoing research, and the literature in the field is rapidly growing from fundamental insights to device engineering towards a more and more promising photoconversion technology based on organic materials.

2.5 Stability Challenges

Despite the great steps forward in organic photoconversion research in the last decades, performance is not the only factor to take into account for assessment of OPV and OPD technology. In fact, long-term stability is also an essential requirement towards commercialisation, and a lifetime over a T_{80} (*i.e.*, the time over which PCE drops 20% of its initial value in OPVs) of 10 years should be ideally provided.[230] In this respect, the most efficient OPV materials are still far from this target, and several aspects need to be taken into account for a systematic understanding of what determines PCE degradation over time.

In particular, performance loss is strictly related to the environmental conditions of OPV operation, and stability investigations generally distinguish intrinsic

photostability (in inert atmosphere with purely light stress), thermal stability at high temperature, and photochemical stability (with exposure to ambient gases such as oxygen and aqueous vapour).[231] Intrinsic shelf life in dark and nitrogen is also often assessed, although the relevance to device application is limited. In general, systematic testing conditions are prescribed by international standards such as the International Summit of Organic solar cell Stability (ISOS, 2011),[232] although experimental protocols are in practice different among research groups and a unified lifetime testing method and result reporting are urgently needed.

In this section, an illustration of the main degradation mechanisms and examples of promising strategies to control them are given. Here, we focus on the light-induced processes directly involving the active layer, although full device engineering including charge extraction/transport layers and electrodes should be considered for industrially-relevant applications.

2.5.1 Chemical Stability

Regarding direct degradation of photoactive materials, photoageing mechanisms are severely accelerated by exposure to ambient gases. In fact, it is well known that oxygen in the presence of light triggers harmful chemical reactions in NFA-based systems. In analogy with C_{60}, C=C bonds can be disrupted by oxygen with breaking of conjugation,[233,234] and several weak points have been identified in the molecular structure of ITIC, such as double bonds in core thiophenes or between donor and acceptor units.[235] IDTBR family also suffers from air-induced instability, with the BT unit susceptible of conformational twist leading to photo-oxidation and chromophore bleaching.[236] Although these loss pathways can be eliminated by device encapsulation, intrinsic degradation occurs under light, with an initial phase of sharp PCE drop - the so called *burn-in* - typically observed in the initial 10-100 hours of operations.[237,238] For fullerene-based systems this has been traced back to phenomena such as PCBM dimerisation[189] and spinodal demixing,[187] but alternative explanations are needed for NFA devices.

For example, light-induced conjugation breaking with increased energetic disorder is found in ITIC-based OPVs,[230] and the choice of end-group functionalisation is essential to reduce photochemical degradation and increase device lifetime. In fact, as illustrated in Figure 2.12, double-methylated ITIC shows the most severe degradation of all photovoltaic parameters, while fluorination leads to almost unchanged J_{SC} and FF over about 1800 hours. In general, it has been reported that halogenation is favourable to photostability,[230] with chlorination preferential com-

pared to fluorination,[235] while methyl end-capped groups are typically degrading faster.[230] However, there is currently no univocal conclusion whether methylated NFAs are more stable than halogenated ones, which seems to depend on device architecture and degradation conditions[239] (see excellent stability of methylated NFAs presented in Chapter 4). These processes affecting chemical structure typically lead to creation of energetic and structural traps, with adverse effects like electric field building-in, lowered mobility, and increased charge recombination.[218] This has been demonstrated in several D:A systems, where the increased recombination order upon photoageing has been ascribed to trap formation under light.[237,238]

Removal of weak bonds is also crucial, and can be achieved by a wide range of chemical modifications (*e.g.*, molecular core, end groups, conjugated linkages, nonconjugated side chains). Several examples show the importance of NFA rigidity for good photostability, realised by conformational lockers such as noncovalent bonds between donor and acceptor units,[240–242] or by high structural planarity.[235,236] For instance, outer core alkyl chains in Y6 restrict conformational rotation around the alkene bond,[212] while initially large dihedral angles in NFA structures (*e.g.*, in IDFBR) accelerate light-induced twisting and photo-oxidation.[236] Side-chain engineering can also make a difference, as shown for *meta*-alkyl *vs.* *ortho*-alkyl onto phenyl side groups in ITIC, which avoid excessive aggregation and large domain segregation for better tolerance to high temperatures.[243]

The role of end groups and conformational lockers in ITIC derivatives for OPVs is explored in Chapter 4, where combination of heteroatom core substitution and end-group methylation results in a PCE loss of only 5% over >450 hours of operation.

2.5.2 Morphological Stability

Morphology instability is another crucial aspect of OPV and OPD degradation, since D/A domains in BHJ are typically in a meta-stable configuration formed during the quick film drying.[186] Under light exposure, BHJ morphology can be severely affected, such as with vertical D/A separation[244] and phase segregation induced by poor D/A compatibility.[245] At this regard, the Flory-Huggins interaction parameters can inform on D/A miscibility to guide optimum choice of photoactive materials (as shown for EH-IDT *vs.* ITIC and IDIC in blend with PTB7-Th[245]), and thermodynamic stability also needs to be analysed for each D/A pair (depending on diffusion coefficients, mixing ratio...).[199] Moreover, initial active layer formation by materials crystallinity, substrate temperature and thermal annealing is determinant

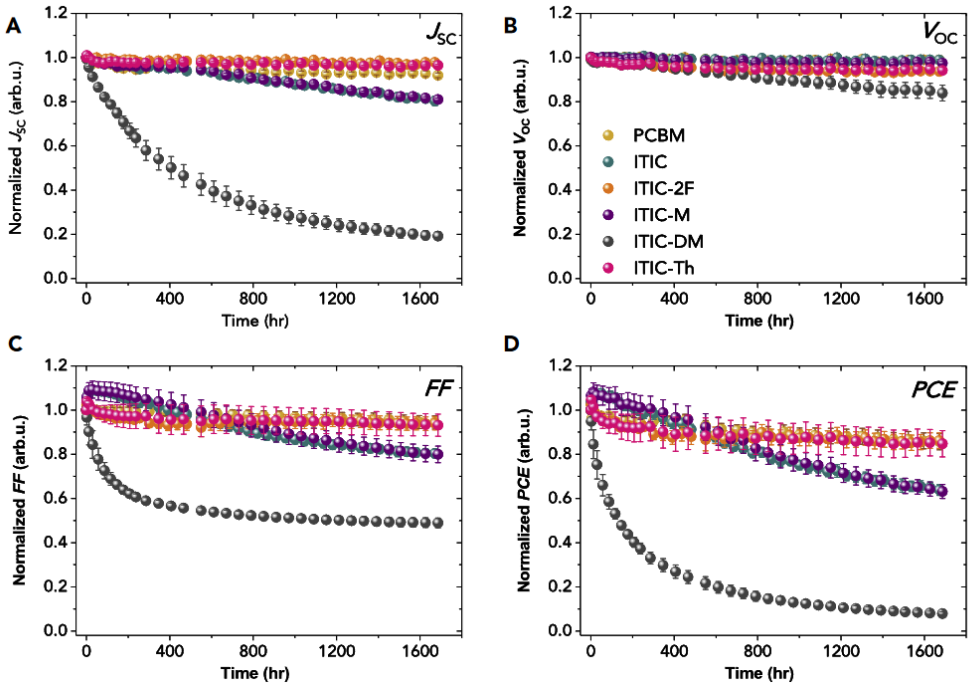


Fig. 2.12: Evolution of PV parameters during light exposure (1 Sun by white LED) for BHJ devices using different ITIC derivatives or PCBM, in combination with PBDB-T donor polymer. From [230], with permission.

for packing order and π-π stacking in NFAs, resulting in optimum morphology and domain size.[246,247] For example, as illustrated in Chapter 4, the use of a more crystalline ITIC-derivative results in larger domains, less prone to undergo further phase segregation during device operation, for excellent OPV stability.

Control of initial morphology by thermal treatments or solvent additives has also been explored as an effective tool for increased photostability. In fact, large-sized NFA molecules have a low molecular diffusivity in the polymer matrix compared to small C_{60} derivatives. Under light or thermal stresses, NFA migration to the amorphous D/A interfacial regions is extremely slow and leads to formation of isolated clusters disconnected from percolation pathways, with creation of morphological traps (schematised in Figure 2.13).[191] However, this can be significantly reduced by initial optimisation of D/A interfaces, with a neater contact area achieved by annealing or solvent additives.[191,248,249]

Moreover, significant lifetime improvements have been demonstrated by the introduction of a third BHJ component, such as for IDFBR in P3HT:IDTBR[163] or IDTBR in PM6:Y6.[250] In fact, a minor fraction of a second small molecule acceptor increases exciton lifetime, fosters energy cascading in the active layer,[163] and helps extraction of trapped carriers from D and A domains.[250] Here, careful selection of

well-matched materials is crucial, so that the third component is not excessively miscible, creating small purer aggregates at the D/A interfacial regions.[163,251] A polymeric third component can also be beneficial, with optimisation of morphology and percolation pathways as for the N2200 polymer acceptor.[252] Since light exposure is often correlated with device heating and thermal degradation, a third polymeric component can be helpful not only for charge transport, but also for faster heat diffusion. As shown for PBDB-T:ITIC-4F solar cells,[253] a small portion of N2200 can mitigate performance loss due to both energetic traps and local heating during illumination, with significant suppression of FF decay.

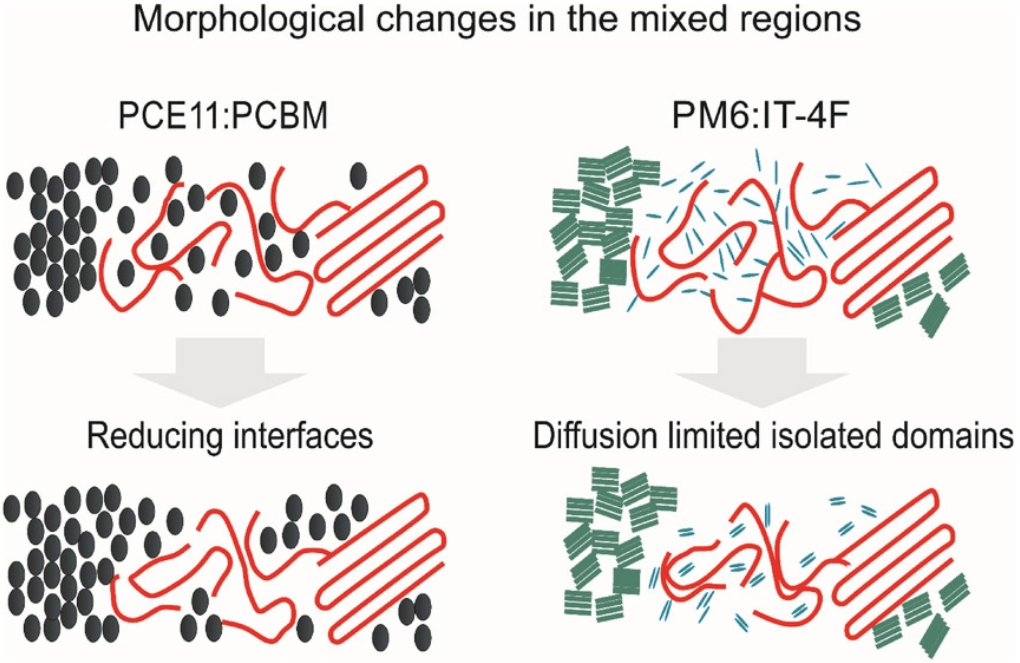


Fig. 2.13: Schematic of photoinduced morphology reorganisation in fullerene *vs.* NFA-based BHJ systems. In particular, the larger dimension and lower diffusivity of NFAs preserve part of the intermixed region at the interface with donor, crucial for efficient exciton separation. From [191], with permission.

In contrast with the plethora of stability studies for OPVs, little is known on the specific degradation mechanisms in OPD working conditions and their impact on OPD performance metrics. Although environmental factors (*e.g.*, air, humidity) can be controlled by encapsulation, thermal and electric stress may negatively affect noise current and D^*,[14] especially under the constant reverse bias required during operation. Also in this case, morphological stability appears crucial to ensure long device lifetime, with recent studies showing the potential of NFA-based systems. For example, EH-IDTBR devices deliver excellently constant photocurrent under reverse bias and illumination when compared to fullerene counterparts.[90] Also here, the low energetic disorder and favourable miscibility are found to be crucial to control

morphology segregation and extend device lifetime.

3 | Methods

The unique characteristics of OSCs, such as molecular structures based on π-conjugated backbones, structural disorder, and morphological complexity in solid state films, call for a specific choice of experimental assays for materials characterisation. In this chapter, after an overview of the sample fabrication protocol, the different techniques utilised in the work presented in this thesis will be illustrated, with a particular focus on the probes for structural and energetic investigation. Details of fabrication and characterisation protocols used for specific experiments will be given in the relevant chapters in the following.

3.1 Sample and Device Fabrication

All solution-processed films and devices are fabricated at Imperial College London, in a cleanroom environment (Experimental Solid State cleanroom facility) to minimise contamination from atmospheric particulate matter. All samples are deposited by spin-coating, which consists of dripping a small amount (20-50 μL) of material dissolved in a suitable solvent onto a conductive (ITO) or non-conductive (glass, quartz) substrate with 1 cm x 1 cm dimension, followed by high-speed rotation of the substrate to allow for solvent drying and film formation. Material concentration, choice of solvent and high-boiling-point solvent additives, solution temperature, spin speed and duration are all important parameters influencing film crystallisation and they are optimised depending on specific samples. Preliminary to spin-coating, the substrates are cleaned by a sequence of ultra-sonication baths in 2% Hellmanex detergent in water, deionised water, acetone, and isopropyl alcohol (10-15 min each), followed by drying on a hot plate (120°C for 10 min) or in an oven (80°C overnight). Ashing by ozone plasma (Emitech K1050X oxygen plasma asher, 80 W for 4 min) just before deposition is crucial to ensure no environmental particles are left on the surface. Materials are dissolved in organic solvents such as chlorobenzene and chloroform, with typical concentration ranging between 10 and 20 mg mL^{-1}, and mixed overnight on a hot plate (40-65°C) by a magnetic stir bar

for complete dissolution. Solutions are constantly kept in sealed vials with dark encapsulation to avoid any photo-oxidation. Prior to spin coating, the substrates are blown by a nitrogen gun and a suitable amount of solution is dropped by a micropipette before or during substrate spinning (typically at a rate of 2000-3000 rpm for 40-60 s). Depending on the chosen fabrication conditions, samples can be thermally annealed to assist film crystallisation, which is done on a hot plate after transfer to a nitrogen-filled glovebox. For full device fabrication in typical inverted structure, an additional zinc oxide (ZnO) electron transport layer is deposited on ITO before the active layer. This is prepared by sol-gel method, dissolving 0.11 g mL^{-1} of zinc acetate dihydrate in 2-methoxyethanol with 3 vol% of ethanolamine, and sonicating for over 3 h. After spin coating (typically at 4500 rpm for 45 s), the films are annealed on a hot plate at 190°C for 20 minutes in air. Top contacts are deposited following active layer coating by thermal evaporation in vacuum (10^{-6}-10^{-7} mbar), with 10 nm of MoO_3 as hole transport layer and 100 nm of Ag as anode, constantly controlling evaporation rate for optimised deposition. A patterned mask is used to determine device area, with a typical pixel size of 4.5 or 6 mm^2. To ensure effective electrical contact, bottom ZnO is scratched from the common ITO cathode after deposition by a cotton bud, and the evaporated electrode is also removed soon after deposition to form the common contact to the bottom ITO.

3.2 Raman Spectroscopy

3.2.1 Fundamentals of Raman Spectroscopy

Raman spectroscopy is a type of vibrational spectroscopy based on the inelastic scattering of incident light, typically provided by a laser source with excitation in the optical range. In the case of an incident photon with energy lower than the optical bandgap of the material (*i.e.*, non-resonant Raman), electrons are excited from the first singlet state S_0 into a virtual excited state, followed by ultrafast decay to S_0. In case of a decay exactly to the same initial vibrational level V_i within S_0, the system undergoes elastic scattering, often referred to as *Rayleigh scattering*. However, if the system relaxes to a different final vibronic level V_f within S_0, the energy corresponding to the difference between V_f and V_i is gained or released by the scatterer. This is therefore an inelastic process, going under the name of *Raman scattering*, more specifically *Stokes scattering* if V_f is at higher energy compared to V_i, and *anti-Stokes* in the opposite case, as illustrated in the energy diagram in Figure 3.1.[254] Due to occupation probability in a quantum mechanic model, initial population is significantly lower for higher vibrational states, so that only Stokes

scattering is normally analysed. The so-called *Raman shift* is therefore the energy

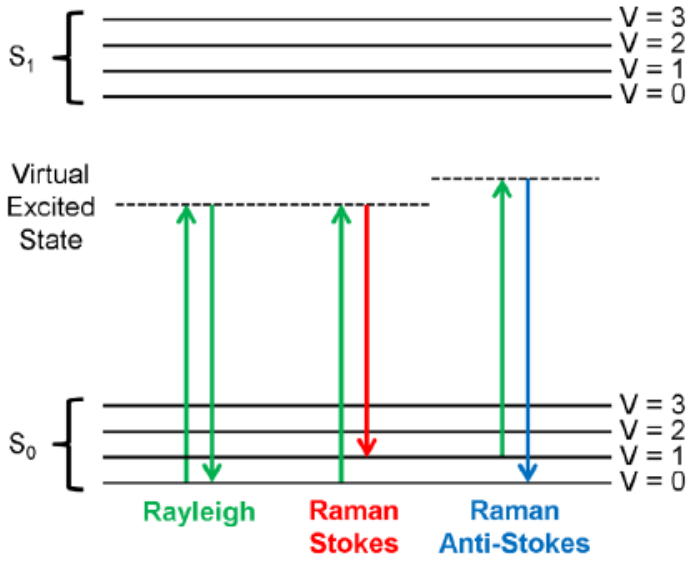


Fig. 3.1: Schematics of the energy transitions involved in elastic (Rayleigh) and inelastic (Stokes and anti-Stokes) scattering of light. From [254], with permission.

difference between the incident and scattered photons, often expressed in cm^{-1}, and a typical Raman spectrum is comprised of multiple peaks - depending on the scattering intensity for different modes - plotted against the Raman shift. Owing to the complexity of vibrational modes available in π-conjugated systems, Raman spectroscopy is one of the techniques of choice for the characterisation of OSCs, with the advantage of straightforward implementation only requiring the sample to be exposed to the excitation source. This allows for the investigation of active materials within complex device architectures and studies in controlled environments (*e.g.*, depending on temperature, electrical bias, or atmospheric composition). Moreover, since E_g of most organic materials lies within the optical range, selection of a suitable laser source can excite the sample to a "real" electronic state S_1 before decay to S_0, which greatly enhances the Raman cross-section and the intensity of associated peaks (*i.e.*, resonant Raman).

In a classical interpretation of Raman scattering, the scatterer is a polarisable medium under the effect of a time dependent electric field $E(t)$ (*i.e.*, the incident light). This incoming field causes a distortion of the electron distribution over the system, creating an induced dipole moment μ, linearly depending on the scatterer polarisability α:

$$\mu(t) = \alpha E(t). \tag{3.1}$$

Here α varies with the vibrational coordinate Q following the vibrational modes of

the system, so that $\alpha = \alpha_0 + (\frac{\partial \alpha}{\partial Q})_0 Q + ...$, with α_0 being the equilibrium polarisability and $(\frac{\partial \alpha}{\partial Q})_0$ the partial derivative of the polarisability with respect to the vibrational coordinate at the equilibrium position. Considering a sinusoidal time dependence for the incoming field with amplitude E_0 and frequency ω_0, and describing the vibrational modes as harmonic oscillations with amplitude Q_0 and frequency ω_v, so that

$$\begin{aligned} E(t) &= E_0 cos(\omega_0 t), \\ Q(t) &= Q_0 cos(\omega_v t), \end{aligned} \tag{3.2}$$

Equation 3.1 can be expressed as

$$\mu(t) = E_0 \alpha_0 cos(\omega_0 t) + \frac{E_0 Q_0}{2} (\frac{\partial \alpha}{\partial Q})_0 [cos[(\omega_0 - \omega_v)t] + cos[(\omega_0 + \omega_v)t]]. \tag{3.3}$$

The three terms in Equation 3.3 respectively represent the Rayleigh, Stokes, and anti-Stokes contributions to the induced oscillating dipole moment, in a simple model that can be extended to n-dimensions (*i.e.*, for n possible vibrational modes). Therefore, every vibrational mode present in the system will give rise to a peak in the Raman spectrum, provided that it is *Raman active* - *i.e.*, it determines a change in polarisability at the equilibrium position so that $(\frac{\partial \alpha}{\partial Q})_0 \neq 0$.

Despite the elegant explanation of vibrational spectroscopy provided by the classical model, several points such as the relative probability of Stokes and anti-Stokes scattering and the existence of selection rules are not addressed, so that a quantum mechanical framework is required for a rigorous treatment. In quantum physics, molecular polarisability is expressed in terms of transitions between discrete states, respectively the initial i, a virtual excited v, and the final f, in the Kramer-Heisenberg-Dirac relation:

$$(\alpha_{\rho\sigma})_{fi} = \frac{1}{\hbar} \sum_{v \neq i,f} (\frac{\langle f|\hat{p}_\rho|v\rangle\langle v|\hat{p}_\sigma|i\rangle}{\omega_{vf} - \omega_0 - i\Gamma_v} + \frac{\langle f|\hat{p}_\sigma|v\rangle\langle v|\hat{p}_\rho|i\rangle}{\omega_{vi} - \omega_0 + i\Gamma_v}), \tag{3.4}$$

where $(\alpha_{\rho\sigma})_{fi}$ are the components of the polarisability for the transition between i and f with polarisation directions ρ and σ for incident and scattered light respectively, $\hat{p}_\rho$ and $\hat{p}_\sigma$ are the components of the dipole moment operator along ρ and σ, ω_{vf} and ω_{vi} are respectively the v-f and v-i frequency differences, ω_0 the frequency of the incident light, i the imaginary unit, and Γ_v the natural half-width of state v. Here, considering the second term negligible and using the Born-Oppenheimer

approximation, Equation 3.4 can be simplified as

$$(\alpha_{\rho\sigma})_{fi} \sim \frac{1}{\hbar} M_{vi}^2(R_0) \sum_{v \neq i,f} \frac{\Phi_{R_f}|\Phi_{R_v}\Phi_{R_v}|\Phi_{R_i}}{\omega_{vi} - \omega_0 - i\Gamma_v} + \\ + \frac{1}{\hbar} M_{vi}(R_0)(\frac{\partial M_{vi}}{\partial R_E})_{R_0}(R_0) \sum_{v \neq i,f} \frac{\Phi_{R_f}|R_E|\Phi_{R_v}\Phi_{R_v}|\Phi_{R_i} + \Phi_{R_f}|\Phi_{R_v}\Phi_{R_v}|R_E|\Phi_{R_i}}{\omega_{vi} - \omega_0 - i\Gamma_v}, \tag{3.5}$$

where Φ is the vibrational part of the wavefunction depending on nuclear coordinates only, M_{vi}=M_{fv} is the i-v or v-f transition moment, and the dependence of M_{vi} on the nuclear coordinate is approximated as $M_{vi}(R_N) = M_{vi}(R_0) + (\frac{\partial M_{vi}}{\partial R_E})_{R_0} R_E + ...$, since in the Raman transition timescale no significant nuclear coordinate change occurs (R_0 is its equilibrium position and R_E its displacement). In Equation 3.5 only the first two significant terms are considered, respectively known as Franck-Condon and Herzberg-Teller terms. In particular, the first one predominates in resonant conditions, while the second one for the non-resonant case and is subject to quantum selection rules only allowing transitions if i and f are separated by one energy quantum.

A useful parameter that can be experimentally accessible is the *Raman cross-section* σ for a specific vibrational mode, which is proportional to the square of the polarisability.[254] In fact, the scattering intensity I_R can be related to the incident light intensity I_0 and the frequency of the scattered light ω_s by

$$I_R = \frac{8\pi\omega_s^4 I_0}{9c^4} \sum_{\rho\sigma} |(\alpha_{\rho\sigma})_{fi}|^2, \tag{3.6}$$

being c the speed of light. Equation 3.6 can be translated into experimentally measurable parameters as

$$I_R = I_0 \sigma D dz, \tag{3.7}$$

with D the number density of scatterers and dz the depth of field. For a more immediate relation with the integrated area of the peak associated with a specific mode, differential Raman cross-section

$$\beta = \frac{d\sigma}{d\Omega} \tag{3.8}$$

is commonly used, expressed in $m^2 molecule^{-1} sr^{-1}$, where only the light scattered in the solid angle Ω accessed by the detector is considered.

3.2.2 Raman Spectroscopy in Organic Semiconductors

Organic semiconductors are especially suitable systems to investigate by Raman spectroscopy. This is because the delocalised π-electrons create a highly polarisable charge density, where electronic transitions are associated with conformational changes in the conjugated backbone.[255–257] In particular, resonant Raman spectroscopy maximises this effect by electron excitations above the bandgap, which are strongly coupled to the local vibrational modes of the molecule. Therefore, using different excitation wavelengths matching various electronic transitions, it is possible to selectively investigate specific molecular sites.[258] This allows to answer several interesting questions, such as which bonds are involved in π-electron localisation for different electronic transitions, where the charge density sits on the molecular backbone, and how this is affected by molecular conformation. Moreover, *in-situ* monitoring of Raman spectra during prolonged exposure to thermal gradients, light illumination, or electric fields is an invaluable tool to understand evolution of molecular structure and film morphology during degradation processes and to identify the "weak points" in the materials chemical design.

A relevant illustration of the capabilities of Raman spectroscopy is given by the case study of DPP-based polymers.[258]

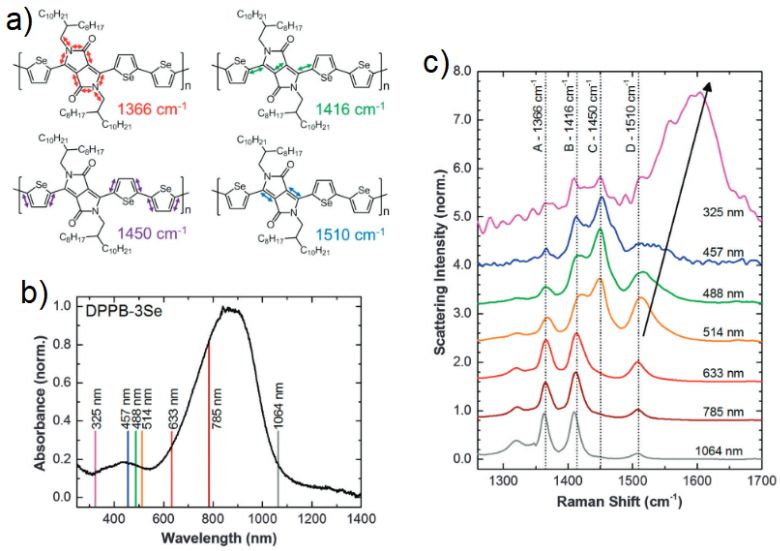


Fig. 3.2: (a) Assignment of DPPB-3Se Raman peaks of specified wavenumber to different vibrational modes. (b) Absorption spectrum of DPPB-3Se, with indicated the different wavelengths used as Raman probes. (c) Evolution of DPPB-3Se Raman spectrum using different resonant and non-resonant probe wavelengths. Adapted from [258], with permission.

As schematised in Figure 3.2a, the main Raman active modes in DPPB-3Se can

be grouped into delocalised modes involving the conjugated backbone (*i.e.*, modes B and D) and modes localised on specific units (*i.e.*, mode A on DPP and mode C partially on selenophene). By selective excitation with different wavelengths resonant with the dominant absorption features (Figure 3.2b), it is possible to investigate the nature of the electronic transitions involved. For example, a low energy excitation (785 nm, resonant with the dominant absorption) enhances mode A (Figure 3.2c), so that the main absorption peak can be assigned to a localised transition on DPP unit. On the contrary, a high energy probe (457 nm, resonant with a weak absorption band) emphasises modes B and C, related to the delocalised nature of this π-π^* transition. Therefore, the main electronic transition is identified as charge redistribution within the same molecular unit, with both HOMO and LUMO localised on the ambipolar DPP moiety.

Wavelength-dependent Raman is also useful for studying the degree of packing order in thin films.[259] A model system in this sense is P3HT, where the crystalline order can be easily manipulated in the regioregular (RR) and regiorandom (RRa) forms. By tracking the evolution of the main Raman modes in P3HT films upon blending and annealing, it is possible to determine the portion of ordered polymer and how this is affected by fabrication conditions. For example, the changes in peak ratio and peak position under resonant conditions (488 nm excitation) show that 42% of pristine RR-P3HT in crystalline phase is in ordered form, increasing to 94% upon thermal annealing. On the contrary, annealing has negligible effect on RRa-P3HT due to the disordered side chains impairing systematic packing. Here, different excitation wavelengths induce strong shift of Raman peaks for RRa-P3HT. This phenomenon, known as *Raman dispersion*, is due to selective resonance with molecular segments of different conjugation lengths, which is highly relevant to quantify packing order.

Degradation processes and BHJ morphology evolution can also be fruitfully understood by Raman studies, as demonstrated in several D:A systems.[236,260,261] For example, irreversible peak ratio changes in DPPTTT:$PC_{70}BM$ blends can be assigned to crystallisation transitions at mild temperatures (~150°C), followed by phase segregation and further ordering beyond 240°C.[260] Moreover, *in-situ* degradation studies even enable to follow chemical processes, such as photo-oxidation and molecular breaking, typically identified as multi-step evolution of Raman spectra.[236,261] Advanced Raman applications also include *in-operando* characterisation of devices such as chemiresistors or electrochemical transistors.[262–264] For example, polaron formation, trapping, and transport have been investigated in organic gas sensors using electric-field-dependent Raman.[262] In P3HT-based systems, the response to different

gases can be rationalised in terms of structural changes and π-electron redistribution in the polymer upon interactions with polar or non-polar analytes.

3.2.3 Raman Experimental Details

Raman spectra are measured by a Renishaw inVia Raman microscope in backscattering configuration, keeping the samples under a nitrogen flow in a Linkam chamber to reduce photoinduced degradation. A 514 nm argon-ion laser (12 mW power at sample) with a $\sim$10 µm diameter, 25% defocused on the sample is used, unless otherwise specified. The diffracted light is separated by a 2400 lines/mm diffraction grid, and the spectrometer is calibrated by a Si reference. Laser power, exposure time, and measurement accumulation number are optimised for each sample and kept consistent for the same experiment. Multiple spectra are taken at different spots on the sample surface to confirm consistency and reproducibility. PL background is removed by polynomial fitting to Raman spectra.

3.3 Energetics

The investigation of organic semiconductor energetics is of great importance to relate to materials molecular structure and to understand the origin of device performance. In this work, the characterisation of work function Φ and HOMO level is carried out by Kelvin probe (KP) and air photoemission spectroscopy (APS), respectively, integrating both measurements in ambient-pressure conditions. The same conductive tip (gold alloy, 2 mm diameter) is used either as a vibrating probe with applied bias to counter the potential difference with the sample (*i.e.*, as a Φ probe) or to collect the photoemitted electrons from the materials DOS (*i.e.*, as a HOMO probe), as detailed in the following.

3.3.1 Air Photoemission Spectroscopy

As described by I. Baikie *et al.*,[265] APS is a photoemission technique based on the detection of ionised atmospheric gases following electron emission from the sample. The system utilises a deuterium source for the production of deep UV photons, illuminating a 3 x 4 mm^2 portion of the sample surface. Deuterium is a low energy source compared to He typically used in ultraviolet photoemission spectroscopy experiments, reaching a maximum of around 7.3 eV, which is enough for the HOMO range of most OSCs and significantly reduces unwanted sample degradation. Once the photons with energy higher than semiconductor ionisation

potential E_{ph}>IP_{sc} are absorbed, electrons are emitted from the sample surface (*i.e.*, within the electron inelastic mean free path), as schematised in Figure 3.3 in the case of a metal (in this case Φ is considered instead of IP). This leaves behind a positively charged surface creating an image force up to ∼30 nm from the sample, after which scattering by air molecules and interactions with the external electric fields dominate. In these conditions, the electron mean free path is in the range of 1-3 µm, during which scattering with atmospheric gases produces ions such as N_2^-, O_2^-, and OH^-. These are attracted by the KP tip, positively biased at 10 V, corresponding to a 10 V/mm field. This potential gradient is not high enough for charge tunnelling or barrier-height lowering, so that absolute measurements of materials energetics are possible. Therefore, APS detects the ionic current generated by photoemitted electrons as a function of incoming photon energy, with a sensitivity of 0.1 fA - 100 nA. In a typical output graph, the square root or cube root of photoemission intensity is plotted against E_{ph}, corresponding to Fowler's theory for metals[266] and its adaptation to semiconductors,[267] respectively. The intersection between the fit to the linear part of the photoemission spectrum square or cube root and the zero baseline corresponding to the noise level is extracted as materials HOMO level.

Interestingly, APS also provides information on the tail states (*i.e.*, shallow traps), corresponding to the photoemission spectrum part at energy lower than the extracted HOMO level. Tail states are present in most OSCs due to their disordered nature, with a Gaussian distribution of energy states around the HOMO.[218] Since they often act as shallow traps, they have a great impact on materials photophysics,[218,268] so that ready investigation by APS is of great benefit in OSC characterisation.

3.3.2 Kelvin Probe and Surface Photovoltage

The KP technique is based on the electric contact established between a conductive tip and the surface of a metallic or semiconducting sample, and the equilibration of their contact potential difference (CPD). As shown in Figure 3.4, a CPD of energy eV_{CPD}, with e being the elementary charge, exists before contact, corresponding to the tip-sample Φ difference ($e\Phi_{sample}$-$e\Phi_{tip}$, see Figure 3.4a). Upon contact (Figure 3.4b), the charge flow from the low to the high Φ material brings the system towards Fermi level alignment. This creates a net electric field between the materials, which can be modified by applying a bias V_B to the tip. In the KP technique, the tip is vibrated in proximity to the sample surface so that a variable capacity with peak-to-peak voltage V_{ptp} is generated, with $V_{ptp} \propto V_B - V_{CPD}$. In this conditions, the tip-sample CPD is cancelled for $V_B = V_{CPD}$. Since at zero potential the detection is

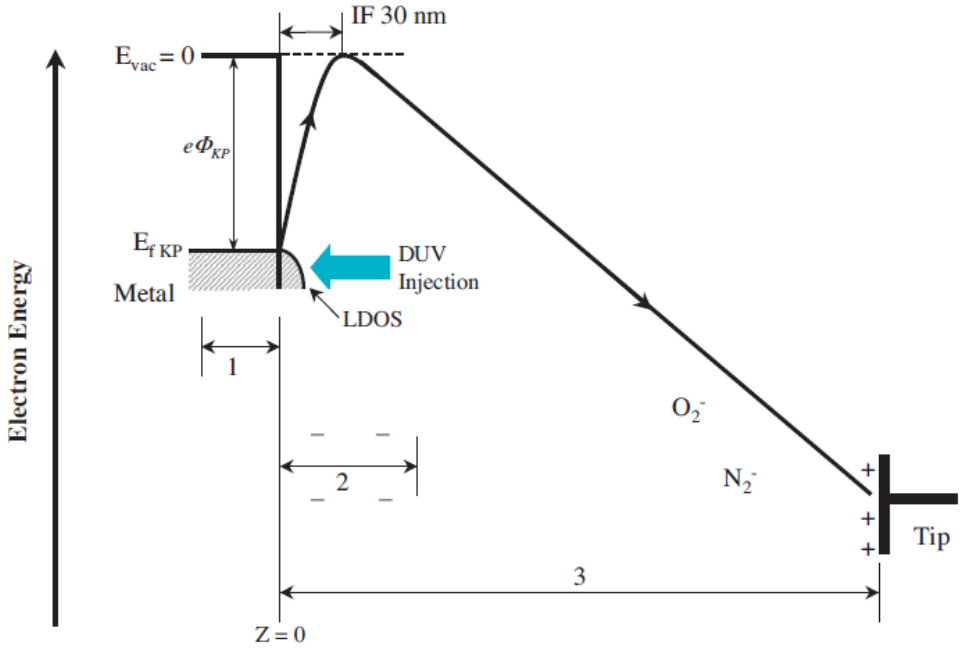


Fig. 3.3: Schematic illustration of photoemission process from a metallic sample. The deep ultraviolet (DUV) photon injection in the local density of states (LDOS) of the sample (1) produces an electron cloud in the proximity of the surface, ionising ambient gases (2). Here, charges are subject to the image force (IF) from the holes accumulated on the metal surface. Finally, ions are collected from the APS tip with positive applied bias (3). From [265], with permission.

significantly affected by noise and stray capacity, a high signal-to-noise ratio can be achieved by applying two tip bias values V_{B1} and V_{B2}, with corresponding outputs V_{ptp1} and V_{ptp2}. As shown in Figure 3.4c, accurate determination of V_{CPD} can be realised from the $V_{ptp}(V_B)$ relation, providing a 1-3 meV resolution.[269]

Applying a white light or monochromatic background illumination during the measurement allows to study the SPV, defined as the change in V_{CPD} between dark and illuminated conditions. This is a powerful tool for investigation of charge generation, redistribution, and trapping in the material, with SPV magnitude and on/off dynamics providing information on the presence of electron or hole traps and transport properties.[270–272]

3.3.3 Energetics Experimental Details

A gold alloy tip of 2 mm diameter is used, vibrating at 70 Hz in the KP mode. The system is enclosed in a Faraday cage for isolation and the sample position can be controlled horizontally and vertically by a motorised xyz stage. Samples can be illuminated *via* a quartz tungsten–halogen lamp with intensity up to 0.2 Sun, where specific wavelengths can be selected by a monochromator between 400 and 1000

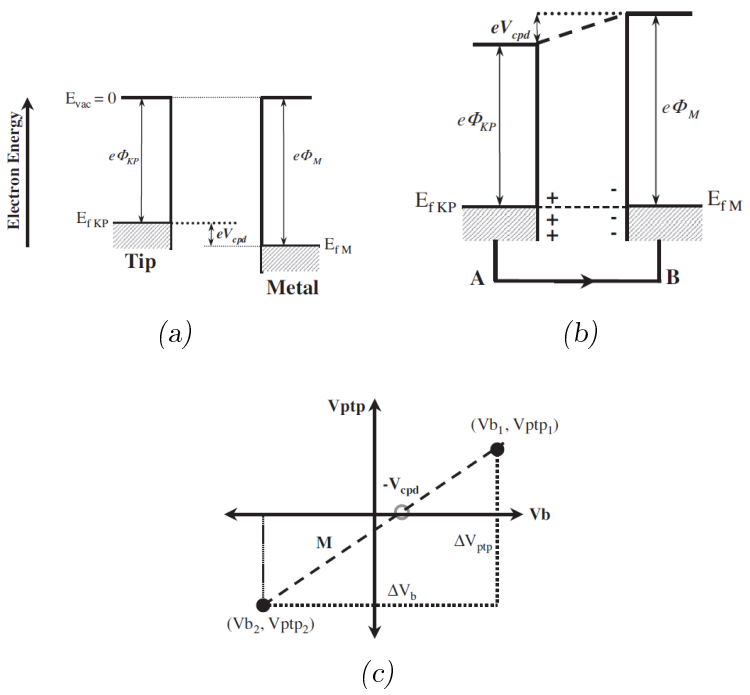


Fig. 3.4: Schematic of the energetic alignment between a Kelvin probe and a metallic sample before (a) and after (b) contact, and calibration curve relating V_{ptp} with V_B for extraction of V_{CPD} (c). Adapted from [265], with permission.

nm. For Φ and HOMO measurements, repeated acquisitions over different points of the sample surface allow for a statistical treatment and calculation of experimental error.

3.4 Absorption Spectroscopy

Thin-film UV-Vis transmittance T is measured by a Shimadzu UV-2550 UV-visible spectrophotometer. Ignoring reflection, scattering, and interference effects (which should be however accounted for in case of spectra with strong low-energy tails or distorted shapes), the absorbance A can be calculated from T as

$$A = log(\frac{T_{sub}}{T_s}), \tag{3.9}$$

with T_{sub} and T_s pertaining to the substrate and sample, respectively. Assuming the low-energy absorption onset comes from charge excitation above the optical bandgap, E_g can be quantified by linear fit to the absorption edge. Combined with the HOMO level measured by APS, this allows for LUMO extraction to reconstruct the whole materials energy diagram.

3.5 Photoluminescence and Transient Photoluminescence

Photoluminescence (PL) spectroscopy measures photon emission following sample excitation by a laser source. This technique gives access to the bright emissive states, informative on materials energetic structure, presence of singlet *vs.* triplet states, radiative recombination losses, and energy transfer processes between BHJ components.[212,273] Moreover, PL can help understand sample morphology, especially by quantification of PL quenching in blended materials compared to neat films, a typically used method to verify effective domain separation in BHJs.[179] This can also be employed for *in-situ* or *ex-situ* tracking of materials degradation upon light or thermal stress. Since PL spectroscopy is a non-disruptive experimental method, it is suitable for direct device screening, with interesting applications in bias-dependent measurements. Applying a voltage to the device electrodes, PL quenching/increase can be analysed, either under bias or during heating/cooling cycles (with no need for electrodes in this case). This is a very important tool for quantifying the binding energies and separation probability of different electronic species, which is crucial to distinguish excitonic and CT states in organic blends and bilayers.[274] An example of this will be given in Chapter 6, where exciton binding energies are extracted from PL quenching data for D:A systems at different blend ratios.

Unless otherwise stated, PL spectra are hereby measured by a Renishaw inVia Raman microscope in backscattering configuration, with a continuous nitrogen flow in a Linkam chamber or sample encapsulation to reduce photo-oxidative degradation. A 514 nm argon-ion laser (12 mW power at sample) with a spot diameter ~10 µm, 25% defocused on the sample is used, with a 300 lines/mm diffraction grid to separate diffracted light. The system is calibrated by a Si reference, and acquisition parameters such as laser power, accumulation number, and exposure time are optimised for each sample to improve data quality. Measurements are repeated at different positions over the sample to ensure reproducibility. To account for the absorbance of different samples, the spectra are corrected by the factor $\frac{1}{1-10^{-A}}$, where A is the sample absorbance at the laser wavelength. Temperature-dependent PL data are collected by controlling the sample holder temperature in a Linkam chamber and setting a heating/cooling ramp (10°C/min, allowing over 2 min for temperature stabilisation before PL acquisition). For bias-dependent PL, the voltage is controlled *via* an Agilent power source, which can also monitor photocurrent response under laser exposure.

To investigate the PL lifetime of different electronic species, time-correlated single photon counting (TCSPC) is used. Thin films are measured in air by a PL spectrometer (FLS1000, Edinburgh Instruments), following sample excitation by lasers of different wavelengths, with samples deposited on quartz to avoid any parasitic PL quenching by conductive substrates. Lifetimes are extracted by multi-exponential fitting using FAST software.

3.6 Atomic Force Microscopy

Atomic force microscopy (AFM) is a powerful technique for mapping the sample surface morphology and resolve its sub-micrometric features. A nanometric sharp tip connected to a cantilever is vibrated across the surface by control of a X-Y piezoelectric stage. In non-contact mode, as used to collect the data presented in this thesis, the tip oscillates at its resonance frequency close to the sample, and the van der Waals interactions with the surface modify the oscillation frequency depending on the tip-sample distance. This activates a feedback loop to maintain either vibration frequency or amplitude constant, adjusting the position of the piezoelectric Z-stage, and therefore recording the height map of sample surface. Additional information such as oscillation phase can be extracted at the same time. Hereby, a Park NX10 AFM system is used, with integrated SmartScan™ acquisition software. Park silicon PPP-NCHR tips are employed in non-contact mode. Post-processing is carried out by Gwyddion open-source software for noise correction with image analysis algorithms, such as line averaging and polynomial background removal.

3.7 Computational Methods (Density Functional Theory)

For screening of materials optoelectronic properties and interpretation of experimental results, simulations of molecular structures by computational methods are an essential tool, extensively used throughout this thesis. For solving the electronic structure in a multi-electron ground-state energy for a given nuclear configuration with a nonrelativistic Born-Oppenheimer approximation, approaches based on density functional theory (DFT) yield reasonably accurate result without excessive computational load. Here, the minimisation of the ground-state energy is calculated using electronic density $n(\mathbf{r})$ instead of electron wavefunction Ψ, where $n(\mathbf{r})d^3$ is the probability of finding an electron in the d^3 volume centred in $\mathbf{r}$.[275] In particular, the DFT method can give information on various fundamental molecular

properties, such as molecular conformation, bond lengths, energy levels, and charge distribution to investigate single-molecule systems in gas phase approximation as well as multiple molecules and solvent effect.

DFT calculations are run on the Gaussian09 software (Imperial College High Performance Computing service),[276] and GaussView 6.0.16 graphical interface is used for result visualisation. Single molecules in gas phase are simulated at the B3LYP expansion with a 6-31G(d,p) or 6-311G(d,p) basis set, approximating long alkyl side chains to methyl groups and polymers to oligomers of various lengths with methyl capping units, as specified in relevant sections later on. Structures are optimised to the global minimum energy from different initial conformations to rule out any local minima. Data on energetics (*e.g.*, HOMO and LUMO levels) and molecular conformation (*e.g.*, bond lengths, dihedral angles) are extracted, and charge distribution analysed in terms of electrostatic potential using Merz-Singh-Kollman model.[277] DFT also allows for simulation of molecular vibrational modes, particularly useful for the assignment of Raman peaks. This is done by comparison of experimental spectra with graphical visualisation of Raman active modes by GaussView software and results from available literature. DFT Raman spectra are scaled by a 0.97 empirical factor in the wavenumber scale.[278] Molecular potential energy is scanned over different configurations by ground-state relaxation with frozen dihedral angles, to analyse the effect of twisting and distortion and the probability of isomer formation.

3.8 Electrical Characterisation

Characterisation of device photovoltaic parameters is conducted by J-V measurements with a Keithley 2400 source meter under dark and 1 Sun illuminated conditions (AM1.5 G, 100 mW/cm^2), using a Newport 6258 Xe arc lamp solar simulator calibrated by a Si photodiode. The system is complemented by in-house acquisition software to extract device PV parameters. Devices are kept in inert atmosphere by encapsulation or using a N_2-filled chamber.

Device lifetime is tested under continuous illumination using a white light LED source with or without the inclusion of IR component, with spectra shown in Figure 3.5 and power density equivalent to 1 Sun. Although UV spectral region is significantly involved in different degradation pathways such as inducing ZnO photocatalytic activity,[279] this can be effectively filtered out in commercial devices. It is therefore a common practice to study light stability patterns under LED sources, which has the additional benefit of reducing sample heating for decoupling of photo-

induced and thermal degradation.[253] For lifetime monitoring, the devices are encapsulated in a nitrogen-filled chamber and held at open-circuit conditions, with J-V characteristics measured at regular intervals by a Keithley 2400 source meter. The same LED source is utilised for simultaneous *ex-situ* degradation of thin films.

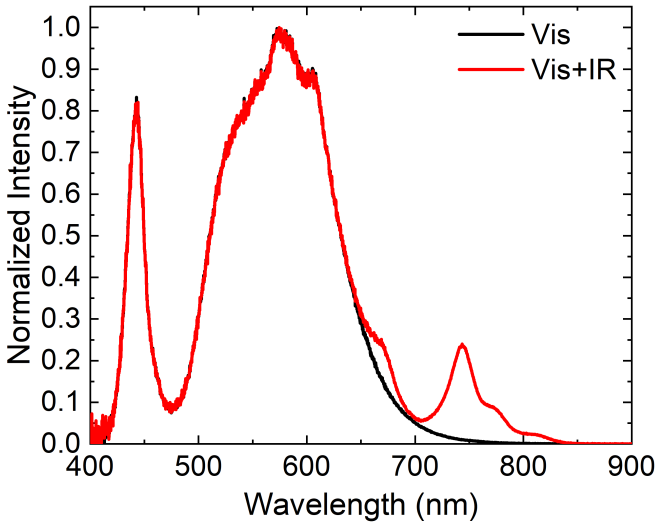


Fig. 3.5: Spectrum of the LED light source used for device lifetime testing and film degradation, with and without inclusion of IR component.

Another important figure of merit for OPVs and OPDs is EQE, quantifying the ratio between the number of photogenerated charge carriers and incident photons resolved by wavelengths of incoming light.[60]. This is measured *via* a tungsten halogen lamp coupled with a grating spectrometer (CS260-RG-4-MT-D). Photocurrent response is collected by a Stanford Research System SR380 lock-in amplifier and EQE is calibrated by a Si photodiode. Although integrated EQE over the whole spectrum should be comparable with J_{SC} from J-V characterisation, discrepancies can be found due to mismatch in light intensity, as a low power density is used for EQE measurement. Bias-dependent EQE analysis is also conducted by holding the devices under reverse voltage controlled by a BK Precision 9110 power source.

Transient photocurrent is measured with a DAQ card connected to a Tektronix TDS3032B oscilloscope, using a red or green LED light source.

For measurements of charge carrier mobility μ, single carrier devices with ITO/PEDOT:PSS/BHJ/MoO_3/Ag (hole only) and ITO/ZnO/BHJ/ZnO nanoparticles/Ag (electron only) structures are used. Mobility is calculated from the dark J-V characteristics using the Mott-Gurney relationship in the regime of space charge

limited current (SCLC):

$$J = \frac{9}{8}\varepsilon_0\varepsilon_r\mu\frac{V_{eff}^2}{d^3}, \tag{3.10}$$

being ε_0 and ε_r=3 the vacuum and active layer permittivities respectively, V_{eff} the difference between applied V and built-in potential in the device, and d the active layer thickness measured by a Dektak surface profilometer.

3.9 Supporting Methods

For further insights into materials properties and investigation of photophysical processes, additional characterisation techniques are accessed through collaborations with different research groups. In particular, transient absorption spectroscopy (TAS) is used for detailed assignment of photogenerated species and identification of their formation/recombination dynamics,[280] transient photovoltage (TPV) and charge extraction (CE) for analysis of photodetection speed and trap distribution in operational devices,[281] and grazing incidence wide-angle X-ray spectroscopy (GI-WAXS) as well as grazing incidence X-ray diffraction (GI-XRD) to study crystalline structure and molecular orientation in thin films.[282]

3.9.1 Transient Absorption Spectroscopy

Helios spectrometer (Spectra Physics, Newport Corp.) is used to measure the broadband pump-probe femtosecond TAS and kinetics for thin film samples. A 1 kHz Ti:sapphire regenerative amplified (Spectra Physics Solstice, Newport Corp.) pumped seed pulses (800 nm, <200 fs, 1 kHz) to an optical parametric amplifier (TOPAS, Light Conversion) is coupled to a frequency mixer (NIRUVIS, Light Conversion) to generate tunable wavelength visible pump pulses (Chemistry department, Imperial College London). The pump pulses are modulated at a frequency of 500 Hz by a mechanical chopper, and attenuated at the desired fluence. Seed pulses are also directed to a mechanical delay stage before being focused into a sapphire crystal (sapphire for the visible region and YAG for the NIR region) to generate a white light supercontinuum broadband probe (400-1600 nm). The probe pulse is split into two by a neutral density filter. One portion of the probe pulse serves as the reference and is directly sent to the fiber-optic coupled multichannel spectrometers (CCD and InGaAs sensors). The rest of the probe pulse together with the pump pulse are focused onto the same spot on the samples with a beam size of around 0.5 mm^2 before sending it to the spectrometer. Samples are contained in a nitrogen-purged cuvette for measurements. To compensate the fluctuations, the measured

spectrum is normalised to the reference spectrum and averaged for several scans to achieve a good signal-to-noise ratio. Data analysis including chirp correction is performed with the commercialised Surface Xplorer software.

3.9.2 Transient Photovoltage and Charge Extraction

The basic set-up of the transient optoelectronic measurements (Chemistry department, Imperial College London) for fully encapsulated devices employed in this thesis uses an oscilloscope (Tektronix TDS 3032B) to record the transient signal, connected to a computer *via* a NI-PCI-6251 DAQ card. A ring of 12 Luxeon Star/O (LXHL-NWE8) white LEDs is applied for illumination (turn-on time of 100 ms to achieve steady state). A Keithley 2400 source meter provides different voltage conditions to the device. For low-light measurements, additional neutral density filters are utilised. Charge extraction transients in open-circuit conditions after reaching saturation are measured over a 50 Ω resistance, and low current values are amplified *via* a low noise amplifier (DLPCA-200 - FEMTO Current Amplifier) and detected by the oscilloscope. All measurements are controlled by computer with in-house written Wavemetrics IGOR Pro software.

3.9.3 Grazing Incidence X-ray Spectroscopy

GIWAXS measurements for structural analysis (Chapter 4) are performed at the 3C-SAXSl beamline in the Pohang Accelerator Laboratory (PAL) using a monochromatised X-ray radiation source at an energy of 10.55 eV (λ = 0.117 nm) and a 2D charge-coupled device (CCD) detector (Mar165 CCD). The samples are mounted onto a z-axis goniometer equipped with a vacuum chamber ($\sim 10^{-3}$ Torr) and placed at a distance of 0.201 m away from the CCD detector. The incident angle of each X-ray beam is set to 0.1°, and the scattering angles are determined from the positions of the X-ray beam reflected from the Si substrate using precalibrated silver behenate.

For the GI-XRD measurements presented in Chapter 7, an Empyrean diffractometer at generator settings of 40 kV, 40 mA is used (Materials department, Imperial College London). Primary optics consists of a hybrid monochromator containing a Ge(220) crystal and producing monochromatic Cu K_α radiation. Secondary optics consists of a 0.27° parallel plate collimator and a PIXcel 3D Medipix3 detector. The grazing angle ω is 0.5°, the scanned 2θ range goes from 5 to 40° with 0.04° step size, and a counting time of 8 s is used.

4 | Improving Stability in Bulk Heterojunction Organic Photovoltaics *via* Selenium-Substituted Nonfullerene Acceptors

While OPV performance is steadily increasing thanks to new-generation NFAs, ensuring long device lifetime and reliable operational stability under illumination still remains as an unsolved challenge. In this chapter, routes for molecular engineering of both core and end units in ITIC-derived NFAs are explored in their effects on OPV photostability. In particular, heteroatom substitution (sulfur to selenium) is applied at different core positions, combined with methylation of end groups. It is found that the conformational locking by Se-O noncovalent bond for outer-core Se substitution rigidifies the molecular backbone for enhanced chemical stability, while also leading to higher film crystallinity. At the same time, end-group methylation fine-tunes charge delocalisation along the backbone and promotes strong intermolecular interactions in both NFA domains and at D/A interfaces. Therefore, combining outer Se position and end-group methylation improves both chemical stability of molecular structures and morphological stability of the well-ordered packing, and excellent operational robustness is demonstrated in OPV devices. Overall, this chapter provides relevant guidelines for molecular design of novel NFAs towards enhanced device lifetime suitable for commercialisation.

4.1 Introduction

In recent years OPVs have seen incredible progress and drawn considerable attention within the scientific community as a source of clean energy, with the possibility of fabricating cheap, transparent, and lightweight solar cells based on biocompatible and solution-processable materials.[283–285] Nevertheless, in order to spark concrete interest in the market OPVs need to fulfill various requirements for their viable commercialisation, such as synthetic ease, batch-to-batch reproducibility, device efficiency, and operational lifetime.[286] In the landscape of current research on BHJ-based OPVs, shifting from the traditional utilisation of fullerene acceptors[28] to fullerene-free alternatives provides a successful way towards these goals. In fact, better light harvesting in the visible and infrared wavelengths[287–289] and wider possibilities of molecular tailoring of NFAs[28,130,132,135,290–293] allow substantial control over optoelectronic and morphological properties, besides facile processing and device fabrication[294] (more details are given in Chapter 2).

While OPV efficiency is rapidly increasing beyond 18% PCE,[10,11,139,143,144,146,148,295–297] device operational lifetime still remains as a key challenge to make OPV technology fully exploitable in the market. Despite eliminating fullerene-specific processes such as light-induced dimerisation,[189,298] photo-oxidation and light-induced trap formation,[233,237,299,300] or spinodal demixing,[187] and outperforming their counterparts in terms of device lifetime,[163,237,238,286,301] NFA-based OPVs still suffer from significant degradation, whose precise origin requires in-depth understanding.[239,286,302]

A number of studies describe the degradation processes as a complex interplay of multiple factors, including chemical instability of materials,[286] BHJ morphological changes,[188,191,236,239] device structure and interactions with charge extraction layers,[239,303] and poor heat diffusivity of the materials.[253] An interesting model developed by Du and co-workers[191] identifies the low NFA molecular diffusion coefficient as a source of small-scale morphology rearrangement under light especially in the amorphous D/A mixed domains. Here, stabilising the initial blend morphology (*e.g.*, by thermal annealing) is crucial for device stability. On the other hand, the intrinsic NFA photostability depending on their chemical structures also plays a key role. Planar NFAs - *e.g.*, IDTBR *vs.* IDFBR - are found to be less susceptible to photodegradation,[236] and more rigid NFAs, such as Y6, lead to low conformational disorder and high chemical stability.[212] End groups are also crucial, with ITIC fluorination improving stability towards photoactivated chemical reactions and phase separation compared to methylation.[286] However, other results show longer lifetime for methylated ITIC.[239] It is therefore evident that NFA structures and their inter-

play with BHJ morphology are crucial to determining OPV lifetimes.[304]

In this context, the molecular origin of photodegradation processes in terms of NFA structures is still not fully clear, and it is highly needed to provide unambiguous guidance for further materials development towards stable OPVs. In this chapter, we systematically study the effects of specific molecular structure modifications of NFAs on operational stability.

We synthesised a group of four NFAs, with chemical structures shown in Figure 4.1a, derived from widely used ITIC.[127] Here, three important structural modifications are carried out. First, two out of the four sulfur (S) atoms on the core backbone unit are replaced by selenium (Se) in either the inner or outer positions. The presence of heavier chalcogens in NFAs is effective at increasing quinoid resonance and decreasing E_g for enhanced absorption and light harvesting.[305,306] Moreover, highly polarisable Se atoms are expected to increase intermolecular interaction strength and tune solid-state packing.[307–309] However, the effect of selenium substitution and its regio-selectivity on OPV stability has not been investigated to date.[310] Second, electron-donating methyl groups are attached to the conjugated end units, to tune energy levels and affect V_{OC} in OPV devices.[311] Third, *m*-alkoxyphenyl groups, which are reported to be beneficial for molecular packing and charge mobility,[312] are attached as nonconjugated side chains, differently from the *p*-alkylphenyl typical of ITIC.

By analysing the synergistic roles of core Se substitution and end-group engineering to determine light-ageing patterns, we hereby identify a key relationship between NFA molecular structure and operational stability in OPVs. In particular, we find an exceptional device lifetime improvement for NFAs with outer Se substitution combined with end-group methylation (SeOutMe). Such a superior stability is attributed to important molecular and morphological characteristics induced by SeOutMe in blends. The heavier and larger Se atoms at outer-core positions rigidify the molecular conformation and enhance charge delocalisation over the molecule, while the methylation fine-tunes the ICT character. This combined effect is found to enhance chemical stability as well as strengthen acceptor domains in blends against light-induced morphological changes, leading to exceptional lifetime improvement in OPVs.

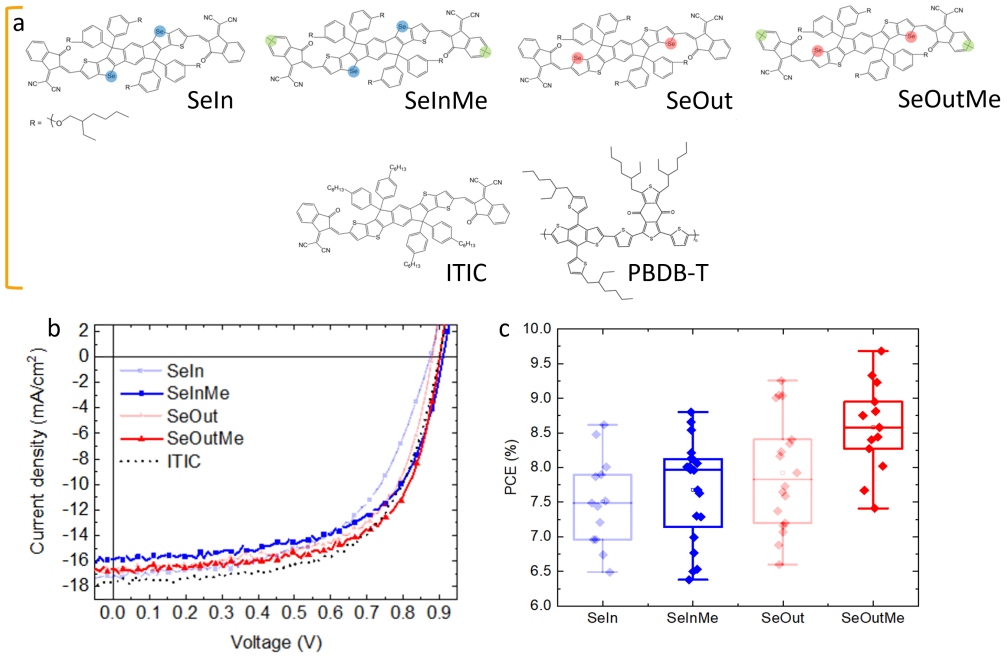


Fig. 4.1: (a) Molecular structure of selenated NFA molecules (with highlighted Se position in the core and methyl units in the end groups), ITIC and PBDB-T. (b) *J-V* characteristics and (c) *PCE* distribution (∼15 samples for each NFA) of PBDB-T:NFA devices, with photovoltaic parameters summarised in Table 4.1.

4.2 Results and Discussion

4.2.1 Device Performances and Operational Stability

The four NFA molecules SeIn, SeInMe, SeOut, and SeOutMe, derived from ITIC, are synthesized via decarboxylation, Stille coupling reaction, formylation, and Knoevenagel condensation. More details on their full chemical names, synthetic routes, and characterisation by NMR and mass spectroscopy are provided in the Experimental Section, Appendix A, and reference [19]. Figure 4.1a shows the chemical structure of the four acceptors highlighting the specific sites where the structural modification is applied. As in ITIC,[313] their conjugated backbone is based on the push-pull interaction between the electron-rich indacenodithieno[3,2-*b*]thiophene (IDTT) core and electron- withdrawing DCI end groups. In this group of NFAs, branched alkoxy instead of linear alkyl chains are used, attached to the *meta*- instead of *para*-position on nonconjugated phenyl rings as in ITIC. However, the most important modification is the substitution of two of the four thiophenes (S) in the IDTT unit with selenophenes (Se), either in the inner (SeIn) or outer core positions (SeOut). The remaining NFAs, respectively named SeInMe and SeOutMe, present the further addition of methyl groups onto the DCI end units. Here,

we study these synthesised NFAs in order to identify the effects of core heteroatom positions (Se and S) and end-group methylation on OPV performances and stability.

For device fabrication, the photoactive layer (PAL) is prepared by blending each NFA with the donor polymer PBDB-T, including PBDB-T:ITIC reference (ITIC and PBDB-T chemical structures are shown in Figure 4.1a). Details of OPV fabrication are given in the Experimental Section below. The solar cell characteristics of different blends are tested in inverted device structure ITO/ZnO/PAL/MoO_3/Ag, providing the *J-V* curves and the photovoltaic parameters for the champion devices, respectively, reported in Figure 4.1b and Table 4.1.

	V_{OC} (V)	J_{SC} (mA/cm^2)	FF	PCE (%)	T_{50} (h)
SeIn	0.88 (0.86)	17.40 (16.29)	0.56 (0.54)	8.61 (7.50)	140
SeInMe	0.91 (0.90)	15.90 (15.02)	0.61 (0.57)	8.80 (7.68)	860
SeOut	0.88 (0.87)	16.90 (15.68)	0.62 (0.58)	9.25 (7.92)	910
SeOutMe	0.90 (0.89)	16.70 (15.58)	0.64 (0.62)	9.68 (8.58)	5630
ITIC	0.90	17.70	0.62	9.91	410

Tab. 4.1: Champion and average photovoltaic parameters for ∼15 devices and T_{50} lifetime for PBDB-T:NFA solar cells. T_{50}, the time required for PCE to drop to 50% of the original value, is calculated from the starting measurement, without considering the initial fast decay in the burn-in phase. The data are directly measured for SeIn and ITIC, while extrapolated by linear fit for the other NFAs.

Table 4.1 also reports the average performances for the different NFAs (∼15 devices tested for each case), with efficiency distribution shown in 4.1c. A 20-30 mV higher V_{OC} is found in the methylated acceptors (SeInMe and SeOutMe), in line with their shallower LUMO levels (presented later), while their superior FF suggests better domain and/or interface morphology. It was previously reported that end-group methylation in ITIC mainly increases V_{OC}, with minor J_{SC} improvements and FF decrease due to less balanced mobilities.[311,314] However, methylation of these selenated acceptors induces a slightly different effect - *i.e.*, lowering J_{SC} and improving FF. Such differences can be associated with a less intermixed blend morphology observed for SeInMe and SeOutMe blends, where the formation of relatively large, purer domains with higher crystallinity (see PL and GIWAXS data below) can improve charge transport and FF. Among these four NFAs, SeOutMe shows the best efficiency with 9.68% PCE, 0.90 V V_{OC}, 16.7 mA/cm^2 J_{SC}, and 0.64 FF, with perspectives for a >10% PCE upon further device optimisation.

Although PCE for selenated NFAs is comparable to ITIC devices, their operational stability is substantially different (Table 4.1 also reports T_{50} lifetimes ex-

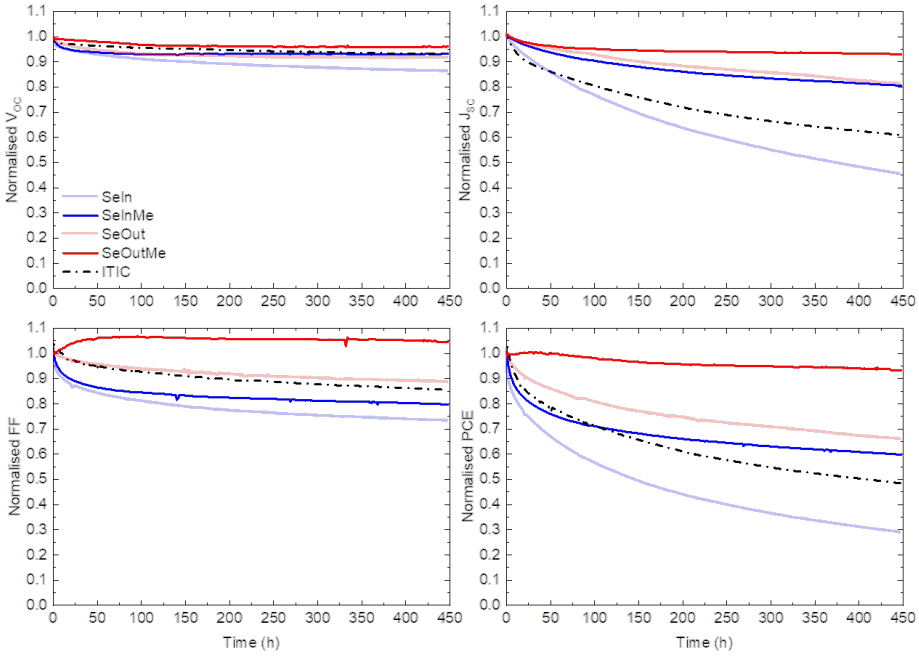


Fig. 4.2: Evolution of photovoltaic parameters under continuous light exposure (white LED) of PBDB-T:NFA devices.

tracted for all devices). After nearly 450 h of continuous operation under white LED (1 Sun equivalent, with devices sealed in a nitrogen-filled environmental chamber), the PCE of reference ITIC cells drops by more than 50%, while three out of the four selenated NFAs maintain higher efficiencies (Figure 4.2). The best results are achieved for SeOutMe, with only a ∼5% drop in initial PCE after the whole exposure time and an extrapolated T_{50} lifetime close to 6000 h. SeInMe and SeOut also show improved stability with respect to ITIC (35-40% efficiency drop), while only SeIn underperforms (70% PCE loss). For all devices, J_{SC} and FF are the main parameters dictating device stability. In particular, J_{SC} stability shows the greatest differences across materials, reduced by 55% for SeIn, by 20% in SeInMe and SeOut, but by only 7% in SeOutMe. As for FF, 75% of the initial value is maintained for SeIn, 80% for SeInMe, but up to 88% for SeOut. Strikingly, a FF enhancement during the first 50 h of operation is observed for SeOutMe, leading to an overall 5% increase after 450 h.

4.2.2 Optoelectronic and Morphological Characterisation

From the evidence that specific chemical modifications of NFA structures have such a significant impact on OPV stability, we perform detailed materials characterisation in terms of optoelectronic properties and thin-film morphology to investigate the origin of this impact. The UV-Vis absorption spectra of thin films of neat as-cast NFAs and PBDB-T (Figure 4.3a) show complementary absorption covering a wide portion of the visible and NIR in the 500-650 and 600-800 nm ranges, respectively. Differences emerge among the four NFAs, with a 10-15 nm bathochromic shift appearing for outer compared to inner Se acceptors, shifting the absorption maximum to 720 nm for SeOut *vs.* 710 nm for SeIn. Conversely, methylation leads to around 5 nm of blue shift. A slightly higher 0-0 *vs.* 0-1 absorption peak is observed for outer Se, which might indicate better head-to-tail interactions between molecules for improved in-plane ordering (detailed structural analysis by GIWAXS will be discussed later).[308,315,316]

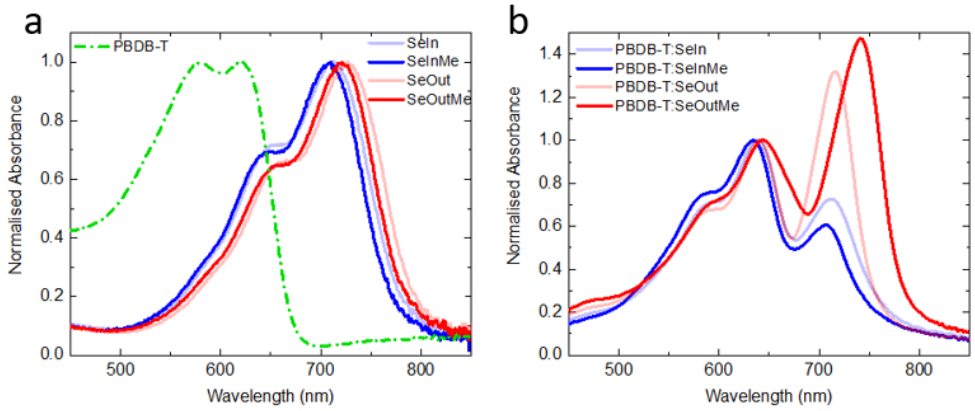


Fig. 4.3: UV-Vis absorption spectra of (a) pristine NFAs and PBDB-T and (b) of PBDB-T:NFA blends treated by thermal annealing.

Upon blending and subsequent thermal annealing (as in the optimised device fabrication protocol; see Experimental Section), the SeOutMe peak shows a significant red shift (Figure 4.3b). This is evident by further comparison with as-cast blends and annealed neat films shown in Figure 4.4. This suggests strong changes in packing and/or orientation of SeOutMe molecules in the blend, in a fashion improving their molecular order. In addition, this red shift is accompanied by a strong absorbance increase, with SeOutMe almost twice the absorbance of inner Se blends. This may indicate preferred in-plane packing of SeOutMe molecules in the blend, induced by less intermixing with the polymer after thermal annealing. As mirrored by the higher EQE in long-wavelength spectral regions (Figure 4.5), this can be largely beneficial for harvesting low energy photons in OPV devices. For the other

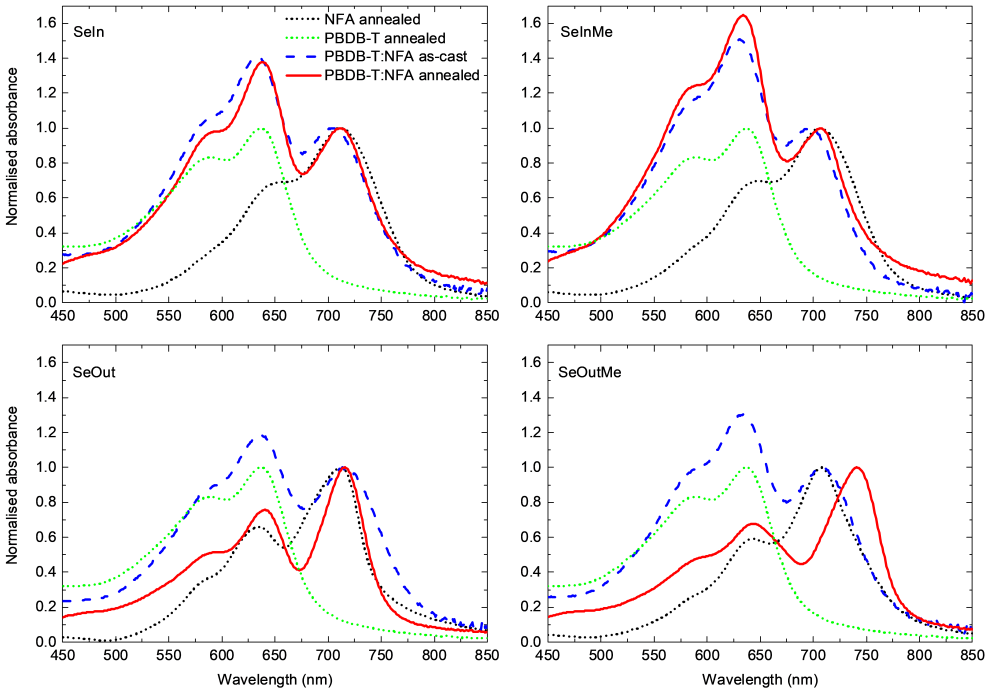


Fig. 4.4: UV-Vis absorption spectra of the different NFA blends, comparing the neat acceptor and donor with the as-cast and annealed thin films of respective blends.

three NFAs in blends, a slight blue shift (8-10 nm) and increased FWHM of both the acceptor- and donor-related peaks are observed, indicating packing disruption by blending with only minor ordering upon annealing.

In order to assess the degree of intermixing between donor and acceptor molecules and its impact on photophysical processes, PL and charge carrier dynamics are analysed. SeIn and SeInMe blends exhibit strong PL quenching with respect to the neat NFAs, whereas the effect is much weaker for SeOut and SeOutMe (Figure 4.6a). The quenching of D and A emission in SeIn blends amounts to 99% and 93%, respectively, indicating highly intermixed blends, while it decreases with methylation and especially outer Se substitution (see Table 4.2).

PL quenching (%)	NFA	PBDB-T
SeIn	93	99
SeInMe	88	99
SeOut	74	97
SeOutMe	44	94

Tab. 4.2: Summary of PL quenching for the different NFA blends with respect to the neat donor and acceptor components.

In particular, SeOutMe PL in the blend is quenched only by 44% compared

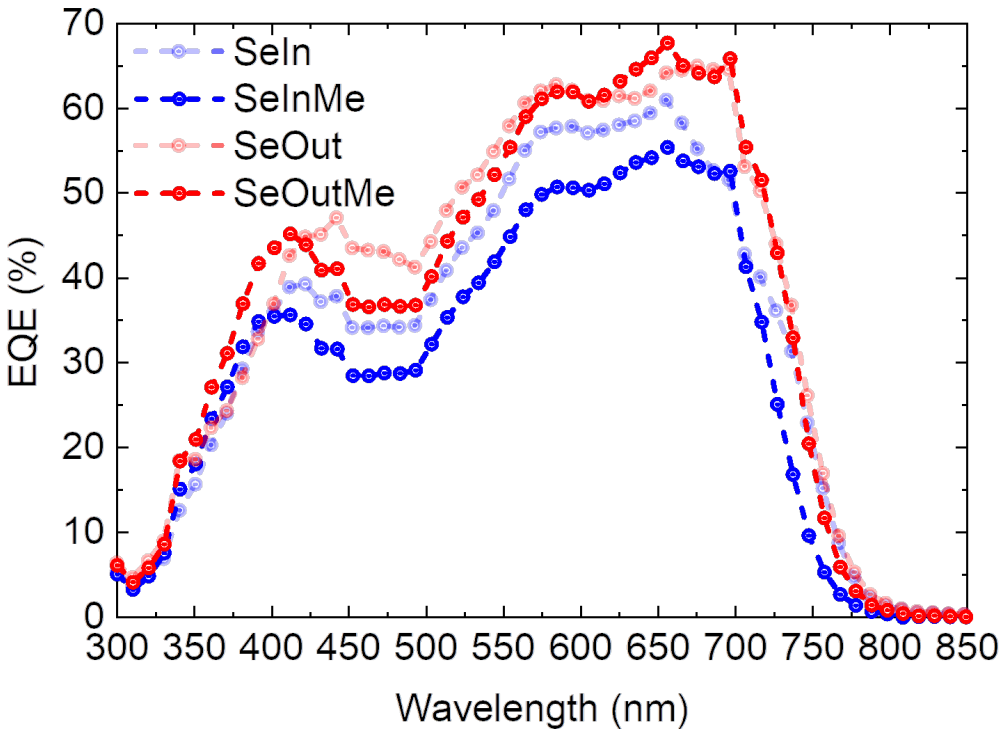


Fig. 4.5: EQE spectra of PBDB-T:NFA devices.

to the neat acceptor (where self-quenching effects may be present). Together with ~6% of donor emission still preserved in the SeOutMe blend, this confirms a much less intermixed D/A morphology in this system. Here, SeOutMe can form purer domains with better in-plane packing (Figure 4.3b), lowering geminate recombination and enhancing charge transport.[46,317,318] As mirrored in the performances of corresponding devices, this is beneficial for FF and V_{OC}, but can have detrimental effects for J_{SC}, highlighting the importance of a trade-off between D/A mixing and phase separation for maximising different device parameters. Note that the amount of PL quenching discussed here cannot be directly compared with the EQE generated from different blends (Figure 4.5), as PL is probed at a single wavelength (*i.e.*, 514 nm, in a region of low absorbance) and for thin films on quartz, where photogenerated carriers cannot be extracted and can only recombine either radiatively or non-radiatively.

The degree of D/A mixing being influenced by an inner or outer Se position is reinforced by charge separation kinetics obtained by TAS. Figure 4.6c shows the exciton and charge dynamics resulting from visible excitation of SeIn and SeOut blends (with pump wavelengths of 725 and 720 nm, respectively, corresponding to NFA absorption maxima), extracted by global analysis of the transient spectra.[19]

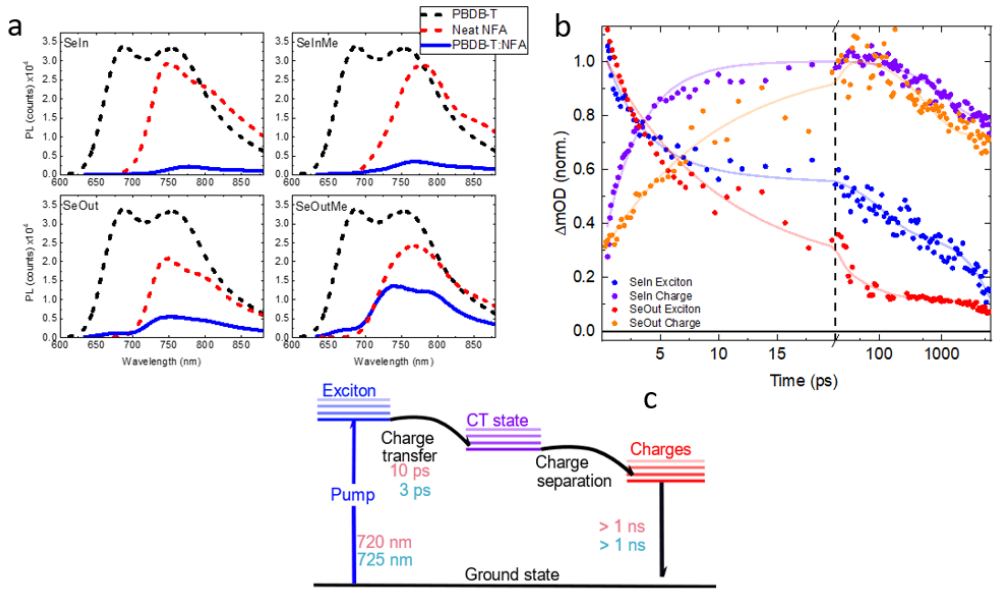


Fig. 4.6: (a) PL spectra for neat PBDB-T and NFAs and their respective blends. (b) TAS kinetics of excitonic and charge species for SeIn and SeOut blends. Solid lines represent exponential fits. (c) Diagram of the charge dynamic processes with characteristic time scales probed by TAS for SeIn (in blue) and SeOut (in red) blends. Note that the relative energies between different states are only indicative and do not necessarily mirror the energy cascade in BHJ systems (*e.g.*, CT states can be considered at higher energy than excitons depending on the description model).

Monoexponential fits of the excitonic components reveal exciton lifetimes of 2.9 ± 0.3 ps for SeIn and 9.7 ± 0.6 ps for SeOut. These decay times agree with the ones of simultaneous growth of charged components (3.1 ± 0.2 ps for SeIn and 10.1 ± 0.8 ps for SeOut), therefore representing the time scale of charge photogeneration from exciton dissociation. A longer process in the SeOut blend suggests larger D/A domains, since pump-generated excitons are likely to be formed further from D/A interfaces than in the comparatively highly intermixed SeIn blend. This is consistent with the observed weaker PL quenching and stronger intermolecular aggregation for SeOut, supporting the claim that both molecular packing and blend intermixing are strongly affected by Se position. In particular, both donor and acceptor components are expected to show more ordered packing and larger domains for SeOut *vs.* SeIn. Further data supporting this model will be presented later from GIWAXS results.

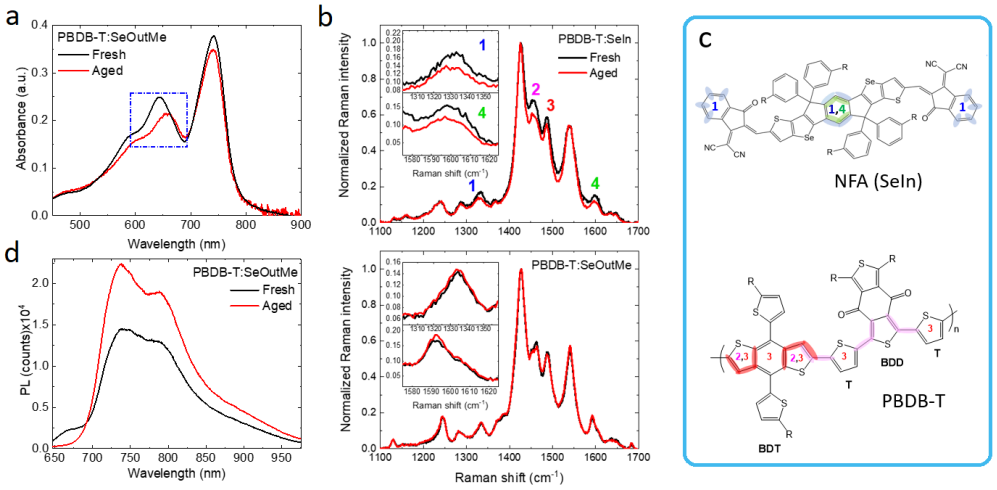


Fig. 4.7: (a) Evolution of UV-Vis absorption spectra upon 200 h of light exposure for SeOutMe blends. (b) Evolution of Raman spectra of the SeIn and SeOutMe blends, normalised to the main peak, with contributions from thiophene unit in PBDB-T and thiophene-selenophene in NFAs. Enlarged view of peaks 1 and 4 is presented in the inset. (c) Schematics and labelling of spectral modes relative to NFA and PBDB-T molecules, with R = 2-ethylhexyl. (d) Evolution of PL spectra for SeOutMe blends.

4.2.3 Investigation of Photostability and Degradation Mechanisms

In order to understand photostability and associated degradation mechanisms in neat materials and blends, we study the effects of prolonged light exposure on their optical and morphological properties. Comparison of absorption spectra of fresh and aged blends (Figure 4.7a for SeOutMe and Figure C.1 in Appendix C for all blends) shows that chemical instability and chromophore quenching in PBDB-T and NFAs are involved in the photodegradation process. SeIn(Me) show stronger bleaching for donor peaks, evidence of unbalanced degradation in D/A domains. However, superior robustness is found in SeOut and SeOutMe blends, with a slightly weaker PBDB-T absorption decrease and a more balanced quenching of donor and acceptor peaks after 450 h of light exposure. Note that the stronger reduction of absolute intensity for acceptor peaks can be related to the significantly stronger absorption coefficient of SeOut and SeOutMe compared with inner Se counterparts. Interestingly, for SeOutMe blends the polymer absorption peak red shifts by ∼10 nm during the first 200 h of light exposure, coinciding with the initial FF enhancement for SeOutMe device. This suggests an important morphological factor to consider in D/A blends towards stable OPVs. Upon blending, highly crystalline NFAs such as SeOutMe produce a much less intermixed morphology with purer D/A domains,

enabling further morphological changes within these domains under continuous light exposure. In the SeOutMe blend, polymer reorganisation leads to optimised blend morphology, for highly stable OPV devices. This fine-tuning of blend morphology and domain separation by D/A miscibility has been indicated in numerous studies on ternary OSCs as a crucial factor to improve device performance, and it is also regarded as a promising strategy towards high light and thermal stability.[319,320]

Further insights into the photo-induced structural changes of D and A molecules in blends are gained by Raman spectroscopy.[188,236] Figure 4.7b shows Raman spectra collected from fresh and aged SeIn and SeOutMe blends (see Figure C.2 for all blends), with the most relevant vibrational modes of NFAs and PBDB-T illustrated in Figure 4.7c. Complete Raman assignment is detailed Appendix C (Figure C.3-Figure C.4 and Table C.1-Table C.2). In agreement with the chromophore bleaching observed in the absorption spectra, Raman data further reveal the changes of molecular structures from specific vibrational peaks. The main modes originate from the core phenyl groups and end phenyl H-wagging of the acceptor (peaks 1 and 4) and the BDD and BDT units along the conjugated backbone of the donor polymer (peaks 2 and 3), with an overall dominance of polymer-related peaks. The strongest peak around 1425 cm^{-1} has a contribution from both the thiophene unit of PBDB-T and thiophene-selenophene of the NFAs, while the peak at 1540 cm^{-1} is assigned to both alkene stretching in the NFAs and a BDT unit mode in PBDB-T. Different degrees of quenching of overall peak intensities are observed in all the four blends, indicating different amounts of photobleaching in both D and A upon light-ageing. By comparison of Raman spectra of fresh and aged blends, several interesting elements can be noticed. First, SeIn shows the most changes in relative peak intensities: peaks 1 and 4 (assigned to the NFA) drop by 5%, and peaks 2 and 3 (assigned to PBDB-T) decrease by 10% and 5%, respectively. By Raman spectra simulation, this can be matched to conformational changes in the NFA molecules with different core-end dihedral angles (Figure C.5). In particular, increasing molecular twisting leads to a quenching of the NFA peaks (1 and 4), similarly to the conformational changes observed in other NFAs during photoageing.[236,321] Second, when SeIn and SeInMe blends are compared (Figure C.2), there is no relative intensity change in NFA-related peaks for the latter, although polymers still show some quenching, indicating that methylation stabilises NFAs against photoageing. Third, quenching for outer Se blends is significantly reduced, with only minor decrease in the polymer peak for SeOut and almost no changes in SeOutMe, indicating superior photostability of SeOutMe blends. Evolution of Raman spectra of neat NFAs under photoageing (Figure C.6) further confirm the greater stability of SeOut and SeOutMe.

Concomitantly with photodegradation of D and A molecules, photo-induced BHJ morphology evolution also occurs, as seen from PL spectra (Figure 4.7d for SeOutMe, with results for the four materials in Figure C.2). All aged blends show enhancement of NFA PL, while polymer emission is now totally quenched. As discussed earlier, we consider this NFA PL recovery as a signature of morphology changes (possibly through heat generated during photoexposure), here demonstrating further segregation of NFAs from the polymer.[191] This also allows polymer chains to better pack and aggregate, as particularly evident from the absorption red shift for SeOutMe (Figure 4.7). The acceptor PL recovery in blends is smaller for outer Se and methylated NFAs, with only a 1.5-time increase for SeOutMe *vs.* a three-fold in SeIn. This indicates that SeOutMe blend morphology, initially segregated to form larger and purer domains, is more robust to further phase segregation. Therefore, a moderate initial phase separation with more crystalline NFA domains is found to be beneficial for long-term photostability: this prevents further light-induced macroscopic D/A segregation while allowing structural evolution of neat polymer domains. On the contrary, SeIn blend morphology shows even macroscopic light-induced changes in surface aggregation (see AFM maps in Figure 4.8), clearly non-ideal for J_{SC} and FF in devices.

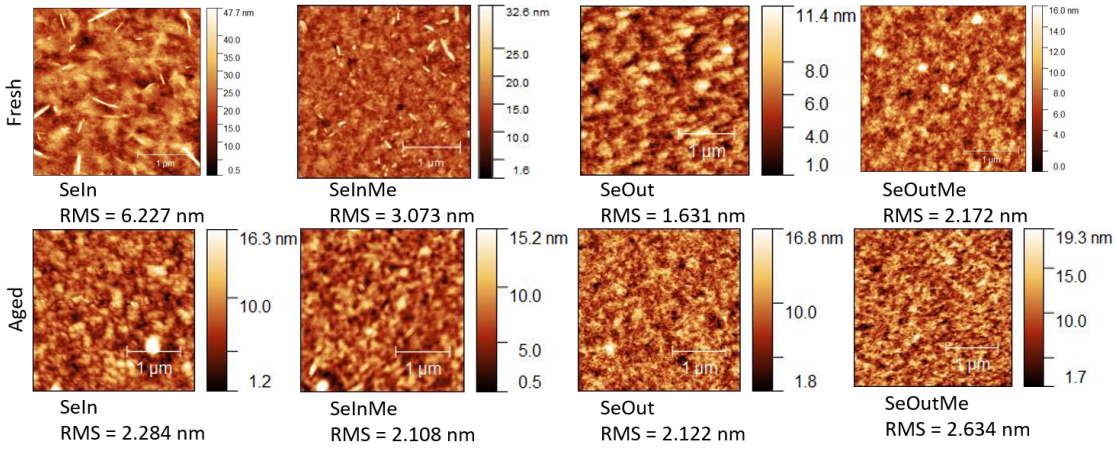


Fig. 4.8: AFM maps of fresh and light-aged PBDB-T:NFA blends.

To confirm that an optimum morphology is achieved by outer Se position and methylation, we now turn to investigate the impact of molecular structure on packing in neat and blended NFAs. GIWAXS measurements for neat and blended SeOutMe are performed to obtain 2D patterns as shown in Figure 4.9a,b, respectively. For the neat SeOutMe film, clear (00L) diffraction families of reflections are observed at q_z (Å^{-1}) = 0.32, 0.64, 1.26, and 1.62, and strong diffraction spots of the (102), (110), and (002) planes along the $q_{x,y}$ direction. This implies a highly ordered crystalline

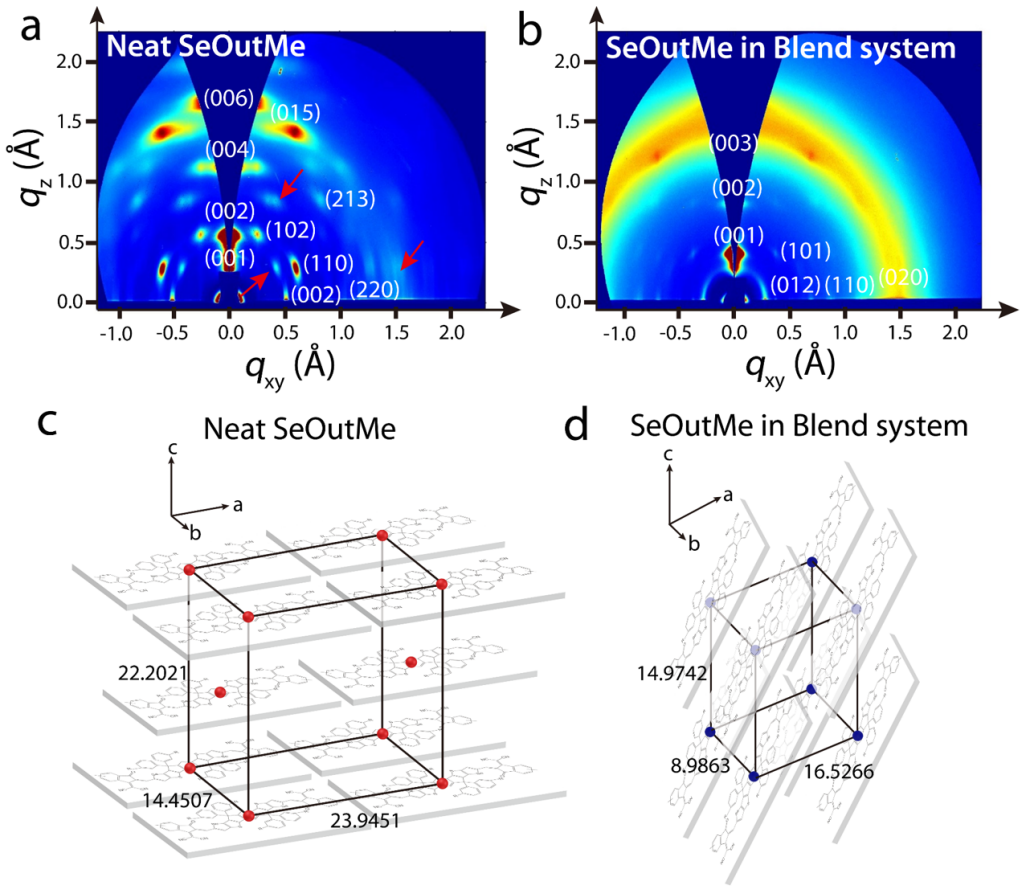


Fig. 4.9: (a,b) GIWAXS 2D maps for neat and blended SeOutMe, with indication of the corresponding crystalline planes. (c,d) Schematic of the crystalline structure for one of the two phases in neat SeOutMe and for the acceptor domains in PBDB-T:SeOutMe blends, respectively, with indication of the lattice parameters in the three directions.

structure, referred to here as *crystal phase 1*. Comparing the 2D GIWAXS patterns of neat SeOutMe with those of the other NFAs, more intense and sharper peaks show that outer Se and methylation improve crystallinity (see detailed information in [19]). Interestingly, the additional diffraction spots marked by red arrows indicate the presence of a second crystal phase coexisting in neat SeOutMe, referred to here as *crystal phase 2*. These 2D GIWAXS patterns combined with diffraction simulation analysis reveal that crystal phase 1 of neat SeOutMe conforms to an orthorhombic unit cell with lattice parameters a = 23.9451 Å, b = 10.4147 Å, c = 22.2021 Å, α = 90°, β = 90°, and γ = 90°. Crystal phase 2 has the same lattice parameters except for b = 14.4507 Å (see Table 4.3 for SeOutMe). The corresponding molecular packing motif of neat SeOutMe can be proposed as shown in Figure 4.9c. In contrast to the neat films, all PBDB-T:NFA blends exhibit a relatively weak intensity of the GIWAXS diffraction pattern and a less uniform

	neat SeOutMe		
	phase 1	phase 2	PBDB-T blend
a (Å)	23.9451	23.9451	16.5266
b (Å)	10.4147	14.4507	8.9863
c (Å)	22.2021	22.2021	14.9742
α (deg)	90	90	90
β (deg)	90	90	90
γ (deg)	90	90	103.446
space group	$Amm2$ (No. 38)	$Amm2$ (No. 38)	$P2$ (No. 3)
cryst. syst.	orthorhombic	orthorhombic	monoclinic

Tab. 4.3: Summary of the lattice parameters, angles, and crystalline structure symmetry for neat and blended SeOutMe.

diffraction spot of the (00L) family, although the obvious amorphous ring pattern originates from the donor polymer. However, SeOutMe blend still shows the most intense acceptor diffraction pattern and polymer ring, indicating that crystallinity of both polymer and NFA are highest for this blend, consistent with the red-shifted absorption and clearer phase segregation indicated by PL. Moreover, there is a noticeable shift in the SeOutMe peak positions towards higher q_z corresponding to the (001) planes and higher $q_{x,y}$ corresponding to the (110) planes, indicating a reduced d spacing in the molecular lattice. This can be evidence of a change in the crystal structure of SeOutMe upon blending, with a more compressed packing, resulting in a monoclinic system with lattice parameters $a = 16.5266$ Å, $b = 8.9863$ Å, $c = 14.9742$ Å, $\alpha = 90°$, $\beta = 90°$, and $\gamma = 103.446°$ (Figure 4.9d). The ability of SeOutMe to form various crystal structures, two in the neat phase and a different one in the blend, and its stronger intensity of crystalline peaks compared to the other acceptors are demonstrative of the particularly strong and versatile intermolecular interactions in SeOutMe. This promotes and stabilises SeOutMe phases in the blend, inhibiting further light-induced phase-segregation. Moreover, the crystalline nature of SeOutMe can also foster the packing order in polymer domains and allow the benign photoinduced PBDB-T reorganisation observed earlier.

To link the origin of solid-state morphology, crucial for photostability, to the specific molecular structure of different NFAs, we seek further understanding of materials properties by DFT analysis. The effects of core heteroatom substitution and end-group engineering are simulated for correlation with the NFA optoelectronic properties experimentally observed. Figure 4.10a shows the potential energy as a function of dihedral angle between the core and the end groups. All acceptors have two potential energy minima around 0 and 180°, where the conjugated backbone is planar. However, when Se is in the outer position, the energy min-

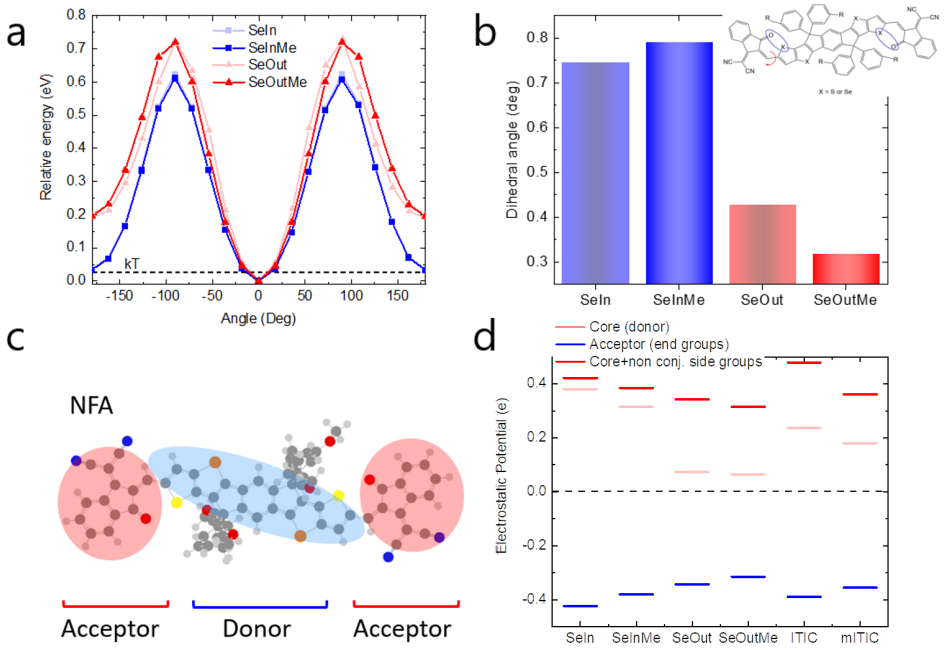


Fig. 4.10: Results of DFT simulations for the different NFA single molecules. (a) Diagram of the molecular potential energy *vs.* the dihedral angle between core and end groups. (b) Dihedral angle between the core and the end groups, indicated as the red arrow in the generalised molecular structure in the inset. (c) Indication of the donor and acceptor building blocks on an example of NFA molecular structure (*i.e.*, SeIn). The donor region does not include the nonconjugated side chains. (d) Positive and negative electrostatic potentials for the donor and acceptor regions, respectively, in the different NFA molecules. The positive potential includes separately the respective contribution of the electron-rich molecular core and the nonconjugated side chains. ITIC and its methylated version (mITIC) with analogous nonconjugated side chains are also included.

imum (corresponding to the configuration in which the carbonyl oxygen and Se are in close proximity) is 0.2 eV lower compared to that at 180°, which originates from Se-O noncovalent interactions.[305,306] Torsion angles between the core and end groups in energy-optimised single molecule geometries of the four NFAs (Figure 4.10b) also show the role of chalcogen-O interactions as a backbone conformational locker. In SeOut(Me) stronger noncovalent interactions with larger Se orbitals reduce the core/end-group dihedrals and planarise the molecule. This is also evident from the shorter interatomic distance for Se-O (outer Se) in comparison with S-O (inner Se) (∼2.725Å for SeIn(Me) and ∼2.625Å for SeOut(Me)). Therefore, SeOut and SeOutMe possess a more planar and especially rigid backbone, fundamental to superior chemical stability and optimum packing in solid state, in good agreement with the observed optical and structural properties of these NFAs. Conversely, in-

ner Se substitution leaves lighter S in the outer position, with S-O interactions less effective at stabilising the molecule. For SeIn and SeInMe this results in a negligible energetic difference between the 0 and 180° configurations. Moreover, the energetic barrier between them is 0.1 eV lower, so that a variety of isomeric conformations can be adopted, which is detrimental for solid-state packing and conformational disorder. This is indeed verified by the larger presence of tail states (see below) and the blue-shifted absorption and larger band gaps for SeIn(Me) *vs.* SeOut(Me). The ESP is further analysed based on the Merz-Kollman model to estimate the ICT character in each acceptor.[277] Grouping the atoms of core, conjugated end groups and nonconjugated side chains, we quantify the amount of charge separation between donor and acceptor units, according to the assignment schematised in Figure 4.10c (in particular, the CH group in the connecting vinyl bond is considered part of the acceptor unit). ESP shown in Figure 4.10d indicates that the ICT character of the molecules is slightly reduced by both outer Se position and methylation. Moreover, outer Se displaces more positive charge from the electron-donating core toward nonconjugated side groups. This can be related to the orbital distribution detailed in Figure 4.11, where only the outer-core chalcogen takes part in the HOMO. In this context, the heavier and more electron-rich Se atoms in the outer positions enhance charge delocalisation with a stronger interaction with the electron-donating oxygen atom in the side chains, whereas the distribution for SeIn(Me) is comparable with the nonsubstituted ITIC with identical side chains (Figure 4.10d).

In this picture, the balance between ICT character of the conjugated backbone and charge localisation in the side chains is crucial to explain the superior stability of SeOutMe, with optimum molecular structure mirrored in solid-state packing. The displacement of more charge density toward the side chains helps them establish induced dipoles and reinforce dispersion interactions in solid-state packing,[322] while increasing the A-D-A character within the conjugated backbone of the NFA. Se-O interactions with the side chains are also possibly beneficial as noncovalent locker, reducing conformational disorder and leading to dense and effective packing. At the same time, methylation mildly decreases negative charge localisation in end groups. This fine-tuning of charge density in the DCI units is helpful to packing enhancement and stabilisation *via* end-group π-π stacking, similarly to what found in other ITIC derivatives.[323] As previously reported, the precise control of charge distribution along and outside the molecular conjugated backbone is a powerful tool to determine the local intermolecular interactions *via* π-orbitals and to optimise transport properties in OPV blends.[324,325]

Since it is clear how the different NFA structures have a great influence on

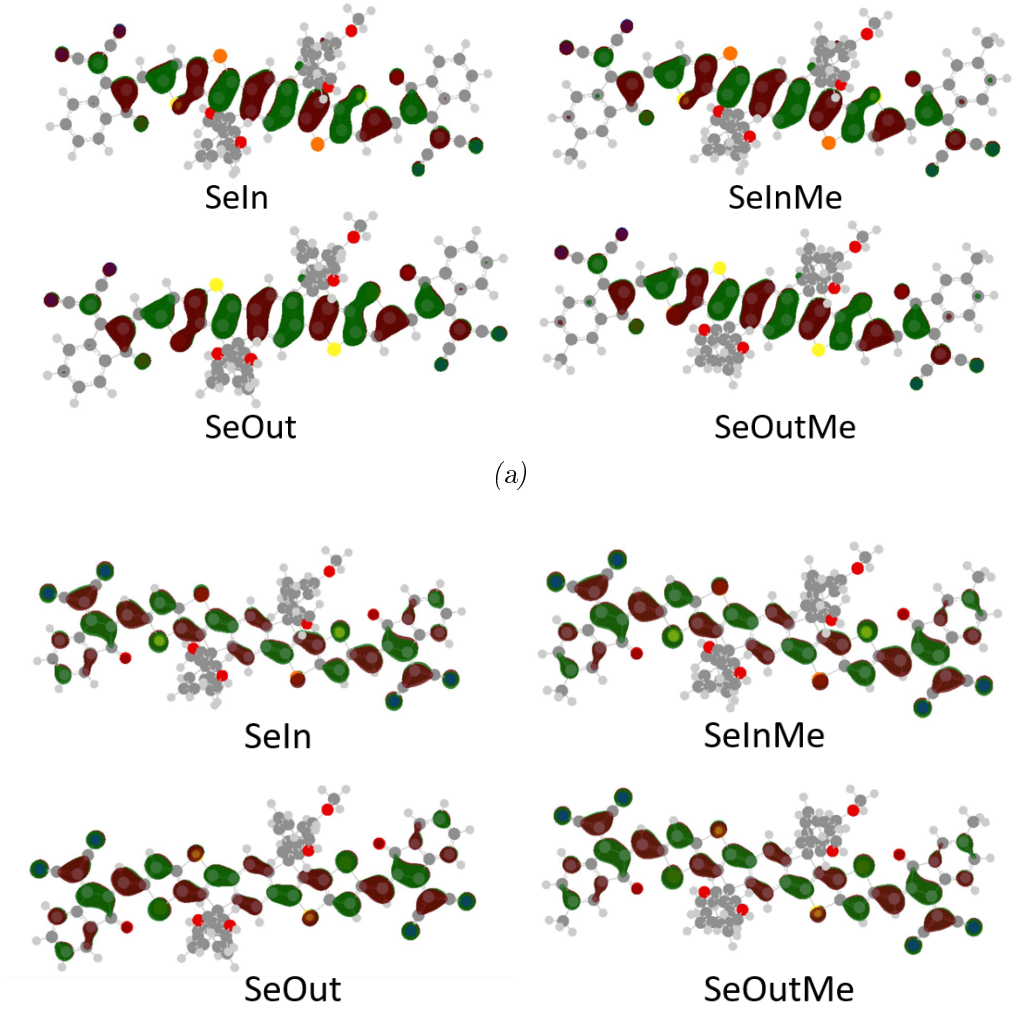


Fig. 4.11: (a) HOMO and (b) LUMO distributions for DFT energy-optimised structures of different NFAs.

molecular packing and therefore on OPV stability, the impact of NFA structures on energetics (namely, HOMO/LUMO levels and sub-bandgap states) is further investigated using APS (Figure 4.12a,b), combined with the optical band gap from UV-Vis absorption (Figure 4.3).[326] As expected from the electron-donating nature of the methyl groups, SeInMe and SeOutMe show shallower energy levels, with the LUMO affected more than the HOMO. Se position has a stronger impact on the LUMO, with slightly deeper energy levels for outer Se. These results are relatively well matched with the energy levels calculated from DFT (Figure 4.12c), showing the impact of NFA chemical structure and conformation on the energetics. The onset in photoelectron emission spectra has been previously used to determine the HOMO or the valence band edge of semiconductors, and the area below the onset

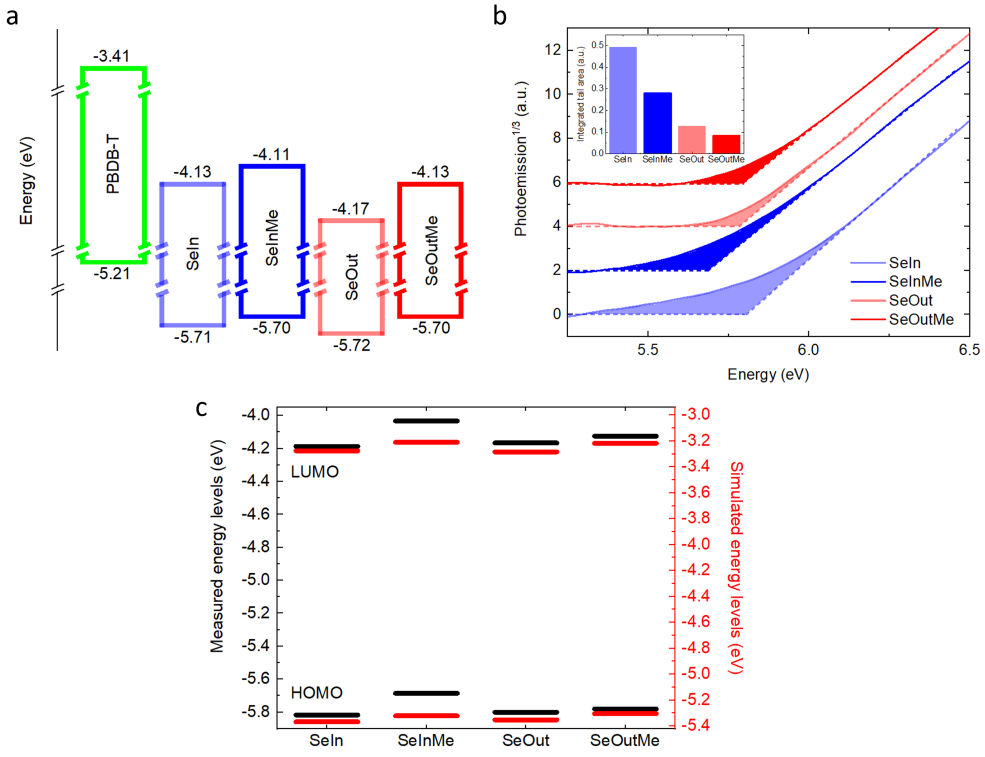


Fig. 4.12: (a) Energy diagram relative to PBDB-T and NFAs. The values for PBDB-T have been drawn from literature, measured from CV as reported in reference [326]. (b) Photoemission intensity from neat NFA thin films (annealed), with linear fit to the emission edge, translated vertically with respect to one another for better reading clarity. The inset shows integrated tail areas below the edge. (c) HOMO and LUMO energy levels for the different neat NFAs, comparing the experimental results with DFT simulated values.

as a proxy for density of sub-bandgap tail states corresponding to traps and/or defects.[212,218,270] A relative comparison of tail states in the four NFAs is made from the integrated area below their photoemission thresholds. As shown in Figure 4.12b, SeOut(Me) exhibits much smaller areas than SeIn(Me). This suggests significantly reduced energetic disorder, related to the more rigid molecular structure and low conformational disorder, playing a key role in the stability of SeOutMe devices.

To summarise, the synergy of the two engineering routes - outer Se substitution and methylation - is the key to the superior stability of SeOutMe-based OPV devices. The rigid molecular geometry of SeOutMe and the fine-tuning of charge distribution over its structure is found to be important for high crystallinity and significantly reduced conformational disorder. This leads to superior chemical stability and robustness toward light-induced phase segregation in blends, while allowing the polymer structural reorganisation towards optimised blend morphology.

4.3 Conclusion

In conclusion, by combining end-group methylation and regio-specific Se substitution in the molecular core of ITIC-derived NFAs, we achieve significant improvements in the operational stability of OPV devices. Positioning Se in outer-core sites is a powerful tool to rigidify the molecular structure *via* noncovalent locking, ensuring a higher intrinsic chemical stability and an optimised charge distribution over the molecule. Here, nonconjugated side chains play an important role to stabilise the interactions with neighbouring molecules. At the same time, the mild electron-donating effect of methylation tunes the molecular ICT character for further control on packing and D/A interactions in blend. All of these characteristics, descending from the NFA molecular design, enhance the crystallinity and photostability of the SeOutMe acceptor. This is highly effective to prevent photoinduced phase segregation and subsequent disruption of its molecular structure in blend.[236] Therefore, SeOutMe devices show excellent operational stability, retaining 95% of the initial PCE after 450 h of operation, with an exceptionally long projected half-lifetime of 5600 h compared to 400 h for ITIC. The need for strong crystallinity of the acceptor for photostability is in line with what recently emerging for the Y-series of NFAs. Also there, a high crystallinity and 3D charge delocalisation have been demonstrated, as well as adaptability to form various crystal phases such as monoclinic and triclinic,[160,162] leading to excellent chemical stability of the acceptor.[212] Overall, the results presented in this chapter shed light on fundamental understanding of the relation between NFA molecular structure, BHJ morphology, and device operational stability, suggesting relevant design guidelines for further materials development for highly-stable OPVs.

4.4 Experimental Section

Sample Fabrication, Device Measurement, and Stability Test

SeIn, SeInMe, SeOut, and SeOutMe are synthesised as detailed in [19], while commercial batches of ITIC and PBDB-T are used (Sigma-Aldrich). Thin films are prepared in a cleanroom from a solution in chlorobenzene with 0.5% DIO additive (20 mg/mL dilution), 1:1 D:A weight ratio in the case of blends. The solutions are stirred by magnetic bars overnight at 250-400 rpm at 60°C on a hot plate, and filtered (0.45 μm, PTFE) before deposition. Films are formed by spin-coating on clean ITO and fused quartz substrates, achieving a 40-80 nm film thickness checked by Dektak surface profilometer. For device fabrication, details about ZnO, MoO_3,

and Ag layers are given in Section 3.1. Annealed films and all devices except for PBDB-T:ITIC ones are thermally treated in a N_2-filled glovebox for 30 min at 160°C. Device *J-V* characteristics are checked by a Keithley 2400 source meter under AM1.5 G illumination provided by a Newport 6258 Xe arc lamp solar simulator calibrated by a Si photodiode. Device and thin-film light ageing are carried out in N_2-filled chambers under white LED with power density equivalent to 1 Sun, without IR component (see Section 3.8 for further details of the spectrum). To measure EQE, a tungsten halogen lamp coupled with a grating spectrometer (CS260-RG-4-MT-D) is used. The photocurrent response is detected by a Stanford Research System SR380 lock-in amplifier, calibrated by a Si photodiode.

Energetics and Morphology

HOMO energy levels of thin films on grounded ITO are measured by APS04 photoemission system. Multiple spots are examined on the sample surface to check reproducibility and calculate experimental errors, and the HOMO is extracted from the linear fit of the cube root of the photoemission intensity as crossing with the zero baseline (see details in Section 3.3).[265] Surface morphology is measured by a Park NX10 AFM in tapping mode with Park silicon PPP-NCHR tips combined with SmartScan software (see Section 3.6).

Absorption, Photoluminescence, and Raman Spectroscopy

PL and Raman spectra are measured by a Renishaw inVia Raman microscope in backscattering configuration, as detailed in Section 3.2 and Section 3.5. Both measurements are carried out with a 514 nm argon-ion laser, 25% defocused on the sample. 2400 lines/mm and 300 lines/mm diffraction grids to obtain Raman and PL spectra, respectively. Multiple spectra are measured at different spots on the sample surface to improve data accuracy. PL background removal from Raman data is performed by polynomial fitting. Thin-film absorbance is measured as detailed in Section 3.4.

Ultrafast Broadband Transient Absorption Spectroscopy

Details on TAS characterisation are provided in Section 3.9. Here, the pump intensity is attenuated to 5 nJ before reaching the sample surface.

Grazing Incidence X-ray Spectroscopy

All details on GIWAXS are reported in Section 3.9.

Computational Methods

Simulations of molecular conformations, energy levels, dihedral scans, and Raman spectra are performed based on DFT, using Gaussian09 software on the Imperial College High Performance Computing service as detailed in Section 3.7, at the B3LYP level with the 6-31G(d,p) basis set. The molecular structures of single NFA molecules in gas phase are optimised to the minimum energy conformation, simplifying the ethylhexyl to methyl side chains to reduce computational load. Electrostatic potential is simulated according to the Merz-Singh-Kollman (MK) scheme using 1.90 Å as the van der Waals radius of Se.[277]

5 Light-Intensity-Dependent Photoresponse Time of Organic Photodetectors and its Molecular Origin

While OPDs are emerging as promising candidates to complement Si-based photodetection technologies thanks to tunable spectral response and inexpensive fabrication, their figures of merit still lag behind inorganic counterparts, especially when it comes to photodetection speed. In this chapter, the origin of slow photocurrent transients in evaporated OPDs is explored, focusing on the role of molecular structure of small-molecule donors. When a twisted and a fully planar candidate are compared, fast photoresponse is found in the planar molecule at relatively high light intensities (*i.e.*, $>$0.5 mW cm^{-2}), while a slow two-phase photocurrent decay appears under weaker illumination, not found for the twisted donor. This is assigned to a density of deep trap states, which are formed by nanoaggregation of the strongly-interacting planar molecules and adduct formation with the fullerene acceptor. Overall, the origin of shallow and deep trap states in OPD systems is investigated, and guidelines are given for molecular design of small-molecule donors to optimise photodetection speed depending on targeted light intensity of operation.

5.1 Introduction

The use of organic semiconductors for photo-sensing applications has recently seen fast progress,[60,327–333] thanks to their promising properties such as narrow absorption and colour-tunability,[334] flexibility, light-weight, transparency, and ease of fabrication. In particular, for top-surface photodetection in integrated, high-resolution imager arrays,[88,178] small-molecule-based photoactive layers are advanta-

geous due to high purity and batch-to-batch reproducibility.[335] For BHJ OPDs, these are typically deposited by co-sublimation of donor and acceptor materials, yielding highly intermixed morphologies for efficient exciton separation.[186] For evaporated active layers, C_{60} acceptor is normally the preferential choice due to its isotropic charge transport and ease of sublimation.[88,178,179,334,336] However, proper selection and design of sublimable donor molecules still remain as a key challenge for OPD optimisation (see detailed discussion in chapter 2).

Recently, promising device performances have been demonstrated for push-pull donors (*i.e.*, having donor and acceptor building blocks along the conjugated backbone),[88,179,334,337] where their D-A character provides effective control of energy levels and optical bandgap. Such structural motifs have also enabled, in blends with C_{60}, to tune the photodetection spectral range, to enhance charge transport properties, and to optimise photoactive layer nanostructure.[88,178,179,334] In particular, good performance has been reported with merocyanine and related dyes, achieving sharp, narrow absorption and fast photoresponse.[88,178,334,337] Various other molecular design strategies such as fusion of the donor unit and functionalisation or elongation of the acceptor unit have also been explored in the donor molecules, achieving excellent OPD figures of merit, including dark currents around 1 nA/cm^2 and detectivities in the order of 10^{13} Jones.[88,178,334,337]

Despite these achievements, the major limitation of OPDs compared with crystalline inorganic counterparts remains their relatively slow photoresponse,[338–340] due to the low carrier mobility intrinsic to organics as discussed in Subsection 2.2.2.[341–346] This poses strong limitations to the achievable frequency bandwidth, and restricts the possibilities of OPD integration with faster inorganic photodetectors.[339] Moreover, OPD photoresponse can become even slower in low-light operating conditions,[347] further limiting their potential applications. Energetic disorder and charge trapping in OSCs[74,212,218,348–351] can stem from multiple factors such as chemical impurity or co-existence of different conformational isomers,[212,218] molecular-structure induced packing and orientation, and sub-optimal domain formation. Even for sublimed OPDs, known for better device performance and reproducibility than solution-processed devices, molecular origin of energetic disorder and charge trapping, therefore of slow photoresponse, remains not fully understood.[88,178,179,337]

In this chapter, we elucidate the role of donor molecular structure on the formation of trap states in co-evaporated C_{60} blends, and its impact on the light-intensity dependent photoresponse speed of BHJ OPDs. In particular, two small molecule donors are used with C_{60} acceptor, featuring distinctive conformations, with either twisted or planar geometry. The planar donor MPTA yields a faster OPD response

under relatively high-light irradiation (1 Sun down to 0.5 mW/cm^2), but shows biphasic photocurrent transients with a slow second phase at low-light levels (*e.g.*, 0.02 mW/cm^2). These light-intensity-dependent photoresponse times are correlated with differences in charge trapping induced by the donor molecular structure. In particular, the slow low-light photoresponse of MPTA is traced back to BHJ nanoaggregation and potential formation of adducts with C_{60}, with creation of deep-trap states. In contrast, the twisted NP-SA shows higher energetic and structural disorder at the band edge, which limits the high-light photoresponse speed. However, the absence of further deep states allows to maintain OPD performances and photoresponse time independently of light intensity. Overall, the results provided in this chapter reveal important insights into the molecular origin of trap states in BHJ OPDs and how molecular design requirements can differ for high- and low-light device operations.

5.2 Results and Discussion

5.2.1 Twisted (NP-SA) and Planar (MPTA) Donor Molecules

Chemical structures of the two small molecule donors, NP-SA and MPTA (full chemical names in Appendix A), are shown in Figure 5.1a. Their synthetic routes are reported in ref. [337] and [20], respectively. Both donors are comprised of electron-donating and electron-withdrawing units (D-A structure) based on fused heterocycle groups, yielding a compact structure suitable for the formation of highly-intermixed interpenetrated networks upon co-evaporation with C_{60}.[88,178,179,337] For NP-SA, the donor unit is constituted by a tertiary amine coordinating benzene and naphthalene units to the selenophene molecular core, while three fused rings form the acceptor unit. NP-SA optimised geometry based on DFT shows twisted 3D-like arrangement of donor unit with a planar linkage between the core and the acceptor units (Figure 5.1a). MPTA has the same three-fused-ring acceptor unit as NP-SA, but the donor unit is made of a single fused heterocyclic group incorporating the amine linkage and the thiophene ring, resulting in a planar geometry. DFT calculations show the preferential HOMO and LUMO distributions to the donor and acceptor units, respectively, for both NP-SA and MPTA (Figure 5.1b). However, the planar MPTA shows smaller electrostatic potential separation on the D and A units, in line with better charge delocalisation along its planar conjugated backbone. Although existing studies suggest that a twisted conformation (out-of-plane branching) is ben-

eficial to prevent excessive molecular aggregation and improve absorption range and dark current,[337] no detailed study comparing twisted to fully-planar donors has been reported for BHJ OPDs.

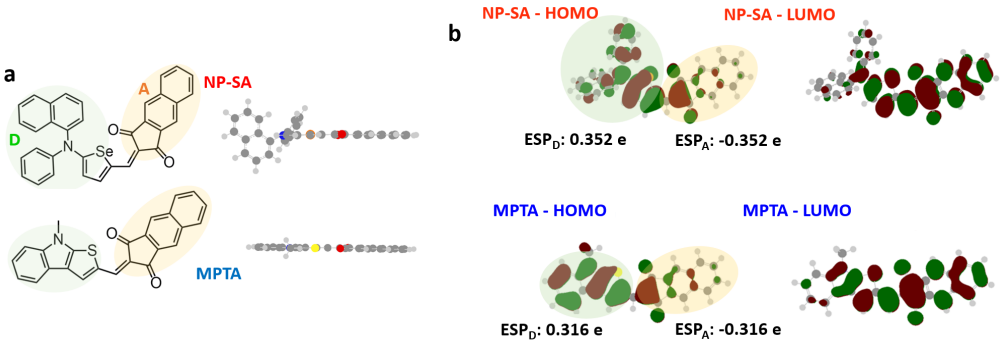


Fig. 5.1: Molecular structure of small molecule donors. (a) Chemical structures of NP-SA and MPTA donors, with their donor and acceptor units indicated. The spatial conformation of donor molecules is illustrated based on the DFT optimised geometries shown as side views. (b) HOMO/LUMO distribution for NP-SA and MPTA molecules in their DFT optimised geometry. Simulated electrostatic potentials for donor and acceptor units (ESP_D and ESP_A, calculated based on Merz-Kollman model) indicate a smaller charge separation in the donor/acceptor units for MPTA, according to the more effective charge delocalisation in a planar molecular structure.

5.2.2 Responsivity and J–V Characteristics

NP-SA:C_{60} and MPTA:C_{60}-based OPDs are green-light selective, extending their detection in the 460-620 nm (NP-SA:C_{60}) and 450–600 nm ranges (MPTA:C_{60}) (see responsivity in Figure 5.2a). Field-dependent responsivity is similar for both devices, as observed for other push-pull small molecules showing bias-dependent CT separation.[179] As illustrated in more detail in reference [20], photocurrent of both NP-SA- and MPTA-based devices grows sub-linearly with light intensity (Φ) for higher Φ, evidence of bimolecular recombination in the finely intermixed BHJs, with these loss mechanisms mitigated under reverse bias. Figure 5.2b shows the J–V characteristics in dark and under AM1.5 G illumination. Although photogenerated currents under 1 Sun are similar, the dark currents are particularly low for the MPTA-C_{60} devices ($\sim 10^{-8}$ A cm^{-2} for a wide reverse bias range from 0 to -5 V), comparable with state-of-the-art OPDs.[71] For MPTA:C_{60}, dark shunt increases under strong reverse bias, suggesting trap-induced mechanisms,[71] consistently with the results discussed below.

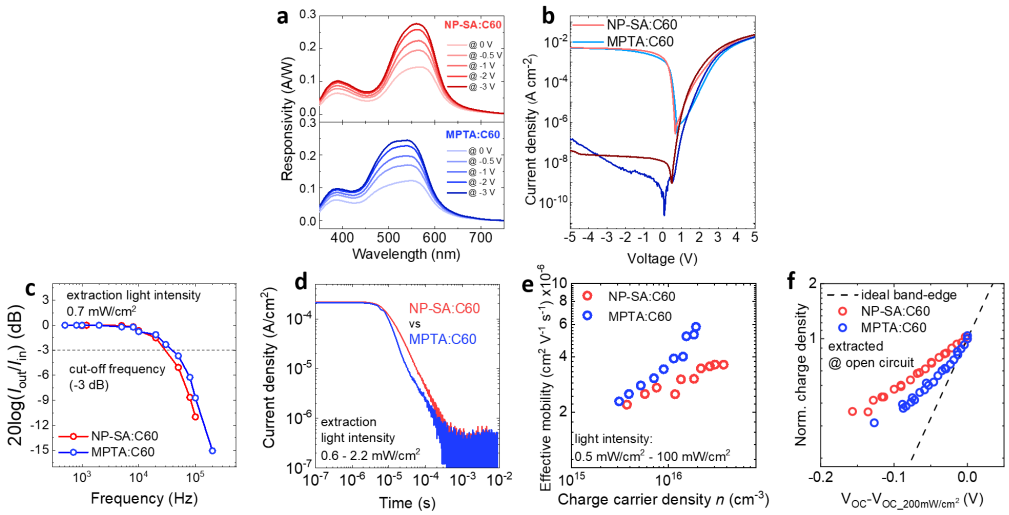


Fig. 5.2: OPD device characteristics at high-light intensity. (a) The responsivity at different bias conditions. (b) Dark and AM1.5 G light *J*-*V* curves in a semi-log plot, shown with darker and brighter colours respectively. (c) The bandwidth of frequency response measured at a light intensity of 0.7 mW/cm^2 at 0 V. (d) Light-off photocurrent transients in a light intensity range of 0.6 – 2.2 mW/cm^2 illumination at 0 V. The device was illuminated for 100 ms before switching off the light. Note that the level of background current is higher than device dark current due to sensitivity limitations of the detector circuit (50 Ω load resistance, 1 mV/div resolution of the oscilloscope). (e) Effective charge carrier mobilities as a function of charge carrier density analysed by CE at 0 V in a light intensity range of 0.5 – 100 mW/cm^2. (f) Normalised plots of the charge carrier density at open circuit versus V_{OC} determined from integration of CE transients as a function of light irradiation intensity (normalised at 200 mW/cm^2 light intensity).

5.2.3 High-Light Device Response Time Governed by Shallow Traps

Firstly, OPD performances of NP-SA- and MPTA-based devices are investigated at relatively high illumination intensities (>0.5 mW/cm^2) by transient optoelectronic analysis (frequency response analysis, transient photovoltage and charge extraction (CE)).[212,218,346] At 0.7 mW/cm^2, OPD frequency response (Figure 5.2c) shows -3 dB cut-off frequencies of 3 kHz and 4 kHz for NP-SA:C_{60} and MPTA:C_{60}, respectively (this light intensity is chosen to prevent bimolecular recombination losses which can reduce photocurrent at higher light intensities). Frequency-dependent OPD photoresponse depends on device circuit *RC* constant and charge transport time,[338,340] with the latter dominating for low mobility OSCs.[338] Photocurrent transient analysis under pulsed light illumination allows further understanding of the charge transport, this method being widely used for mobility characterisation in OPVs.[352] Figure 5.2d shows short-circuit photocurrent transients for NP-SA:C_{60} and

MPTA:C_{60} devices (0.7 mW/cm^2 light intensity, 100 ms pulsed light irradiation to reach steady-state preconditions). MPTA:C_{60} OPDs exhibit faster charge extraction for light intensities from 0.6 to 2.2 mW/cm^2, consistent with the wider frequency response bandwidth. In particular, a photocurrent decay time of the order of microseconds is in line with state-of-the-art OPD performances.[58,60,179] Photocurrent transient integration allows to extract the light-intensity-dependent short-circuit carrier density and, using a simple drift model, the effective active-layer drift charge mobility μ (see reference [353] for calculation details). In high light intensities (>0.5 mW/cm^2), where charge density is >10^{15} cm^{-3}, μ is higher for MPTA:C_{60} compared to NP-SA:C_{60} OPDs (Figure 5.2e). Since charge transport in OSCs proceeds by thermally-activated hopping *via* band tail states (often referred to as *shallow trap* states),[354] hopping site density and thermal activation barriers (*i.e.*, trap density and trap energy) significantly affect μ.[355,356] Analysis of shallow trap density can be carried out from open-circuit CE transients, measured as a function of light intensity.[352,357] Figure 5.2f shows the charge density trend with V_{OC} (corresponding with the quasi-Fermi level splitting in the photoactive layer). At lower light intensity, quasi-Fermi energy splitting decreases, with consistent drop in extracted charge density. However, this drop is clearly shallower than predictions for an ideal semiconductor (see dashed line), indicating the presence of tail states.[212,218] Here, the steeper trend for MPTA:C_{60} OPDs indicates smaller presence of shallow traps in this system, with a narrower energetic distribution, consistent with the faster high-light photoresponse of MPTA:C_{60} devices.[237]

5.2.4 Low-Light Device Response Time Governed by Deep Traps

Depending on OPD applications, operating light intensities can vary across a wide range. Therefore, it is paramount to characterise the frequency response and transient CE of MPTA:C_{60} and NP-SA:C_{60} OPDs at low-light intensities as well (*i.e.*, ≤0.5 mW/cm^2). Compared to high-light conditions (see Figure 5.2d), opposite trend in photoresponse speed is observed at 0.024 mW/cm^2, as illustrated in Figure 5.3. At this low-light intensity, the -3 dB frequency of NP-SA:C_{60} OPDs is ∼5 kHz, but it is now reduced to 2 kHz for MPTA:C_{60} (Figure 5.3a). Therefore, the superior high-light frequency response of MPTA:C_{60} device is compromised at low-light, where NP-SA:C_{60} shows better performance. For further OPD analysis, high sensitivity short-circuit photocurrent transients are shown in Figure 5.3b–d, for initial light intensities from 0.1 to 0.4 mW/cm^2. In low-light, initial decay kinetics are similar to high-light conditions (Figure 5.2d), being faster for MPTA:C_{60} devices. However, a

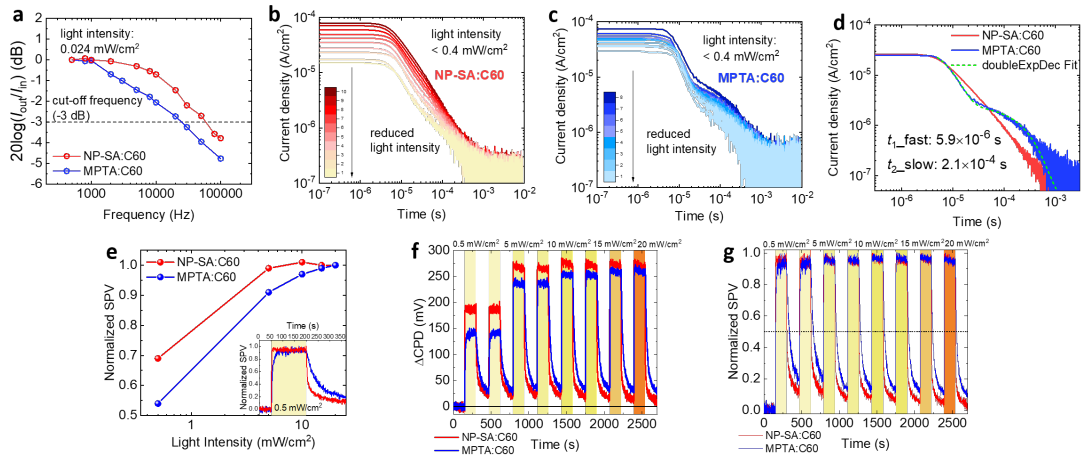


Fig. 5.3: Low-light illumination photocurrent transients. (a) Bandwidth of frequency response at a photocurrent density of 2.7 μA/cm^2, under a 0.024 mW/cm^2 light intensity at 0V. (b) NP-SA:C_{60} and (c) MPTA:C_{60} device photocurrent transient measured by CE at 0 V. (d) Comparison of current transients measured at 0.5 mW/cm^2. MPTA:C_{60} photocurrent transient is fitted with a double exponential (green dash line). (e) Light-intensity-dependent SPV magnitude for NP-SA and MPTA blends, normalised to the SPV at the maximum light intensity. The normalised SPV signal during one illumination cycle at the lowest light intensity is shown in the inset. Absolute (f) and normalised (g) SPV response for NP-SA and MPTA blends scanning through increasing white light intensities. The active layer is deposited on Ag substrate with hole extraction interlayer in between. The positive signal observed in light corresponds to electron accumulation on the surface upon photocharge generation and separation. This is understandable with the film being deposited on hole extraction interlayer and Ag.

slower ($\sim$100 μs) second decay phase appears for this system, which is not observed in NP-SA:C_{60}. Therefore, while state-of-the-art photoresponse times are maintained for NP-SA regardless of illumination conditions,[58,60,179] MPTA performance degrades under lower light intensities. In particular, this biphasic photocurrent transients observed in MPTA:C_{60} have not been previously reported in the OPD literature, and it attributed to the slow extraction of a low density of relatively deep trap states.[358] At this regard, slow charge generation can be ruled out as cause of the slow photocurrent transient, since the timescales of the two phenomena are significantly different (*i.e.*, charge generation occurs in the ps-ns range,[179] compared to the 100 μs of the slow charge transient component).

For detailed analysis, the decay of the MPTA:C_{60} photocurrent transients is fitted with a biexponential decay function (dashed line in Figure 5.3d), with fast and slow decay time constants of 5.9 μs and 210 μs, respectively. As charge extraction speed (v) depends only on μ under a constant drift force F ($v = \mu F$), the difference between slow and fast extraction times depends on a different μ. Assuming a system

with shallow and deep states at distinct energy levels, the difference in extraction times indicates that deep traps are approximately 0.1 eV below the shallow trap states (assuming single trap energies rather than distributions, see details in reference [20]). Charge integration from the slow CE decay gives the density of these deeply trapped species, corresponding to 1×10^{15} cm^{-3} at short circuit under 0.3 mW/cm^2 illumination.

Light-intensity-dependent SPV measurements[36] confirm the presence of deep charge trapping in MPTA:C_{60} OPDs compared to NP-SA:C_{60} (Figure 5.3e-g). In fact, for MPTA:C_{60} blends, the magnitude of SPV response significantly depends on light intensity, showing a strong reduction compared to NP-SA:C_{60} in low-light conditions (notably at 0.5 mW/cm^2), indicating trap-assisted recombination loss. Moreover, MPTA:C_{60} blends show a slower transient time to reach equilibrium in dark after low-light illumination (inset in Figure 5.3e), suggesting slowed-down charge extraction by deep trap states.[359,360] In summary, the slower frequency response of MPTA:C_{60} OPDs at low-light intensities results from the presence of relatively deep trap states, while these are not observed in NP-SA:C_{60}.

5.2.5 Molecular-Structure-Dependent Intermolecular Coupling

In order to identify a possible molecular origin for shallow and deep traps in NP-SA and MPTA systems, the effect of donor molecular structure (twisted *vs.* planar) on intermolecular coupling is investigated by optical and structural probes (Figure 5.4). Both neat donor molecules exhibit a well-defined absorption band in the visible range with a smaller (90 nm) FWHM peaking at 565 nm for NP-SA and a larger (150 nm) FWHM peaking at 495 nm for MPTA, respectively (Figure 5.4a). For MPTA, a clear absorption feature at the low energy shoulder is also observed. Surprisingly, both NP-SA and MPTA spectra get narrower upon blending with C_{60}, particularly in the high energy shoulder. This narrowing is more dominant in MPTA, reducing FWHM by 45 nm compared to 15 nm in NP-SA. More striking differences between the two donors appear in their PL spectra (Figure 5.4b). For neat films, the planar MPTA shows strongly red-shifted, intense PL emission compared to the twisted NP-SA, with PL increasing further upon thermal annealing (Figure 5.5a), indicating stronger intermolecular interactions of MPTA. This is associated with molecular aggregation, arising from the planar molecular structure.

Similar emission characteristics with strongly red-shifted and highly-emissive PL have also been observed in analogous organic planar small molecules, assigned

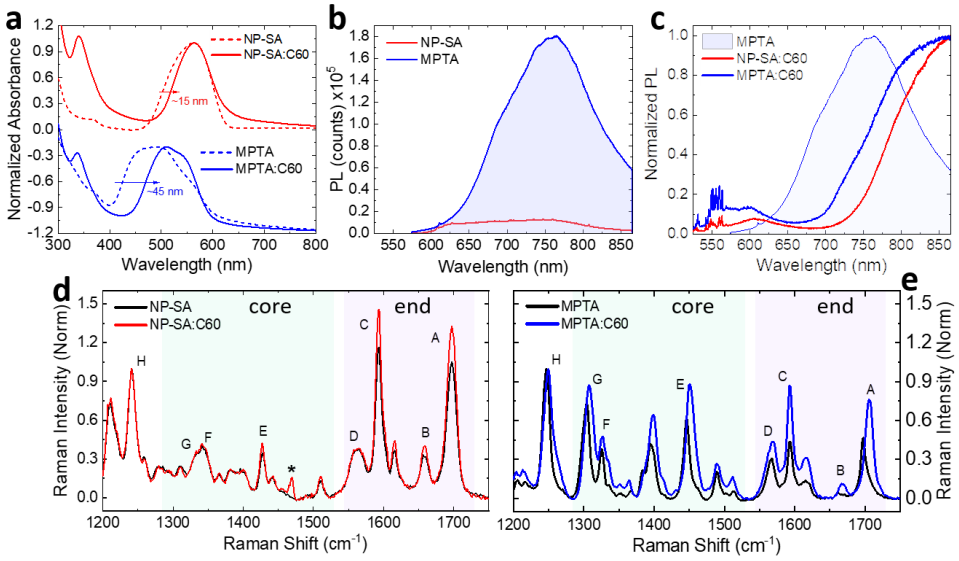


Fig. 5.4: Optical and molecular structural properties. (a) Normalised UV-Vis absorption spectra for NP-SA, MPTA and respective C_{60} blends. (b) Absolute PL for neat donor thin films. (c) Normalised PL for blends and neat MPTA. (d)-(e) Comparison between normalised Raman spectra (*via* 488 nm laser excitation) of neat and blended NP-SA and MPTA films. The peaks are labelled according to the detailed assignment shown in Appendix D and grouped according to core and end-group vibrational modes. The asterisk in (d) indicates the C_{60} vibrational mode appearing in blends.

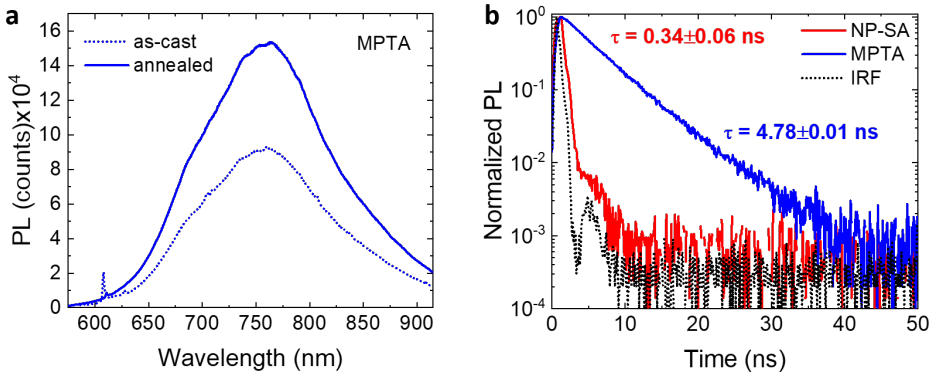


Fig. 5.5: (a) Absolute PL for pristine and annealed MPTA films. (b) TCSPC analysis of PL lifetime for NP-SA and MPTA, respectively monitored at 750 and 770 nm following 405 nm laser excitation. The lifetimes from single exponential fit are indicated in the graph. Instrument response function (IRF) is also included as a reference.

to excimers.[361] The lifetime of these emissive species is found to be in the order of 5 ns by TCSPC analysis (Figure 5.5b), consistent with reported examples of excimeric emission,[362,363] while NP-SA shows a much faster decay (<400 ps limited by the instrument response function). This aggregation in MPTA seems to occur at

the molecular level without any detectable microscopic features (see AFM maps in Figure 5.6).

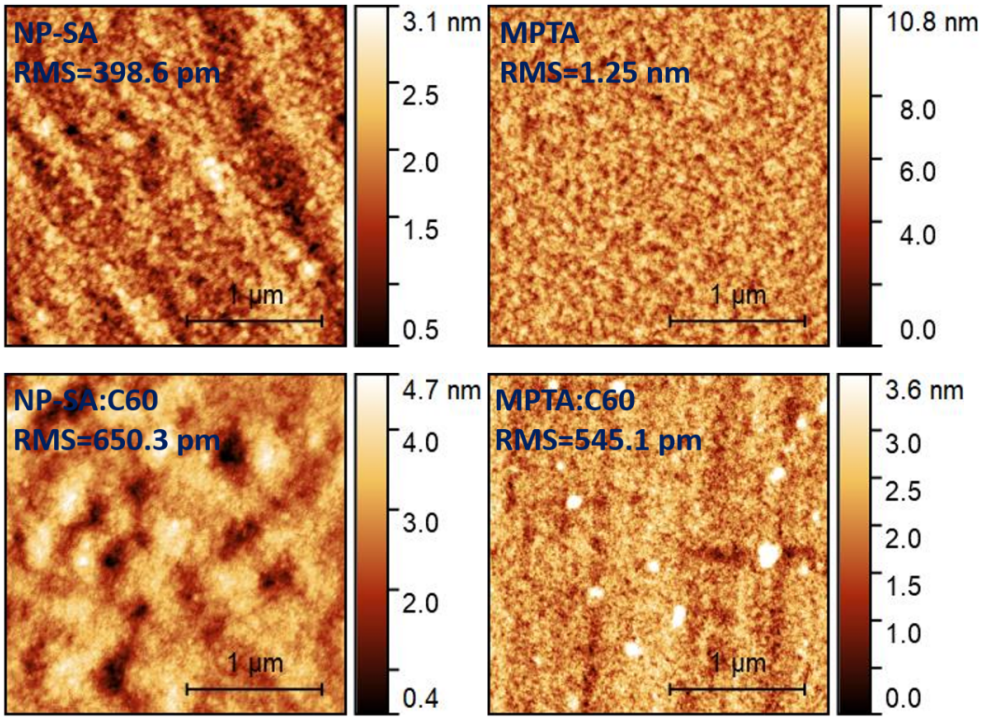


Fig. 5.6: AFM maps of neat donor films and respective blends with C_{60} on quartz substrates. Both donors show root mean square (RMS) roughness ≤1 nm in neat and blend films.

Upon blending with C_{60}, the red-shifted, highly-emissive PL of MPTA is strongly quenched, while a new broad CT state emission appears at lower energy (>800 nm) (Figure 5.4c). This originates from weakly bound electron-hole pairs formed upon photoexcitation at the MPTA/C_{60} interfaces, and it is readily quenched by reverse electric field generating free charges (see PL quenching analysis in Figure 5.7).

Similar red-shifted CT emission is also observed in NP-SA:C_{60} blends. In both MPTA:C_{60} and NP-SA:C_{60} devices, CT dominating PL spectrum is evidence of a highly intermixed morphology for photoactive blends.[179] However, MPTA:C_{60} also shows a higher energy shoulder (<750 nm) as in neat MPTA emission, indicating possible presence of residual MPTA excimeric species. For both blends, a new additional and much weaker PL peak is also observed at high energy (<650 nm), more intense for MPTA:C_{60}. This is attributed to the emission of donor molecules where their intermolecular interactions are largely disturbed by C_{60} acceptors. Based on these absorption and PL properties, it is clear that the planar donor MPTA undergoes more significant changes in the molecular-scale nanomorphology to accommodate C_{60} acceptor in the blend compared with NP-SA. These BHJ structural char-

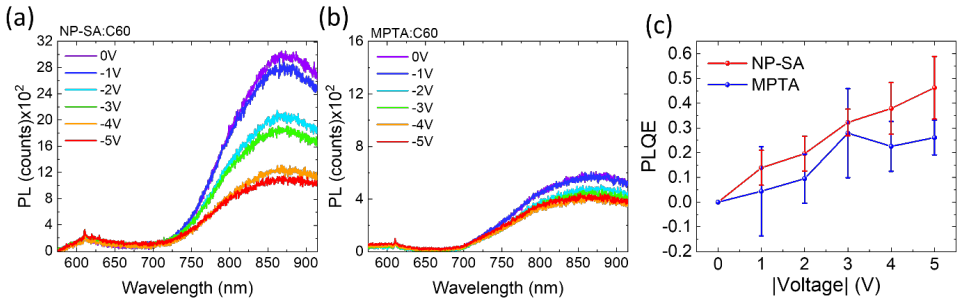


Fig. 5.7: PL quenching analysis in NP-SA:C_{60} and MPTA:C_{60} devices.(a)-(b) Bias-dependent evolution of absolute PL for NP-SA:C_{60} and MPTA:C_{60} devices, respectively. (c) PL quenching efficiency as a function of reverse bias, averaged from 3-4 points on the devices, with error bars indicated as standard deviation. PL quenching efficiency is calculated as PLQE = ($PL_{V=0}$- PL_V)/$PL_{V=0}$, with $PL_{V=0}$ and PL_V respectively being the PL at zero bias and at the applied reverse bias, at the wavelength of maximum emission.

acteristics can be explored in more details by molecular vibrational spectroscopy.

The Raman spectra of NP-SA and MPTA are shown in Figure 5.4d,e, respectively, comparing neat and blend films. The main peaks appear at low (1300-1500 cm^{-1}) and high (1550-1800 cm^{-1}) frequencies, mainly originating from the core unit (*i.e.*, central selenophene/thiophene and amine linkage) and the end-group (*i.e.*, acceptor unit, phenyl, and naphthalene) vibrations of molecules,[179] respectively (see Figure D.1 and Table D.1 in Appendix D for detailed assignment). In neat films, MPTA shows much stronger and sharper core peaks, indicating enhanced π-electron density in the fused donor unit compared to non-fused donor in NP-SA.[254,262,364] Blending with C_{60} leads to completely different changes in vibrational modes. For NP-SA, this affects only the high energy vibrations (peaks A and C) with increased relative intensities, consistent with a certain degree of selective molecular twisting in the end groups only.[179] On the other hand, C_{60} loading induces significant structural changes in MPTA, involving all vibrational modes, with increased relative intensities and large peak broadening towards high frequencies. This does not match the Raman spectra of twisted MPTA (Figure 5.8), indicating that molecular twisting is not the main cause of the Raman changes observed in the blend.

On the contrary, such significant changes reflect the more dramatic impact that C_{60} blending has on MPTA, disturbing its intermolecular interactions.[254,259,260,365,366] As planar MPTA exhibits strong intermolecular coupling in neat films, evident from its red-shifted and intense PL, effective mixing with C_{60} requires profound modifications of MPTA packing and relative molecular orientation, leading to significant changes in MPTA:C_{60} nanomorphology as probed herein by Raman spectroscopy. Strikingly, these changes occur at the molecular scale without any measurable mi-

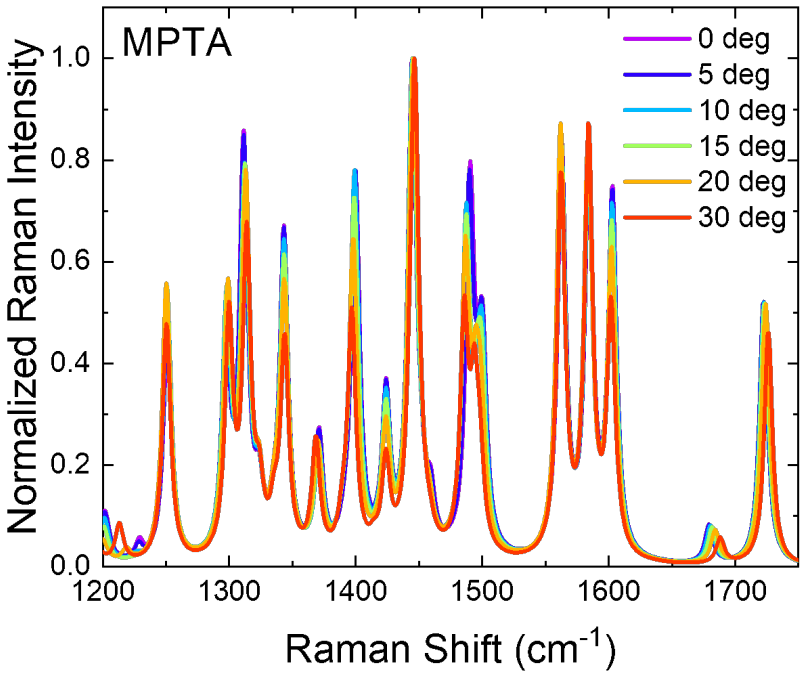


Fig. 5.8: DFT simulation of MPTA Raman spectra for different twisting angles between the donor and the acceptor unit.

croscopic reorganisation (Figure 5.6).

Besides the structural changes induced by blending, the addition of C_{60} can also result in the formation of MPTA-C_{60} adducts[367–369] (see chemical structure and calculated energy levels in Figure 5.9a,b). Chemical reactions are only possible for the planar MPTA, with no bulky side groups at the amine centre, so that the lone electron pair in the N atom can interact with C_{60} π-electrons. Figure 5.9c,d show the calculated Raman spectra of the MPTA-C_{60} adduct, which is compatible with the experimental data for the MPTA blend. In fact, both show similar changes in Raman intensity and peak width compared to neat MPTA. Namely, the relative quenching of peaks H and G can be attributed to the locking of the amine bond by fullerene addition, and the broadening of peak E towards high energies involves adduct contributions. In summary, it is found that the MPTA-C_{60} adduct formation is possible in MPTA:C_{60} blends due to the planar donor structure. When C_{60} is highly intermixed with MPTA in BHJ, the strong intermolecular interactions of MPTA molecules are disturbed, allowing new MPTA-C_{60} interaction to form adducts through lone pair–π interactions.[368,369] Both morphology changes and adduct formation upon C_{60} loading significantly affect the MPTA vibrational modes, consistently with what observed from Raman measurements.

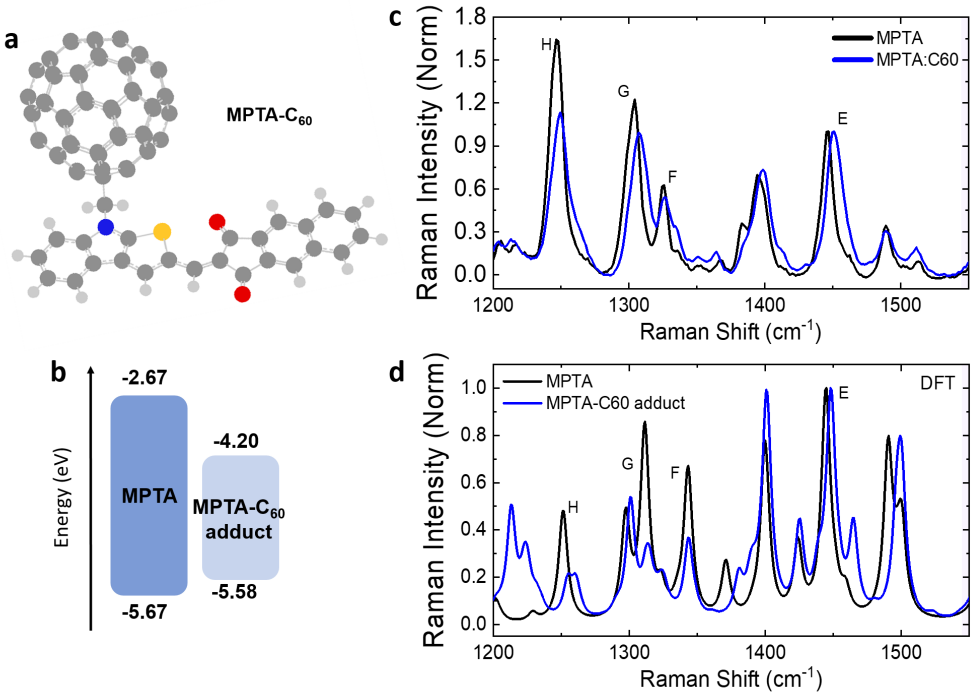


Fig. 5.9: MPTA-C_{60} adduct. (a) Chemical structure of MPTA-C_{60} adduct, in DFT optimised structure. (b) Calculated energy levels for MPTA and MPTA-C_{60} adduct. (c) Measured Raman spectra of neat and blended MPTA, normalised to peak E from the core thiophene. (d) DFT simulated Raman spectra for MPTA and MPTA-C_{60} adduct.

5.2.6 Molecular Origins of Shallow and Deep Traps

Finally, it is crucial to investigate the effect of donor molecular structure (twisted NP-SA *vs.* planar MPTA) on the formation of shallow and deep trap states in BHJ blends, combining DFT simulation and energetics measurements (Figure 5.10).

We first analyse the conformation of the two donor molecules. Figure 5.10a shows the molecular potential energy as a function of structural twisting using DFT simulations, in which the potential energy is calculated at different dihedral angles between the D-A building blocks (*i.e.*, between selenophene/thiophene and alkene bond in the A unit for NP-SA/MPTA). Both donor molecules exhibit a planar D-A geometry (0 dihedral angle) at the lowest potential energy, with the chalcogen and oxygen atoms at the same side of the structure, lowering the potential energy through their noncovalent bond. Notice that the optimised NP-SA geometry has a 3D coordination in the amine donor unit, but a planar conformation between the selenophene core and the acceptor unit (Figure 5.1a). For NP-SA, a large potential energy difference (∼200 meV) is calculated for its isomer, where the dihedral

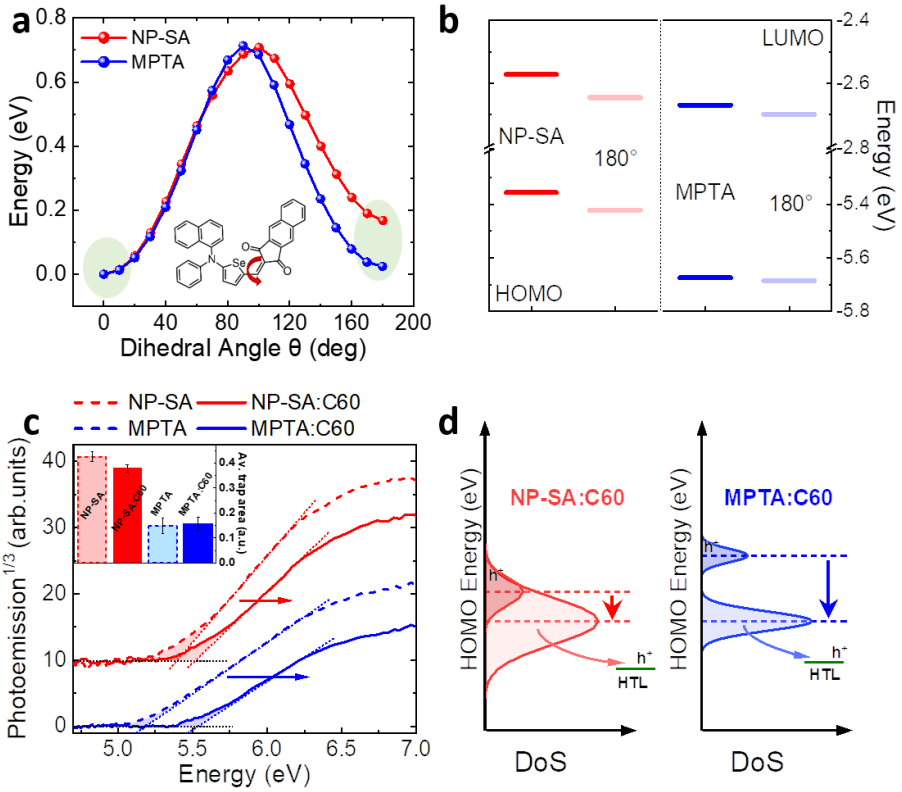


Fig. 5.10: Energetic analysis of NP-SA:C_{60} and MPTA:C_{60} blends. (a) The potential energy scan as a function of alkene bond dihedral angle between donor and acceptor units (*e.g.*, as indicated for NP-SA in the inset), with highlighted the lower energy configuration at 0 and 180° dihedral angles for NP-SA and MPTA. (b) HOMO and LUMO energy levels for optimised geometries of NP-SA and MPTA and their isomeric forms, respectively with 0 and 180° D-A dihedral angle, calculated by DFT. (c) Photoemission spectra of neat and blended donors measured by APS, with the linear fits to the emission edge for HOMO extraction (dotted lines). The inset shows the density of tail states from the integrated area below the HOMO onset, indicative of shallow trap density (error bars as standard deviation across multiple measurements). (d) Distribution of deep and shallow trap states. MPTA:C_{60} has a narrower shallow trap distribution and the presence of a deeper trap DOS. The trap states are filled by photogenerated holes from low to high energy states with light intensity increase. In low light, hole extraction from MPTA:C_{60} deep states is harder than the extraction from shallow states, due to the higher energy barrier, leading to deep hole trapping.

angle between the D-A building blocks is 180°. In contrast, the two isomers (0 and 180° dihedral angles) have a very similar potential energy in MPTA, attributed to the weaker S-O interaction compared to stronger Se-O interaction in NP-SA. The HOMO and LUMO energy levels calculated for the two MPTA isomers are also very similar (Figure 5.10b), while they are largely different (∼100 meV) for NP-SA. This holds even considering the possible non-equilibrium configurations (20° around the local minima), which can represent the highly intermixed blend morphology.

The HOMO level dispersion is ∼70 meV for NP-SA, but only ∼30 meV for planar MPTA (Figure 5.11). This indicates an important intrinsic structural advantage of the planar MPTA molecule. Even with the possible formation of isomers in films, no additional energetic disorder is introduced by this planar molecule, leading to narrow tail-state distribution (*i.e.*, low density of shallow traps), consistent with the fast charge transport and OPD photoresponse at high-light levels.

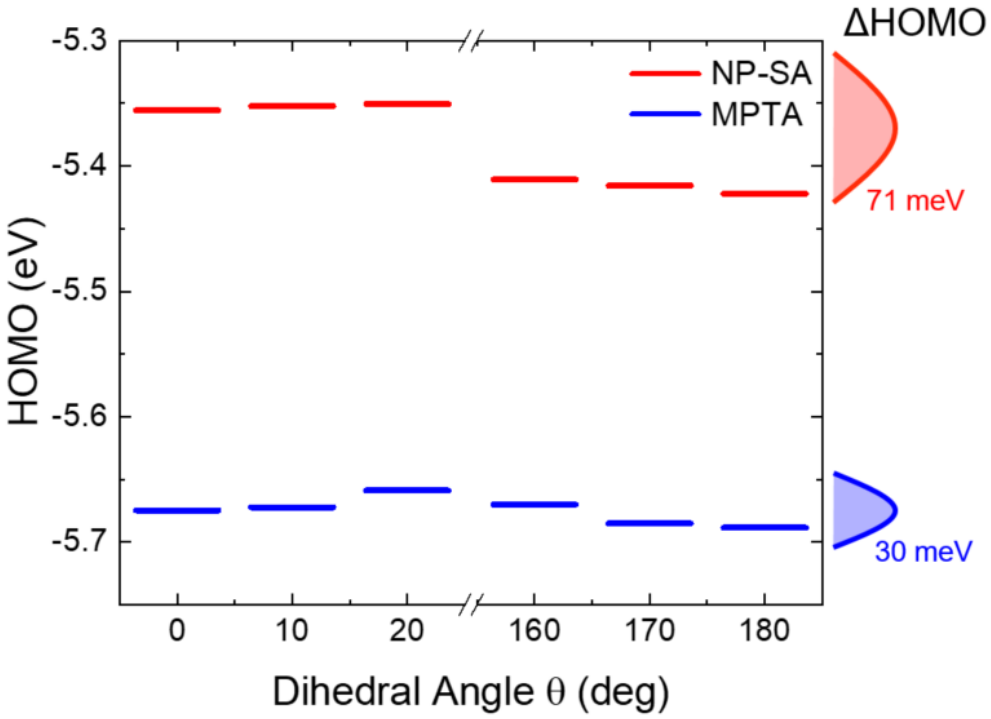


Fig. 5.11: DFT simulated HOMO levels for NP-SA and MPTA for the near-equilibrium configurations 20° around the possible isomeric forms. The HOMO dispersion is indicated on the right.

At this regard, it is important to point out that selenation plays a role in the stabilisation of the molecular potential energy minimum, therefore on the propensity for the formation of isomers. However, the changes in DOS distribution upon isomer creation are mainly dictated by the specific molecular structure of different donors (*i.e.*, planar *vs.* twisted). In fact, as visible in Figure 5.12, the selenated equivalent of MPTA has a stronger potential difference between optimised and 180° conformations similarly to NP-SA, but the difference in HOMO and LUMO levels between isomers remains low (∼30 meV).

In order to gain further insight into the molecular origin of trap states, we measure the energetics of neat and blend films by APS.[212] The extracted HOMO of neat MPTA is much shallower than that of NP-SA (5.16 eV *vs.* 5.37 eV) (Fig-

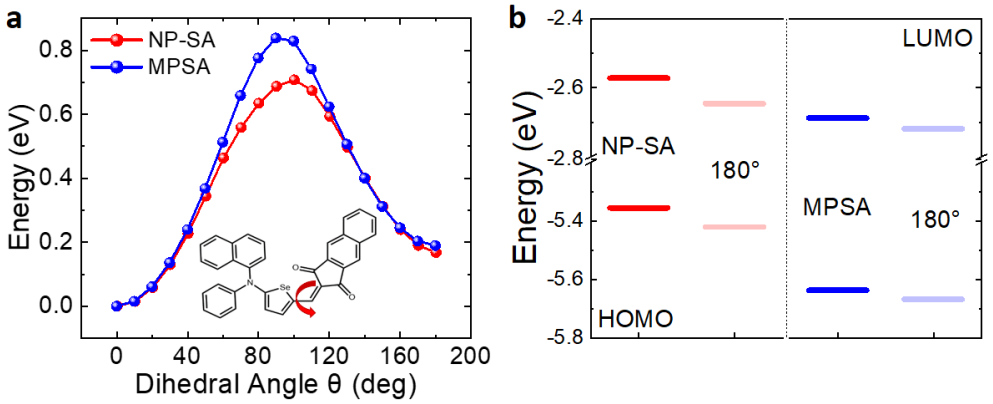


Fig. 5.12: DFT calculations for NP-SA compared with the selenium substituted version of MPTA. (a) Potential energy scan as a function of alkene bond dihedral angle between donor and acceptor units (as indicated in the inset) for NP-SA and the selenated analogous of MPTA (referred to as MPSA). (b) HOMO and LUMO energy levels for optimised geometries of NP-SA and MPSA and their isomers, respectively with 0 and 180° dihedrals between donor and acceptor units.

ure 5.10c). This supports the strong intermolecular coupling of the planar MPTA in solid state, leading to a ∼0.50 eV shallower HOMO compared to single-molecule gas-phase DFT simulations, while measured HOMO is consistent with the calculated value for NP-SA. Upon blending with C_{60}, a clear HOMO level deepening is visible for both donors, with a much larger shift for MPTA (370 meV *vs.* 100 meV for NP-SA). This is accompanied by a more prominent narrowing of the DOS in MPTA blend (Figure 5.13). Analysis of sub-gap features from the APS spectra[212] (see the inset in Figure 5.10c) clearly reveals a low density of tail states intrinsic to the planar MPTA, which is preserved even after blending. Consistent with the narrow tail-state distribution extracted by CE transients (Figure 5.2f), this low density of tail states near the band edge (*i.e.*, shallow trap states) is attributed to the smaller energetic disorder in the highly planar MPTA, where potential isomer formation does not introduce additional energetic broadening. This low shallow-trap density and stronger intermolecular coupling lead to the superior charge transport and fast photoresponse time in MPTA:C_{60} OPDs when operating at higher light intensity (Figure 5.2d).

Moreover, the highly planar MPTA exhibits strong intermolecular coupling in neat film forming a low-bandgap, highly-emissive electronic state (see excimeric emission in Figure 5.4b). However, significant disturbance is induced by C_{60} in BHJ, breaking strong intermolecular interactions between MPTA molecules and introducing a new larger-bandgap MPTA electronic state with significantly deeper HOMO level. As such, any residual low-bandgap electronic state from MPTA nanoaggre-

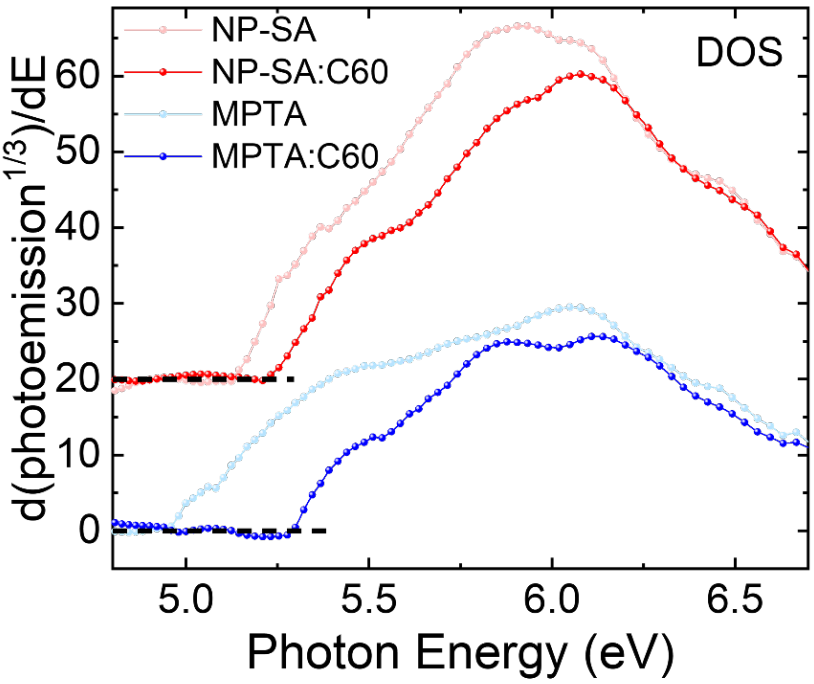


Fig. 5.13: DOS from photoemission spectra of neat and blended NP-SA and MPTA, with respective baselines indicated as black dashed lines. The spectra have been separated for clearer display by vertical shift of NP-SA pair.

gation will act as intraband deep trap state in the blend. Besides this, also the formation of a small density of MPTA-C_{60} adducts[367–369] would result in additional electronic states. According to calculated energetics of MPTA-C_{60} (Figure 5.9b), the adduct exhibits a ∼90 meV shallower HOMO level compared to MPTA, which can also act as a deep trap state in MPTA:C_{60} devices. This provides a molecular origin for the slower photoresponse of MPTA:C_{60} devices at low light intensities, with deep states resulting in slow photocurrent decay and strong light-intensity dependence of SPV response (Figure 5.3).

5.3 Conclusion

In this chapter, molecular structure-dependent charge trapping and its impact on OPD light intensity-dependent photoresponse speed are investigated. Due to the promising perspective for OPDs in low-light-operating devices, this analysis is crucial for further materials development for targeted OPD applications. In particular, the control of the density of shallow trap states achieved in MPTA by its highly planar molecular conformation is a key factor for the fast charge transport and

OPD photoresponse under standard illumination conditions (high-light intensity) observed in MPTA:C_{60} devices. However, this highly planar structure also leads to strong intermolecular coupling in MPTA forming a low-bandgap state. Upon blending with C_{60}, the coupling is largely disrupted, resulting in a significant HOMO deepening for most MPTA molecules (see schematic in Figure 5.10d). In these conditions, residual low-bandgap states by MPTA nanoaggregation and the additional formation of MPTA-C_{60} adducts are the primary origin of deep trapping, leading to biphasic photocurrent transients and limited photoresponse bandwidth in low-light conditions. On the contrary, deep trap states are not formed in NP-SA:C_{60} devices, as C_{60} blending has minor impact on NP-SA morphology and energetics due to the twisted and more amorphous donor nature. Moreover, the stronger steric hindrance by the bulky phenyl and naphthalene groups in NP-SA prevents amine reaction and creation of C_{60}-adducts. This more amorphous morphology, with weaker intermolecular interactions, results in a slower photoresponse time under standard (high-light) operation conditions, making the highly planar MPTA a preferential candidate for high efficiency OPDs. However low-light performance of MPTA:C_{60} OPDs is degraded by deep charge trapping, so that NP-SA is a more suitable choice for low-light OPDs applications. Overall, these results provide a full analysis of trap distribution in state-of-the-art OPD systems and reveal important insights into the relation between donor molecular structure and OPD performance under different operating conditions. From here, it clearly emerges that selection of appropriate candidate materials for high-efficiency OPDs strongly depends on the targeted application, and consideration of device operating conditions is therefore paramount.

5.4 Experimental Section

Fabrication of Devices and Thin Films

All materials are purified *via* sublimation under high vacuum ($<10^{-6}$ Torr) prior to use. Thin films are fabricated by thermal evaporation under high vacuum ($<10^{-7}$ Torr, 0.35 Å/s rate) on dried glass or quartz substrates cleaned with isopropyl alcohol and acetone in an ultrasonic bath. OPDs are fabricated on ITO-coated glass by sequential deposition of hole-extraction layer (5 nm), donor:C_{60} BHJ (100 nm, 1:1 weight ratio), electron extraction layer (Ytterbium, 2 nm), and ITO electrode (10 nm), as in the structure shown in Figure 5.14. All organic films are thermally evaporated in high vacuum ($<10^{-7}$ Torr), and ITO electrodes by magnetron sputter before device encapsulation with glass (98.5% transmittance). Active pixel area is 0.04 cm^2. After deposition, films are thermally annealed at 160°C on a hot plate for

>3 h, followed by natural cooling to room temperature. Electrical characterisation of devices by *J-V* scan and EQE analysis is carried out as described in Section 3.8.

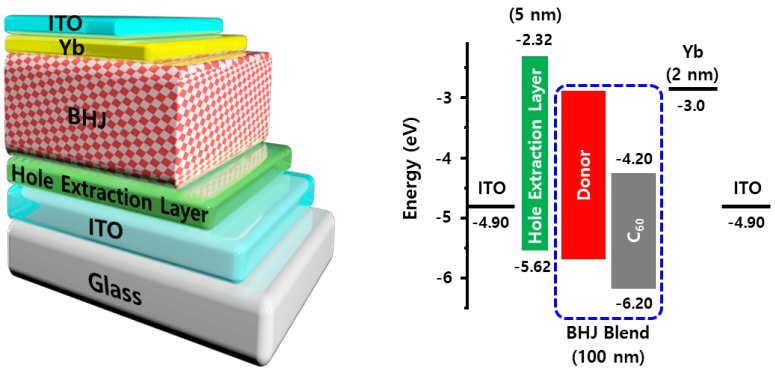


Fig. 5.14: Device structure and energetic diagram of donor:C_{60} OPDs.

Transient Optoelectronic Measurements

All the details on the set-up used for transient optoelectronic characterisation are described in Section 3.9, and all measurements are performed on fully encapsulated devices. TCSPC measurements are carried out as described in Section 3.5, exciting the samples by 405 nm laser.

Steady-State Optical and Structural Characterisation.

PL and Raman spectra are measured by a Renishaw inVia Raman microscope as described in Section 3.2, by 514 nm laser excitation for PL and 488 nm for Raman (Argon, Titanium Sapphire lasers, 25% defocused on sample surface). Diffraction grids of 2400 lines/mm and 300 lines/mm are used for Raman and PL, respectively. PL spectra are corrected to account for sample absorption at excitation wavelength. PL is also measured on encapsulated devices applying reverse bias to the electrodes by an Agilent power source. Thin film absorption is measured as described in Section 3.4.

Energetic and Morphological Characterisation

HOMO energy levels of materials on ITO substrates are measured as described in Section 3.3 *via* APS04 system, by the crossing of the linear fit to the photoemis-

sion cube root with the zero baseline.[265] Repeated measurements over the sample surface allow for reproducibility check and experimental error calculation. DOS is extracted as first derivative from photoemission cube root spectra by in-house software analysis. APS04 tip is also used as Kelvin probe to measure the changes in surface potential over cycles of dark and illuminated conditions (tunable white bulb light source, with intensity up to 0.2 Sun). Surface morphology was measured by a Park NX10 AFM in tapping mode as described in Section 3.6.

Computational methods

Gaussian09 software on the Imperial College High Performance Computing service is used to simulate molecular conformations and energy levels, Raman spectra, and dihedral scans, according to the protocol detailed in Section 3.7. DFT is applied at the B3LYP level with 6-311G(d,p) basis set.

6 | Nonfullerene Acceptor Dilution as a Facile Strategy for Device Optimisation towards High-Efficiency Solution-Processed Bulk Heterojunction Organic Photodetectors

While the importance of molecular design to tune spectral response and increase device performance in OPDs is a widely discussed subject in the field, the role of D:A blending ratio and BHJ structure in solution-processed devices has received comparatively little attention. In this chapter, PM6:Y6-based OPDs are prepared with either balanced or donor-rich (*i.e.*, diluted Y6) formulations, and their photodetection performance is explored. Notably, large J_d suppression is found for diluted blends, with strongly bias-dependent responsivity under reverse field, leading to a D^*~5×10^{12} Jones at -4 V. This is accompanied by faster photodetection, for overall superior performances of diluted OPDs. By detailed photophysical and energetic analysis, it is found that dissociation of strongly-bound interfacial CT states in donor-rich BHJs requires electric-field assistance, but the dominant polymer matrix provides efficient transport pathways once e-h pairs are separated. At the same time, the larger D/A energetic offsets and shallow PM6 energetics drive efficient hole transfer and suppress dark injection, while large bandgaps of majority PM6 and strongly-bound CT character mitigate thermal J_d contribution. Overall, the use of large polymer content is proposed as a strategy for facile OPD optimisation, which is highly promising also from the point of view of thermal stability and scalable fabrication.

6.1 Introduction

As illustrated in previous chapters, OSCs are showing great performance advancement in organic optoelectronic applications, with especially promising demonstrations of high-efficiency OPDs to rival Si-based counterparts in NIR photodetection - largely due to the emergence of NFAs. However, in order to further boost organic device performance, both materials design and photoactive layer engineering need to be carefully considered. In particular, exciton dissociation *via* intermediate CT states should be optimised.[370,371] As seen in details in Chapter 2, this process occurs at the D/A interface in BHJs, driven by the D-A HOMO offset[159] and by the external electric field applied in OPD operations.[60]

In terms of materials design, the emergence of fused benzothiadiazole-core-based[138,295] Y6 have enabled record-breaking performances in OPVs, owing to the unique photophysics of this NFA (A-DA′D-A calamitic structure, high quadrupole moment, strong π-π stacking), as discussed in Appendix B. This leads to efficient CT generation, barrierless charge dissociation, and low voltage losses.[140,157–159,212] However, Y6 application in OPDs is more limited, due to formation of relatively large BHJ domains with small D/A interfacial area,[160] whereas photocurrent generation in OPDs under reverse bias can benefit from a more intermixed morphology. In addition, the small bandgap and broad absorption spectrum of Y6 might not be preferred, particularly for narrowband photodetection.[372,373] Therefore, it is paramount to address the sub-optimal OPD performances of Y6 systems,[374,375] to make them suitable for wavelength-specific photodetection with high efficiency.

In particular, for effective use of high-performance OPV systems as OPDs, J_d should be maintained as low as possible, taking into account both contributions from dark injection from the contacts and thermal generation of electron-hole pairs followed by drift under reverse field.[60] Detailed understanding of J_d origin and strategies to minimise it are still the subject of ongoing research, as discussed in Subsection 2.2.2. For example, it has been shown[71] that J_d scales with device V_{OC} as the diode dark saturation current J_0

$$J_0 \sim J_{SC} e^{-\frac{eV_{OC}}{k_B T}}, \tag{6.1}$$

valid for $V_{\mathrm{OC}} \gg \frac{k_B T}{e}$, where T is the temperature of the system. Therefore, low J_d requires high V_{OC}, which can be manipulated by HOMO/LUMO tuning towards high E_{CT} and by D/A interface engineering.[71,174,376] However, more factors are involved in J_d origin, such as energetic disorder at semiconductor band edge, trap-assisted

charge generation,[71] and incomplete contacts at the electrodes.[60] At this regard, the PM6:Y6 system shows favourable characteristics, such as narrow tail-state distribution and extremely low trap density.[212] Moreover, efficient OPDs require fast photoresponse times, related to continuous percolation pathways in BHJ and good transport in D and A species.[46,60,373] Here, polymeric materials are highly promising, since they demonstrate high carrier mobilities (>1 $cm^2V^{-1}s^{-1}$ for adequate crystalline packing) and strong morphological connectivity.[377,378]

OPD performances can also be optimised by engineering of the photoactive layer, with an important parameter being the D/A blend ratio. While balanced D/A proportions are preferred in OPVs for ideal domain size,[139,284] blend ratio tuning can induce interesting effects on the BHJ photophysics.[379] For example, an increase in V_{OC} for PM6:Y6 OPVs with higher PM6 content has been ascribed to higher E_{CT}, although precise origin has not been identified.[380] However, higher Y6 content yields satisfactory PCE with a great tolerance, due to preservation of polymer transport properties even in low concentration.[381–384] In fullerene-based systems, blend ratio dependence of V_{OC} and E_{CT} seems related to D and A packing, with higher polymer crystallinity[385] or higher content of aggregated fullerene[386] leading to lower E_{CT} and V_{OC}. The role of energetics should also be considered, with V_{OC} increase at high fullerene content due to higher BHJ effective gap[387] and possible work function change in the charge transport layers.[388] Other reports suggest that reduction of D/A interfacial area *via* blend ratio engineering suppresses electron-hole encounter and recombination losses, increasing V_{OC} independently from E_{CT}.[376] In this case, materials with long exciton diffusion lengths are required to achieve efficient charge separation with small D/A interface area.[216] Therefore, increasing V_{OC} by energy level tuning or voltage loss suppression is crucial to achieve low J_d through reduced J_0. However, limited research has been devoted to the role of blend ratio control on OPD performances,[389] and detailed studies on solution-processed polymer:NFA systems are highly needed.

In this chapter, efficient OPDs are demonstrated using highly diluted Y6 acceptors in a PM6 polymer matrix (*i.e.*, "diluted" BHJ with a 1:0.1 D/A weight ratio, compared to a "balanced" 1:1.2 blend). By increasing the donor ratio in the blend, J_d is effectively suppressed up to 10^{-9} A cm^{-2}, while responsivity under reverse bias is maintained to adequate levels, so that an excellent specific detectivity of 5×10^{12} Jones is achieved. Together with a narrower, wavelength-specific spectral response and a faster photodetection (*i.e.*, <4.5 µs fall times), polymer donor-rich devices show record figures of merit among the state-of-the-art solution-processed BHJ OPDs. By detailed optoelectronic characterisation using electric-field-dependent

techniques and transient spectroscopy, the origin of superior OPD performance in diluted blends is identified. In particular, this is attributed to effective dissociation of bound CT states under reverse electric field, while the continuous percolation network in the polymer matrix ensures fast charge transport and hence fast photoresponse. At the same time, energetic analysis supports reduced J_d mainly due to the shallower PM6 energy levels in donor-rich BHJs. This is beneficial to prevent dark charge injection, while the high portion of large-bandgap polymer donor and strongly-bound character of interfacial CT states suppress the thermal J_d contribution. Overall, these results show that polymer-rich BHJ devices are very promising as high performance OPDs, and should be taken into consideration for industrially-relevant applications due to facile processability,[390–392] with added potential benefits of great thermal stability[37,38,164,253,393] and appealing mechanical properties.[394,395]

6.2 Results and Discussion

6.2.1 Impact of Acceptor Dilution on Optoelectronic Properties

Firstly, the optical properties of PM6:Y6 BHJs with various D/A ratios are compared, including progressive dilution of acceptor content (see molecular structure of PM6 and Y6 in Figure 6.1a). Absorption PL spectra of neat and BHJ films are shown in Figure 6.1b and c, respectively. Full series of data without normalisation are shown in Figure 6.2. As apparent from the UV-Vis spectra, increasing PM6 content shifts the Y6 absorption to higher energies (from 830 nm of neat Y6 to 780 nm for 1:0.1 dilution). This indicates changes in Y6 crystallinity, with disruption of systematic packing order as the polymer donor content increases. At the same time, the 0-1 absorption peak of PM6 around 575 nm is enhanced for higher PM6 content, which is related to the increase in H-aggregation between the polymer chains.[308,315,396] In the PL spectra, Y6 dilution in PM6 results in an even stronger blue shift, with over 75 nm difference from neat acceptor to diluted BHJ films (*i.e.*, 1:0.1 weight ratio). In addition, PM6 emission in the 650-800 nm region is almost completely quenched by blending of small Y6 content (*e.g.*, up to 10%), with the majority of PL arising from the acceptor excitons[397] at low energies (*i.e.*, >800 nm). This indicates efficient energy transfer from PM6 to Y6 upon exciton formation,[159] which requires subsequent hole transfer to PM6 as main charge generation pathway.

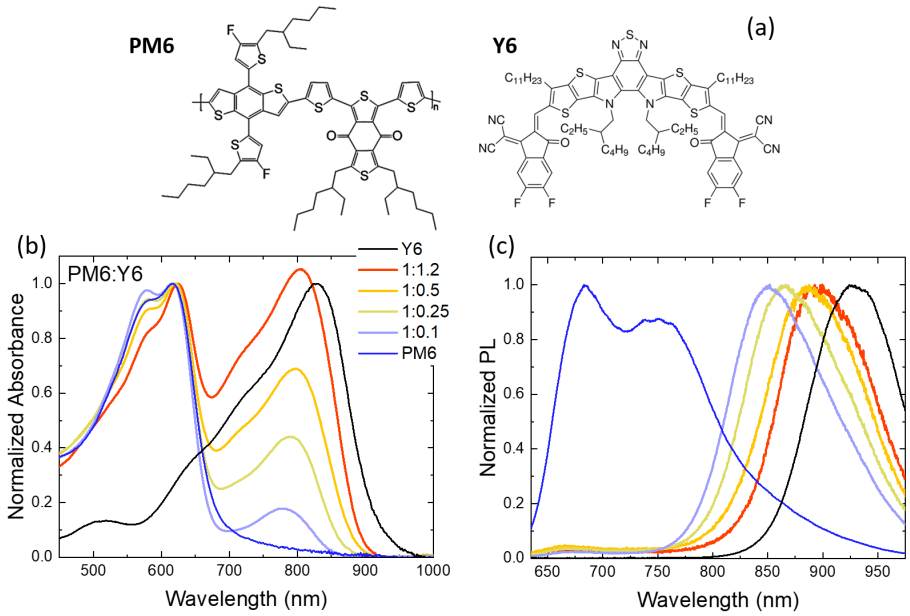


Fig. 6.1: Optical properties of PM6:Y6 blends with different D/A blend ratios. (a) Molecular structures of PM6 and Y6. (b) UV-Vis absorbance, normalised to the PM6 0-0 peak. (c) Photoluminescence spectra, normalised to the main emission of PM6 or Y6.

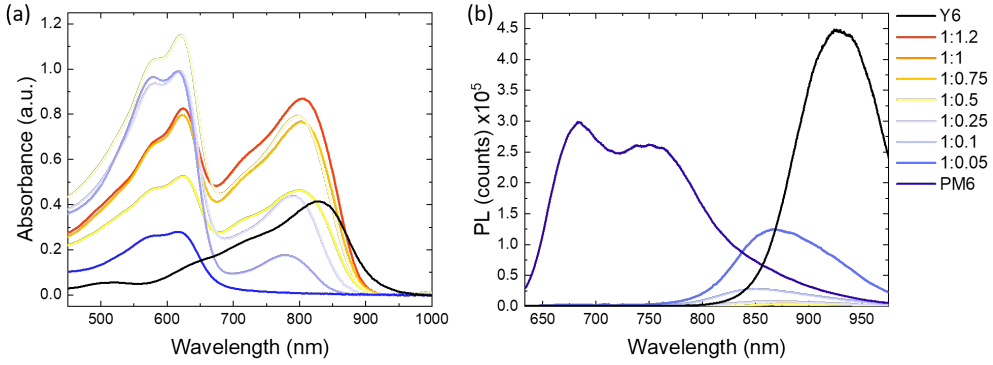


Fig. 6.2: Absolute absorbance (a) and PL (b) spectra of PM6:Y6 blends with different D/A blend ratios.

6.2.2 Impact of Acceptor Dilution on Photodetector Performance

PM6:Y6 OPDs with various blend ratios are characterised in device with inverted architecture ITO/ZnO/BHJ/MoO_3/Ag, and results are shown in Figure 6.3. *J-V* characteristics (Figure 6.3a) reveal a strongly suppressed J_d in reverse bias for higher polymer content. At -4 V, J_d reaches 6.5×10^{-9} A cm^{-2} for diluted devices, compared to the 8×10^{-6} A cm^{-2} for the balanced case. Neat PM6 also shows excellent J_d levels of 8.4×10^{-9} A cm^{-2} at -4 V. This represents a first benefit for

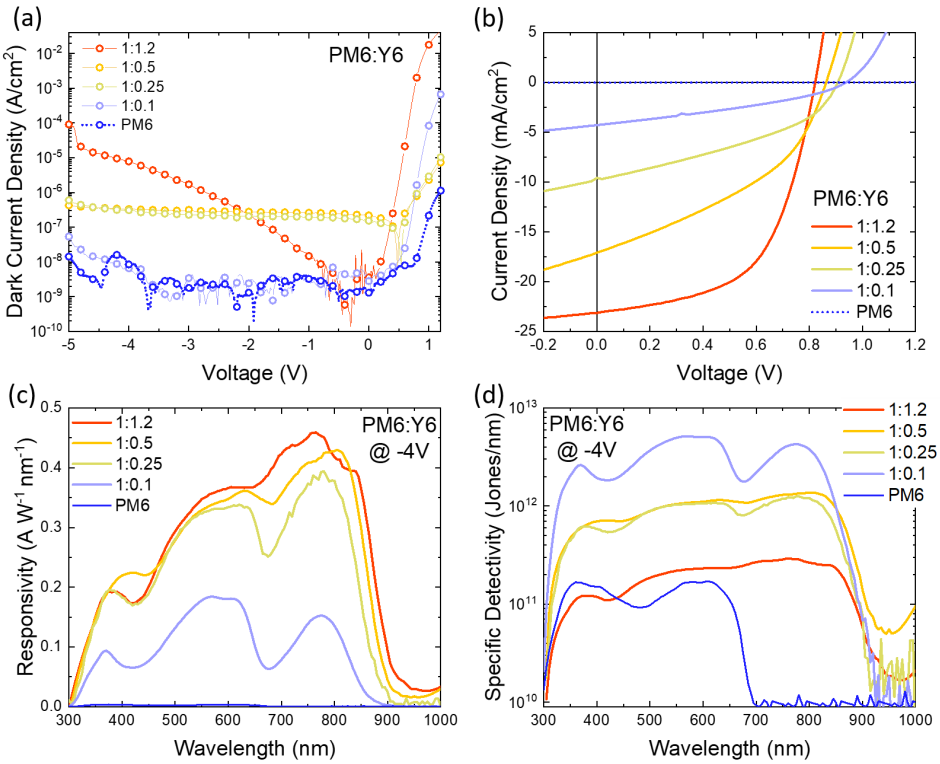


Fig. 6.3: Device characterisation for PM6:Y6 active layer with increasing donor content. *J-V* curves in (a) dark and (b) illuminated (AM1.5 G) conditions, (c) responsivity at -4 V and (d) specific detectivity at -4 V.

diluted Y6 devices in terms of OPD applications, whereas for OPV operations optimal performance is seen in balanced blends (see 1 Sun *J-V* curves in Figure 6.3b and summary of PV parameters in Figure 6.4). In fact, photocurrent generation under 1 Sun illumination is more efficient at high D/A interfacial area and well-intermixed morphology achieved in 1:1.2 optimised blends,[381,384] resulting in higher J_{SC}, FF, and overall PCE. However, a strong and continuous increase in V_{OC} is observed upon Y6 dilution, from 0.82 V in the balanced device to 1.03 V for the 1:0.05, approaching the intrinsic V_{OC} for neat PM6 (1.12 V), which is likely related to reduced interfacial voltage losses for less intermixed systems. This is consistent with the suppressed J_d values for increasing PM6 content, according to Equation 6.1. In terms of responsivity (R, see Figure 6.3c), reverse bias allows to achieve high values even for diluted blends, with a maximum of *circa* 0.2 A W^{-1} nm^{-1}.

In the assumption of J_d being dominated by the shot noise contribution (see Subsection 2.2.2), specific detectivity can be calculated as $D^* = R/\sqrt{2eJ_d}$. Here, thanks to the successfully suppressed J_d in diluted BHJ devices, exceptional values of over $5{\times}10^{12}$ Jones (-4 V) are achieved in 1:0.1 blends despite a lower R, more than 15 times higher than the 1:1.2 blend case (Figure 6.3d). These data indicate

a significant advantage of the diluted Y6 systems for operation as OPDs, achieving state-of-the-art performances thanks to J_d suppression and enhanced D^*.

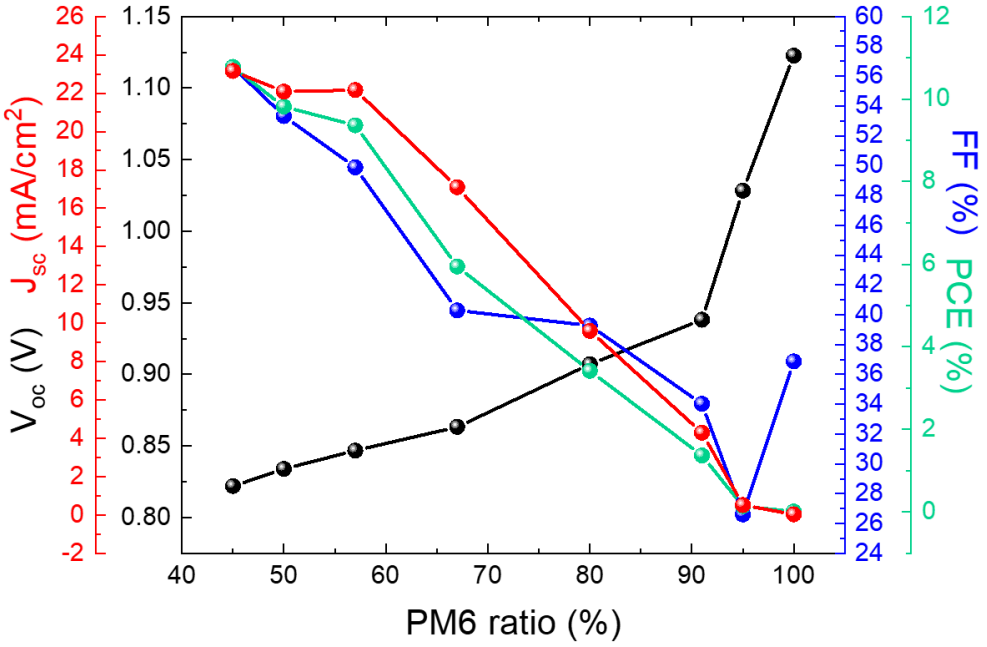


Fig. 6.4: Photovoltaic parameters for PM6:Y6 devices with different BHJ blend ratios.

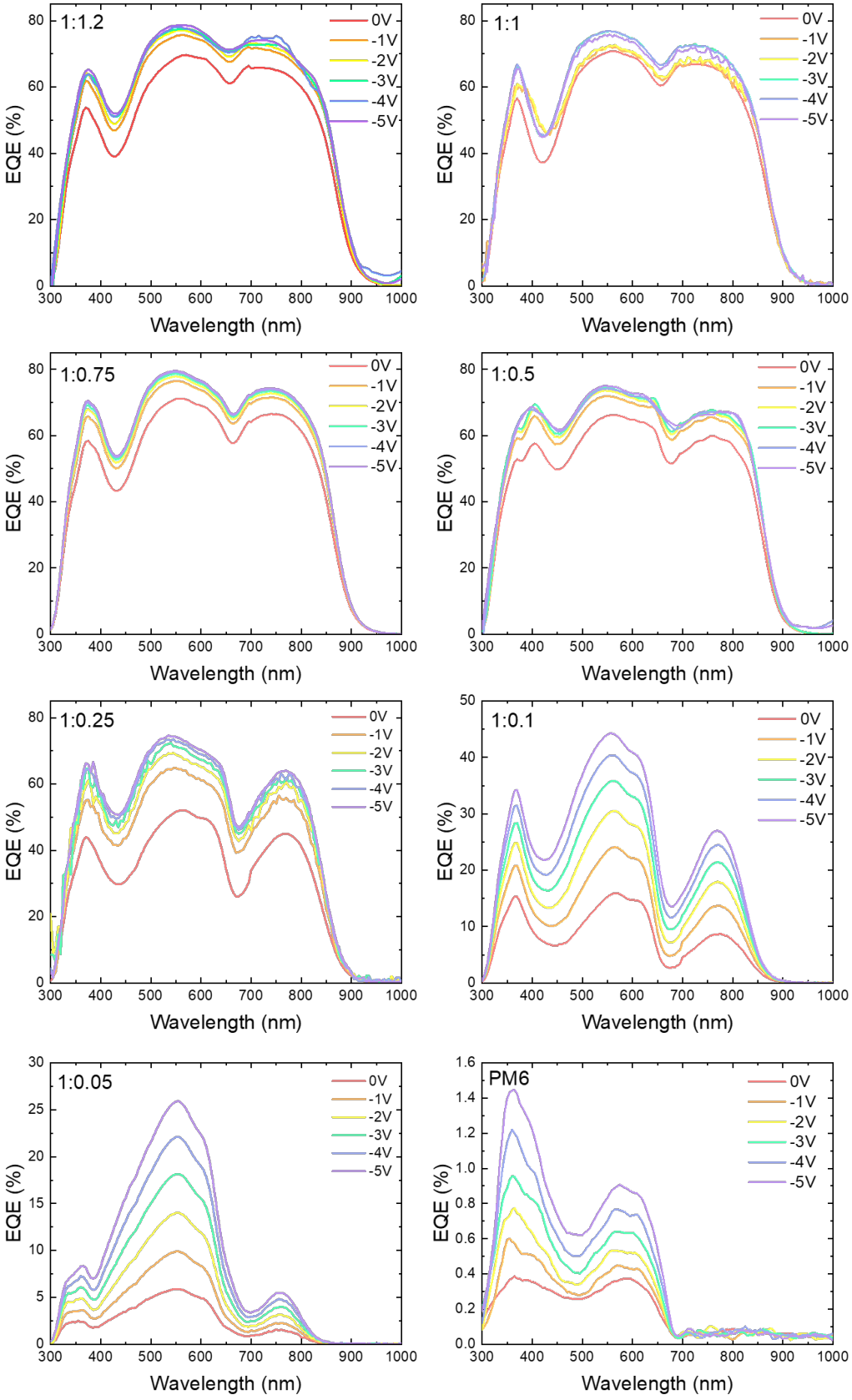


Fig. 6.5: EQE spectra for PM6:Y6 devices with different blend ratios, measured at increasing reverse bias.

6.2.3 The Origin of Blend-Ratio-Dependent OPD Performance: the Nature of Electronic Species

In order to understand the origin of device performance and the impact of blend ratio on the OPD operation mechanisms, detailed characterisation of optoelectronic properties and transient photophysics in PM6:Y6 devices is carried out under reverse bias. Figure 6.5 shows the effect of reverse bias on EQE spectra for diluted devices. The spectra span from 300 to 900 nm, showing effective charge generation and collection over the whole absorption range of both PM6 and Y6 (consistently with absorption spectra). Especially, high EQE of 27% (at -5 V) is achieved in the Y6 range even at low acceptor content. At this regard, it should be noted that the EQE shape is broad for balanced BHJs (Figure 6.5a-d),[139,160,212] becoming more defined around PM6 and Y6 peaks for increasing acceptor dilution. Here, the low EQE at 0 V for diluted BHJ devices (a maximum of 15.9%) is strongly increased under reverse bias (*circa* 44% at -5 V), unlike the almost bias-independent EQE in balanced blends. This arises from an overall enhancement in charge generation and/or extraction across the whole wavelength range, in agreement with the negligible changes in EQE spectral shapes (see normalised EQE data in Figure 6.6).

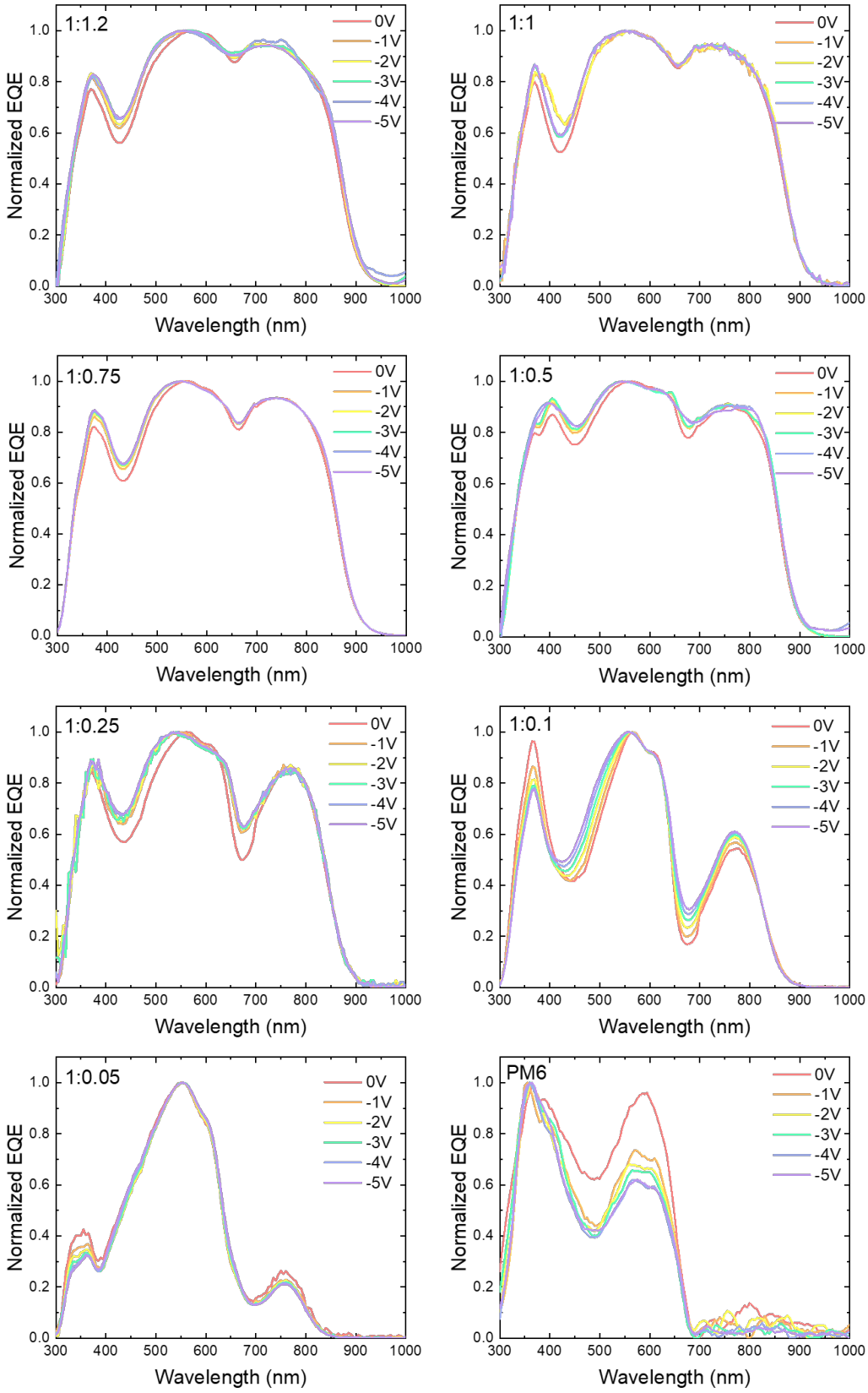


Fig. 6.6: Normalised EQE spectra for PM6:Y6 devices with different blend ratios, measured at increasing reverse bias.

To further identify the origin of photocurrent increase, field-dependent PL measurements are carried out, with a comparison between balanced and diluted cases shown in Figure 6.7. As the main emission in PM6:Y6 blends can be assigned to the excitonic species in Y6,[397] the PL evolution under electric field is attributed to changes in radiative recombination and charge generation/dissociation in the BHJ. In particular, PL is quenched under reverse bias, with a much stronger trend in diluted compared to balanced blends (Figure 6.7a,b). Therefore, the dramatic bias-dependent EQE increase for diluted blends can be related to the field-driven dissociation of emissive species, leading to a parallel evolution of PL quenching efficiency (PLQE, Figure 6.7c) and EQE gain (Figure 6.8a).

In particular, an impressive two-fold EQE increase at -5 V is found for high Y6 dilution, while balanced blends show a $<$0.25 gain, consistently with trends in photocurrent generation (Figure 6.8b). At the same time, PLQE is approximately 20% stronger for diluted *vs.* balanced BHJs, with the difference plateauing at high bias around -10 V. Finally, exceptional photocurrent increase is observed for diluted blends under reverse bias (Figure 6.9 and Figure 6.10), while little enhancement appears in the balanced case despite higher absolute values.

Overall, this gives some important initial insights into the origin of field-dependent device performance in diluted systems. When small Y6 domains are embedded in the dominant PM6 matrix (*i.e.*, for high donor content), D-to-A energy transfer efficiency is not disrupted even at low Y6 content, but the photogenerated species are prone to recombination due to reduced D/A interfacial area (*i.e.*, limited charge transfer at D/A interfaces), resulting in six-fold higher PL emission (Figure 6.7). Therefore, additional driving force is required for effective charge separation. Indeed, strong PLQE is achieved upon bias assistance, evidence of suppressed radiative recombination and enhanced charge separation, and mirrored in EQE and photocurrent increase. On the other side, balanced blends with well-intermixed morphology and large D/A interfacial area are intrinsically optimised for exciton dissociation, so that reverse bias cannot assist further the photocurrent enhancement. Note that relative PL is significantly quenchable also in balanced blends, as residual interfacial CT states still benefit from electric-field-assisted dissociation. However, the PL yield of these states is very weak in highly intermixed BHJs, so that no significant photocurrent gain can be achieved by their separation (Figure 6.8).

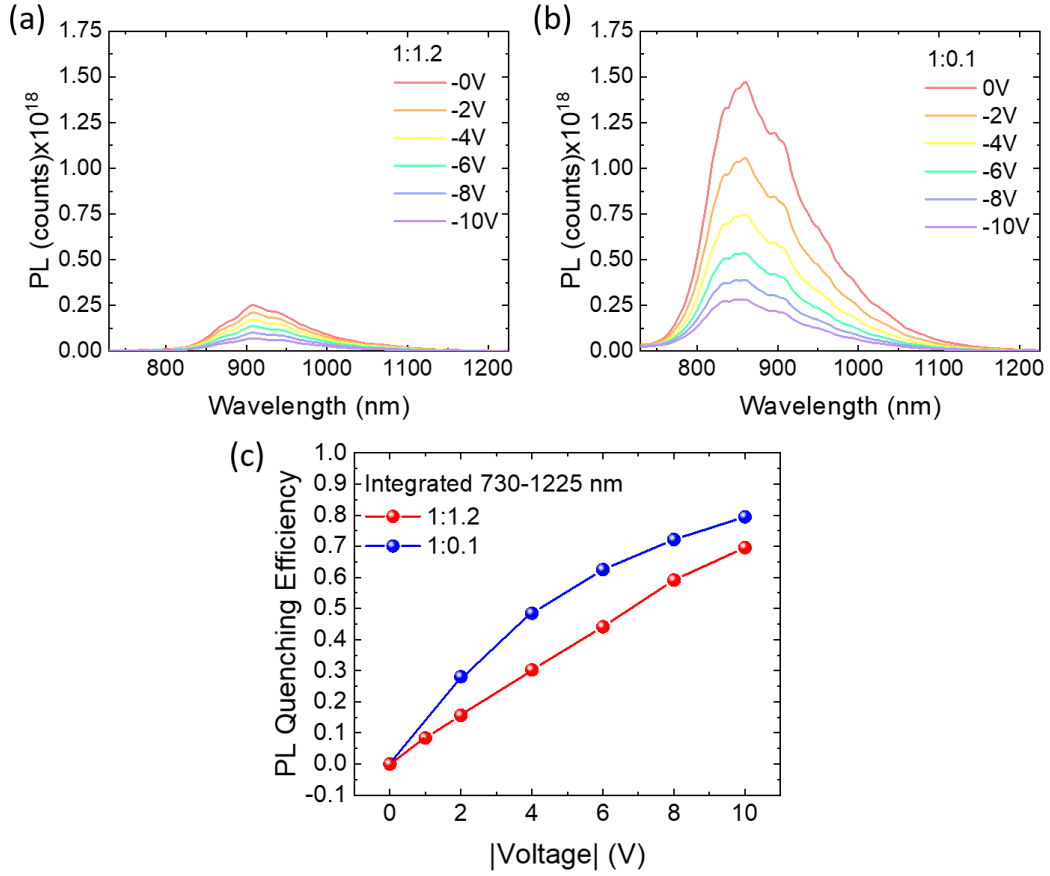


Fig. 6.7: Bias-dependent PL analysis for balanced and diluted PM6:Y6-based devices. Bias-dependent PL spectra under reverse bias for (a) 1:1.2 and (b) 1:0.1 PM6:Y6-based OPD devices. (c) PLQE under reverse bias for balanced and diluted BHJ devices, calculated as $(PL_{V=0}\text{-}PL_V)/PL_{V=0}$, where $PL_{V=0}$ is the PL at null bias and PL_V the PL at a voltage V, and integrated over the whole spectrum.

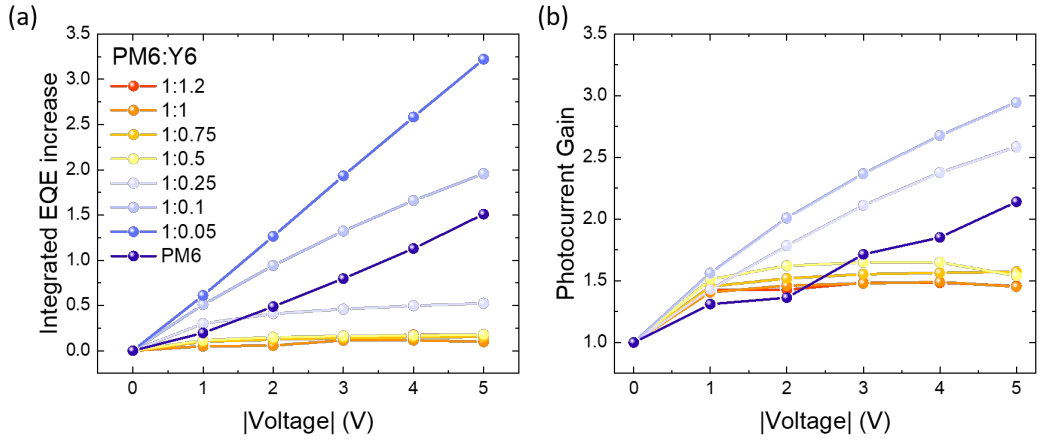


Fig. 6.8: Electric characterisation under reverse bias of PM6:Y6 devices with different blend ratios. (a) EQE increase under reverse bias calculated as (EQE_V-$EQE_{V=0}$)/$EQE_{V=0}$, where EQE_V is the EQE at a voltage V and $EQE_{V=0}$ the EQE at null bias. EQE is integrated over the whole 300-1000 nm spectrum. (b) Photocurrent gain under reverse bias calculated as (I_V-$I_{V=0}$)/$I_{V=0}$, where I_V is the photocurrent under red LED (633 nm) excitation (see Figure 6.9 below) at a voltage V and $I_{V=0}$ the photocurrent at null bias.

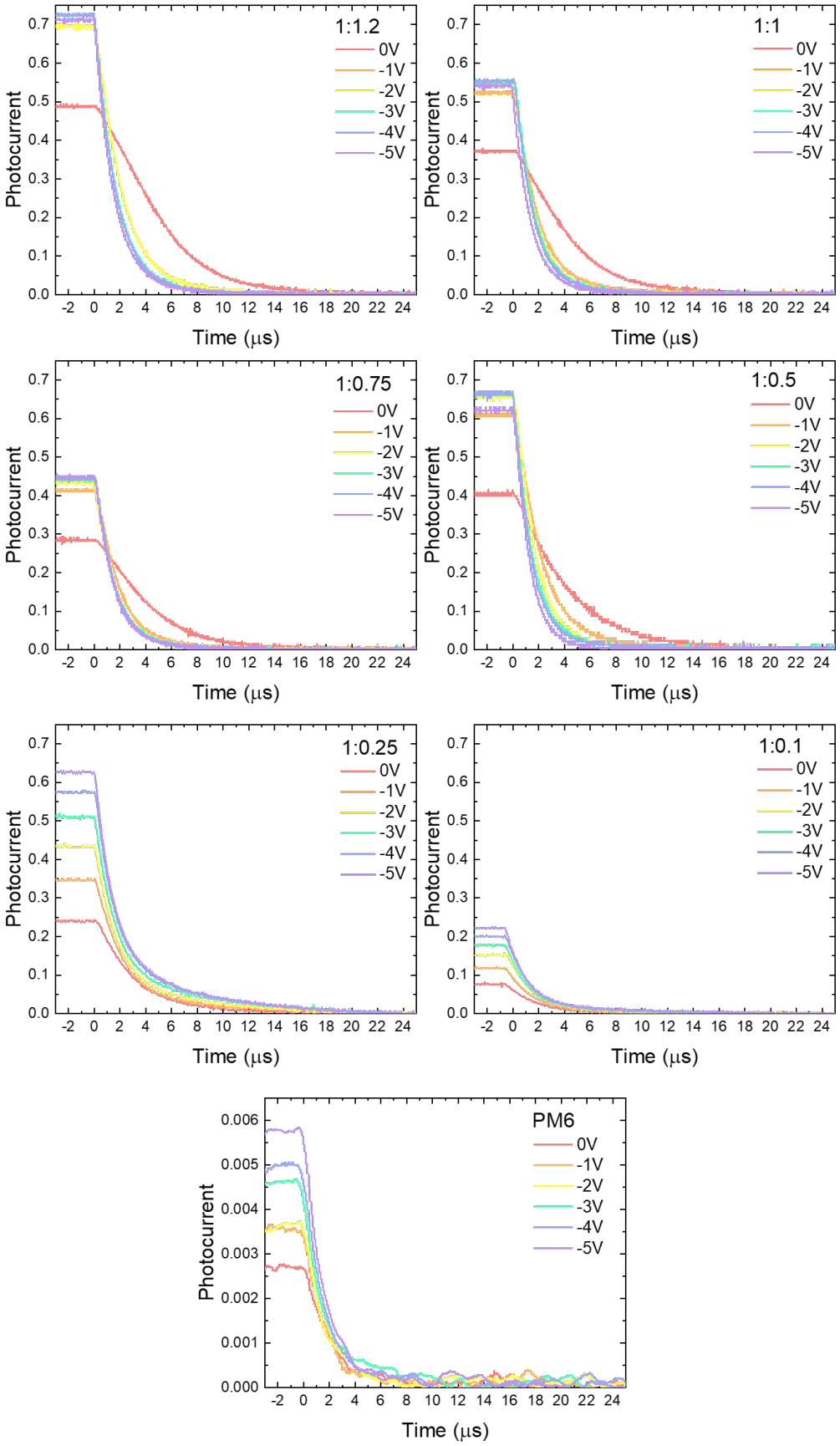


Fig. 6.9: Transient photocurrent decay after red LED (633 nm) excitation for PM6:Y6 devices with different blend ratios, measured under increasing reverse bias.

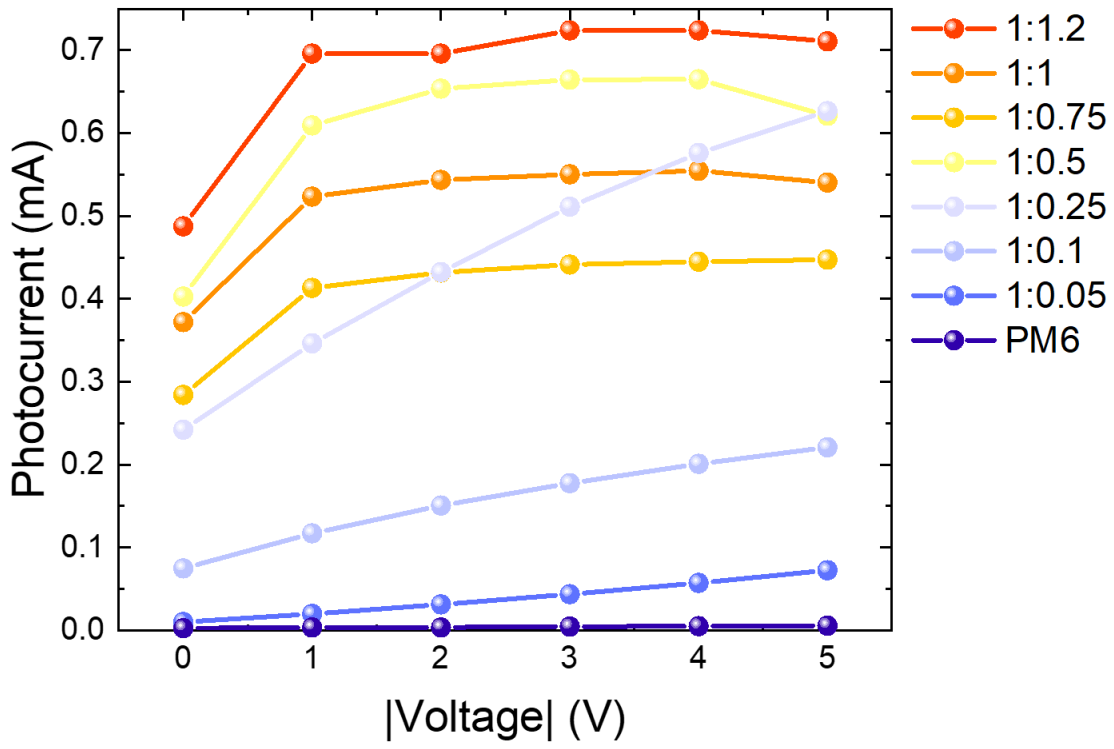


Fig. 6.10: Transient photocurrent under red LED (633 nm) excitation for PM6:Y6 devices with different blend ratios, measured under increasing reverse bias.

In addition to charge generation and dissociation, the processes of transport and extraction also determine OPD performances (*e.g.*, EQE), and they should be taken into consideration for a complete picture of device photophysics. For this purpose, photocurrent transients are analysed upon pulsed LED excitation, focusing on the fall times τ_{fall} of photogenerated signals. As shown in Figure 6.11 and Figure 6.12, τ_{fall} is extremely fast for diluted BHJs, in line with figures of merit of state-of-the-art OPDs.[55,60,170,374,398,399] With no applied bias, a τ_{fall} of 4.70 µs is observed, compared to 9.0 µs for the balanced case. This is maintained with a slight improvement under reverse bias, reaching a τ_{fall} of 4.46 µs at -2 V. Therefore, external bias in diluted blends is essential to increase photocurrent output (Figure 6.8b, Figure 6.9, and Figure 6.10), but less crucial for fast charge extraction, whereas electric field is required for a quick photoresponse in balanced blends (from 9.0 µs at 0 V to 4.59 µs at -2 V). These results give further indications on the photophysical mechanisms responsible for device performances. In fact, efficient charge generation is already achieved by optimum BHJ morphology for balanced blends, but the electric field is required to assist transport and enhance charge extraction in the highly

intermixed system (*i.e.*, high ratio of D/A boundaries disrupting charge transport). On the other side, charge generation is the limiting step for diluted blends, and it is strongly enhanced under reverse bias by quenching the bound emissive state, while the polymer matrix and homogeneous morphology (*i.e.*, limited presence of domain boundaries) provide intrinsically superior transport properties. These are confirmed by the much higher hole mobility in diluted blend devices (8.1×10^{-4} cm^2 V^{-1} s^{-1}), compared to balanced (1.8×10 cm^{-4} V^{-1} s^{-1}), as in Figure 6.13. Here, it is interesting to notice that hole transport has the dominant role to determine device photophysics, since electron mobility is significantly lower, despite intrinsically similar mobilities for neat PM6 and Y6. In fact, whereas the charge transit time τ_{tr} in OPDs is generally determined by the slowest carrier in the active layer, it is likely that at very unbalanced blend ratios it is the mobility of the majority carrier to dominate instead. In conclusion, inefficient charge generation for donor-rich devices can be fixed under reverse bias, which, combined with optimum transport, ensures superior OPD performances under mild electric fields.

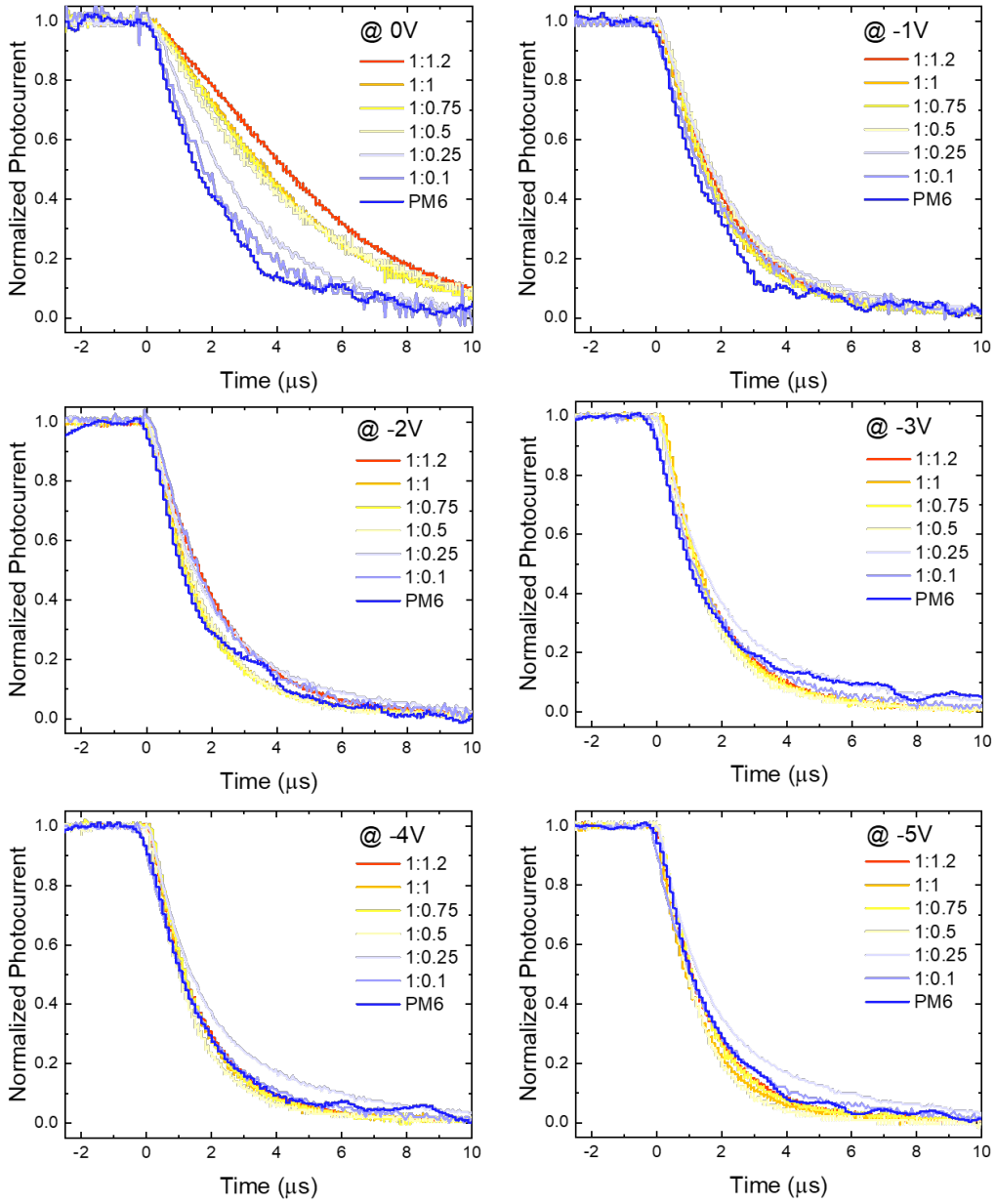


Fig. 6.11: Normalised transient photocurrent decay after red LED (633 nm) excitation for PM6:Y6 devices with different blend ratios, measured at increasing reverse bias.

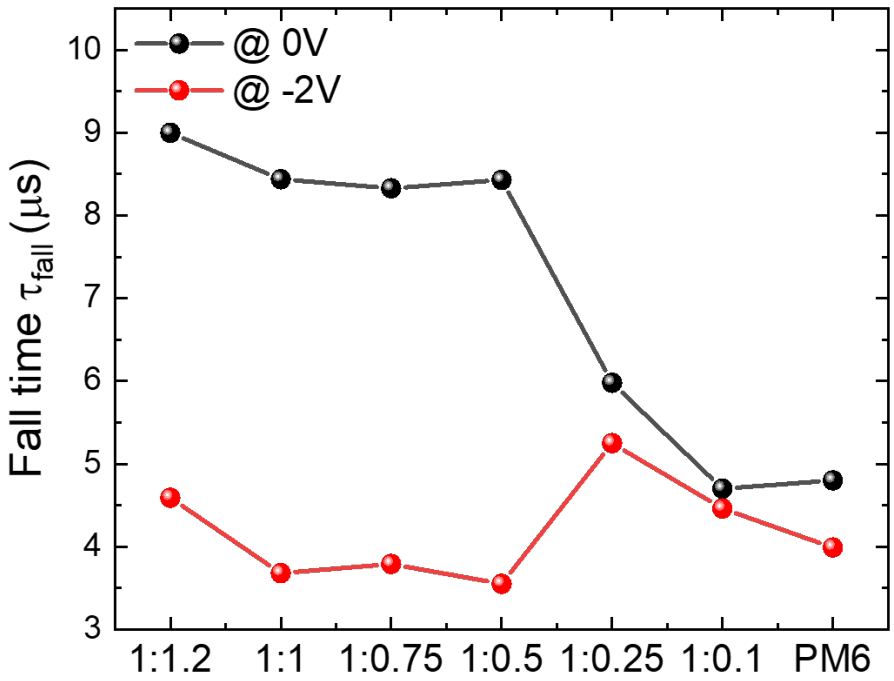


Fig. 6.12: τ_{fall} of transient photocurrent for PM6:Y6 devices with different blend ratios, at null bias and under reverse bias (-2V).

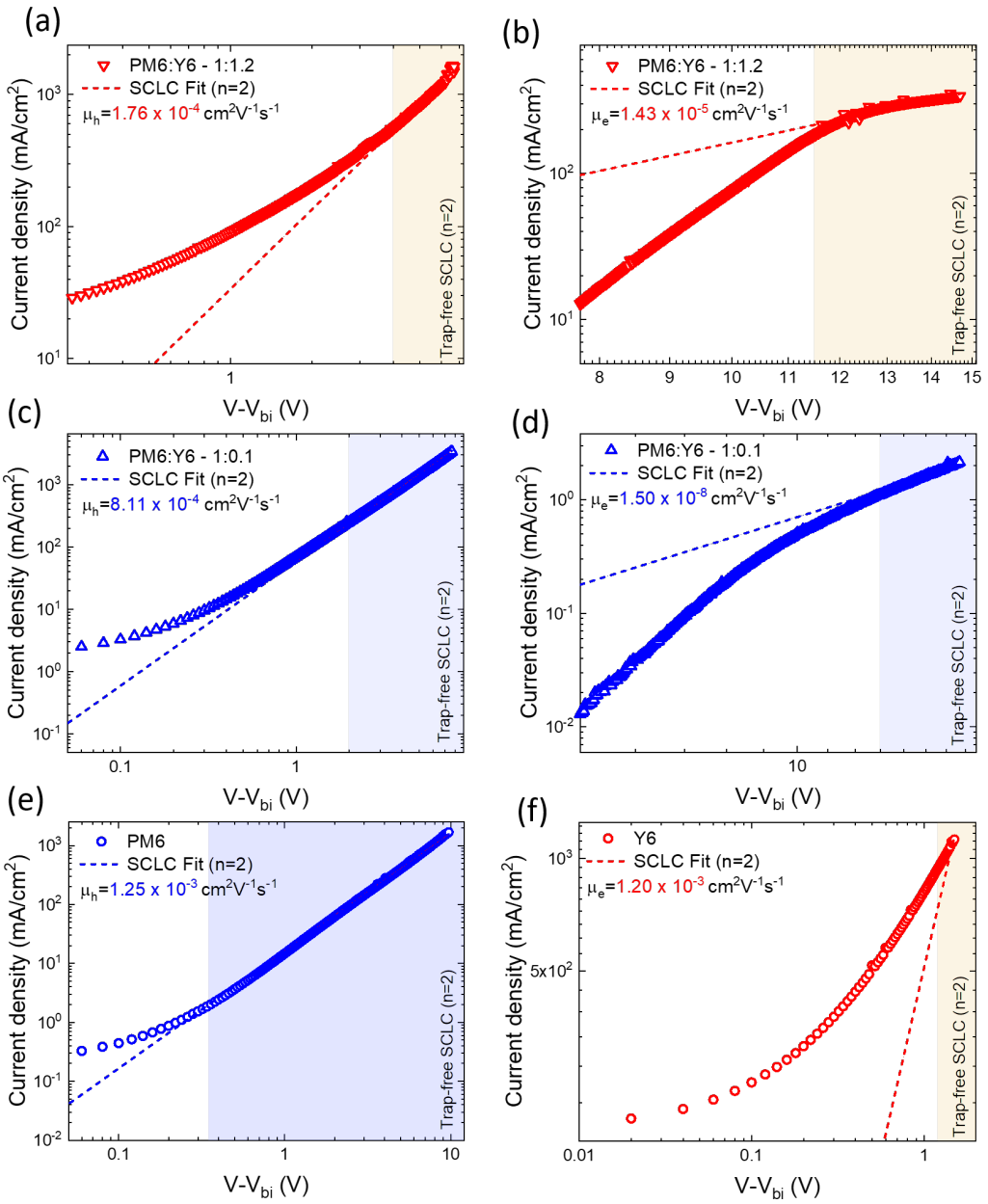


Fig. 6.13: J-V plots for single carrier devices with ITO/PEDOT:PSS/BHJ/MoO_3/Ag (hole only) and ITO/ZnO/BHJ/ZnO nanoparticles/Ag (electron only) structures, for 1:1.2 (a,b) and 1:0.1 (c,d) blend ratios, PM6 (hole only, e) and Y6 (electron only, f). Electron and hole mobilities are extracted by fitting with the Mott-Gurney equation in the SCLC region indicated in the figure, and its value is indicated in the legend.

For gaining more insight into the exact nature of charge generation and dissociation processes, we turn to ultrafast TAS investigation of BHJ films. As presented in Figure 6.14a,b, the samples are excited at the Y6 absorption (750 nm) in order to probe the hole transfer process from A to D. Figure 6.14a shows that the ground state bleaching (GSB) of Y6 is visible below 900 nm, and photoinduced absorption

(PIA) bands appear at 950 nm and 1350 nm.[159,160,380,400,401] The PIA at 950 nm has been assigned to exciton absorption. As pump-probe time delay increases, this PIA shifts to a longer-wavelength region in both balanced and diluted blends, attributed to hole transfer from Y6 to PM6.

Fluence-dependent analysis shows a clear distinction between balanced and diluted BHJ systems (Figure 6.14c,d). While for the balanced case kinetics accelerate at higher fluence, diluted sample has a clearly fluence-independent behaviour. This reveals that bimolecular recombination of charge carriers dominates in balanced BHJs, while recombination in diluted blends is mainly monomolecular, proceeding *via* interfacial CT-like states. In fact, the intermixed nature of balanced BHJs helps fast exciton dissociation into electron-hole pairs, which mostly recombine non-geminately. Conversely, when Y6 is diluted into a PM6 matrix, the photogenerated species are strongly bound (CT-like character) and tend to recombine previous to complete dissociation (*i.e.*, geminately). This is further supported by the long-lived PL component observed in diluted blends (lifetime >5 ns), compared to the very fast decay in balanced BHJs (see transient PL following selective Y6 excitation, Figure 6.15). Moreover, detailed analysis of temperature-dependent CT dissociation allows to estimate a CT binding energy of around 180 meV for diluted blends (see Appendix E), confirming the strongly bound character of interfacial species compared to balanced BHJs. In this context, it is clear how an external electric field has a much stronger effect on dissociation of strongly bound species (*i.e.*, diluted BHJ) rather than loosely bound electron-hole pairs (*i.e.*, balanced BHJ). Therefore, field-driven CT separation is the key to efficient photocurrent generation in diluted BHJs despite limited domain intermixing. At the same time, the strong binding energy of interfacial species can contribute to low J_d, suppressing the thermal component of dark carriers generation.[60,174] This is further alleviated due to high content of large-bandgap PM6 and blue-shifted Y6 absorption in diluted blends.

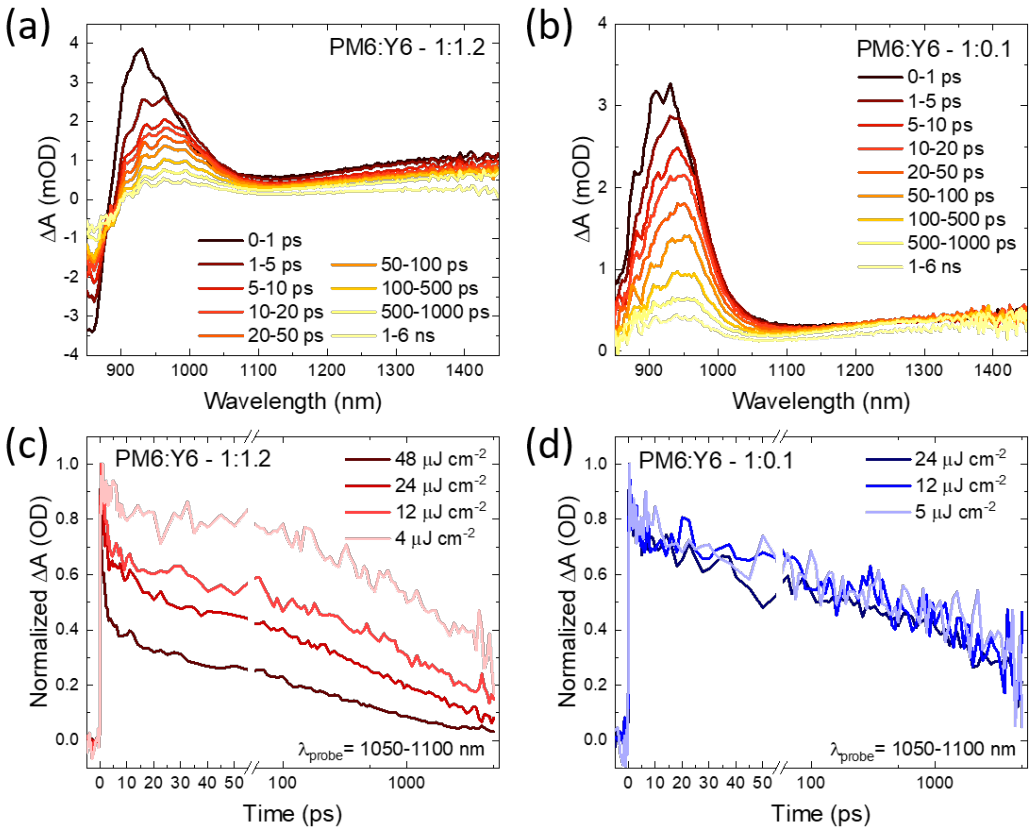


Fig. 6.14: Transient absorption spectroscopy. TAS spectra of diluted (a) and balanced (b) PM6:Y6 BHJ thin films. Fluence-dependent kinetics are shown in (c) and (d), respectively.

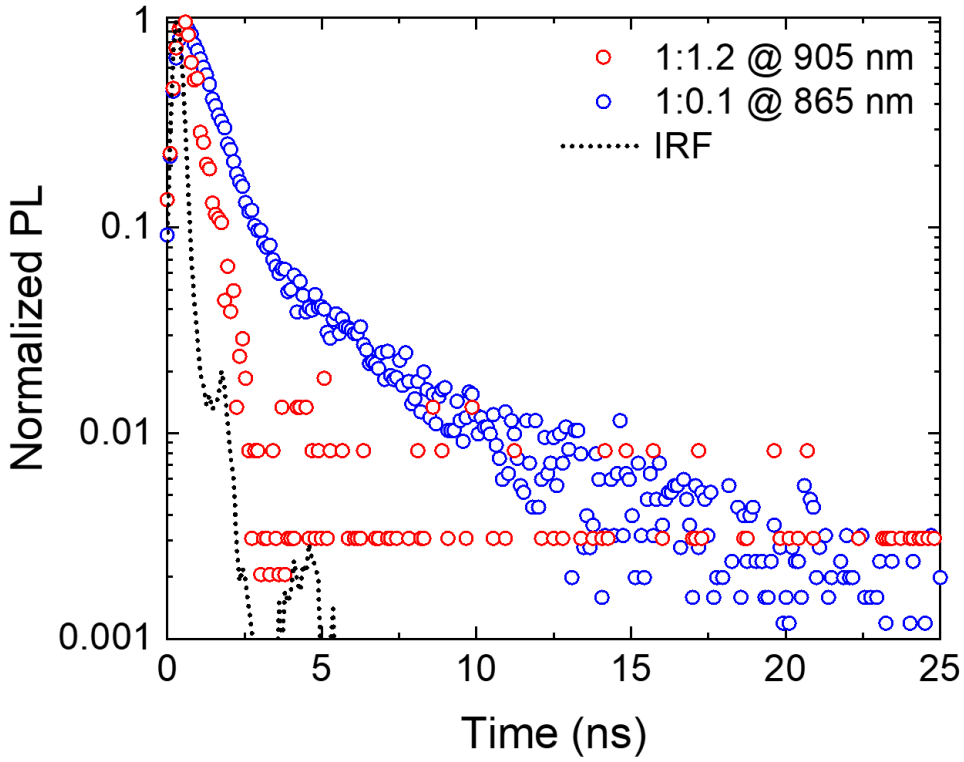


Fig. 6.15: Transient PL for balanced and diluted PM6:Y6 blends, following selective Y6 excitation at 800 nm. The balanced BHJ shows a very fast PL decay with a lifetime τ of 0.40±0.05 ns, severely limited by the instrument response function (IRF), while for high donor content a second ling-lived decay component is visible (τ_1 = 0.73±0.02 ns, τ_2 = 5.06±0.01 ns).

6.2.4 The Origin of Blend-Ratio-Dependent OPD Performance: Energetic Landscape upon Acceptor Dilution

To understand charge dissociation in BHJ systems and identify the origin of J_d, the energetic landscape at D/A interface should be considered. In particular, initial efficient energy transfer to Y6 (Figure 6.1c) *via* Förster resonance[159] makes hole transfer to PM6 the main charge generation mechanism, so that interfacial HOMO offset plays an essential role in device photophysics. Here, we carry out a detailed analysis of BHJ energetics by APS, providing information on HOMO energy levels and DOS.[19,271,402] As shown in Figure 6.16a (see Figure E.2a,b in Appendix E for full blend series), the photoemission onset in blends arises from the PM6 HOMO (*i.e.*, the shallowest component). With increasing Y6 load, this is continuously deepened compared to neat PM6 HOMO up to ∼200 mV, reaching -5.25 eV for balanced

BHJs, due to factors such as charge-quadrupole interaction at D/A interfaces[214] or PM6 conjugation loss in intermixed phases.[207] Conversely, high polymer content brings PM6 HOMO close to its intrinsic level, with -5.09 eV for diluted BHJs. In addition, although extracting information on the deeper Y6 energetics in blends is more challenging, DOS analysis suggests a deepening of Y6 HOMO for increasing dilution (Figure 6.16b and Figure E.2c,d in Appendix E), presumably related to the increasing bandgap upon packing disruption. Therefore, the combination of shallower PM6 and possibly deeper Y6 energy levels in diluted blends results in a larger HOMO offset compared to balanced counterparts (see schematics in Figure 6.16c,d). This leads to more efficient hole transfer, once dissociation of strongly bound states is achieved by sufficient driving force (*e.g.*, electric field). At the same time, the shallower PM6 energetics is also beneficial to prevent dark electron injection from MoO_3 HTL to the PM6 LUMO, while injection into Y6 LUMO is prevented by the limited MoO_3/Y6 contact areas.[403] This, combined with efficient hole transport and high mobility in the continuous polymer matrix, rationalises the extremely low J_d for donor-rich BHJs.[404]

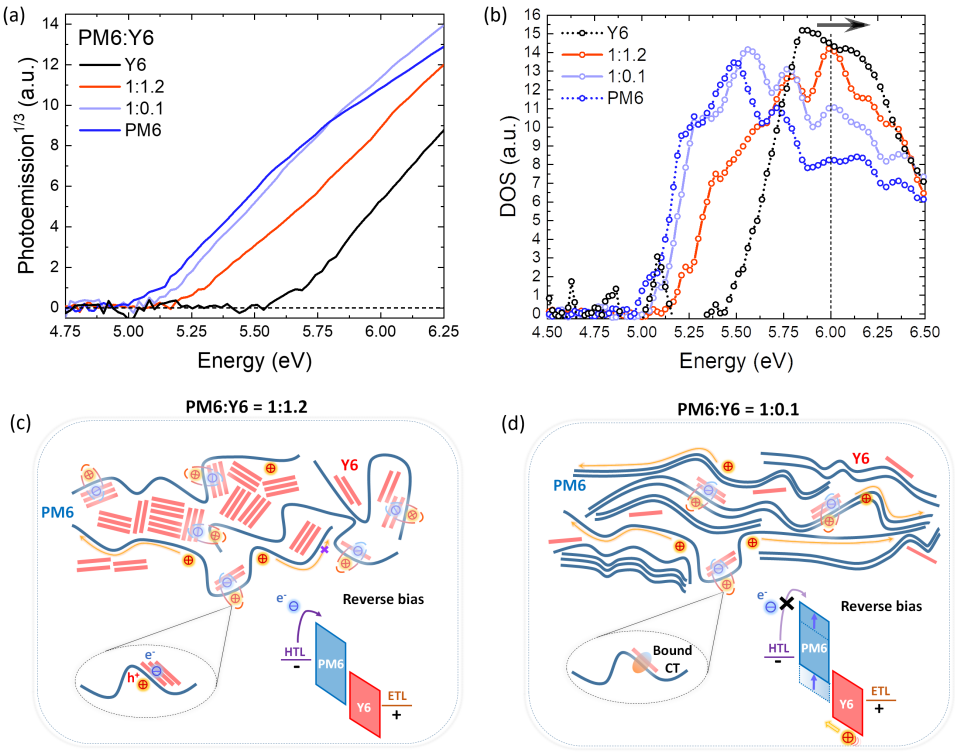


Fig. 6.16: Energetic analysis and schematics of BHJ photophysical mechanisms. (a) Photoemission and (b) DOS spectra of PM6, Y6, and their blends. The shift in the Y6 region upon blending is indicated in the DOS spectra. Illustration of charge generation and transport in PM6:Y6 blends, with balanced (c) and diluted (d) blend ratios. Generation of electron/hole pairs at the D/A interface is followed by hole transport through the polymer chains, which is more efficient at high PM6 content due to the interconnected network of polymer chains (see top of panel). Formation of interfacial states is different depending on blend ratio, with efficient interface charge separation in balanced blends and creation of bound CT-like species for diluted ones (bottom left). Device operation under reverse bias is driven by D/A energetics (bottom right). The shallower PM6 HOMO and LUMO in diluted BHJs is beneficial to suppress J_d and assist hole transfer from Y6.

6.3 Conclusion

In summary, a detailed study of optoelectronic properties and device photophysics of PM6:Y6 systems depending on blend ratio is presented in this chapter, showing the advantages of high donor content for OPD operations. As summarised in the schematics in Figure 6.16c,d, exciton dissociation mainly occurs at the D/A interface, involving energy transfer to Y6 and subsequent hole transfer to PM6. This is followed by hole transport through the PM6 polymer matrix, which is highly efficient at high donor content due to continuous percolation pathways. Moreover,

the findings presented here demonstrate that blend ratio engineering is a powerful tool to control the nature of photogenerated species. In particular, in isolated and poorly packed Y6 domains strongly CT-like interfacial states are formed, while well-intermixed BHJs with good D and A crystalline packing fosters effective electron/hole dissociation. At this regard, it should be noted that a lack of aggregation-induced interfacial energy cascade by Y6 dispersion[207,405] may contribute to the bound CT character of interfacial states in diluted blends. This effect would be particularly strong when Y6 rather than PM6 crystallinity is disrupted, due to the sizeable NFA quadrupole moments determining interfacial electrostatic potential effects for charge separation.[159] Therefore, diluted BHJs are best suited for OPD operations, where external driving force is provided by reverse bias. This ensures effective dissociation of interfacial states, resulting in excellent photocurrent increase. At the same time, the larger HOMO offset and shallow energetics of PM6 in donor-rich systems allow more efficient hole transfer, followed by effective charge transport through the polymer matrix (*i.e.*, fast photoresponse). The shallow PM6 energetics is also beneficial to suppress dark injection contribution to J_d, while the large bandgap of majority PM6 and strongly-bound CT nature reduce the thermal contribution. All these factors enable to achieve an extremely low J_d, key for excellent D^* in devices.

Therefore, donor-rich BHJs are a viable strategy towards efficient OPDs with reduced fabrication complexity. Here, it is demonstrated that 5%-10% of acceptor content is sufficient to achieve relevant photocurrent generation under reverse bias, while concomitant J_d suppression yields record figures of D^*. At the same time, fast transport through the polymer matrix ensures fast photoresponse, crucial for high-frequency photodetection. Moreover, such a low amount of acceptor alleviates fabrication complexity, requiring minimum effort for morphology optimisation (*e.g.*, thermal treatments, solvent additives) compared to the delicate BHJ engineering for balanced D/A ratios. High polymer donor content is also expected to be beneficial for device lifetime, due to the superior robustness to chemical and thermal degradation of polymeric components,[37,38,164,253,393] so that diluted BHJs are greatly promising for industrially-scalable, stable, and highly efficient OPDs.

6.4 Experimental Section

Sample and Device Fabrication and Electrical Characterisation

For preparation of thin films and devices, PM6 and Y6 (Solarmer Materials) are mixed in different blend ratios in chloroform solvent (18 mg/mL), heated at 45°C overnight for complete dissolution. Details of substrate cleaning procedure and ZnO, MoO_3, and Ag layers are given in Section 3.1. PM6:Y6 active layer are spin-coated at 2500 rpm for 30 s, achieving 100-150 nm film thicknesses measured by Dektak surface profilometer. Single carrier devices for SCLC measurements are fabricated with similar procedures, using ITO/PEDOT:PSS/BHJ/MoO_3/Ag (hole only) and ITO/ZnO/BHJ/ZnO NP/Ag (electron only) structures, with spin-coated PEDOT:PSS and ZnO nanoparticles, and evaporated MoO_3 and Ag. Mobility is calculated using Mott-Gurney relationship (Equation 3.10). Electrical characterisation of devices is performed as described in Section 3.8. For bias-dependent OPD photocurrent transients, devices are excited by a 633 nm LED, and voltage is controlled by a BK Precision 9110 power supply.

Optical Characterisation

Absorbance of thin films is measured as described in Section 3.4. Details of steady-state and transient PL analysis are given in Section 3.5. Bias-dependent PL is measured by a 532 nm laser, and TCSPC exciting the samples with a 800 nm laser.

Energetic Characterisation

Energetics of materials on grounded ITO substrates is measured as detailed in section 3.3, and DOS is calculated as first derivative from photoemission cube root spectra by in-house written software.

Transient Absorption Spectroscopy

Details on TAS analysis are found in Subsection 3.9.1.

7 | Efficient Nonfullerene-Based Organic Photodetectors Enabled by Reduced Deep Traps with Highly Intermixed Evaporated Bulk Heterojunction Systems

As shown in Chapter 5, molecular design of sublimable materials for BHJ OPDs is crucial to control density of shallow and deep trap states and photoresponse speed at different illumination conditions. In particular, the planar small-molecule donor MPTA appears as a promising candidate for efficient photodetection at high light intensities, but the nanoaggregation and adduct formation with the fullerene acceptor deteriorate low-light photoresponse speed by deep-trap formation. In this chapter, the potential of the planar donor MPTA is fully utilised by matching with a sublimable NFA (Cl_6-SubPc) and thickness optimisation of the photoactive layer. Firstly, upon thickness increase, the strong intermolecular interactions in MPTA are harnessed towards a more systematic face-on orientation in the solid-state packing. Secondly, more effective D:A intermixing is achieved with Cl_6-SubPc compared to C_{60} acceptors, so that the origin of deep-trap states (*i.e.*, nanoaggregation, MPTA-C_{60} adduct formation) is suppressed. This leads to superior OPD performance thanks to the higher yield of interfacial CT states and faster low-light photodetection. Overall, relevant guidelines for structural optimisation in evaporated BHJs emerge from this study, and NFA-based small-molecule OPDs are shown as promising candidates for high-performance, trap-free photodetection.

7.1 Introduction

In the pursue for high-efficiency OPDs with up-scaling potential, one of the most industrially-relevant fabrication techniques is thermal evaporation in high vacuum,[406] offering optimum control on every functional layer in the device stack, excellent batch-to-batch reproducibility, and precise tuning of active layer morphology.[407] However, strict requirements are imposed on the materials to have optimum sublimability, and only small molecules with no side chains and low molecular weight are suitable candidates.[408] In particular, the choice of acceptor materials has been typically dominated by fullerenes (*i.e.*, C_{60} and C_{70}),[71,88,178,180,334,337,406,409] where facile evaporation is accompanied by isotropic transport with high electron mobility, long exciton diffusion length, and suitable energy levels for good electron transfer (see Section 2.3).[87,407] As a drawback, fullerene molecular structure shows limited energetic tunability[410] – especially in side-chain-free sublimable molecules – and problematic morphology control. In fact, fullerene segregation[187,188,411] or dimerisation[189,412] have been reported, leading to sub-optimal BHJ formation and severe device instability,[237,238] which is also observed in solution-processed PCBM systems. Since it has been suggested that a major source of J_d in OPDs is the electric-field-assisted detrapping of charge carriers,[71] the role of fullerenes in creating trap states[300,413] can also contribute to sub-optimal performances in C_{60}-based devices.

In Chapter 5,[20] the potential of the small molecule donor MPTA to realise efficient BHJ OPDs in conjunction with C_{60} acceptor is introduced. The planarity of this molecule is essential to ensure low band-edge energetic disorder and high charge mobility, for excellent performance in standard illumination conditions (*i.e.*, from 1 Sun down to 0.5 mW cm^{-2}), with effective packing achieved by strong intermolecular interactions in MPTA. However, these strong intermolecular interactions cause residual MPTA aggregation in BHJ, responsible for deep-trap formation and slowed down photodetection speed in low-light conditions (*i.e.*, $<$ 0.4 mW cm^{-2}). Adduct formation by reaction of the C_{60} C-C cage with the unhindered amine lone-pair in MPTA[367–369] also concurs to the creation of deep traps. Therefore, the substitution of C_{60} with an alternative acceptor appears as a promising route for trap state suppression.

Materials to be considered as effective fullerene alternatives need to fulfil several requirements, including affordable sublimation temperature (ideally $<$400°C), adequate morphology, and matching energetics with MPTA. At this regard, molecules of the boron subphthalocyanine chloride (SubPc) family have proved to be suitable

candidates in various BHJ systems, especially demonstrated in fullerene-free organic photovoltaics.[151,371,414,415] Attractive properties of the SubPc family include high extinction coefficient ($\sim 10^5$ cm^{-1}), narrow absorbance in the green range (FWHM$<$100 nm), good charge-carrier mobility, and chemical and thermal robustness,[407,416] making them viable replacements to C_{60}. In particular, the characteristic rigid cone-shaped geometry of SubPc derivatives allows great adaptability to several packing motifs, with limited tendency to aggregation.[417,418] This appears as a promising way to improve the BHJ morphology in MPTA systems. Moreover, a rich toolbox of chemical modifications is available to tailor SubPc structure and tune its energetics, using routes such as peripheral substitution, axial grafting, or π-extension.[417,418] In this work, Cl_6-SubPc is chosen as an adequate match for MPTA, with the partial peripheral halogenation providing appropriate energy levels.[419] However, limited knowledge is available on SubPc-based BHJ OPDs, with most of the demonstrations focusing on planar heterojunction architectures.[154] Among the few examples of BHJ devices, SubPc has been used in blend with N,N-dimethyl quinacridone (DMQA), showing fast photodetection and extremely low J_d in comparison with other linear NFAs.[420] High EQE and fast response time have also been reported for N,N'-dimethyl-2,9-DMQA:SubPc, where selective green detection enables application in integrated organic-silicon CMOS imagers.[421]

In addition to the choice of appropriate materials, the engineering of active layer thickness is an important factor for device performance optimisation, and evaporation-based deposition offers precise control over it. It is known from previous studies that thickness increase is detrimental for charge collection efficiency due to enhanced recombination pathways[379] and charge accumulation in tail states,[218] which limit OPD responsivity above a threshold thickness.[422,423] On the other side, thicker photodetectors typically show improved J_d,[63,424,425] although this is verified only if shunt resistance is the dominating factor, since a thick BHJ enables better film quality with no pinholes and surface defects.[71,338,426] Because of OPDs being typically operated under reverse bias, the active layer thickness has a primary effect on the net electric field experienced by the photocarriers,[174] leading to thickness-dependence not only of J_d, but also of photoresponse speed.[66] Moreover, the tuning of BHJ thickness can have a secondary effect on morphology, with additional influence on device photophysics,[422,425] although further understanding is required for evaporated OPDs.

In this chapter, Cl_6-SubPc is utilised as an NFA substitute to C_{60} in co-evaporated BHJ OPDs, in combination with the planar MPTA donor molecule. By careful device optimisation, the role of active layer thickness not only in J_d sup-

pression by increased shunt resistance,[63] but also in active-layer morphology control is demonstrated. Namely, at BHJ thickness > 50 nm, optimum D/A intermixing is achieved, with virtually absence of BHJ nanodomains (*i.e.*, microscopic phase segregation) and systematic orientation of MPTA molecules. This results in optimised OPD performances in thick devices, with a J_d ~10^{-8} A cm^{-2}, a D^* of 5×10^{12} Jones, and response times of about 10 µs. In particular, the performance origin is attributed to the high yield of emissive interfacial CT states in the finely intermixed BHJ, which can be easily dissociated under electric field. Therefore, the effective intercalation of Cl_6-SubPc into the MPTA packing enables full disruption of MPTA aggregation, which acted as a major source of deep trap states in MPTA:C_{60} devices. Combined with the suppression of chemical reactions between MPTA amine lone-pair and C_{60} (*i.e.*, adduct formation), the Cl_6-SubPc substitution of C_{60} proves to be highly suitable to prevent trap-assisted recombination, with reduced J_d and enhanced low-light photodetection. Overall, the results presented in this chapter provide important guidelines not only for the optimisation of active layer architecture in OPDs, but also about the materials selection for high-efficiency OPDs, and paves the way towards trap-free photodetection in NFA-based devices.

7.2 Results and Discussion

7.2.1 Thickness-Dependent Optoelectronic Properties

The planar small-molecule donor MPTA and the cone-shaped Cl_6-SubPc NFA are selected as candidate materials for the co-evaporated BHJ fabrication (chemical structure and full device architecture in Figure 7.1a). First, the influence of film thickness on optoelectronic properties is investigated. As shown in Figure 7.1b, the spectral response of the D:A blend is extended from 450 to 650 nm, with the contribution in the 450-550 nm range coming from MPTA, and the 575-600 nm peak from Cl_6-SubPc Q-band.[418] Here, the optical absorbance of BHJ samples constantly increases with film thickness, with a clear trend from 20 nm to 60 nm. However, this effect is not solely due to the higher photon flux absorbed in thicker BHJs, but also involves film morphology and molecular orientation. In fact, normalised spectra (Figure 7.1c) reveal an increased contribution in the MPTA region with evident absorption broadening in the short wavelength range. This can be ascribed to an increased intermixing in the BHJ morphology for thicker films, accompanied by a more systematic orientation of the planar MPTA molecules in a face-on motif. This thickness-dependent evolution of molecular orientation is supported by grazing-incidence X-ray diffraction (GI-XRD). From the 1D profiles in the out-of-

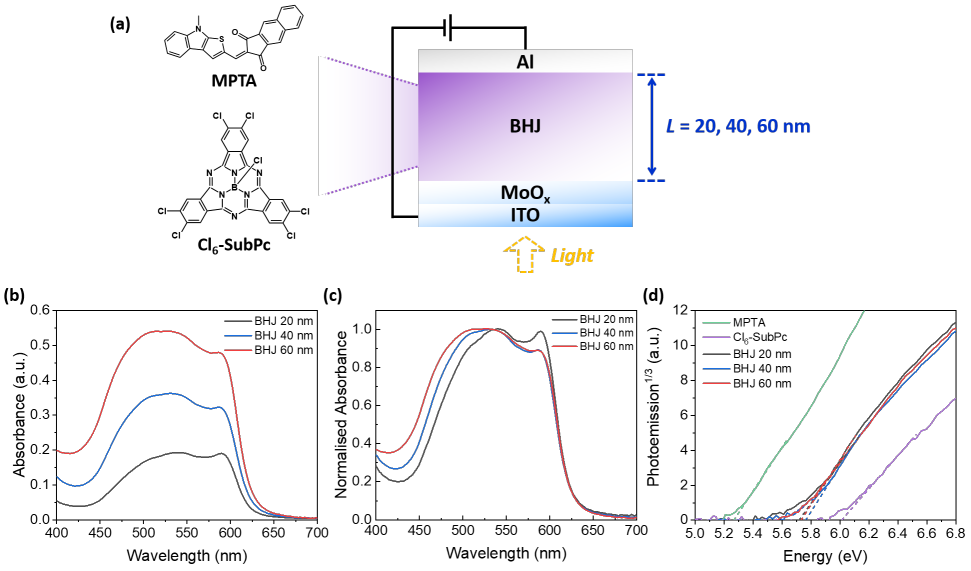


Fig. 7.1: Thickness-dependent optoelectronic properties of MPTA:Cl_6-SubPc films. (a) Molecular structure of MPTA donor and Cl_6-SubPc acceptor materials, with illustration of device structure. (b) Absolute and (c) normalised absorbance for MPTA:Cl_6-SubPc blends with different thicknesses. (d) Photoemission spectra with linear fits to HOMO levels for neat MPTA (10 nm) and Cl_6-SubPc (30 nm), as well as different thicknesses of their blends.

plane direction (Figure 7.2), significant packing order is seen in neat MPTA, with both lamellar and π-π peaks (at $q < 1$ Å^{-1} and $q \sim 2.2$ Å^{-1}, respectively). It is interesting to note that the lamellar peak at $q \sim 0.7$ Å^{-1} is strongly enhanced from 20 nm to 60 nm thick MPTA, evidence of stronger packing and more systematic orientation by thickness increase. Upon blending, only π-π stacking peaks are maintained and the *d*-spacing of the π-π stacking is increased from $\sim$ 2.8 Å to $>$ 2.9 Å (see Table 7.1). This is indicative of preserved order with systematic face-on orientation in the MPTA domains as well as intimate mixing with Cl_6-SubPc acceptor, with an amorphous broad feature dominating at $q > 1$ Å^{-1}. Note that it is challenging to extract precise thickness-dependent packing information on MPTA in blends due to the higher disorder, but we can refer to neat films about MPTA orientation in BHJ. Moreover, a slight increase in π-π spacing for thicker blends suggests a stronger D:A intermixing.

This picture is complemented by the energetic analysis shown in Figure 7.1d, where the HOMO levels of neat and blended materials are measured by APS. Here, neat MPTA HOMO lies at -5.2 eV with respect to the vacuum level, while it is deeper for Cl_6-SubPc, at *circa* -6.0 eV. Strong changes appear upon blending the two materials, with over 500 meV deepening of the MPTA HOMO (here MPTA is the moiety which can be probed in blend, having the shallowest energetics). Such

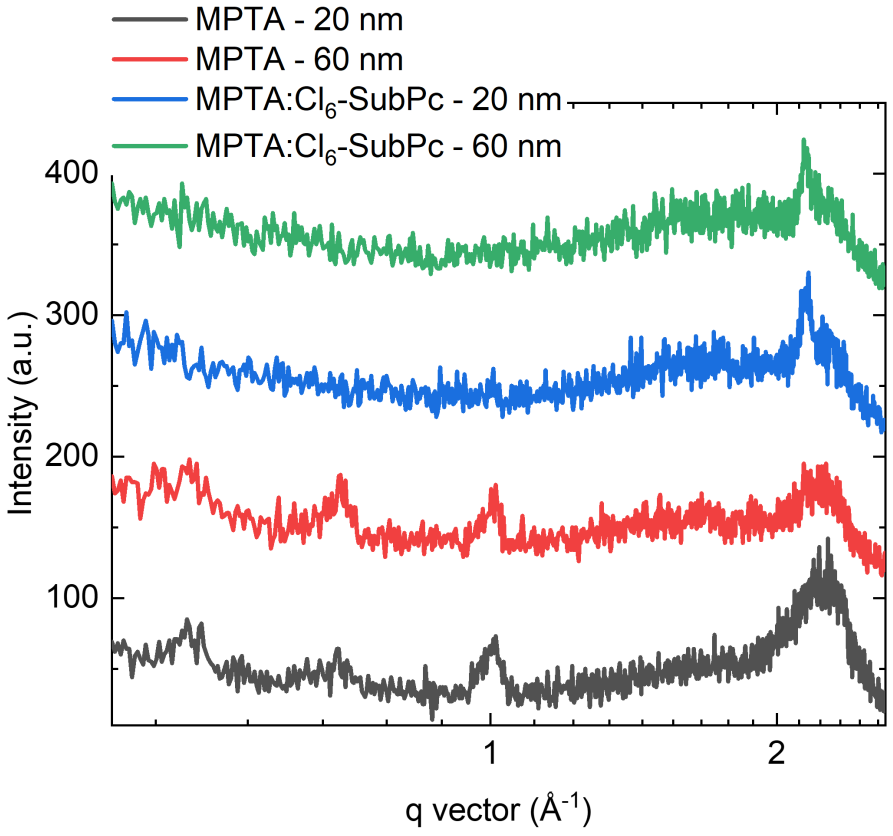


Fig. 7.2: Grazing-incidence X-ray diffraction profiles in the out-of-plane direction for neat and blended MPTA films.

	Lamellar stacking $d_{lamellar}$ (Å)	π-π stacking $d_{\pi-\pi}$ (Å)
MPTA – 20 nm	6.22, 9.11, 12.9	2.77
MPTA – 60 nm	6.22, 9.01, 13.1	2.83
MPTA:Cl_6-SubPc – 20 nm	n/a	2.92
MPTA:Cl_6-SubPc – 60 nm	n/a	2.94

Tab. 7.1: Summary of lamellar and π-π stacking distances in neat and blended MPTA films calculated from GI-XDR data.

a sizeable HOMO shift indicates a significant disruption in the packing of pristine donor, pointing to effective intermolecular mixing in the BHJ. A slight effect of film thickness is also present, with the thicker samples having a deeper HOMO than the thinnest one (*i.e.*, -5.72 eV for 20 nm *vs.* -5.77 eV at 60 nm), therefore supporting the increased intermixing. This is also consistent with the surface topography measured by atomic force microscopy (AFM, Figure 7.3), being much smoother (roughness ~1 nm) and with less prominent grain boundaries at a thickness of 60 nm.

The strong tendency to intermolecular interactions of the small-molecule planar donor MPTA has been already demonstrated in Chapter 5.[20] Here, it is shown

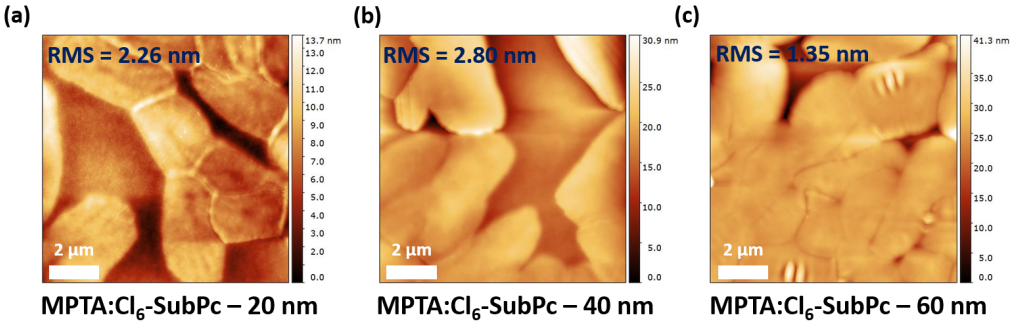


Fig. 7.3: AFM maps of MPTA:Cl_6-SubPc BHJ films of (a) 20 nm, (b) 40 nm, and (c) 60 nm thickness, with root mean square roughness indicated as inset.

that this characteristic can be harnessed for packing and orientation control by thickness engineering. At this regard, a possible role can be played by interactions with the substrate, where a thickness increase above a threshold allows to overcome templating effects and achieve an "intrinsic" packing arrangement governed by intermolecular interactions of MPTA.

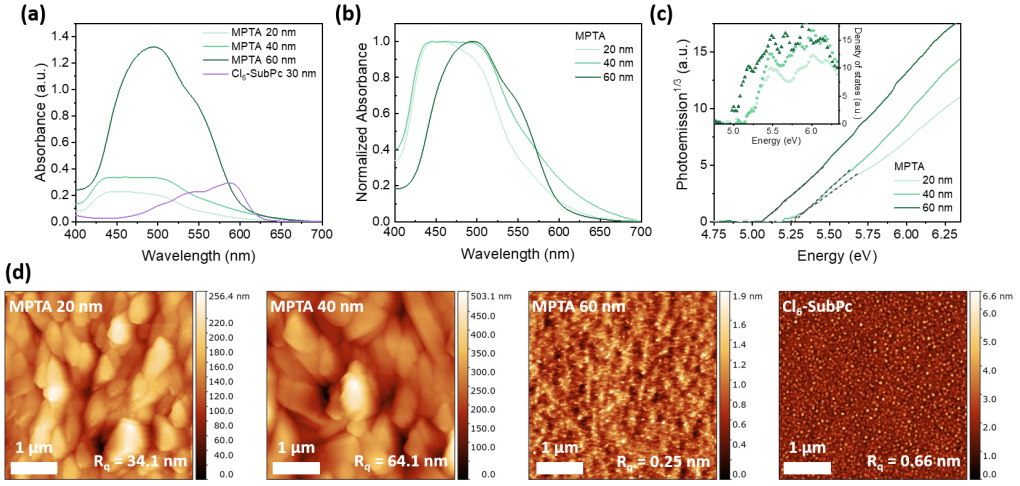


Fig. 7.4: Thickness-dependent optoelectronics and morphology of neat MPTA and Cl_6-SubPc films. (a) Absolute absorbance of neat MPTA films of different thicknesses and Cl_6-SubPc. (b) Normalised absorbance of MPTA films of different thicknesses. (c) Photoemission spectra measured by APS for MPTA films of different thicknesses, with corresponding density of states shown as inset. (d) AFM maps of neat MPTA and Cl_6-SubPc films, with root mean square roughness indicated as inset.

Further understanding of this mechanism can be gathered by absorption analysis of neat MPTA films with increasing thickness (namely, 20, 40, and 60 nm, as in BHJ). Figure 7.4a,b shows the increasing absorbance for thicker MPTA, which becomes dramatic at 60 nm. This is accompanied by continuous spectral red shift and enhancement of the low-energy shoulder. At the same time, MPTA energetics

(Figure 7.4c) become shallower with thickness, passing from -5.25 eV (20 nm) to -5.10 eV (60 nm), with higher density of states. All these characteristics can be attributed to a more systematic orientation (*i.e.*, face-on) of MPTA molecules at large thickness, for enhanced packing order in the film. The increased order is further confirmed by AFM topography images (Figure 7.4d), showing a striking smoothing of MPTA morphology at 60 nm, with roughness < 1 nm. At this thickness, it is likely that the influence of the substrate drops, so that film growth becomes homogeneous, whereas for thin films the morphology is dominated by macroscopic grain clusters. Moreover, PL of neat MPTA also changes with thickness, as shown in Figure 7.5. Here, the absolute PL intensity starts decreasing for thick films above 40 nm, with a clear spectral broadening. In neat MPTA, this broad PL centred at $\sim$ 730 nm has been assigned to excimeric species formed by substantial intermolecular interaction between neighbouring molecules (Chapter 5),[20] so that the further broadening of this emission supports increased packing control by thickness increase.

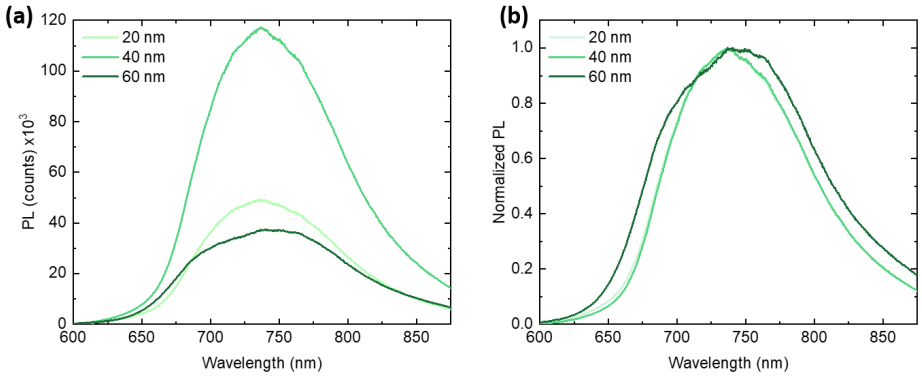


Fig. 7.5: Photoluminescence spectra of neat MPTA films of different thicknesses.

Overall, the results presented so far show how the strong intermolecular interactions in MPTA planar donor can be harnessed for controlling film morphology in BHJ, by using a simple tool like thickness optimisation. In particular, above a thickness of $\sim$ 50 nm, a highly intermixed BHJ structure appears (thanks to effective intercalation with Cl_6-SubPc acceptor), but MPTA-to-MPTA interactions are preserved for a systematic face-on orientation of donor molecules with increased structural order in the whole BHJ. This careful control of active layer architecture results in lower density of trap states for thicker blend films (see Figure 7.6), and it is key towards enhanced OPD performance, as will be discussed in the following.

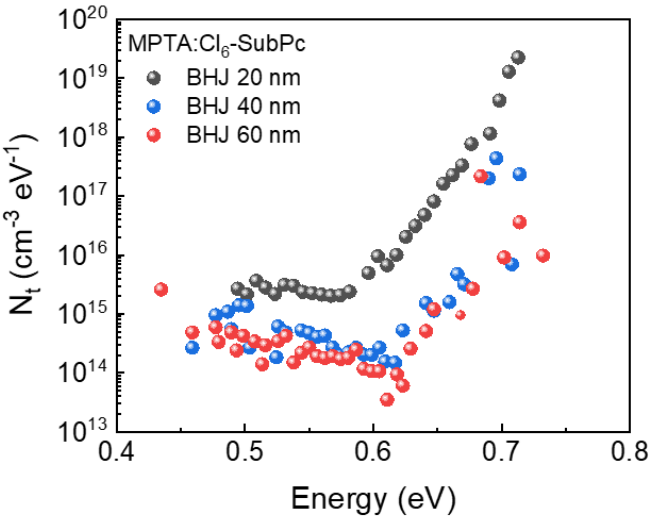


Fig. 7.6: Density of trap states for MPTA:Cl_6-SubPc BHJs of different thicknesses, quantified by charge extraction analysis.

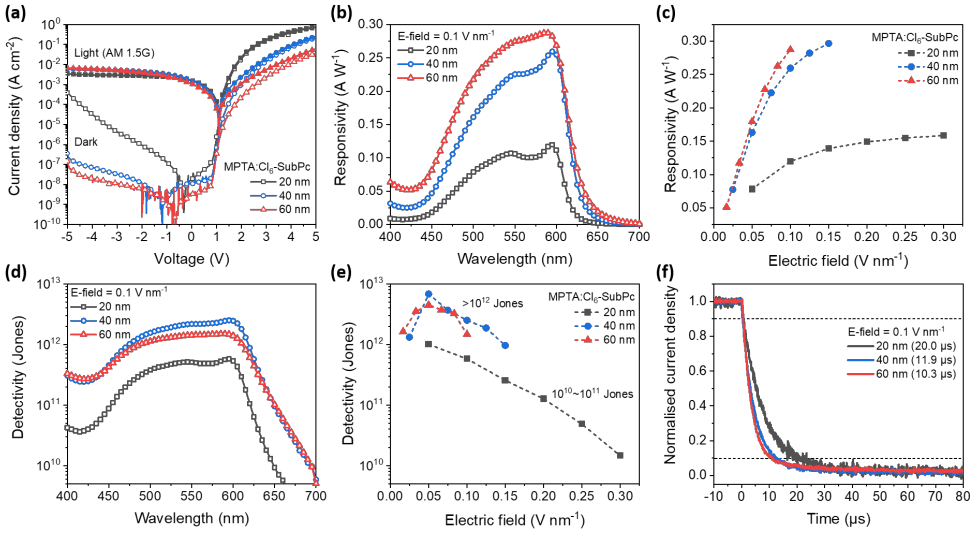


Fig. 7.7: Thickness-dependent OPD characterisation of MPTA:Cl_6-SubPc-based devices. (a) *J-V* characteristics measured under 1 Sun illumination and in dark. (b) OPD responsivity at the same electric field strength of 0.1 V nm^{-1}. (c) Responsivity evolution with electric field variation. (d) OPD detectivity at 0.1 V nm^{-1}. (e) Detectivity evolution with electric field variation. (f) Transient photocurrent dynamic at 0.1 V nm^{-1} for analysis of photoresponse speed (off-time).

7.2.2 Organic Photodetector Performance

To understand the impact of BHJ thickness control on OPD operations, devices are fabricated with ITO/MoO_3/BHJ/Al structure by sequential thermal evaporation of different layers. Their figures of merit are summarised in Figure 7.7. *J-V* characteristics show that the photocurrent density generated under 1 Sun illumination increases with active layer thickness in the photodetection regime (*i.e.*, under

negative voltage), while J_d decreases (Figure 7.7a), in line with what previously reported in literature.[63,338,425]

For a 60 nm thick active layer, J_d reaches a very low value of $\sim 10^{-8}$ A cm^{-2} at a moderate bias around -3 V, comparable with state-of-the-art BHJ devices.[14] At the same time, increased thickness is beneficial for R and EQE, approaching a R of 0.30 A W^{-1} at 60 nm for equal electric field conditions (namely, 0.1 V nm^{-1}, see Figure 7.7b). Although the R measured in short-circuit conditions is inferior for thick devices, as usually observed due to increased carrier recombination and more problematic charge collection/extraction,[218,379] this is steadily enhanced under reverse bias, and comparably more effectively for higher BHJ thickness (see the steeper R increase with electric field in Figure 7.7c, with corresponding EQE in Figure 7.8a-c). This occurs with homogenous contribution from both blend components and no changes in the spectral response shape (see normalised EQE in Figure 7.8d-f), indicating overall improvement in charge generation, transport, and/or collection for thicker devices under reverse bias, as discussed more extensively below. From the combination of J-V and R analyses, D^* can be calculated as Equation 2.12, considering the shot noise as the dominant source of J_d (see Subsection 2.2.2). As shown in Figure 7.7d, the trade-off between reduced J_d and increased R results in the highest D^* at 40 nm approaching 10^{13} Jones (at 0.05 V nm^{-1}), with 60 nm thick devices only slightly inferior. The J_d increase under reverse voltage results in a decreasing trend for D^* above $\sim$ 0.05 V nm^{-1} (Figure 7.7e). However, this negative bias impact is only significant for the 20 nm BHJ, where excessive leakage current can be attributed to shunting of the thin active layer, resulting in D^* dropping from $\sim 10^{12}$ Jones at reverse bias close to 0 V to $\sim 10^{10}$ Jones at -5 V. On the contrary, D^* is more robust for thicker devices, stable above 10^{12} Jones for the whole electric field range.

Thicker devices also show superior performances in terms of photodetection speed. In Figure 7.7f, this is calculated as τ_{fall} from 90% to 10% of the maximum transient photocurrent (TPC) extracted under green LED. At equal electric field conditions, τ_{fall} appears significantly shorter for thick OPDs, with almost two-fold faster speed for the 60 nm device (τ_{fall} = 10.3 µs) compared to the 20 nm one (τ_{fall} = 20.0 µs). Note that the τ_{RC} decay time constant due to the circuit/device resistance R and capacitance C should not be the limiting factor here, since the 40 and 60 nm thick devices show a very similar τ_{fall} despite the different thicknesses and C. Therefore, it is clear how the thickness increase with optimisation of BHJ structure is crucial to achieve excellent OPD performances, including not only suppressed J_d and enhanced R, but also fast photoresponse time.

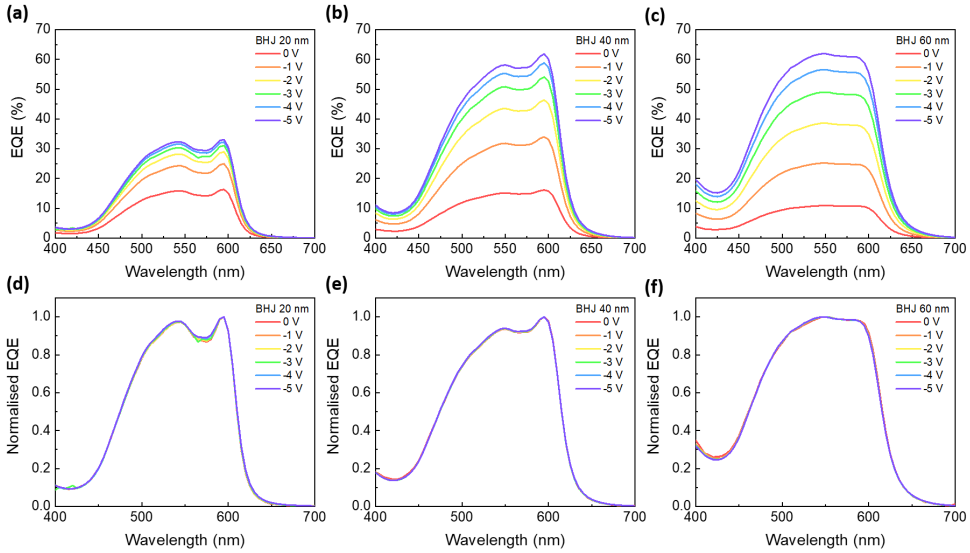


Fig. 7.8: (a)-(c) Absolute and (d)-(f) normalised bias-dependent EQE spectra of MPTA:Cl_6-SubPc BHJ devices with different active layer thicknesses.

7.2.3 Exploring the Origin of Device Performance

To understand the origin of OPD performance upon active layer engineering in terms of molecular physics, in-depth PL characterisation in operating devices under electric field is carried out (Figure 7.9). As shown in Figure 7.9a, the PL emission in BHJ films occurs in the 650-850 nm range, with significantly lower intensity compared to neat MPTA and Cl_6-SubPc, evidence of effective exciton dissociation in intermixed MPTA:Cl_6-SubPc blends. The PL spectral shape is analysed in detail in Figure 7.9b, where three main emission peaks can be distinguished at 620, 685, and 730 nm, respectively. By the spectral overlap with the neat Cl_6-SubPc emission and the short lifetime revealed by transient PL, the 620 nm emission is assigned to acceptor excitons decay (Figure 7.9c). This high-energy PL is strongly quenched in the 60 nm BHJ, supporting the highly intermixed nature of thick active layers with suppressed Cl_6-SubPc aggregation.

However, the attribution of low energy PL peaks (685 and 730 nm) is more ambiguous, since both CT state emission expected from the blend energetics (see later sections) and neat MPTA excimeric emission (Chapter 5) would both occur in the same spectral range (*i.e.*, $\sim$ 730 nm). In this case, the increase in absolute PL intensity with blend thickness (Figure 7.9a) and the long PL decay for the 685 and 730 nm emissions (lifetimes $\tau \sim 2$ ns) support the assignment of dominant BHJ emission to CT states. Here, it is interesting to notice the distinct transient characteristics compared to neat MPTA emissive species, where a longer monoexponential PL decay was observed ($\tau \sim 5$ ns), assigned to MPTA excimeric species,

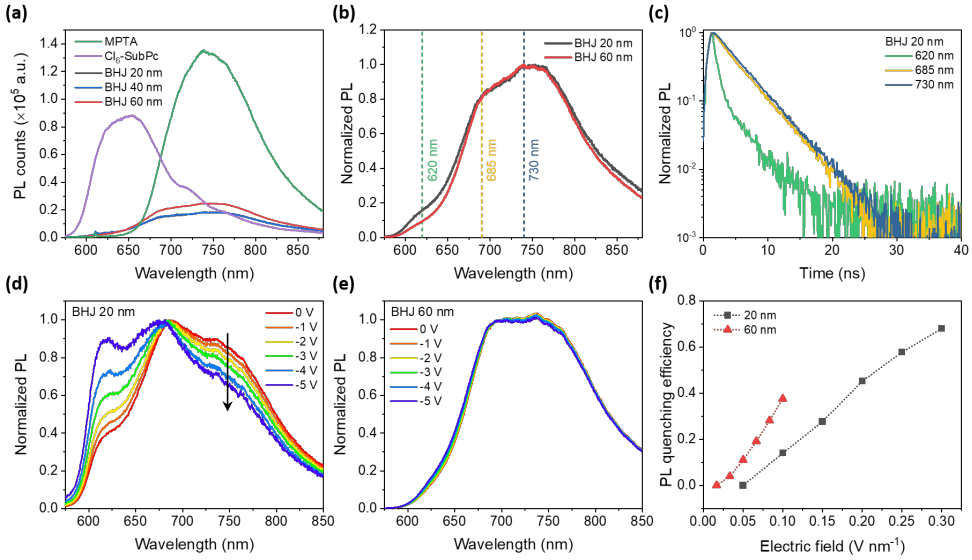


Fig. 7.9: Photoluminescence emission analysis in MPTA:Cl_6-SubPc BHJ. (a) Absolute PL intensity for neat MPTA (10 nm) and Cl_6-SubPc (30 nm) films, as well as MPTA:Cl_6-SubPc blends of different thickness. (b) Comparison of normalised PL in thin (20 nm) and thick (60 nm) BHJs, with indicated the main emission wavelengths. (c) Time-resolved PL decay for MPTA:Cl_6-SubPc films (20 nm) upon 405 nm laser excitation, probed at different wavelengths corresponding to the main PL peaks identified in (b). Decay lifetimes are extracted by double-exponential fit at 620 nm as $\tau_1 = 0.69 \pm 0.04$ ns and $\tau_2 = 5.70 \pm 0.04$ ns, and by stretched monoexponential fit at 685 nm ($\tau = 1.78 \pm 0.01$ ns) and 730 nm ($\tau = 2.29 \pm 0.01$ ns). Bias-dependent normalised PL for (d) 20 nm and (e) 60 nm devices. Selective quenching of low-energy emission is highlighted in (d). (f) PL quenching efficiency upon increasing reverse bias for 20 nm and 60 nm OPD devices, integrated over the whole spectral range.

as discussed in Chapter 5. In the results presented there, bright CT states formed at D/A interfaces are demonstrated in MPTA blends with C_{60},[20] and it is expected that a highly intermixed MPTA:Cl_6-SubPc BHJ (*i.e.*, 60 nm) with even larger interfacial area would enhance PL yield from these CT species. Regardless of the precise assignment of the emissive states in PL spectra, it is worth underlining that both 685 and 730 nm peaks are related to weakly-bound, delocalised electronic species with a largely intermolecular nature.

Further insight into the nature of the different emissive species can be gathered by the analysis of PL evolution under electric field, with bias-dependent measurements in full operational devices. In Figure 7.9d,e, normalised PL spectra upon increasing reverse bias are compared for thin (20 nm) and thick (60 nm) OPDs, while absolute PL can be seen in Figure 7.10. Here, dramatic differences in PL evolution are apparent in the two cases. In fact, the thin BHJ shows a selective bias-induced quenching of low-energy PL (> 700 nm), while in the high-energy re-

gion (600-625 nm) a relative increase occurs (*i.e.*, very limited quenching in the absolute PL). This further supports the assignment of the two different emissive species to Cl_6-SubPc excitons (high-energy, 620 nm) and interfacial CT states (low-energy, 730 nm), where the latter can be effectively separated under electric field. On the other hand, the PL of the thick BHJ predominantly comes from CT states, so that it can be homogeneously quenched over the whole spectral range.

From these data, the PL quenching efficiency (PLQE) can be calculated as PLQE = $(PL_{V=0}\text{-}PL_V)/PL_{V=0}$, where $PL_{V=0}$ and PL_V are respectively the PL at zero bias and at the applied reverse bias V, integrated over the whole spectral range. In Figure 7.9f, it can be seen that PLQE increases more effectively for thick devices for comparable electric field strength, since the BHJ structure control enables high yield of quenchable CT states. Therefore, it is clear how the highly intermixed morphology with a higher ratio of D/A interfacial area in thick BHJs is crucial to achieve efficient charge separation assisted by electric field in operational OPDs. In this way, the performance enhancement by thickness optimisation can be mostly attributed to improved separation of CT states.

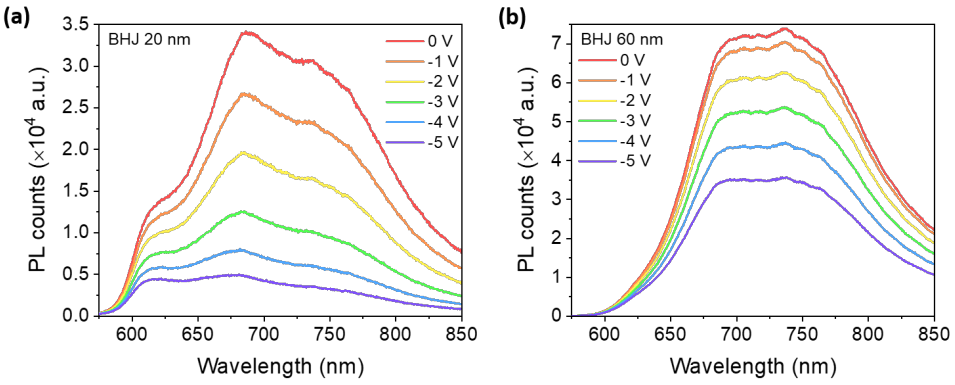


Fig. 7.10: Absolute bias-dependent PL spectra of (a) thin (20 nm) and (b) thick (60 nm) MPTA:Cl_6-SubPc BHJ devices.

7.2.4 Photophysics in Fullerene *versus* Nonfullerene-Based OPDs

So far, the importance of active layer engineering in NFA-based OPDs has been demonstrated, with optimum BHJ morphology and enhanced device performance achieved for $>$ 50 nm thicknesses. A comparative analysis of optoelectronic properties and device photophysics of MPTA:Cl_6-SubPc and MPTA:C_{60} systems is now shown, to investigate the potential for fullerene substitution in evaporated OPD devices.

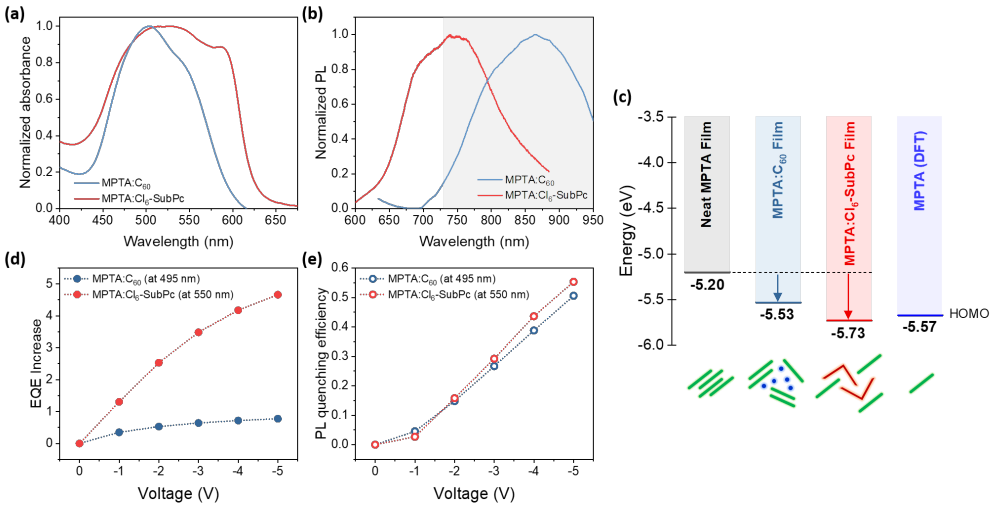


Fig. 7.11: Comparison of photophysics in MPTA:Cl_6-SubPc and MPTA:C_{60} BHJ systems. Normalised (a) absorbance and (b) PL spectra for MPTA:Cl_6-SubPc and MPTA:C_{60} films. (c) Schematic of energy levels for MPTA:Cl_6-SubPc and MPTA:C_{60} blends, compared to neat MPTA and its DFT predictions. The cartoons illustrate molecular packing in different cases. Bias-dependent (d) EQE increase and (e) PL quenching efficiency for MPTA:C_{60} and MPTA:Cl_6-SubPc-based devices.

Firstly, Figure 7.11 presents a comparison of optoelectronic properties for the two blends. While the absorption spectrum of MPTA:Cl_6-SubPc (Figure 7.11a) extends from *circa* 450 nm to 625 nm, including the NFA region at long wavelengths, MPTA:C_{60} blend has a narrower spectrum in the visible (*i.e.*, 450-575 nm), due to C_{60} weak absorption in this range. This can be a potential advantage for broadband photodetection using NFA-based systems, with ample room for colour selection and full-spectrum response by the facile bandgap tunability of NFAs - particularly for the SubPc family.[419,427]

Considering the energetics of the two blends (summarised in Figure 7.12), the different PL spectra (Figure 7.11b) can be understood, with CT emission located at much lower wavelengths for Cl_6-SubPc-based BHJ (namely, at $\sim$ 730 nm *versus* $>$ 850 nm for MPTA:C_{60}). Moreover, the HOMO deepening upon MPTA blending with the two acceptors (Figure 7.11c) is significantly stronger for Cl_6-SubPc, which informs on the degree of BHJ intermixing. In fact, the neat MPTA HOMO is located at around -5.2 eV, as measured by APS in Figure 7.1d. This is almost 500 meV shallower than what predicted by DFT in single-molecule gas-phase simulations, and it is attributed to the aggregation effect in strongly interacting MPTA molecules. Upon blending, most aggregation is disrupted, and MPTA HOMO in BHJ deepens towards intrinsic MPTA energetics. Here, the HOMO level of MPTA:Cl_6-SubPc blends closely matches the DFT single-molecule results (*i.e.*, -5.73 eV), whereas it is

much shallower for MPTA:C_{60} BHJs (*i.e.*, -5.53 eV). This indicates a virtually complete nanoscale intermixing in MPTA:Cl_6-SubPc blend systems, while some residual aggregation is maintained for C_{60} counterparts, consistently with the slightly broader absorbance in the MPTA region in Cl_6-SubPc blends (Figure 7.11a). Since incomplete C_{60} intercalation and persisting MPTA nanoaggregation in blend has been identified in Chapter 5 as a source of deep-trap states for fullerene-based OPDs, the BHJ morphology of NFA systems is highly promising for trap-free devices, with the impact on photodetector performance illustrated in the following.

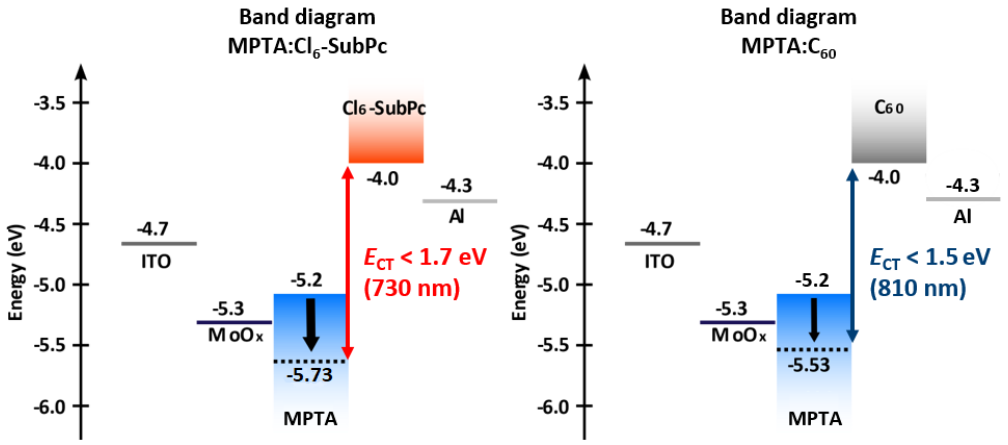


Fig. 7.12: Schematics of the energy diagram in the MPTA:Cl_6-SubPc and MPTA:C_{60} devices, with the energy of the interfacial CT states indicated from the difference between MPTA HOMO and acceptor LUMO.

To further confirm the BHJ structure in C_{60} and Cl_6-SubPc blend systems, in-depth understanding of photophysical processes is provided by ultrafast TAS, studying the changes in absorbance after selective photoexcitation of MPTA at 500 nm. As presented in Figure 7.13a,b, ultrafast electron transfer within instrument response (200 fs) is observed for both C_{60} and Cl_6-SubPc acceptors. However, clear differences between the two systems emerge from the analysis of recombination dynamics by fluence-dependent TAS (Figure 7.13c-e). While both BHJs show evidence of geminate CT recombination at moderate pump fluence (fluence-independent dynamics), the overall kinetics is faster for MPTA:Cl_6-SubPc, indicating accelerated recombination. This is consistent with the larger D/A interfacial area in NFA-based systems, and further supports the more intermixed nature of its BHJ morphology. Here, it is important to note that such a highly intermixed morphology may be detrimental for photovoltaic operations due to increased recombination rate at null electric field as in TAS measurements. However, under reverse bias this allows for higher yield of interfacial CT states, which can be effectively separated and extracted as in OPD devices.

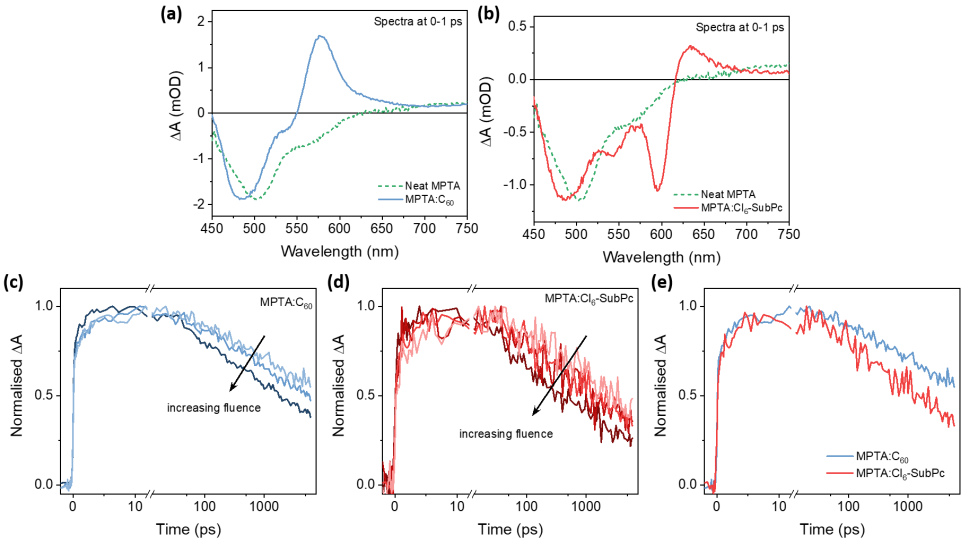


Fig. 7.13: TAS spectra for (a) MPTA:C_{60} and (b) MPTA:Cl_6-SubPc BHJs, compared with results of neat MPTA. Fluence-dependent TAS kinetics for (c) MPTA:C_{60} and (d) MPTA:Cl_6-SubPc BHJs, with comparison at the lowest fluence shown in (e).

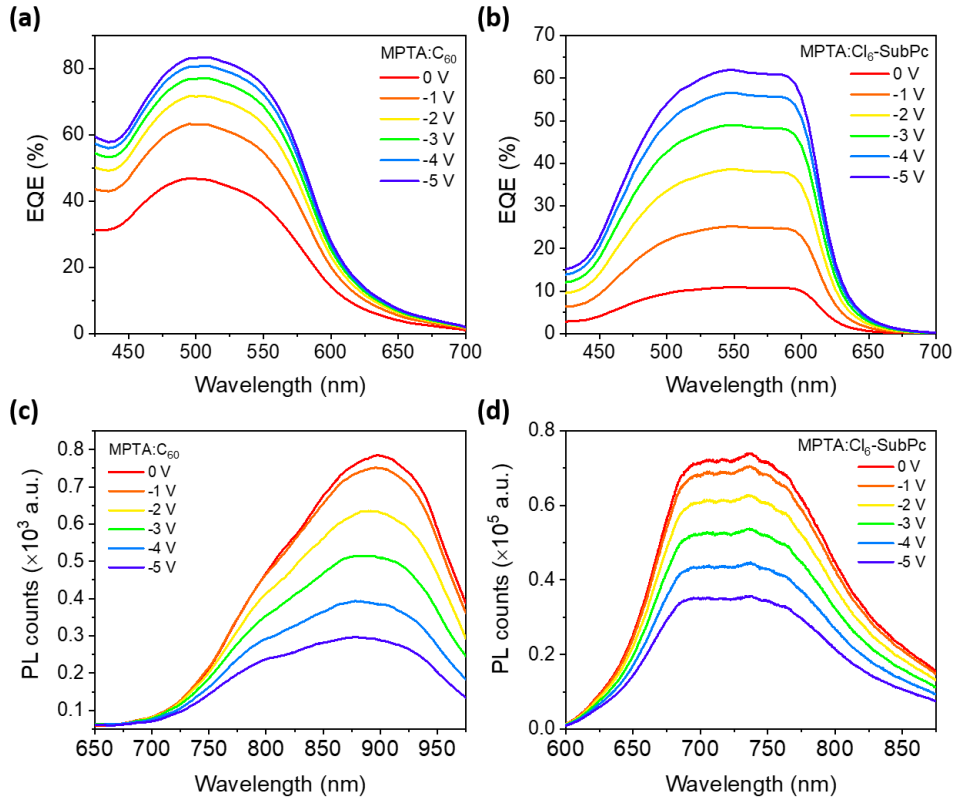


Fig. 7.14: Bias-dependent (a,b) EQE and (c,d) absolute PL for MPTA:C_{60} and MPTA:Cl_6-SubPc-based devices.

Moving to the analysis of OPD photophysics under electric field, MPTA:C_{60} and MPTA:Cl_6-SubPc-based devices of equal active layer thickness (60 nm) are anal-

ysed in their EQE and PL evolution upon increasing reverse bias. Figure 7.14a,b show relatively high EQE for C_{60}-based devices, starting from $\sim$ 40% at 0 V and overcoming 80% at -5 V, which may be due to the slightly different energy alignment in the device. However, only limited increase rate is achieved in this system, compared with the impressive EQE enhancement in MPTA:Cl_6-SubPc, with a five-fold increase from 0 to -5 V (summarised in Figure 7.11d). This can benefit from the higher yield of quenchable interfacial CT states in the highly intermixed MPTA:Cl_6-SubPc BHJs, giving a PL intensity almost 100 times higher than for the MPTA:C_{60} counterpart (see 0 V spectra in Figure 7.14c,d). However, the phenomenon cannot be fully understood by increased CT state dissociation, since bias-dependent PLQE exhibits the same trend for the two systems (Figure 7.11e). Thus, the study moves to further device characterisation to investigate the role of charge transport and extraction in the photodetection performance of NFA- and fullerene-based OPDs.

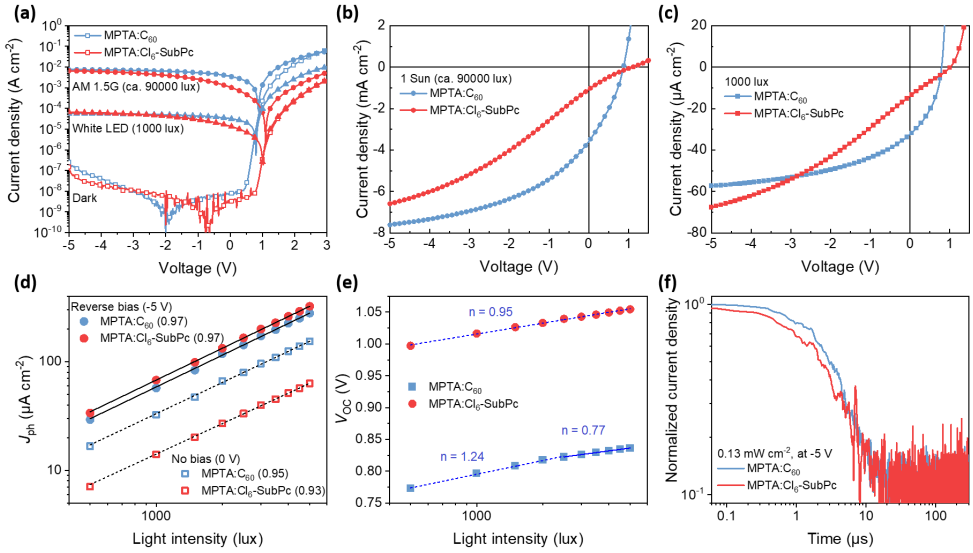


Fig. 7.15: Comparison of trap state impact on device performance in MPTA:C_{60} and MPTA:Cl_6-SubPc OPDs. (a) *J-V* characteristics of MPTA:C_{60} and MPTA:Cl_6-SubPc devices in dark and under AM1.5 G or 1000 lux illumination. Enlarged view of *J-V* characteristics in linear scale, for (b) AM1.5 G and (c) 1000 lux conditions. (d) Photocurrent density *vs.* light intensity analysis at 0 V (open symbol) and under reverse bias at -5 V (solid symbol). (e) Open-circuit voltage *vs.* light intensity analysis, with indicated the respective *n* values. (f) Transient photocurrent decay under reverse bias at low light intensity.

As shown in the *J-V* characteristics in Figure 7.15a-c, the photocurrent generation at high light intensity (1 Sun) is superior for MPTA:C_{60} devices, in line with the higher EQE. However, at low light (1000 lux, white LED) the situation is different, with higher photocurrent for the NFA-based devices from $<$ -3 V. Moreover, MPTA:Cl_6-SubPc OPDs show lower J_d values, approaching 10^{-8} A cm^{-2} below -3

V.

To understand the impact of charge recombination on photocurrent generation, photocurrent density J_{ph} and open-circuit voltage V_{OC} are analysed as a function of light intensity I. J_{ph} is known to follow a power-law dependence on I, $J_{ph} \propto I^{\alpha}$, with $\alpha = 1$ for ideal monomolecular recombination and $\alpha < 1$ indicating bimolecular processes.[238] From Figure 7.15d, it is clear that the influence of bimolecular recombination is minor in both systems, with $\alpha = 0.93$ for MPTA:Cl_6-SubPc and $\alpha = 0.95$ for MPTA:C_{60} devices in short-circuit conditions, becoming fully negligible under reverse bias ($\alpha = 0.97$ in both cases). On the contrary, significant differences are observed for the V_{OC} analysis, shown in Figure 7.15e. The trend of V_{OC} *vs.* I in a semi-logarithmic plot is expected to follow a linear relationship with slope nk_BT/e, with k_B, T, and e being respectively the Boltzmann constant, the temperature, and the elementary charge. For $n = 1$, electron-hole pairs only recombine bimolecularly, approaching $n = 2$ if trap-assisted recombination also contributes.[36,238] Here, n is close to unity for MPTA:Cl_6-SubPc (*i.e.*, absent trap-assisted recombination), while trap-induced losses are present for MPTA:C_{60} devices at low light intensity ($n = 1.24$ for $I < 2500$ lux).

Therefore, NFA-based OPDs show clear advantages in suppressing trap-assisted recombination, as further supported by the significantly lower density of trap states for MPTA:Cl_6-SubPc compared to MPTA:C_{60} devices identified by charge extraction analysis (Figure 7.16). Note that $n = 0.77$ for $I > 2500$ lux in MPTA:C_{60} devices might originate from significant surface recombination,[428–430] whereas this is not observed in MPTA:Cl_6-SubPc devices. In this context, it is interesting to observe that TAS and light-intensity-dependent J-V analyses are complementary to inform on the different recombination mechanisms. In fact, geminate processes can be easily distinguished under TAS laser illumination, while V_{OC} analysis allows to access trap-mediated processes occurring under low light.

Finally, a comparison of device photoresponse speed is shown in Figure 7.15f, with TPC measured at low light intensity under reverse bias, where a faster photocurrent decay is observed for the Cl_6-SubPc-based OPD. Moreover, although under electric field (-5 V) the impact of deep traps is reduced, a change in slope occurs for the MPTA:C_{60} device TPC after 5 µs, while photocurrent decay is monophasic for MPTA:Cl_6-SubPc. Again, this confirms the effective suppression of deep trap states by C_{60} substitution in MPTA-based OPDs.

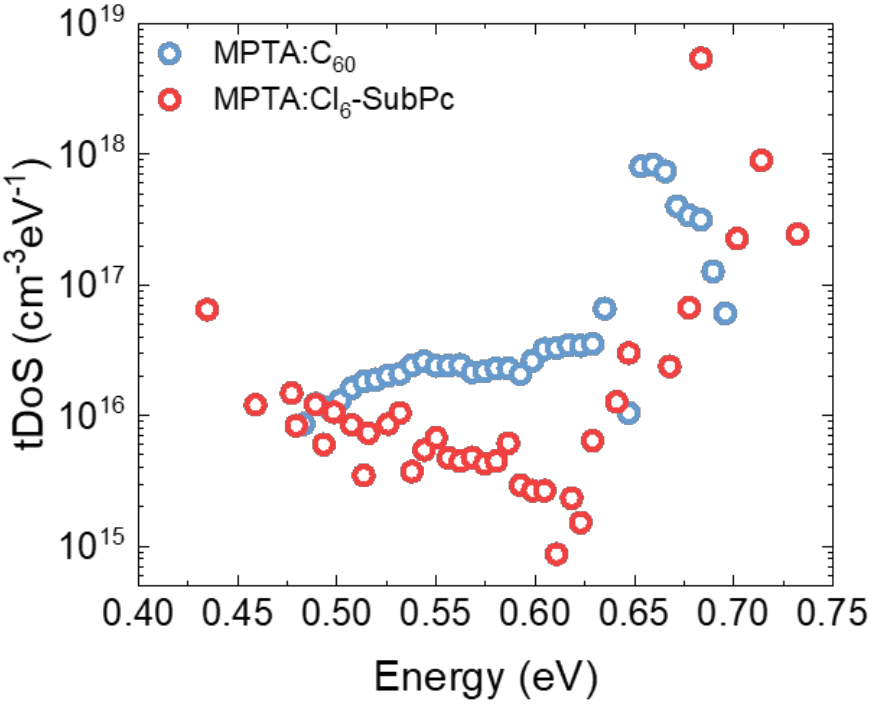


Fig. 7.16: Density of trap states for MPTA:C_{60} and MPTA:Cl_6-SubPc devices (60 nm), quantified by charge extraction analysis.

7.3 Conclusion

The results shown in this chapter elucidate the potential advantage of NFA small molecules to substitute fullerenes in evaporated OPDs. In particular, this can overcome the sub-optimal device performance for MPTA:C_{60} under low light intensity due to charge trapping in deep states. In Chapter 5, these have been attributed to the residual presence of MPTA nanoaggregation in incompletely intermixed BHJ morphology and to the creation of MPTA-C_{60} adducts by chemical reactions in blend. Here, the choice of Cl_6-SubPc is highly beneficial to suppress both pathways for trap formation.

Firstly, the addition reaction between the MPTA amine lone pair and the π-conjugated carbons in fullerene[367,368] is readily prevented using Cl_6-SubPc. Secondly, the SubPc NFA presented here, with larger dimensions and more complex 3D geometry (*i.e.*, cone-shaped) compared to C_{60}, is more prone to disturb the MPTA packing network, for effective intermixing with virtually no nanoscale domains. As explained above, this is fully achieved in MPTA:Cl_6-SubPc BHJs with thicknesses above 50 nm. Therefore, thickness engineering does not simply increase the active layer dimension as a common strategy to limit J_d, but also controls the BHJ

structure by harnessing the strong intermolecular interactions in MPTA. Namely, we suggest that a finely intermixed D/A network and systematic face-on MPTA orientation are achieved for thick active layers, with positive effects on OPD performance - as seen in the lower J_d, higher R, and faster photoresponse speed. In particular, the advantages of a thick active layer are related to a predominant presence of emissive CT states at high D/A interfacial area, identified by PL analysis, which can be effectively separated and harvested under electric field. The specific characteristics of the planar small-molecule donor (here, MPTA), prone to strong intermolecular interactions and packing ordering, combined with an effective disruption of its aggregation for intimately intermixed BHJs (here, achieved by bulky Cl_6-SubPc acceptor) are thus key to the superior performances of NFA-based evaporated BHJ OPDs. Especially, this prevents the formation of deep-trap states and enables excellent photodetection performance even at low light intensity, as observed by charge extraction, J-V, and TPC measurements.

In conclusion, this chapter investigates the role of active layer morphology and materials selection for state-of-the-art evaporated OPDs. By demonstrating the importance of the active layer thickness to control BHJ morphology and by systematic comparison of NFAs with fullerene counterparts, these results provide relevant guidelines not only for choice of appropriate candidate molecules, but also for optimum active layer structure. This paves the way to extensive utilisation of NFA alternatives in evaporated OPDs for trap-free photodetection, suggesting that the advantages of fullerene substitution in terms of BHJ morphology can be further confirmed for other NFA families.

7.4 Experimental Section

Fabrication of Devices and Thin Films

All materials are purified *via* sublimation under high vacuum ($<10^{-6}$ Torr) prior to use. Thin films are fabricated by thermal evaporation under high vacuum ($<10^{-7}$ Torr, 0.35 Å/s rate) on ITO or quartz substrates cleaned with isopropyl alcohol and acetone in an ultrasonic bath. OPDs are fabricated on ITO-coated glass by sequential deposition of hole-extraction layer (MoO_3, 30 nm), donor:C_{60} BHJ with variable thickness (1:1 weight ratio), and Al electrode (100 nm), with device encapsulation by glass (98.5% transmittance). Active pixel area is 0.04 cm^2. Electrical characterisation of devices by J-V scan and EQE analysis is carried out as described in Section 3.8.

Energetic and Morphological Characterisation

HOMO energy levels of materials are measured on grounded ITO substrates using the procedure detailed in Section 3.3. DOS is calculated as first derivative of the photoemission cube root by in-house software analysis. Surface topography is measured by a Park NX10 AFM as described in Section 3.6.

Steady-State Optical and Structural Characterisation

PL is measured by a Renishaw inVia Raman microscope on thin films (details in Section 3.2). Measurements are also carried out on encapsulated devices applying reverse bias to the electrodes by an Agilent power source. Optical absorbance is measured as described in Section 3.4. All details on GI-XRD are reported in Section 3.9.

Device Electrical Characterisation

J-V characteristics are measured with a Keithley 2400 source calibrated at 1 Sun (Section 3.8), using neutral-density filters for light-intensity dependent measurements. An LED light source calibrated by digital Luxmeter is used for low-light *J-V* analysis. Bias-dependent EQE is collected as detailed in Section 3.8.

Transient Optoelectronic Measurements

Transient absorption spectroscopy, transient photovoltage, and charge extraction are carried out as described in Subsection 3.9.1 and Subsection 3.9.2. TCSPC is measured as illustrated in Section 3.5, exciting the samples by a 405 nm laser. For transient photocurrent analysis, the devices are illuminated by a green LED (523 nm) with tunable intensity, with further details in Section 3.8.

Computational Methods

DFT simulations at the B3LYP level with 6-311G(d,p) basis set are performed as described in Section 3.7.

8 | Conclusion and Further Work

8.1 Conclusion

The work presented in this thesis analyses the role of molecular design of organic semiconductors and active layer engineering in optimising photon-to-electron conversion processes in organic electronic devices. By a combination of optoelectronic, structural, and device *in-operando* characterisation, several strategies for increasing OPV/OPD efficiency and stability are taken into consideration, studying both solution-processed and vacuum-evaporated systems.

In Chapter 4, the effect of NFA chemical design on OPV operational stability is investigated, combining core and end-group engineering. By a comparative study of novel ITIC derivatives with core selenation and end-group methylation used in solution-processed OPVs, relevant guidelines for extending device lifetimes are identified. In particular, the importance of NFA backbone rigidification and charge distribution fine-tuning along the molecule is highlighted. These factors allow to establish effective intermolecular interactions in the BHJ systems, where mechanisms of chemical and morphological degradation under light can be successfully minimised. In particular, the combination of outer-core selenation and end-group methylation appears as the optimum molecular design to extend OPV lifetime, showing over 95% of initial PCE maintained after ~450 hours of 1 Sun operation.

In addition to chemical design, the complementary role of structural control in organic small molecules is analysed in Chapter 5, comparing OPD photophysics for a twisted (NP-SA) and a planar (MPTA) donor used in co-evaporated BHJs with C_{60}. Here, the molecular geometry has a strong impact on light-intensity-dependent photoresponse speed, with the planar MPTA being faster in high-light conditions, but showing a slow, biphasic photoresponse under low-light. By detailed analysis of materials optoelectronics and morphology, a superior band-edge energetic order is found for MPTA, with minimal presence of shallow traps and superior transport properties in high-light. However, the strong intermolecular interactions between the

planar molecules result into nanoaggregation in the BHJ and potential formation of MPTA-C_{60} adducts. These species are identified as origin of deep-trap states, whose incomplete filling in low-light limits photoresponse in MPTA devices. Overall, these findings pinpoint several mechanisms involved in trap formation in state-of-the-art OPD materials. Moreover, the results show that suitable OPD small-molecule candidates need to be selected depending on light-intensity operating conditions of target applications.

Moving to the role of device active layer engineering, Chapter 6 examines the influence of D:A blend ratio in solution-processed BHJ OPDs. Focusing on highly-diluted Y6 systems in PM6, the study shows great enhancement of OPD performance at high polymer load, with dramatic dark-current suppression, faster photoresponse speed, and bias-dependent EQE increase. By analysis of electric-field dependent photophysics, it is found that minimal amount of NFA is already effective for the formation of interfacial CT states, which can be easily separated under mild reverse bias for photocurrent generation. At the same time, the dominant polymer matrix can drive efficient and fast charge transport in well-interconnected percolation pathways, and the shallow PM6 energetics in diluted BHJs can suppress dark injection and minimise dark current. Overall, a simple tool as blend ratio control is proposed for effective optimisation of photoconversion mechanisms in D-A blends towards high-performance OPDs.

Finally, in Chapter 7 the role of thickness control in vacuum-deposited BHJ active layers is investigated. In fullerene-free OPDs (MPTA:Cl_6-SubPc), it is shown that the strong intermolecular interactions between planar MPTA molecules (Chapter 5) can be harnessed for thickness-dependent morphology control. In particular, above a 50 nm thickness the BHJ is optimised, with systematic MPTA face-on orientation and effective intercalation of Cl_6-SubPc. This allows to suppress deep-trap formation routes identified in Chapter 5, with a highly intermixed BHJ morphology (absence of nanoaggregation) and D-A adduct creation prevented by the bulky NFA molecules. Therefore, superior OPD performances are observed for thicker devices, including fast photoresponse, minimised dark current, and strong field-dependent EQE enhancement, which cannot be solely attributed to the change in applied electric field at different thicknesses. These results are highly promising in demonstrating the potential of NFA-based BHJ in high-efficiency evaporated OPDs, and demonstrate the importance of thickness control in tuning active layer ordering *via* intermolecular interactions.

8.2 Further Work

Overall, this thesis has demonstrated that both molecular engineering of acceptor and donor small molecules and active-layer engineering are powerful tools to control the physics of photon-to-electron conversion processes in OSC-based systems towards high-efficient and stable organic electronics (OPVs, OPDs).

From Chapter 4, regio-selective selenation of NFAs appears highly promising to extend OPV lifetimes. At this regard, other selenium-substituted materials are worth investigating beyond ITIC family. For example, recent reports of selenated Y6 derivatives[306] also show encouraging results in terms of OPV stability, and a variety of novel molecules with different side chains and end groups could be systematically studied. Moreover, the synergistic role of the polymer donor in influencing photo-induced degradation mechanisms[431] should be addressed, to find the optimum molecular design to combine with selenated NFAs.

Since molecular conformation is also a crucial factor determining OSC photophysics (Chapter 5), other small molecules with characteristic structures can be studied in evaporated systems (*e.g.*, star-shaped, fully-fused PDIs...) to verify whether a universal relation between molecular geometry and trap-state formation can be identified. Potentially, this study can be extended to solution-processed BHJ devices, where other parameters such as solvent choice, film drying kinetics, and D:A miscibility can come into play.

Further work to understand the role of D:A blending ratio would also be highly relevant. Moving from the results in Chapter 6, the effect of acceptor dilution could to be investigated in several NFA- or fullerene-based blends to generalise a photophysical model for charge generation, dissociation, and transport depending on D:A ratio. In particular, an interesting question is about the influence of mixing on the energetics of BHJ components, which further characterisation would help answer, including space-resolved APS or energetics depth profiles to disentangle D and A energy levels.

Finally, as the potential of fullerene-free vacuum-processed BHJs have been demonstrated (as for OPDs in Chapter 7), more understanding of morphology and trap formation for other NFA choices would be beneficial to further boost device performance. Here, coupling the same MPTA donor with alternative SubPc derivatives could solve some of the limitations compared to C_{60}-based OPDs (lower EQE, S-shaped J-V characteristics). For example, the different energetics and quadrupole moments across the SubPC series with various end groups could strongly affect

charge transfer and extraction in BHJs, active layer ordering and packing, and overall device figures of merit.

9 | List of Publications

- C. Labanti, Y. Dong, S.Y. Park, Y.-C. Chin, J. Luke, J.R. Durrant, J.-S. Kim. *Nonfullerene Acceptor Dilution as a Facile Strategy for Device Optimization towards High-Efficiency Solution-Processed Bulk Heterojunction Organic Photodetectors*, in Draft
- C. Labanti, S.Y. Park, A. Rana, Y. Dong, S. Yun, F. Fang, J.I. Park, J. Shin, K.-B. Park, J.R. Durrant, J.-S. Kim. *Efficient Nonfullerene-based Organic Photodetectors Enabled by Reduced Deep Traps with Highly Intermixed Evaporated Bulk Heterojunction Systems*, in Draft
- A. Rana*, C. Labanti*, S.Y. Park*, F. Fang*, S. Yun, Y. Dong, J.I. Park, J. Shin, K.-B. Park, J.-S. Kim, J.R. Durrant. *High Octupole Moment Driven Free Charge Generation in Partially Chlorinated Subphthalocyanine for Planar Heterojunction Organic Photodiodes*, in Draft
- J. Luke, E.J. Yang, C.Labanti, S.Y. Park, J.-S. Kim. *Key Molecular Structure Perspectives for Organic Photovoltaic Stability*, Accepted
- S.Y. Park*, C. Labanti*, T.H. Lee, R.A. Pacalaj, Y. Dong, Y.-C. Chin, J. Luke, G. Ryu, D. Minami, S. Yun, J.-I. Park, F. Fang, K.-B. Park, J.R. Durrant., J.-S. Kim *Solution-Processed Single-Component Organic Photodetectors - Strong Quadrupole Moments in Molecules Enable the State-of-the-Art Performance*, Preprint, DOI:https://doi.org/10.21203/rs.3.rs-2700964/v1, under Peer review
- Y. Wang, J. Luke, A. Privitera, N. Rolland, C. Labanti, G. Londi, V. Lemaur, D.T.W. Toolan, A.J. Sneyd, S. Jeong, D. Qian, Y. Olivier, L. Sorace, J.-S. Kim, D. Beljonne, Z. Li, A.J. Gillett. *The Critical Role of the Donor Polymer in the Stability of High-Performance Non-Fullerene Acceptor Organic Solar Cells*, Joule 2023, **7**, 810-829
- Y. Fu, T.H. Lee, Y.-C. Chin, R.A. Pacalaj, C. Labanti, S.Y. Park, Y. Dong, H.W. Cho, J.Y. Kim, D. Minami, J.R. Durrant, J.-S. Kim. *Molecular Orientation-*

Dependent Energetic Shifts in Solution-Processed Non-Fullerene Acceptors and Their Impact on Organic Photovoltaic Performance, Nat. Commun. 2023, **14**, 1870

- A.A. Mohapatra, M. Pranav, S. Yadav, C. Gangadharappa, J. Wu, C. Labanti, J. Wolansky, J. Benduhn, J.-S. Kim, J.R. Durrant, S. Patil. *Interface Engineering in Perylene Diimide-based Organic Photovoltaics with Enhanced Photovoltage*, ACS Appl. Mater. Interfaces 2023, **15**, 25224–25231
- C. Labanti, J. Wu, J. Shin, S. Limbu, S. Yun, F. Fang, S.Y. Park, C.-J. Heo, Y. Lim, T. Choi, H.-J. Kim, H. Hong, B. Choi, K.-B. Park, J. Durrant, J.-S. Kim. *Light-Intensity Dependent Photoresponse Time of Organic Photodetectors and Its Molecular Origin*, Nat. Commun. 2022, **13**, 3745
- J. Luke, E.J. Yang, Y.-C. Chin, Y. Che, L. Winkler, D. Whatling, *C. Labanti*, S.Y. Park, J.-S. Kim. *Strong Intermolecular Interactions Induced by High Quadrupole Moments Enable Excellent Photostability of Non-Fullerene Acceptors for Organic Photovoltaics*, Adv. Energy Mater. 2022, **12**, 2201267
- S.Y. Park, C. Labanti, J. Luke, Y.-C. Chin, J.-S. Kim. *Organic Bilayer Photovoltaics for Efficient Indoor Light Harvesting*, Adv. Energy Mater. 2021, **2103237**
- C. Labanti, M.J. Sun, J. Luke, S. Kwon, R. Kumar, J. Hong, J. Kim, A.A. Bakulin, S.-K. Kwon, Y.-H. Kim, J.-S. Kim. *Selenium-Substituted Non-Fullerene Acceptors: A Route to Superior Operational Stability for Organic Bulk Heterojunction Solar Cells*, ACS Nano 2021, **4**, 7700-7712
- Y. Wang, J. Lee, X. Hou, C. Labanti, J. Yan, E. Mazzolini, A. Parhar, J. Nelson, J.-S. Kim, Z. Li. *Recent Progress and Challenges toward Highly Stable Nonfullerene Acceptor-Based Organic Solar Cells*, Adv. Energy Mater. 2021, **11**, 2003002
- M.Ahmadpour, A.L. Fernandes Cauduro, C. Methivier, B. Kunert, C. Labanti, R. Resel, V. Turkovic, H.-G. Rubahn, N. Witkowski, A.K. Schmid, M. Madsen. *Crystalline Molybdenum Oxide Layers as Efficient and Stable Hole Contacts in Organic Photovoltaic Devices*, ACS Appl. Energy Mater. 2019, **2**, 420-427

Bibliography

1. *Why Population Growth Matters for Sustainable Development* UN Department of Economic and Social Affairs (DESA) Policy Briefs (Apr. 2022).
2. *Global Governance and the Emergence of Global Institutions for the 21st Century* (eds Dahl, A. L., Lopez-Claros, A. & Groff, M.) 3–29 (Cambridge University Press, Cambridge, 2020).
3. *EIA - International Energy Outlook 2009-World Energy Demand and Economic Outlook* https://www.eia.gov/outlooks/archive/ieo09/world.html.
4. Magnan, A. K. *et al.:* Estimating the Global Risk of Anthropogenic Climate Change. *Nat. Clim. Chang.* **11**, 879–885 (Oct. 2021).
5. *Transforming Our World: The 2030 Agenda for Sustainable Development | Department of Economic and Social Affairs* https://sdgs.un.org/2030agenda.
6. *Growing Opportunities in the Internet of Things | McKinsey* https://www.mckinsey.com/industries/private-equity-and-principal-investors/our-insights/growing-opportunities-in-the-internet-of-things.
7. *Total Surface Area Required to Fuel the World With Solar* Aug. 2009.
8. Louwen, A., van Sark, W., Schropp, R. & Faaij, A.: A Cost Roadmap for Silicon Heterojunction Solar Cells. *Solar Energy Materials and Solar Cells* **147**, 295–314 (Apr. 2016).
9. *Silicon's 300% Surge Throws Another Price Shock at the World* https://www.bloomberg.com/news/articles/2021-10-01/silicon-s-300-surge-throws-another-price-shock-at-the-world. Oct. 2021.
10. Liu, Q. *et al.:* 18% Efficiency Organic Solar Cells. *Science Bulletin* (Jan. 2020).
11. Li, C. *et al.:* Non-Fullerene Acceptors with Branched Side Chains and Improved Molecular Packing to Exceed 18% Efficiency in Organic Solar Cells. *Nat Energy* **6**, 605–613 (June 2021).
12. Sun, R. *et al.:* Single-Junction Organic Solar Cells with 19.17% Efficiency Enabled by Introducing One Asymmetric Guest Acceptor. *Advanced Materials* **34**, 2110147 (2022).
13. Zheng, Z. *et al.:* Tandem Organic Solar Cell with 20.2% Efficiency. *Joule* **6**, 171–184 (Jan. 2022).

14. Liu, J. *et al.:* Challenges and Recent Advances in Photodiodes-Based Organic Photodetectors. *Materials Today* **51**, 475–503 (Dec. 2021).
15. *Our Projects and Achievements* https://www.asca.com/projects/.
16. *HeliaFilm - Heliatek GmbH* https://www.heliatek.com/en/products/heliafilm/.
17. *Product* https://www.epishine.com/product.
18. Lan, Z., Lee, M.-H. & Zhu, F.: Recent Advances in Solution-Processable Organic Photodetectors and Applications in Flexible Electronics. *Advanced Intelligent Systems* **4**, 2100167 (2022).
19. Labanti, C. *et al.:* Selenium-Substituted Non-Fullerene Acceptors: A Route to Superior Operational Stability for Organic Bulk Heterojunction Solar Cells. *ACS Nano* **15**, 7700–7712 (Apr. 2021).
20. Labanti, C. *et al.:* Light-Intensity-Dependent Photoresponse Time of Organic Photodetectors and Its Molecular Origin. *Nat Commun* **13**, 3745 (June 2022).
21. Köhler, A. & Bässler, H.: *Electronic Processes in Organic Semiconductors* (Wiley-VCH Verlag GmbH & Co. KGaA, Weinheim, Germany, May 2015).
22. Alcácer, L.: *Electronic Structure of Organic Semiconductors: Polymers and Small Molecules* (Morgan & Claypool Publishers, Dec. 2018).
23. Myers, J. D. & Xue, J.: Organic Semiconductors and Their Applications in Photovoltaic Devices. *Polymer Reviews* **52**, 1–37 (Jan. 2012).
24. Knupfer, M.: Exciton Binding Energies in Organic Semiconductors. *Appl. Phys. A* **77**, 623–626 (Oct. 2003).
25. Coropceanu, V. *et al.:* Charge Transport in Organic Semiconductors. *Chem. Rev.* **107**, 926–952 (Apr. 2007).
26. Bronstein, H., Nielsen, C. B., Schroeder, B. C. & McCulloch, I.: The Role of Chemical Design in the Performance of Organic Semiconductors. *Nat Rev Chem* **4**, 66–77 (Feb. 2020).
27. F. Haneef, H., M. Zeidell, A. & D. Jurchescu, O.: Charge Carrier Traps in Organic Semiconductors: A Review on the Underlying Physics and Impact on Electronic Devices. *Journal of Materials Chemistry C* **8**, 759–787 (2020).
28. Hou, J., Inganas, O., Friend, R. H. & Gao, F.: Organic Solar Cells Based on Non-Fullerene Acceptors. *Nature Materials* **17**, 119–128 (2018).
29. Fahlman, M. *et al.:* Interfaces in Organic Electronics. *Nature Reviews Materials* **4**, 627–650 (2019).
30. Forrest, S. R. & Thompson, M. E.: Introduction: Organic Electronics and Optoelectronics. *Chem. Rev.* **107**, 923–925 (Apr. 2007).
31. Zhang, G. *et al.:* Renewed Prospects for Organic Photovoltaics. *Chem. Rev.* **122**, 14180–14274 (Sept. 2022).
32. Wang, B., Biesold, G. M., Zhang, M. & Lin, Z.: Amorphous Inorganic Semiconductors for the Development of Solar Cell, Photoelectrocatalytic and Photocatalytic Applications. *Chem. Soc. Rev.* **50**, 6914–6949 (2021).

33. He, Y. *et al.:* Unraveling the Charge-Carrier Dynamics from the Femtosecond to the Microsecond Time Scale in Double-Cable Polymer-Based Single-Component Organic Solar Cells. *Advanced Energy Materials* **12**, 2103406 (2022).
34. Jao, M. H., Liao, H. C. & Su, W. F.: Achieving a High Fill Factor for Organic Solar Cells. *Journal of Materials Chemistry A* **4**, 5784–5801 (2016).
35. Karki, A., Gillett, A. J., Friend, R. H. & Nguyen, T.-Q.: The Path to 20% Power Conversion Efficiencies in Nonfullerene Acceptor Organic Solar Cells. *Advanced Energy Materials* **11**, 2003441 (2021).
36. Park, S. Y., Labanti, C., Luke, J., Chin, Y.-C. & Kim, J.-S.: Organic Bilayer Photovoltaics for Efficient Indoor Light Harvesting. *Advanced Energy Materials* **12**, 2103237 (2022).
37. Feng, G. *et al.:* Thermal-Driven Phase Separation of Double-Cable Polymers Enables Efficient Single-Component Organic Solar Cells. *Joule* **3**, 1765–1781 (July 2019).
38. He, Y. *et al.:* Unraveling the Charge-Carrier Dynamics from the Femtosecond to the Microsecond Time Scale in Double-Cable Polymer-Based Single-Component Organic Solar Cells. *Advanced Energy Materials* **12**, 2103406 (Jan. 2022).
39. Marcus, R. A. *Protein Electron Transfer* (Garland Science, 1996).
40. Marcus, R. A.: On the Theory of Oxidation-Reduction Reactions Involving Electron Transfer. I. *The Journal of Chemical Physics* **24**, 966–978 (1956).
41. Street, R. A., Davies, D., Khlyabich, P. P., Burkhart, B. & Thompson, B. C.: Origin of the Tunable Open-Circuit Voltage in Ternary Blend Bulk Heterojunction Organic Solar Cells. *J. Am. Chem. Soc.* **135**, 986–989 (Jan. 2013).
42. Kooistra, F. B. *et al.:* Increasing the Open Circuit Voltage of Bulk-Heterojunction Solar Cells by Raising the LUMO Level of the Acceptor. *Org. Lett.* **9**, 551–554 (Feb. 2007).
43. Shockley, W. & Queisser, H. J.: Detailed Balance Limit of Efficiency of P-n Junction Solar Cells. *Journal of Applied Physics* **32**, 510–519 (1961).
44. Azzouzi, M. *et al.:* Nonradiative Energy Losses in Bulk-Heterojunction Organic Photovoltaics. *Physical Review X* **8**, 031055 (Sept. 2018).
45. Eisner, F. D. *et al.:* Hybridization of Local Exciton and Charge-Transfer States Reduces Nonradiative Voltage Losses in Organic Solar Cells. *J. Am. Chem. Soc.* **141**, 6362–6374 (Apr. 2019).
46. Jao, M. H., Liao, H. C. & Su, W. F.: Achieving a High Fill Factor for Organic Solar Cells. *Journal of Materials Chemistry A* **4**, 5784–5801 (2016).
47. Kudo, K. & Moriizumi, T.: Spectrum-controllable Color Sensors Using Organic Dyes. *Appl. Phys. Lett.* **39**, 609–611 (Oct. 1981).
48. Yu, G., Wang, J., McElvain, J. & Heeger, A. J.: Large-Area, Full-Color Image Sensors Made with Semiconducting Polymers. *Advanced Materials* **10**, 1431–1434 (1998).

49. Liu, S.-W. *et al.:* Transparent Organic Upconversion Devices for Near-Infrared Sensing. *Advanced Materials* **27**, 1217–1222 (2015).
50. Büchele, P. *et al.:* X-Ray Imaging with Scintillator-Sensitized Hybrid Organic Photodetectors. *Nature Photon* **9**, 843–848 (Dec. 2015).
51. Takada, E. *et al.:* Response of Organic Photodiode Fabricated Directly on Plastic Scintillator to X-rays. *Journal of Nuclear Science and Technology* **52**, 104–108 (Jan. 2015).
52. An, K. H., O'Connor, B., Pipe, K. P., Zhao, Y. & Shtein, M.: Scanning Optical Probe Microscopy with Submicrometer Resolution Using an Organic Photodetector. *Appl. Phys. Lett.* **93**, 033311 (July 2008).
53. Xu, X., Davanco, M., Qi, X. & Forrest, S. R.: Direct Transfer Patterning on Three Dimensionally Deformed Surfaces at Micrometer Resolutions and Its Application to Hemispherical Focal Plane Detector Arrays. *Organic Electronics* **9**, 1122–1127 (Dec. 2008).
54. Wang, X. *et al.:* Integrated Thin-Film Polymer/Fullerene Photodetectors for on-Chip Microfluidic Chemiluminescence Detection. *Lab Chip* **7**, 58–63 (Dec. 2006).
55. Huang, J. *et al.:* A High-Performance Solution-Processed Organic Photodetector for Near-Infrared Sensing. *Advanced Materials* **32**, 1906027 (Jan. 2020).
56. Lochner, C. M., Khan, Y., Pierre, A. & Arias, A. C.: All-Organic Optoelectronic Sensor for Pulse Oximetry. *Nat Commun* **5**, 5745 (Dec. 2014).
57. Lan, Z. *et al.:* Dual-Band Organic Photodetectors for Dual-Channel Optical Communications. *Laser & Photonics Reviews* **16**, 2100602 (2022).
58. Liu, J. *et al.:* Fast Response Organic Tandem Photodetector for Visible and Near-Infrared Digital Optical Communications. *Small* **17**, 2101316 (2021).
59. Yang, D. & Ma, D.: Development of Organic Semiconductor Photodetectors: From Mechanism to Applications. *Advanced Optical Materials* **7**, 1–23 (2019).
60. Simone, G., Dyson, M. J., Meskers, S. C., Janssen, R. A. & Gelinck, G. H.: Organic Photodetectors and Their Application in Large Area and Flexible Image Sensors: The Role of Dark Current. *Advanced Functional Materials* **30**, 1904205 (May 2020).
61. Siegmund, B. *et al.:* Organic Narrowband Near-Infrared Photodetectors Based on Intermolecular Charge-Transfer Absorption. *Nat Commun* **8**, 15421 (June 2017).
62. Liu, J., Wen, H. & Shen, L.: Highly Sensitive, Broadband, Fast Response Organic Photodetectors Based on Semi-Tandem Structure. *Nanotechnology* **31**, 214001 (Mar. 2020).
63. Tang, Z. *et al.:* Polymer:Fullerene Bimolecular Crystals for Near-Infrared Spectroscopic Photodetectors. *Advanced Materials* **29**, 1702184 (2017).

64. Yang, D. & Ma, D.: 1,1-Bis[(Di-4-Tolylamino)Phenyl]Cyclohexane for Fast Response Organic Photodetectors with High External Efficiency and Low Leakage Current. *J. Mater. Chem. C* **1**, 2054–2060 (Feb. 2013).
65. Christ, N. S. *et al.:* Nanosecond Response of Organic Solar Cells and Photodetectors. *Journal of Applied Physics* **105**, 104513 (May 2009).
66. Valouch, S., Nintz, M., Kettlitz, S. W., Christ, N. S. & Lemmer, U.: Thickness-Dependent Transient Photocurrent Response of Organic Photodiodes. *IEEE Photonics Technology Letters* **24**, 596–598 (Apr. 2012).
67. Züfle, S., Christ, N., Kettlitz, S. W., Valouch, S. & Lemmer, U.: Influence of Temperature-Dependent Mobilities on the Nanosecond Response of Organic Solar Cells and Photodetectors. *Appl. Phys. Lett.* **97**, 063306 (Aug. 2010).
68. Zaus, E. S., Tedde, S., Fürst, J., Henseler, D. & Döhler, G. H.: Dynamic and Steady State Current Response to Light Excitation of Multilayered Organic Photodiodes. *Journal of Applied Physics* **101**, 044501 (Feb. 2007).
69. McNeill, C. R., Hwang, I. & Greenham, N. C.: Photocurrent Transients in All-Polymer Solar Cells: Trapping and Detrapping Effects. *Journal of Applied Physics* **106**, 024507 (July 2009).
70. Christ, N., Kettlitz, S. W., Züfle, S., Valouch, S. & Lemmer, U.: Nanosecond Response of Organic Solar Cells and Photodiodes: Role of Trap States. *Phys. Rev. B* **83**, 195211 (May 2011).
71. Kublitski, J. *et al.:* Reverse Dark Current in Organic Photodetectors and the Major Role of Traps as Source of Noise. *Nature Communications* **12**, 1–9 (Dec. 2021).
72. Xia, Y., Aguirre, L. E., Xu, X. & Inganäs, O.: All-Polymer High-Performance Photodetector through Lamination. *Advanced Electronic Materials* **6**, 1901017 (2020).
73. Kuksenkov, D. V., Temkin, H., Osinsky, A., Gaska, R. & Khan, M. A.: Low-Frequency Noise and Performance of GaN p-n Junction Photodetectors. *J. Appl. Phys.* **83**, 6 (1998).
74. Sandberg, O. J. *et al.:* Mid-Gap Trap State-Mediated Dark Current in Organic Photodiodes. *Nat. Photon.* **17**, 368–374 (Apr. 2023).
75. Huang, J. *et al.:* Understanding and Countering Illumination-Sensitive Dark Current: Toward Organic Photodetectors with Reliable High Detectivity. *ACS Nano* **15**, 1753–1763 (Jan. 2021).
76. Yoon, S., Ha, J., Cho, J. & Chung, D. S.: Nonabsorbing Acceptor-Based Planar Heterojunction for Color-Selective and High-Detectivity Polymer Photodiodes. *Advanced Optical Materials* **4**, 1933–1938 (2016).
77. Shekhar, H., Solomeshch, O., Liraz, D. & Tessler, N.: Low Dark Leakage Current in Organic Planar Heterojunction Photodiodes. *Applied Physics Letters* **111**, 223301 (Nov. 2017).

78. Zhou, X., Yang, D. & Ma, D.: Extremely Low Dark Current, High Responsivity, All-Polymer Photodetectors with Spectral Response from 300 Nm to 1000 Nm. *Advanced Optical Materials* **3**, 1570–1576 (2015).
79. Kielar, M., Dhez, O., Pecastaings, G., Curutchet, A. & Hirsch, L.: Long-Term Stable Organic Photodetectors with Ultra Low Dark Currents for High Detectivity Applications. *Sci Rep* **6**, 39201 (Dec. 2016).
80. Biele, M. *et al.:* Spray-Coated Organic Photodetectors and Image Sensors with Silicon-Like Performance. *Advanced Materials Technologies* **4**, 1800158 (2019).
81. Fuentes-Hernandez, C. *et al.:* Large-Area Low-Noise Flexible Organic Photodiodes for Detecting Faint Visible Light. *Science* **370**, 698–701 (Nov. 2020).
82. Li, C. *et al.:* Ultrafast and Broadband Photodetectors Based on a Perovskite/Organic Bulk Heterojunction for Large-Dynamic-Range Imaging. *Light Sci Appl* **9**, 31 (Mar. 2020).
83. Guo, F., Xiao, Z. & Huang, J.: Fullerene Photodetectors with a Linear Dynamic Range of 90 dB Enabled by a Cross-Linkable Buffer Layer. *Advanced Optical Materials* **1**, 289–294 (2013).
84. Stolterfoht, M. *et al.:* Photocarrier Drift Distance in Organic Solar Cells and Photodetectors. *Sci Rep* **5**, 9949 (Apr. 2015).
85. Stolterfoht, M. *et al.:* Charge Transport without Recombination in Organic Solar Cells and Photodiodes. *J. Phys. Chem. C* **119**, 26866–26874 (Dec. 2015).
86. Mi, D., Kim, J.-H., Kim, H. U., Xu, F. & Hwang, D.-H.: Fullerene Derivatives as Electron Acceptors for Organic Photovoltaic Cells. *Journal of Nanoscience and Nanotechnology* **14**, 1064–1084 (Feb. 2014).
87. Wadsworth, A. *et al.:* Critical Review of the Molecular Design Progress in Non-Fullerene Electron Acceptors towards Commercially Viable Organic Solar Cells. *Chem. Soc. Rev.* **48**, 1596–1625 (Mar. 2019).
88. Lee, G. H. *et al.:* Green-Light-Selective Organic Photodiodes for Full-Color Imaging. *Optics Express* **27**, 25410 (2019).
89. Bulliard, X. *et al.:* Dipolar Donor-Acceptor Molecules in the Cyanine Limit for High Efficiency Green-Light-Selective Organic Photodiodes. *Journal of Materials Chemistry C* **4**, 1117–1125 (2016).
90. Jang, W. *et al.:* Superior Noise Suppression, Response Time, and Device Stability of Non-Fullerene System over Fullerene Counterpart in Organic Photodiode. *Advanced Functional Materials* **30**, 2001402 (2020).
91. Eun, H. J. *et al.:* Effective Dark Current Suppression for High-Detectivity Organic Near-Infrared Photodetectors Using a Non-Fullerene Acceptor. *ACS Appl. Mater. Interfaces* **13**, 11144–11150 (Mar. 2021).
92. Wu, Z. *et al.:* Noise and Detectivity Limits in Organic Shortwave Infrared Photodiodes with Low Disorder. *npj Flex Electron* **4**, 1–8 (Apr. 2020).

93. Lin, H.-W. *et al.:* Highly Efficient Visible-Blind Organic Ultraviolet Photodetectors. *Advanced Materials* **17**, 2489–2493 (2005).
94. Su, Z. *et al.:* High Response Organic Ultraviolet Photodetector Based on Blend of 4,4′,4″-Tri-(2-Methylphenyl Phenylamino) Triphenylaine and Tris-(8-Hydroxyquinoline) Gallium. *Appl. Phys. Lett.* **93**, 103309 (Sept. 2008).
95. Wu, S.-h. *et al.:* High Response Deep Ultraviolet Organic Photodetector with Spectrum Peak Focused on 280 Nm. *Appl. Phys. Lett.* **96**, 093302 (Mar. 2010).
96. Liu, C., Wang, K., Gong, X. & Heeger, A. J.: Low Bandgap Semiconducting Polymers for Polymeric Photovoltaics. *Chem. Soc. Rev.* **45**, 4825–4846 (Aug. 2016).
97. Qi, J. *et al.:* High-Detectivity All-Polymer Photodetectors with Spectral Response from 300 to 1100 Nm. *Macromolecular Chemistry and Physics* **217**, 1683–1689 (2016).
98. Hu, L. *et al.:* Naphthalene Diimide–Diketopyrrolopyrrole Copolymers as Non-Fullerene Acceptors for Use in Bulk-Heterojunction All-Polymer UV–NIR Photodetectors. *Polym. Chem.* **8**, 528–536 (Jan. 2017).
99. Hu, L. *et al.:* Side-Chain Engineering for Fine-Tuning of Molecular Packing and Nanoscale Blend Morphology in Polymer Photodetectors. *Polym. Chem.* **8**, 2055–2062 (Mar. 2017).
100. Xia, Y. *et al.:* Photocurrent Response Wavelength up to 1.1μm from Photovoltaic Cells Based on Narrow-Band-Gap Conjugated Polymer and Fullerene Derivative. *Appl. Phys. Lett.* **89**, 081106 (Aug. 2006).
101. Han, J. *et al.:* Low-Bandgap Donor–Acceptor Polymers for Photodetectors with Photoresponsivity from 300 Nm to 1600 Nm. *J. Mater. Chem. C* **5**, 159–165 (Dec. 2016).
102. Tsai, K.-W. *et al.:* Bulk-Heterojunction Adjustment Enables a Self-filtering Organic Photodetector with a Narrowband Response. *ACS Appl. Mater. Interfaces* **14**, 38004–38012 (Aug. 2022).
103. Li, L., Huang, Y., Peng, J., Cao, Y. & Peng, X.: Highly Responsive Organic Near-Infrared Photodetectors Based on a Porphyrin Small Molecule. *J. Mater. Chem. C* **2**, 1372–1375 (Jan. 2014).
104. Binda, M. *et al.:* Fast and Air Stable Near-Infrared Organic Detector Based on Squaraine Dyes. *Organic Electronics* **10**, 1314–1319 (Nov. 2009).
105. Hu, L., Yan, Z. & Xu, H.: Advances in Synthesis and Application of Near-Infrared Absorbing Squaraine Dyes. *RSC Adv.* **3**, 7667–7676 (May 2013).
106. Schulz, M., Mack, M., Kolloge, O., Lützen, A. & Schiek, M.: Organic Photodiodes from Homochiral L-proline Derived Squaraine Compounds with Strong Circular Dichroism. *Phys. Chem. Chem. Phys.* **19**, 6996–7008 (Mar. 2017).
107. Perzon, E. *et al.:* A Conjugated Polymer for Near Infrared Optoelectronic Applications. *Advanced Materials* **19**, 3308–3311 (2007).

108. Jacoutot, P. *et al.:* Infrared Organic Photodetectors Employing Ultralow Bandgap Polymer and Non-Fullerene Acceptors for Biometric Monitoring. *Small* **18**, 2200580 (2022).
109. Yang, C.-M. *et al.:* Infrared Photocurrent Response of Charge-Transfer Exciton in Polymer Bulk Heterojunction. *Appl. Phys. Lett.* **92**, 083504 (Feb. 2008).
110. Shafian, S., Hwang, H. & Kim, K.: Near Infrared Organic Photodetector Utilizing a Double Electron Blocking Layer. *Opt. Express, OE* **24**, 25308–25316 (Oct. 2016).
111. Gong, X. *et al.:* High-Detectivity Polymer Photodetectors with Spectral Response from 300 Nm to 1450 Nm. *Science* **325**, 1665–1667 (Sept. 2009).
112. Zhang, G. *et al.:* Nonfullerene Acceptor Molecules for Bulk Heterojunction Organic Solar Cells. *Chemical Reviews* **118**, 3447–3507 (2018).
113. Sharma, V., Koenig, J. D. B. & Welch, G. C.: Perylene Diimide Based Non-Fullerene Acceptors: Top Performers and an Emerging Class Featuring N-annulation. *J. Mater. Chem. A* **9**, 6775–6789 (Mar. 2021).
114. Zhan, X. *et al.:* Rylene and Related Diimides for Organic Electronics. *Advanced Materials* **23**, 268–284 (2011).
115. Li, C., Liu, M., Pschirer, N. G., Baumgarten, M. & Müllen, K.: Polyphenylene-Based Materials for Organic Photovoltaics. *Chem. Rev.* **110**, 6817–6855 (Nov. 2010).
116. Würthner, F.: Perylene Bisimide Dyes as Versatile Building Blocks for Functional Supramolecular Architectures. *Chem. Commun.,* 1564–1579 (July 2004).
117. Arnaud, A. *et al.:* Aqueous Supramolecular Polymer Formed from an Amphiphilic Perylene Derivative. *Angewandte Chemie International Edition* **43**, 1718–1721 (2004).
118. Zhang, X., Rehm, S., Safont-Sempere, M. M. & Würthner, F.: Vesicular Perylene Dye Nanocapsules as Supramolecular Fluorescent pH Sensor Systems. *Nature Chem* **1**, 623–629 (Nov. 2009).
119. Dittmer, J. J., Marseglia, E. A. & Friend, R. H.: Electron Trapping in Dye/Polymer Blend Photovoltaic Cells. *Advanced Materials* **12**, 1270–1274 (2000).
120. Singh, R. *et al.:* Fullerene-Free Organic Solar Cells with an Efficiency of 3.7% Based on a Low-Cost Geometrically Planar Perylene Diimide Monomer. *J. Mater. Chem. A* **2**, 14348–14353 (Aug. 2014).
121. Hartnett, P. E. *et al.:* Slip-Stacked Perylenediimides as an Alternative Strategy for High Efficiency Nonfullerene Acceptors in Organic Photovoltaics. *J. Am. Chem. Soc.* **136**, 16345–16356 (Nov. 2014).
122. Cai, Y. *et al.:* High Performance Organic Solar Cells Based on a Twisted Bay-Substituted Tetraphenyl Functionalized Perylenediimide Electron Acceptor. *Advanced Energy Materials* **5**, 1500032 (2015).

123. Rajaram, S., Shivanna, R., Kandappa, S. K. & Narayan, K. S.: Nonplanar Perylene Diimides as Potential Alternatives to Fullerenes in Organic Solar Cells. *Journal of Physical Chemistry Letters* **3**, 2405–2408 (Sept. 2012).
124. Sun, D. *et al.:* Non-Fullerene-Acceptor-Based Bulk-Heterojunction Organic Solar Cells with Efficiency over 7%. *Journal of the American Chemical Society* **137**, 11156–11162 (2015).
125. Liu, J. *et al.:* Fast Charge Separation in a Non-Fullerene Organic Solar Cell with a Small Driving Force. *Nat Energy* **1**, 1–7 (June 2016).
126. Winzenberg, K. N. *et al.:* Indan-1,3-Dione Electron-Acceptor Small Molecules for Solution-Processable Solar Cells: A Structure–Property Correlation. *Chem. Commun.* **49**, 6307–6309 (June 2013).
127. Lin, Y. *et al.:* An Electron Acceptor Challenging Fullerenes for Efficient Polymer Solar Cells. *Advanced Materials* **27**, 1170–1174 (2015).
128. Holliday, S. *et al.:* High-Efficiency and Air-Stable P3HT-based Polymer Solar Cells with a New Non-Fullerene Acceptor. *Nature Communications* **7**, 11585 (June 2016).
129. Li, Y. *et al.:* Non-Fullerene Acceptor with Low Energy Loss and High External Quantum Efficiency: Towards High Performance Polymer Solar Cells. *J. Mater. Chem. A* **4**, 5890–5897 (Apr. 2016).
130. Li, S. *et al.:* Energy-Level Modulation of Small-Molecule Electron Acceptors to Achieve over 12% Efficiency in Polymer Solar Cells. *Advanced Materials* **28**, 9423–9429 (2016).
131. Zhao, F., Dai, S., You, W. & Zhan, X.: Single-Junction Binary-Blend Nonfullerene Polymer Solar (2017).
132. Zhao, W. *et al.:* Molecular Optimization Enables over 13% Efficiency in Organic Solar Cells. *Journal of the American Chemical Society* **139**, 7148–7151 (2017).
133. Wu, Y. *et al.:* A Planar Electron Acceptor for Efficient Polymer Solar Cells. *Energy Environ. Sci.* **8**, 3215–3221 (Oct. 2015).
134. Lin, Y. *et al.:* High-Performance Electron Acceptor with Thienyl Side Chains for Organic Photovoltaics. *Journal of the American Chemical Society* **138**, 4955–4961 (2016).
135. Yang, Y. *et al.:* Side-Chain Isomerization on an n-Type Organic Semiconductor ITIC Acceptor Makes 11.77% High Efficiency Polymer Solar Cells. *Journal of the American Chemical Society* **138**, 15011–15018 (2016).
136. Zhu, W. *et al.:* Crystallography, Morphology, Electronic Structure, and Transport in Non-Fullerene/Non-Indacenodithienothiophene Polymer:Y6 Solar Cells, 57.
137. Li, S., Li, C.-Z., Shi, M. & Chen, H.: New Phase for Organic Solar Cell Research: Emergence of Y-Series Electron Acceptors and Their Perspectives. *ACS Energy Lett.* **5**, 1554–1567 (May 2020).

138. Yuan, J. *et al.:* Fused Benzothiadiazole: A Building Block for n-Type Organic Acceptor to Achieve High-Performance Organic Solar Cells. *Advanced Materials* **31**, 1807577 (2019).
139. Yuan, J. *et al.:* Single-Junction Organic Solar Cell with over 15% Efficiency Using Fused-Ring Acceptor with Electron-Deficient Core. *Joule* **3**, 1140–1151 (2019).
140. Yuan, J. *et al.:* Enabling Low Voltage Losses and High Photocurrent in Fullerene-Free Organic Photovoltaics. *Nat Commun* **10**, 570 (Feb. 2019).
141. Feng, L. *et al.:* Thieno[3,2-b]Pyrrolo-Fused Pentacyclic Benzotriazole-Based Acceptor for Efficient Organic Photovoltaics. *ACS Appl. Mater. Interfaces* **9**, 31985–31992 (Sept. 2017).
142. Liu, S. *et al.:* High-Efficiency Organic Solar Cells with Low Non-Radiative Recombination Loss and Low Energetic Disorder. *Nat. Photonics* **14**, 300–305 (May 2020).
143. Cui, Y. *et al.:* Over 16% Efficiency Organic Photovoltaic Cells Enabled by a Chlorinated Acceptor with Increased Open-Circuit Voltages. *Nature Communications* **10**, 1–8 (2019).
144. Fan, B. *et al.:* Achieving over 16% Efficiency for Single-Junction Organic Solar Cells. *Science China Chemistry* **62**, 746–752 (Mar. 2019).
145. Wang, H. *et al.:* Bromination: An Alternative Strategy for Non-Fullerene Small Molecule Acceptors. *Advanced Science* **7**, 1903784 (2020).
146. He, C. *et al.:* Manipulating the D:A Interfacial Energetics and Intermolecular Packing for 19.2% Efficiency Organic Photovoltaics. *Energy Environ. Sci.* **15**, 2537–2544 (June 2022).
147. Gao, H.-H. *et al.:* Achieving Both Enhanced Voltage and Current through Fine-Tuning Molecular Backbone and Morphology Control in Organic Solar Cells. *Advanced Energy Materials* **9**, 1901024 (2019).
148. Jiang, K. *et al.:* Alkyl Chain Tuning of Small Molecule Acceptors for Efficient Organic Solar Cells. *Joule* **3**, 3020–3033 (2019).
149. Hong, L. *et al.:* Eco-Compatible Solvent-Processed Organic Photovoltaic Cells with Over 16% Efficiency. *Advanced Materials* **31**, 1903441 (2019).
150. Cui, Y. *et al.:* Organic Photovoltaic Cell with 17% Efficiency and Superior Processability. *National Science Review* **7**, 1239–1246 (July 2020).
151. de la Torre, G., Bottari, G. & Torres, T.: Phthalocyanines and Subphthalocyanines: Perfect Partners for Fullerenes and Carbon Nanotubes in Molecular Photovoltaics. *Advanced Energy Materials* **7**, 1601700 (2017).
152. Sullivan, P. *et al.:* Halogenated Boron Subphthalocyanines as Light Harvesting Electron Acceptors in Organic Photovoltaics. *Advanced Energy Materials* **1**, 352–355 (2011).
153. Ball, M. L. *et al.:* Design of UV-Absorbing Donor Molecules for Nearly Imperceptible Organic Solar Cells. *ACS Energy Lett.* **7**, 180–188 (Jan. 2022).

154. Su, D., Dong, J., Wang, L. & Su, Z.: Panchromatic Organic Photodetectors with SubPc as a Non-Fullerene Acceptor. *Mater. Res. Express* **6**, 105103 (Sept. 2019).
155. Classen, A. *et al.:* The Role of Exciton Lifetime for Charge Generation in Organic Solar Cells at Negligible Energy-Level Offsets. *Nature Energy* **5**, 711–719 (Sept. 2020).
156. Lu, B. *et al.:* Recent Progress of Y-series Electron Acceptors for Organic Solar Cells. *Nano Select* **2**, 2029–2039 (2021).
157. Zhang, G. *et al.:* Delocalization of Exciton and Electron Wavefunction in Non-Fullerene Acceptor Molecules Enables Efficient Organic Solar Cells. *Nat Commun* **11**, 3943 (Aug. 2020).
158. Perdigón-Toro, L. *et al.:* Barrierless Free Charge Generation in the High-Performance PM6:Y6 Bulk Heterojunction Non-Fullerene Solar Cell. *Adv. Mater.* **32**, 1906763 (Mar. 2020).
159. Karuthedath, S. *et al.:* Intrinsic Efficiency Limits in Low-Bandgap Non-Fullerene Acceptor Organic Solar Cells. *Nature Materials* **20**, 378–384 (Mar. 2021).
160. Zhu, W. *et al.:* Crystallography, Morphology, Electronic Structure, and Transport in Non-Fullerene/Non-Indacenodithienothiophene Polymer:Y6 Solar Cells. *J. Am. Chem. Soc.* **142**, 14532–14547 (Aug. 2020).
161. Zhu, L. *et al.:* Efficient Organic Solar Cell with 16.88% Efficiency Enabled by Refined Acceptor Crystallization and Morphology with Improved Charge Transfer and Transport Properties. *Advanced Energy Materials* **10**, 1904234 (May 2020).
162. Xiao, C., Li, C., Liu, F., Zhang, L. & Li, W.: Single-Crystal Field-Effect Transistors Based on a Fused-Ring Electron Acceptor with High Ambipolar Mobilities. *J. Mater. Chem. C* **8**, 5370–5374 (Apr. 2020).
163. Baran, D. *et al.:* Reducing the Efficiency-Stability-Cost Gap of Organic Photovoltaics with Highly Efficient and Stable Small Molecule Acceptor Ternary Solar Cells. *Nature Materials* **16**, 363–369 (2017).
164. Fu, H., Wang, Z. & Sun, Y.: Polymer Donors for High-Performance Non-Fullerene Organic Solar Cells. *Angewandte Chemie International Edition* **58**, 4442–4453 (2019).
165. Wang, Q., Qin, Y., Li, M., Ye, L. & Geng, Y.: Molecular Engineering and Morphology Control of Polythiophene:Nonfullerene Acceptor Blends for High-Performance Solar Cells. *Advanced Energy Materials* **10**, 2002572 (2020).
166. Liang, Z. *et al.:* Optimization Requirements of Efficient Polythiophene:Nonfullerene Organic Solar Cells. *Joule* **4**, 1278–1295 (June 2020).
167. Han, J., Yang, D., Ma, D., Qiao, W. & Wang, Z. Y.: Low-Bandgap Polymers for High-Performance Photodiodes with Maximal EQE near 1200 Nm and Broad Spectral Response from 300 to 1700 Nm. *Advanced Optical Materials* **6**, 1800038 (2018).

168. Lee, D. W. *et al.:* Morphology and Charge Recombination Effects on the Performance of Near-Infrared Photodetectors Based on Conjugated Polymers. *Organic Electronics* **64**, 274–279 (Jan. 2019).
169. Lee, J. *et al.:* Side-Chain Engineering of Nonfullerene Acceptors for Near-Infrared Organic Photodetectors and Photovoltaics. *ACS Energy Lett.* **4**, 1401–1409 (June 2019).
170. Babics, M. *et al.:* Non-Fullerene-Based Organic Photodetectors for Infrared Communication. *Journal of Materials Chemistry C* **9**, 2375–2380 (2021).
171. Verstraeten, F. *et al.:* Efficient and Readily Tuneable Near-Infrared Photodetection up to 1500 Nm Enabled by Thiadiazoloquinoxaline-Based Push–Pull Type Conjugated Polymers. *J. Mater. Chem. C* **8**, 10098–10103 (July 2020).
172. Bristow, H. *et al.:* Nonfullerene-Based Organic Photodetectors for Ultrahigh Sensitivity Visible Light Detection. *ACS Appl. Mater. Interfaces* **12**, 48836–48844 (Oct. 2020).
173. Zhang, L. *et al.:* Toward Highly Sensitive Polymer Photodetectors by Molecular Engineering. *Advanced Materials* **27**, 6496–6503 (2015).
174. Simone, G. *et al.:* On the Origin of Dark Current in Organic Photodiodes. *Advanced Optical Materials* **8**, 1901568 (2020).
175. Yoon, S. *et al.:* High-Performance Near-Infrared-Selective Thin Film Organic Photodiode Based on a Molecular Approach Targeted to Ideal Semiconductor Junctions. *J. Phys. Chem. Lett.* **10**, 5647–5653 (Sept. 2019).
176. Ko, H., Park, S., Son, H. J. & Chung, D. S.: Wide-Linear-Dynamic-Range Polymer Photodiode with a New Benzo[1,2-b:4,5-B′]Dithiophene-Copolymer: The Role of Crystalline Orientation. *Chem. Mater.* **32**, 3219–3228 (Apr. 2020).
177. Zhu, L. *et al.:* Single-Junction Organic Solar Cells with over 19% Efficiency Enabled by a Refined Double-Fibril Network Morphology. *Nat. Mater.* **21**, 656–663 (June 2022).
178. Lim, Y. *et al.:* Green-Light-Selective Organic Photodiodes with High Detectivity for CMOS Color Image Sensors. *ACS Applied Materials and Interfaces* **12**, 51688–51698 (Nov. 2020).
179. Limbu, S. *et al.:* Identifying the Molecular Origins of High-Performance in Organic Photodetectors Based on Highly Intermixed Bulk Heterojunction Blends. *ACS Nano* **15**, 1217–1228 (Jan. 2021).
180. Chul Lim, H. *et al.:* Effect of a π-Linker of Push–Pull D–π–A Donor Molecules on the Performance of Organic Photodetectors. *Journal of Materials Chemistry C* **8**, 11145–11152 (2020).
181. Firdaus, Y. *et al.:* Key Parameters Requirements for Non-Fullerene-Based Organic Solar Cells with Power Conversion Efficiency >20%. *Advanced Science* **6**, 1802028 (2019).

182. Würfel, U., Neher, D., Spies, A. & Albrecht, S.: Impact of Charge Transport on Current–Voltage Characteristics and Power-Conversion Efficiency of Organic Solar Cells. *Nat Commun* **6**, 6951 (Apr. 2015).
183. Jang, W. *et al.:* Strong Dark Current Suppression in Flexible Organic Photodetectors by Carbon Nanotube Transparent Electrodes. *Nano Today* **37**, 101081 (Apr. 2021).
184. Liu, Z.-X. *et al.:* Achieving Efficient Organic Solar Cells and Broadband Photodetectors via Simple Compositional Tuning of Ternary Blends. *Nano Energy* **63**, 103807 (Sept. 2019).
185. Song, Y., Yu, G., Xie, B., Zhang, K. & Huang, F.: Visible-to-near-Infrared Organic Photodiodes with Performance Comparable to Commercial Silicon-Based Detectors. *Appl. Phys. Lett.* **117**, 093302 (Aug. 2020).
186. Wadsworth, A., Hamid, Z., Kosco, J., Gasparini, N. & McCulloch, I.: The Bulk Heterojunction in Organic Photovoltaic, Photodetector, and Photocatalytic Applications. *Advanced Materials* **32** (Sept. 2020).
187. Li, N. *et al.:* Abnormal Strong Burn-in Degradation of Highly Efficient Polymer Solar Cells Caused by Spinodal Donor-Acceptor Demixing. *Nature Communications* **8**, 1–9 (2017).
188. Limbu, S. *et al.:* Impact of Initial Bulk-Heterojunction Morphology on Operational Stability of Polymer:Fullerene Photovoltaic Cells. *Advanced Materials Interfaces* **6**, 1–10 (2019).
189. Meletov, K. P., Arvanitidis, J., Christofilos, D., Kourouklis, G. A. & Davydov, V. A.: Raman Study of the Temperature-Induced Decomposition of the Fullerene Dimers C120. *Chemical Physics Letters* **654**, 81–85 (2016).
190. Price, M. B. *et al.:* Free Charge Photogeneration in a Single Component High Photovoltaic Efficiency Organic Semiconductor. *Nat Commun* **13**, 2827 (May 2022).
191. Du, X. *et al.:* Unraveling the Microstructure-Related Device Stability for Polymer Solar Cells Based on Nonfullerene Small-Molecular Acceptors. *Advanced Materials* **32**, 1908305 (Apr. 2020).
192. Zhu, L. *et al.:* Efficient Organic Solar Cell with 16.88% Efficiency Enabled by Refined Acceptor Crystallization and Morphology with Improved Charge Transfer and Transport Properties. *Advanced Energy Materials* **10** (May 2020).
193. Karki, A. *et al.:* The Role of Bulk and Interfacial Morphology in Charge Generation, Recombination, and Extraction in Non-Fullerene Acceptor Organic Solar Cells. *Energy Environ. Sci.* **13**, 3679–3692 (Oct. 2020).
194. Zhao, W., Zhang, S. & Hou, J.: Realizing 11.3% Efficiency in Fullerene-Free Polymer Solar Cells by Device Optimization. *Science China Chemistry* **59**, 1574–1582 (2016).

195. Karki, A. *et al.:* Unifying Charge Generation, Recombination, and Extraction in Low-Offset Non-Fullerene Acceptor Organic Solar Cells. *Adv. Energy Mater.* **10**, 2001203 (Aug. 2020).
196. He, Q. *et al.:* Crucial Role of Fluorine in Fully Alkylated Ladder-Type Carbazole-Based Nonfullerene Organic Solar Cells. *ACS Appl. Mater. Interfaces* **12**, 9555–9562 (Feb. 2020).
197. Tang, H. *et al.:* Deciphering the Role of Fluorination: Morphological Manipulation Prompts Charge Separation and Reduces Carrier Recombination in All-Small-Molecule Photovoltaics. *Solar RRL* **4**, 1900528 (2020).
198. Ye, L. *et al.:* Quenching to the Percolation Threshold in Organic Solar Cells. *Joule* **3**, 443–458 (Feb. 2019).
199. Ghasemi, M. *et al.:* Delineation of Thermodynamic and Kinetic Factors That Control Stability in Non-fullerene Organic Solar Cells. *Joule* **3**, 1328–1348 (May 2019).
200. Rezasoltani, E. *et al.:* Correlating the Phase Behavior with the Device Performance in Binary Poly-3-hexylthiophene: Nonfullerene Acceptor Blend Using Optical Probes of the Microstructure. *Chem. Mater.* **32**, 8294–8305 (Oct. 2020).
201. Guo, X. *et al.:* High Efficiency Polymer Solar Cells Based on Poly(3-Hexylthiophene)/Indene-C70 Bisadduct with Solvent Additive. *Energy Environ. Sci.* **5**, 7943–7949 (June 2012).
202. Liu, X. *et al.:* Solution-Processed near-Infrared Polymer Photodetectors with an Inverted Device Structure. *Organic Electronics* **13**, 2929–2934 (Dec. 2012).
203. Montenegro Benavides, C. *et al.:* Improving Spray Coated Organic Photodetectors Performance by Using 1,8-Diiodooctane as Processing Additive. *Organic Electronics* **54**, 21–26 (Mar. 2018).
204. Chen, S. *et al.:* A Synergetic Effect of Molecular Weight and Fluorine in All-Polymer Solar Cells with Enhanced Performance. *Advanced Functional Materials* **27**, 1603564 (2017).
205. Liu, X., Wang, H., Yang, T., Zhang, W. & Gong, X.: Solution-Processed Ultrasensitive Polymer Photodetectors with High External Quantum Efficiency and Detectivity. *ACS Appl. Mater. Interfaces* **4**, 3701–3705 (July 2012).
206. Zhang, D., Zhao, D., Wang, Z. & Yu, J.: Processes Controlling the Distribution of Vertical Organic Composition in Organic Photodetectors by Ultrasonic-Assisted Solvent Vapor Annealing. *ACS Appl. Electron. Mater.* **2**, 2188–2195 (July 2020).
207. Cha, H. *et al.:* Suppression of Recombination Losses in Polymer:Nonfullerene Acceptor Organic Solar Cells Due to Aggregation Dependence of Acceptor Electron Affinity. *Advanced Energy Materials* **9**, 1901254 (2019).
208. Clarke, T. M. & Durrant, J. R.: Charge Photogeneration in Organic Solar Cells. *Chemical Reviews* **110**, 6736–6767 (Nov. 2010).

209. Li, W., Hendriks, K. H., Furlan, A., Wienk, M. M. & Janssen, R. A. J.: High Quantum Efficiencies in Polymer Solar Cells at Energy Losses below 0.6 eV. *J. Am. Chem. Soc.* **137**, 2231–2234 (Feb. 2015).
210. Eftaiha, A. F., Sun, J.-P., Hill, I. G. & Welch, G. C.: Recent Advances of Non-Fullerene, Small Molecular Acceptors for Solution Processed Bulk Heterojunction Solar Cells. *J. Mater. Chem. A* **2**, 1201–1213 (Dec. 2013).
211. Hoke, E. T. *et al.:* Recombination in Polymer:Fullerene Solar Cells with Open-Circuit Voltages Approaching and Exceeding 1.0 V. *Advanced Energy Materials* **3**, 220–230 (2013).
212. Wu, J. *et al.:* Exceptionally Low Charge Trapping Enables Highly Efficient Organic Bulk Heterojunction Solar Cells. *Energy and Environmental Science* **13**, 2422–2430 (2020).
213. Bertrandie, J. *et al.:* The Energy Level Conundrum of Organic Semiconductors in Solar Cells. *Advanced Materials* **34**, 2202575 (2022).
214. Fu, Y. *et al.:* Molecular Orientation-Dependent Energetic Shifts in Solution-Processed Non-Fullerene Acceptors and Their Impact on Organic Photovoltaic Performance. *Nat Commun* **14**, 1870 (Apr. 2023).
215. Park, S. Y. *et al.: Solution-Processed Single-Component Organic Photodetectors - Strong Quadrupole Moments in Molecules Enable the State-of-the-Art Performance* Preprint (In Review, Mar. 2023).
216. Lee, T. H. *et al.:* Organic Planar Heterojunction Solar Cells and Photodetectors Tailored to the Exciton Diffusion Length Scale of a Non-Fullerene Acceptor. *Advanced Functional Materials* **32**, 2208001 (2022).
217. An, N. *et al.:* Solution-Processed Organic Solar Cells with High Open-Circuit Voltage of 1.3 V and Low Non-Radiative Voltage Loss of 0.16 V. *Advanced Materials* **32**, 2002122 (2020).
218. Wu, J. *et al.:* Tail State Limited Photocurrent Collection of Thick Photoactive Layers in Organic Solar Cells. *Nature Communications* **10** (Dec. 2019).
219. Zhang, X. *et al.:* On the Understanding of Energy Loss and Device Fill Factor Trade-Offs in Non-Fullerene Organic Solar Cells with Varied Energy Levels. *Nano Energy* **75**, 105032 (Sept. 2020).
220. Azzouzi, M., Kirchartz, T. & Nelson, J.: Factors Controlling Open-Circuit Voltage Losses in Organic Solar Cells. *Trends in Chemistry. Special Issue: Big Questions in Chemistry* **1**, 49–62 (Apr. 2019).
221. Benduhn, J. *et al.:* Intrinsic Non-Radiative Voltage Losses in Fullerene-Based Organic Solar Cells. *Nat Energy* **2**, 1–6 (Apr. 2017).
222. Ullbrich, S. *et al.:* Emissive and Charge-Generating Donor–Acceptor Interfaces for Organic Optoelectronics with Low Voltage Losses. *Nat. Mater.* **18**, 459–464 (May 2019).

223. Chen, X.-K., Ravva, M. K., Li, H., Ryno, S. M. & Brédas, J.-L.: Effect of Molecular Packing and Charge Delocalization on the Nonradiative Recombination of Charge-Transfer States in Organic Solar Cells. *Advanced Energy Materials* **6**, 1601325 (2016).
224. Ran, N. A. *et al.:* Impact of Interfacial Molecular Orientation on Radiative Recombination and Charge Generation Efficiency. *Nat Commun* **8**, 79 (July 2017).
225. Qian, D. *et al.:* Design Rules for Minimizing Voltage Losses in High-Efficiency Organic Solar Cells. *Nature Materials* **17**, 703–709 (2018).
226. Benduhn, J. *et al.:* Impact of Triplet Excited States on the Open-Circuit Voltage of Organic Solar Cells. *Advanced Energy Materials* **8**, 1800451 (2018).
227. Xue, L. *et al.:* Side Chain Engineering on Medium Bandgap Copolymers to Suppress Triplet Formation for High-Efficiency Polymer Solar Cells. *Advanced Materials* **29**, 1703344 (2017).
228. Hou, L. *et al.:* Effects of Fluorination on Fused Ring Electron Acceptor for Active Layer Morphology, Exciton Dissociation, and Charge Recombination in Organic Solar Cells. *ACS Appl. Mater. Interfaces* **12**, 56231–56239 (Dec. 2020).
229. Luke, J. *et al.:* Strong Intermolecular Interactions Induced by High Quadrupole Moments Enable Excellent Photostability of Non-Fullerene Acceptors for Organic Photovoltaics. *Advanced Energy Materials* **12**, 2201267 (2022).
230. Du, X. *et al.:* Efficient Polymer Solar Cells Based on Non-fullerene Acceptors with Potential Device Lifetime Approaching 10 Years. *Joule* **3**, 215–226 (2019).
231. Wang, Y. *et al.:* Recent Progress and Challenges toward Highly Stable Nonfullerene Acceptor-Based Organic Solar Cells. *Advanced Energy Materials* **11** (Feb. 2021).
232. Reese, M. O. *et al.:* Consensus Stability Testing Protocols for Organic Photovoltaic Materials and Devices. *Solar Energy Materials and Solar Cells* **95**, 1253–1267 (May 2011).
233. Lee, H. K. H. *et al.:* The Role of Fullerenes in the Environmental Stability of Polymer:Fullerene Solar Cells. *Energy and Environmental Science* **11**, 417–428 (2018).
234. Brumboiu, I. E. *et al.:* The Influence of Oxygen Adsorption on the NEXAFS and Core-Level XPS Spectra of the C60 Derivative PCBM. *Journal of Chemical Physics* **142**, 054306 (2015).
235. Guo, J. *et al.:* Suppressing Photo-Oxidation of Non-Fullerene Acceptors and Their Blends in Organic Solar Cells by Exploring Material Design and Employing Friendly Stabilizers. *Journal of Materials Chemistry A* **7**, 25088–25101 (2019).
236. Luke, J. *et al.:* Twist and Degrade—Impact of Molecular Structure on the Photostability of Nonfullerene Acceptors and Their Photovoltaic Blends. *Advanced Energy Materials* **9** (2019).

237. Cha, H. *et al.:* An Efficient, "Burn in" Free Organic Solar Cell Employing a Nonfullerene Electron Acceptor. *Advanced Materials* **29**, 1–8 (2017).
238. Gasparini, N. *et al.:* Burn-in Free Nonfullerene-Based Organic Solar Cells. *Advanced Energy Materials* **7**, 1–7 (2017).
239. Doumon, N. Y. *et al.:* Energy Level Modulation of ITIC Derivatives: Effects on the Photodegradation of Conventional and Inverted Organic Solar Cells. *Organic Electronics* **69**, 255–262 (June 2019).
240. Zhang, W. *et al.:* Highly Planar Cross-Conjugated Alternating Polymers with Multiple Conformational Locks: Synthesis, Characterization and Their Field-Effect Properties. *Journal of Materials Chemistry C* **4**, 9266–9275 (Oct. 2016).
241. Zhang, Z. *et al.:* Conformation Locking on Fused-Ring Electron Acceptor for High-Performance Nonfullerene Organic Solar Cells. *Advanced Functional Materials* **28**, 1–8 (2018).
242. Liu, Y. *et al.:* Exploiting Noncovalently Conformational Locking as a Design Strategy for High Performance Fused-Ring Electron Acceptor Used in Polymer Solar Cells. *J. Am. Chem. Soc.* **139**, 3356–3359 (Mar. 2017).
243. Xin, Y., Zeng, G., Ouyang, J. Y., Zhao, X. & Yang, X.: Enhancing Thermal Stability of Nonfullerene Organic Solar Cells: Via Fluoro-Side-Chain Engineering. *Journal of Materials Chemistry C* **7**, 9513–9522 (2019).
244. Wang, Y. *et al.:* Stability of Nonfullerene Organic Solar Cells: From Built-in Potential and Interfacial Passivation Perspectives. *Advanced Energy Materials* **9**, 1900157 (2019).
245. Xiao, J. *et al.:* An Operando Study on the Photostability of Nonfullerene Organic Solar Cells. *Solar RRL* **3**, 1–9 (2019).
246. Li, W. *et al.:* Retarding the Crystallization of a Nonfullerene Electron Acceptor for High-Performance Polymer Solar Cells. *Advanced Functional Materials* **29**, 1–8 (2019).
247. Yu, L. *et al.:* Diffusion-Limited Crystallization: A Rationale for the Thermal Stability of Non-Fullerene Solar Cells. *ACS Applied Materials and Interfaces* (2019).
248. Upama, M. B. *et al.:* Effect of Annealing Dependent Blend Morphology and Dielectric Properties on the Performance and Stability of Non-Fullerene Organic Solar Cells. *Solar Energy Materials and Solar Cells* **176**, 109–118 (Mar. 2018).
249. Yang, X. *et al.:* Suppressing Thermally Induced Fullerene Aggregation in Organic Solar Cells by Employing Plastic Network. *Journal of Physical Chemistry C* **122**, 9843–9851 (May 2018).
250. Gasparini, N. *et al.:* Exploiting Ternary Blends for Improved Photostability in High-Efficiency Organic Solar Cells. *ACS Energy Letters* **51**, 1371–1379 (2020).
251. Shi, M. *et al.:* Two Similar Near-Infrared (IR) Non-Fullerene Acceptors as near IR Sensitizers for Ternary Solar Cells. *Organic Electronics* **85**, 1566–1199 (Oct. 2020).

252. Zheng, N. *et al.:* Improving the Efficiency and Stability of Non-Fullerene Polymer Solar Cells by Using N2200 as the Additive. *Nano Energy* **58**, 724–731 (Apr. 2019).
253. Yin, H. *et al.:* Enhanced Electron Transport and Heat Transfer Boost Light Stability of Ternary Organic Photovoltaic Cells Incorporating Non-Fullerene Small Molecule and Polymer Acceptors. *Advanced Electronic Materials* **5**, 1–10 (2019).
254. Wood, S., Hollis, J. R. & Kim, J. S.: Raman Spectroscopy as an Advanced Structural Nanoprobe for Conjugated Molecular Semiconductors. *Journal of Physics D: Applied Physics* **50**, 073001 (Jan. 2017).
255. Cheng, P. & Zhan, X.: Stability of Organic Solar Cells: Challenges and Strategies. *Chemical Society Reviews* **45**, 2544–2582 (2016).
256. Diao, Y., Shaw, L., Bao, Z. & B. Mannsfeld, S. C.: Morphology Control Strategies for Solution-Processed Organic Semiconductor Thin Films. *Energy & Environmental Science* **7**, 2145–2159 (2014).
257. Huang, Y., Kramer, E. J., Heeger, A. J. & Bazan, G. C.: Bulk Heterojunction Solar Cells: Morphology and Performance Relationships. *Chem. Rev.* **114**, 7006–7043 (July 2014).
258. Wood, S. *et al.:* Natures of Optical Absorption Transitions and Excitation Energy Dependent Photostability of Diketopyrrolopyrrole (DPP)-Based Photovoltaic Copolymers. *Energy and Environmental Science* **8**, 3222–3232 (2015).
259. Tsoi, W. C. *et al.:* The Nature of In-Plane Skeleton Raman Modes of P3HT and Their Correlation to the Degree of Molecular Order in P3HT : PCBM Blend Thin Films, 9834–9843 (2011).
260. Tsoi, W. C. *et al.:* In-Situ Monitoring of Molecular Vibrations of Two Organic Semiconductors in Photovoltaic Blends and Their Impact on Thin Film Morphology. *Applied Physics Letters* **102**, 173302 (Apr. 2013).
261. Razzell-Hollis, J. *et al.:* Photochemical Stability of High Efficiency PTB7:PC70BM Solar Cell Blends. *J. Mater. Chem. A* **2**, 20189–20195 (Nov. 2014).
262. Stewart, K. *et al.:* Molecular Understanding of a π-Conjugated Polymer/Solid-State Ionic Liquid Complex as a Highly Sensitive and Selective Gas Sensor. *Journal of Materials Chemistry C* **8**, 15268–15276 (2020).
263. Limbu, S. *et al.:* Solid-State Ionic Liquid: Key to Efficient Detection and Discrimination in Organic Semiconductor Gas Sensors. *ACS Appl. Electron. Mater.* **3**, 2152–2163 (May 2021).
264. Nightingale, J. *et al.:* Small Molecule Additive for Low-Power Accumulation Mode Organic Electrochemical Transistors. *Journal of Materials Chemistry C* **8**, 8846–8855 (2020).
265. Baikie, I. D., Grain, A. C., Sutherland, J. & Law, J.: Ambient Pressure Photoemission Spectroscopy of Metal Surfaces. *Applied Surface Science* **323**, 45–53 (2014).

266. Fowler, R. H.: The Analysis of Photoelectric Sensitivity Curves for Clean Metals at Various Temperatures. *Phys. Rev.* **38**, 45–56 (July 1931).
267. Baikie, I. D., Grain, A. C., Sutherland, J. & Law, J.: Dual Mode Kelvin Probe: Featuring Ambient Pressure Photoemission Spectroscopy and Contact Potential Difference. *Energy Procedia. Advanced Materials and Characterization Techniques for Solar Cells II* **60**, 48–56 (Jan. 2014).
268. Wu, J. *et al.:* Exceptionally Low Charge Trapping Enables Highly Efficient Organic Bulk Heterojunction Solar Cells. *Energy & Environmental Science* (2020).
269. Baikie, I. D. & Estrup, P. J.: Low Cost PC Based Scanning Kelvin Probe. *Review of Scientific Instruments* **69**, 3902–3907 (Nov. 1998).
270. Daboczi, M. *et al.:* Origin of Open-Circuit Voltage Losses in Perovskite Solar Cells Investigated by Surface Photovoltage Measurement. *ACS Appl. Mater. Interfaces* **11**, 46808–46817 (2019).
271. Daboczi, M. *et al.:* Optimal Interfacial Band Bending Achieved by Fine Energy Level Tuning in Mixed-Halide Perovskite Solar Cells. *ACS Energy Lett.* **6**, 3970–3981 (Nov. 2021).
272. Chin, Y.-C., Daboczi, M., Henderson, C., Luke, J. & Kim, J.-S.: Suppressing PEDOT:PSS Doping-Induced Interfacial Recombination Loss in Perovskite Solar Cells. *ACS Energy Lett.* **7**, 560–568 (Feb. 2022).
273. Cai, Y. *et al.:* Vertically Optimized Phase Separation with Improved Exciton Diffusion Enables Efficient Organic Solar Cells with Thick Active Layers. *Nat Commun* **13**, 2369 (May 2022).
274. Perdigón-Toro, L. *et al.:* Excitons Dominate the Emission from PM6:Y6 Solar Cells but This Does Not Help the Open-Circuit Voltage of the Device, 15.
275. Burke, K. & Wagner, L. O.: DFT in a Nutshell. *International Journal of Quantum Chemistry* **113**, 96–101 (2013).
276. *G09 | Gaussian.Com* https://gaussian.com/glossary/g09/.
277. Besler, B. H., Merz, K. M. & Kollman, P. A.: Atomic Charges Derived from Semiempirical Methods. *Journal of Computational Chemistry* **11**, 431–439 (May 1990).
278. Sivaprakash, S., Prakash, S., Mohan, S. & Jose, S. P.: Molecular Structure, Vibrational Analysis (IR and Raman) and Quantum Chemical Investigations of 1-Aminoisoquinoline. *Journal of Molecular Structure* **1149**, 835–845 (2017).
279. Jiang, Y. *et al.:* Photocatalytic Effect of ZnO on the Stability of Nonfullerene Acceptors and Its Mitigation by SnO2 for Nonfullerene Organic Solar Cells. *Mater. Horiz.* **6**, 1438–1443 (Aug. 2019).
280. Miao, T. J. & Tang, J.: Characterization of Charge Carrier Behavior in Photocatalysis Using Transient Absorption Spectroscopy. *J. Chem. Phys.* **152**, 194201 (May 2020).

281. Credgington, D., Hamilton, R., Atienzar, P., Nelson, J. & Durrant, J. R.: Non-Geminate Recombination as the Primary Determinant of Open-Circuit Voltage in Polythiophene:Fullerene Blend Solar Cells: An Analysis of the Influence of Device Processing Conditions. *Advanced Functional Materials* **21**, 2744–2753 (2011).

282. Mahmood, A. & Wang, J.-L.: A Review of Grazing Incidence Small- and Wide-Angle X-Ray Scattering Techniques for Exploring the Film Morphology of Organic Solar Cells. *Solar RRL* **4**, 2000337 (2020).

283. Zhang, J., Tan, H. S., Guo, X., Facchetti, A. & Yan, H.: Material Insights and Challenges for Non-Fullerene Organic Solar Cells Based on Small Molecular Acceptors. *Nature Energy* **3**, 720–731 (2018).

284. Chen, W. & Zhang, Q.: Recent Progress in Non-Fullerene Small Molecule Acceptors in Organic Solar Cells (OSCs). *Journal of Materials Chemistry C* **5**, 1275–1302 (2017).

285. Chen, Y., Wan, X. & Long, G.: High Performance Photovoltaic Applications Using Solution-Processed Small Molecules. *Accounts of Chemical Research* **46**, 2645–2655 (2013).

286. Du, X. *et al.:* Efficient Polymer Solar Cells Based on Non- Fullerene Acceptors with Potential Device Lifetime Approaching 10 Years Efficient Polymer Solar Cells Based on Non-fullerene Acceptors with Potential Device Lifetime Approaching 10 Years. *Joule,* 1–12 (2018).

287. Bauer, N. *et al.:* Comparing Non-Fullerene Acceptors with Fullerene in Polymer Solar Cells: A Case Study with FTAZ and PyCNTAZ. *Journal of Materials Chemistry A* **5**, 4886–4893 (2017).

288. Yao, H. *et al.:* Design and Synthesis of a Low Bandgap Small Molecule Acceptor for Efficient Polymer Solar Cells. *Advanced Materials* **28**, 8283–8287 (2016).

289. Gao, L. *et al.:* High-Efficiency Nonfullerene Polymer Solar Cells with Medium Bandgap Polymer Donor and Narrow Bandgap Organic Semiconductor Acceptor. *Advanced Materials* **28**, 8288–8295 (2016).

290. Lin, Y. *et al.:* A Facile Planar Fused-Ring Electron Acceptor for As-Cast Polymer Solar Cells with 8.71% Efficiency. *Journal of the American Chemical Society* **138**, 2973–2976 (2016).

291. Li, Y. *et al.:* A Near-Infrared Non-Fullerene Electron Acceptor for High Performance Polymer Solar Cells. *Energy and Environmental Science* **10**, 1610–1620 (July 2017).

292. Zhang, Z. *et al.:* Energy-Level Modulation of Non-Fullerene Acceptors to Achieve High-Efficiency Polymer Solar Cells at a Diminished Energy Offset. *Journal of Materials Chemistry A* **5**, 9649–9654 (2017).

293. Fei, Z. *et al.:* Correction to: An Alkylated Indacenodithieno[3,2-b]Thiophene-Based Nonfullerene Acceptor with High Crystallinity Exhibiting Single Junction Solar

Cell Efficiencies Greater than 13% with Low Voltage Losses (Adv. Mater., (2018), 30, (1705209), 10.1002/Adma. *Advanced Materials* **30**, 1–7 (2018).

294. Yu, Y. Y., Tsai, T. W., Yang, C. C. & Chen, C. P.: Highly Efficient Non-Fullerene Organic Photovoltaics Processed from o-Xylene without Using Additives. *Journal of Physical Chemistry C* **121**, 21969–21974 (2017).
295. Chen, H.: Electron-Deficient Core Fused-Ring Based Non-Fullerene Acceptor Enables over 15% Efficiency in Single Junction Organic Solar Cells. *Science China Chemistry* **62**, 403–404 (Apr. 2019).
296. Jiang, W. *et al.:* Ternary Nonfullerene Polymer Solar Cells with 12.16% Efficiency by Introducing One Acceptor with Cascading Energy Level and Complementary Absorption. *Advanced Materials* **30**, 1703005 (Jan. 2018).
297. Zhan, L. *et al.:* Over 17% Efficiency Ternary Organic Solar Cells Enabled by Two Non-Fullerene Acceptors Working in an Alloy-like Model. *Energy and Environmental Science* **13**, 635–645 (2020).
298. Distler, A. *et al.:* The Effect of PCBM Dimerization on the Performance of Bulk Heterojunction Solar Cells. *Advanced Energy Materials* **4**, 1–6 (2014).
299. Heumueller, T. *et al.:* Reducing Burn-in Voltage Loss in Polymer Solar Cells by Increasing the Polymer Crystallinity. *Energy and Environmental Science* **7**, 2974–2980 (2014).
300. Speller, E. M. *et al.:* Impact of Aggregation on the Photochemistry of Fullerene Films: Correlating Stability to Triplet Exciton Kinetics. *ACS Appl. Mater. Interfaces* **9**, 22739–22747 (July 2017).
301. Peters, C. H. *et al.:* The Mechanism of Burn-in Loss in a High Efficiency Polymer Solar Cell. *Advanced Materials* **24**, 663–668 (2012).
302. Doumon, N. Y. *et al.:* Photostability of Fullerene and Non-Fullerene Polymer Solar Cells: The Role of the Acceptor. *ACS Applied Materials and Interfaces* **11**, 8310–8318 (Feb. 2019).
303. Park, S. & Son, H. J.: Intrinsic Photo-Degradation and Mechanism of Polymer Solar Cells: The Crucial Role of Non-Fullerene Acceptors. *Journal of Materials Chemistry A* **7**, 25830–25837 (2019).
304. Wang, Y. *et al.:* Recent Progress and Challenges toward Highly Stable Nonfullerene Acceptor-Based Organic Solar Cells. *Advanced Energy Materials* **11** (Feb. 2021).
305. Yu, H. *et al.:* Tailoring Non-Fullerene Acceptors Using Selenium-Incorporated Heterocycles for Organic Solar Cells with over 16% Efficiency. *J. Mater. Chem. A* **8**, 23756–23765 (Nov. 2020).
306. Fan, B., Lin, F., Wu, X., Zhu, Z. & Jen, A. K.-Y.: Selenium-Containing Organic Photovoltaic Materials. *Acc. Chem. Res.* **54**, 3906–3916 (Oct. 2021).

307. Li, Y. *et al.:* Non-Fullerene Polymer Solar Cells Based on a Selenophene-Containing Fused-Ring Acceptor with Photovoltaic Performance of 8.6%. *Energy and Environmental Science* **9**, 3429–3435 (2016).
308. Wang, J. L. *et al.:* Selenopheno[3,2-b]Thiophene-Based Narrow-Bandgap Nonfullerene Acceptor Enabling 13.3% Efficiency for Organic Solar Cells with Thickness-Insensitive Feature. *ACS Energy Letters* **3**, 2967–2976 (2018).
309. Tsai, C. E. *et al.:* Synthesis of a 4,9-Didodecyl Angular-Shaped Naphthodiselenophene Building Block to Achieve High-Mobility Transistors. *Chemistry of Materials* **28**, 5121–5130 (2016).
310. Fan, B. *et al.:* Formation of Vitrified Solid Solution Enables Simultaneously Efficient and Stable Organic Solar Cells. *ACS Energy Lett.* **6**, 3522–3529 (Oct. 2021).
311. Li, S. *et al.:* Energy-Level Modulation of Small-Molecule Electron Acceptors to Achieve over 12% Efficiency in Polymer Solar Cells. *Advanced Materials* **28**, 9423–9429 (2016).
312. Yang, Y. *et al.:* Side-Chain Isomerization on an n-Type Organic Semiconductor ITIC Acceptor Makes 11.77% High Efficiency Polymer Solar Cells. *Journal of the American Chemical Society* **138**, 15011–15018 (Nov. 2016).
313. Lin, Y. *et al.:* An Electron Acceptor Challenging Fullerenes for Efficient Polymer Solar Cells. *Advanced Materials* **27**, 1170–1174 (2015).
314. Zhao, W. *et al.:* Fullerene-Free Polymer Solar Cells with over 11% Efficiency and Excellent Thermal Stability. *Advanced Materials* **28**, 4734–4739 (2016).
315. Bi, P. *et al.:* Dual Förster Resonance Energy Transfer Effects in Non-Fullerene Ternary Organic Solar Cells with the Third Component Embedded in the Donor and Acceptor. *Journal of Materials Chemistry A* **5**, 12120–12130 (2017).
316. Más-Montoya, M. & Janssen, R. A.: The Effect of H- and J-Aggregation on the Photophysical and Photovoltaic Properties of Small Thiophene–Pyridine–DPP Molecules for Bulk-Heterojunction Solar Cells. *Advanced Functional Materials* **27** (Apr. 2017).
317. Lin, F. *et al.:* Regio-Specific Selenium Substitution in Non-Fullerene Acceptors for Efficient Organic Solar Cells. *Chemistry of Materials* **31**, 6770–6778 (Sept. 2019).
318. Liao, H. C. *et al.:* Bi-Hierarchical Nanostructures of Donor-Acceptor Copolymer and Fullerene for High Efficient Bulk Heterojunction Solar Cells. *Energy and Environmental Science* **6**, 1938–1948 (2013).
319. Ma, R. *et al.:* Adding a Third Component with Reduced Miscibility and Higher LUMO Level Enables Efficient Ternary Organic Solar Cells. *ACS Energy Letters* **5**, 2711–2720 (2020).
320. Yang, T. *et al.:* A Compatible Polymer Acceptor Enables Efficient and Stable Organic Solar Cells as a Solid Additive. *Journal of Materials Chemistry A* **8**, 17706–17712 (Sept. 2020).

321. Newman, M. J. *et al.:* Photo-Stability Study of a Solution-Processed Small Molecule Solar Cell System: Correlation between Molecular Conformation and Degradation. *Science and Technology of Advanced Materials* **19**, 194–202 (2018).
322. Bristow, H. *et al.:* Impact of Nonfullerene Acceptor Side Chain Variation on Transistor Mobility. *Advanced Electronic Materials* **5**, 1900344 (Oct. 2019).
323. Han, G., Guo, Y., Song, X., Wang, Y. & Yi, Y.: Terminal π-π Stacking Determines Three-Dimensional Molecular Packing and Isotropic Charge Transport in an A-π-A Electron Acceptor for Non-Fullerene Organic Solar Cells. *Journal of Materials Chemistry C* **5**, 4852–4857 (2017).
324. Sun, H. *et al.:* PDI Derivative through Fine-Tuning the Molecular Structure for Fullerene-Free Organic Solar Cells. *ACS Applied Materials and Interfaces* **9**, 29924–29931 (2017).
325. Fan, X. *et al.:* Ladder-Type Nonacyclic Arene Bis(Thieno[3,2-b]Thieno)Cyclopentafluorene as a Promising Building Block for Non-Fullerene Acceptors. *Chemistry - An Asian Journal* **14**, 1814–1822 (May 2019).
326. Ma, X. *et al.:* Achieving 14.11% Efficiency of Ternary Polymer Solar Cells by Simultaneously Optimizing Photon Harvesting and Exciton Distribution. *Journal of Materials Chemistry A* **7**, 7843–7851 (2019).
327. Martino, N., Ghezzi, D., Benfenati, F., Lanzani, G. & Antognazza, M. R.: Organic Semiconductors for Artificial Vision. *Journal of Materials Chemistry B* **1**, 3768–3780 (Aug. 2013).
328. Dong, T. & Pires, N. M. M.: Immunodetection of Salivary Biomarkers by an Optical Microfluidic Biosensor with Polyethylenimine-Modified Polythiophene-C70 Organic Photodetectors. *Biosensors and Bioelectronics* **94**, 321–327 (2017).
329. Pires, N. M. M., Dong, T. & Yang, Z.: A Fluorimetric Nitrite Biosensor with Polythienothiophene-Fullerene Thin Film Detectors for on-Site Water Monitoring. *Analyst* **144**, 4342–4350 (July 2019).
330. Chow, P. C. Y. & Someya, T.: Organic Photodetectors for Next-Generation Wearable Electronics. *Advanced Materials* **1902045**, 1902045 (2019).
331. Baeg, K. J., Binda, M., Natali, D., Caironi, M. & Noh, Y. Y.: Organic Light Detectors: Photodiodes and Phototransistors. *Advanced Materials* **25**, 4267–4295 (Aug. 2013).
332. Manousiadis, P. P., Yoshida, K., Turnbull, G. A. & Samuel, I. D.: Organic Semiconductors for Visible Light Communications. *Philosophical Transactions of the Royal Society A: Mathematical, Physical and Engineering Sciences* **378** (2020).
333. Clark, J. & Lanzani, G.: Organic Photonics for Communications. *Nature Photonics* **4**, 438–446 (July 2010).
334. Han, M. G. *et al.:* Narrow-Band Organic Photodiodes for High-Resolution Imaging. *ACS Applied Materials and Interfaces* **8**, 26143–26151 (2016).

335. Lee, G. H. *et al.:* Energy Gap between Photoluminescence and Electroluminescence as Recombination Indicator in Organic Small-Molecule Photodiodes. *Journal of Physical Chemistry C* **120**, 10176–10184 (May 2016).
336. Yan, C. *et al.:* Non-Fullerene Acceptors for Organic Solar Cells. *Nature Reviews Materials* **3**, 1–19 (2018).
337. Bulliard, X. *et al.:* Dipolar Donor–Acceptor Molecules in the Cyanine Limit for High Efficiency Green-Light-Selective Organic Photodiodes. *J. Mater. Chem. C* **4**, 1117–1125 (Jan. 2016).
338. Armin, A. *et al.:* Thick Junction Broadband Organic Photodiodes. *Laser & Photonics Reviews* **8**, 924–932 (Nov. 2014).
339. Jansen-van Vuuren, R. D., Armin, A., Pandey, A. K., Burn, P. L. & Meredith, P.: Organic Photodiodes: The Future of Full Color Detection and Image Sensing. *Advanced Materials* **28**, 4766–4802 (June 2016).
340. Kato, K.: Ultrawide-Band / High-Frequency Photodetectors. *IEEE TRANSACTIONS ON MICROWAVE THEORY AND TECHNIQUES* **47**, 1265–1281 (1999).
341. Batignani, G. *et al.:* Probing Femtosecond Lattice Displacement upon Photo-Carrier Generation in Lead Halide Perovskite. *Nature Communications* **9**, 1971 (Dec. 2018).
342. Cinquanta, E. *et al.:* Ultrafast THz Probe of Photoinduced Polarons in Lead-Halide Perovskites. *Physical Review Letters* **122**, 166601 (Apr. 2019).
343. Strobel, T., Deibel, C. & Dyakonov, V.: Role of Polaron Pair Diffusion and Surface Losses in Organic Semiconductor Devices. *Physical Review Letters* **105**, 266602 (Dec. 2010).
344. Baker, W. J., Keevers, T. L., Lupton, J. M., McCamey, D. R. & Boehme, C.: Slow Hopping and Spin Dephasing of Coulombically Bound Polaron Pairs in an Organic Semiconductor at Room Temperature. *Physical Review Letters* **108**, 267601 (June 2012).
345. Asadi, K. *et al.:* Polaron Hopping Mediated by Nuclear Tunnelling in Semiconducting Polymers at High Carrier Density. *Nature Communications* **4**, 1710 (June 2013).
346. Wu, J. *et al.:* A Comparison of Charge Carrier Dynamics in Organic and Perovskite Solar Cells. *Advanced Materials* **34**, 2101833 (2022).
347. Arca, F. *et al.:* Interface Trap States in Organic Photodiodes. *Scientific Reports* **3**, 1324 (Dec. 2013).
348. Bisquert, J.: On Voltage, Photovoltage, and Photocurrent in Bulk Heterojunction Organic Solar Cells, 1950–1964 (2011).
349. Street, R. A.: Localized State Distribution and Its Effect on Recombination in Organic Solar Cells. **075208** (2011).

350. Gorenflot, J. *et al.:* Nongeminate Recombination in Neat P3HT and P3HT:PCBM Blend Films. *Journal of Applied Physics* **115** (2014).
351. Kirchartz, T., Pieters, B. E., Kirkpatrick, J., Rau, U. & Nelson, J.: Recombination via Tail States in Polythiophene : Fullerene Solar Cells. **115209**, 1–13 (2011).
352. Shuttle, C. G. *et al.:* Charge Extraction Analysis of Charge Carrier Densities in a Polythiophene/Fullerene Solar Cell: Analysis of the Origin of the Device Dark Current. *Applied Physics Letters* **93**, 183501 (Nov. 2008).
353. Shuttle, C. G., Hamilton, R., Nelson, J., O'Regan, B. C. & Durrant, J. R.: Measurement of Charge-Density Dependence of Carrier Mobility in an Organic Semiconductor Blend. *Advanced Functional Materials* **20**, 698–702 (Mar. 2010).
354. Melianas, A. *et al.:* Photo-Generated Carriers Lose Energy during Extraction from Polymer-Fullerene Solar Cells. *Nature Communications* **6**, 8778 (Dec. 2015).
355. Miller, A. & Abrahams, E.: Impurity Conduction at Low Concentrations. *Physical Review* **120**, 745–755 (Nov. 1960).
356. Bässler, H.: Charge Transport in Disordered Organic Photoconductors a Monte Carlo Simulation Study. *physica status solidi (b)* **175**, 15–56 (Jan. 1993).
357. Shuttle, C. G. *et al.:* Experimental Determination of the Rate Law for Charge Carrier Decay in a Polythiophene: Fullerene Solar Cell. *Applied Physics Letters* **92**, 093311 (Mar. 2008).
358. Zarrabi, N. *et al.:* Charge-Generating Mid-Gap Trap States Define the Thermodynamic Limit of Organic Photovoltaic Devices.
359. Ren, Y. *et al.:* Gate-Tunable Synaptic Plasticity through Controlled Polarity of Charge Trapping in Fullerene Composites. *Advanced Functional Materials* **28**, 1805599 (2018).
360. Shubina, T. E. *et al.:* Fullerene Van Der Waals Oligomers as Electron Traps. *J. Am. Chem. Soc.* **136**, 10890–10893 (Aug. 2014).
361. Du, X. *et al.:* Excimer Emission Induced Intra-System Self-Absorption Enhancement-a Novel Strategy to Realize High Efficiency and Excellent Stability Ternary Organic Solar Cells Processed in Green Solvents. *Journal of Materials Chemistry A* **6**, 23840–23855 (2018).
362. Musser, A. J. *et al.:* Intermolecular States in Organic Dye Dispersions: Excimers vs. Aggregates. *J. Mater. Chem. C* **5**, 8380–8389 (2017).
363. Yoo, H., Yang, J., Yousef, A., Wasielewski, M. R. & Kim, D.: Excimer Formation Dynamics of Intramolecular π-Stacked Perylenediimides Probed by Single-Molecule Fluorescence Spectroscopy. *J. Am. Chem. Soc.* **132**, 3939–3944 (Mar. 2010).
364. Nightingale, J., Wade, J., Moia, D., Nelson, J. & Kim, J.-S.: Impact of Molecular Order on Polaron Formation in Conjugated Polymers. *J. Phys. Chem. C* **122**, 29129–29140 (Dec. 2018).
365. Gao, Y. & Grey, J. K.: Resonance Chemical Imaging of Polythiophene/Fullerene Photovoltaic Thin Films: Mapping Morphology-Dependent Aggregated and

Unaggregated C=C Species. *Journal of the American Chemical Society* **131**, 9654–9662 (July 2009).

366. Socci, J., Salzillo, T., Della Valle, R. G., Venuti, E. & Brillante, A.: Fast Identification of Rubrene Polymorphs by Lattice Phonon Raman Microscopy. *Solid State Sciences* **71**, 146–151 (Sept. 2017).
367. Janaki, J., Premila, M., Gopalan, P., Sastry, V. S. & Sundar, C. S.: Thermal Stability of a Fullerene-Amine Adduct. *Thermochimica Acta* **356**, 109–116 (Aug. 2000).
368. Egli, M. & Sarkhel, S.: Lone Pair-Aromatic Interactions: To Stabilize or Not to Stabilize. *Acc. Chem. Res.* **40**, 197–205 (Mar. 2007).
369. Mooibroek, T. J., Gamez, P. & Reedijk, J.: Lone Pair–π Interactions: A New Supramolecular Bond? *CrystEngComm* **10**, 1501–1515 (Nov. 2008).
370. Cheng, P., Li, G., Zhan, X. & Yang, Y.: Next-Generation Organic Photovoltaics Based on Non-Fullerene Acceptors /639/301/299/946 /639/624/399 Review-Article. *Nature Photonics* **12**, 131–142 (2018).
371. Zhang, J., Tan, H. S., Guo, X., Facchetti, A. & Yan, H.: Material Insights and Challenges for Non-Fullerene Organic Solar Cells Based on Small Molecular Acceptors. *Nature Energy* **3**, 720–731 (2018).
372. Kim, J. H. *et al.:* An Efficient Narrowband Near-Infrared at 1040 Nm Organic Photodetector Realized by Intermolecular Charge Transfer Mediated Coupling Based on a Squaraine Dye. *Advanced Materials* **33**, 2100582 (2021).
373. Wang, Y. *et al.:* Narrowband Organic Photodetectors – towards Miniaturized, Spectroscopic Sensing. *Materials Horizons* **9**, 220–251 (2022).
374. Wei, Y. *et al.:* Self-Powered Organic Photodetectors with High Detectivity for Near Infrared Light Detection Enabled by Dark Current Reduction. *Advanced Functional Materials* **31**, 2106326 (2021).
375. Eun, H. J. *et al.:* Strain-Durable Dark Current in near-Infrared Organic Photodetectors for Skin-Conformal Photoplethysmographic Sensors. *iScience* **25**, 104194 (May 2022).
376. Vandewal, K. *et al.:* Increased Open-Circuit Voltage of Organic Solar Cells by Reduced Donor-Acceptor Interface Area. *Advanced Materials* **26**, 3839–3843 (2014).
377. Fratini, S., Nikolka, M., Salleo, A., Schweicher, G. & Sirringhaus, H.: Charge Transport in High-Mobility Conjugated Polymers and Molecular Semiconductors. *Nat. Mater.* **19**, 491–502 (May 2020).
378. Dong, H., Fu, X., Liu, J., Wang, Z. & Hu, W.: 25th Anniversary Article: Key Points for High-Mobility Organic Field-Effect Transistors. *Advanced Materials* **25**, 6158–6183 (2013).

379. Vandewal, K., Himmelberger, S. & Salleo, A.: Structural Factors That Affect the Performance of Organic Bulk Heterojunction Solar Cells. *Macromolecules* **46**, 6379–6387 (Aug. 2013).

380. Zhen-Chuan, W. *et al.:* V OC Variation with Different Molecular Weight Fractions in Highly Efficient Organic Photovoltaic Bulk Heterojunctions. *Journal of Physics D: Applied Physics J. Phys. D: Appl. Phys* **54**, 8 (2021).

381. Yao, N. *et al.:* Efficient Charge Transport Enables High Efficiency in Dilute Donor Organic Solar Cells. *J. Phys. Chem. Lett.* **12**, 5039–5044 (May 2021).

382. Yao, N. *et al.:* Solution-Processed Highly Efficient Semitransparent Organic Solar Cells with Low Donor Contents. *ACS Appl. Energy Mater.* **4**, 14335–14341 (Dec. 2021).

383. Schopp, N. *et al.:* Unraveling Device Physics of Dilute-Donor Narrow-Bandgap Organic Solar Cells with Highly Transparent Active Layers (Adv. Mater. 31/2022). *Advanced Materials* **34**, 2270226 (2022).

384. Zhou, G. *et al.:* Spontaneous Carrier Generation and Low Recombination in High-Efficiency Non-Fullerene Solar Cells. *Energy Environ. Sci.* (June 2022).

385. Vandewal, K. *et al.:* Varying Polymer Crystallinity in Nanofiber Poly(3-Alkylthiophene): PCBM Solar Cells: Influence on Charge-Transfer State Energy and Open-Circuit Voltage. *Appl. Phys. Lett.* **95**, 123303 (Sept. 2009).

386. Piersimoni, F. *et al.:* Influence of Fullerene Ordering on the Energy of the Charge-Transfer State and Open-Circuit Voltage in Polymer:Fullerene Solar Cells. *J. Phys. Chem. C* **115**, 10873–10880 (June 2011).

387. Tietze, M. L. *et al.:* Correlation of Open-Circuit Voltage and Energy Levels in Zinc-Phthalocyanine: C${}_{60}$ Bulk Heterojunction Solar Cells with Varied Mixing Ratio. *Phys. Rev. B* **88**, 085119 (Aug. 2013).

388. Tress, W. R., Pfützner, S., Leo, K. & Riede, M. K.: Open Circuit Voltage and IV Curve Shape of ZnPc:C60 Solar Cells with Varied Mixing Ratio and Hole Transport Layer. *JPE* **1**, 011114 (Jan. 2011).

389. Saggar, S. *et al.:* Toward Faster Organic Photodiodes: Tuning of Blend Composition Ratio. *Advanced Functional Materials* **31**, 2010661 (2021).

390. Zhu, L. *et al.:* Progress and Prospects of the Morphology of Non-Fullerene Acceptor Based High-Efficiency Organic Solar Cells. *Energy & Environmental Science* **14**, 4341–4357 (2021).

391. Moser, M., Wadsworth, A., Gasparini, N. & McCulloch, I.: Challenges to the Success of Commercial Organic Photovoltaic Products. *Advanced Energy Materials* **11**, 2100056 (2021).

392. Phan, S. & Luscombe, C. K.: Recent Advances in the Green, Sustainable Synthesis of Semiconducting Polymers. *Trends in Chemistry* **1**, 670–681 (Oct. 2019).

393. Zhang, Y. *et al.:* Thermally Stable All-Polymer Solar Cells with High Tolerance on Blend Ratios. *Advanced Energy Materials* **8**, 1800029 (2018).

394. Logothetidis, S.: Flexible Organic Electronic Devices: Materials, Process and Applications. *Materials Science and Engineering: B. 4th International Workshop on Nanosciences and Nanotechnologies (NN07)* **152**, 96–104 (Aug. 2008).
395. Wang, M., Baek, P., Akbarinejad, A., Barker, D. & Travas-Sejdic, J.: Conjugated Polymers and Composites for Stretchable Organic Electronics. *Journal of Materials Chemistry C* **7**, 5534–5552 (2019).
396. Más-Montoya, M. & Janssen, R. A.: The Effect of H- and J-Aggregation on the Photophysical and Photovoltaic Properties of Small Thiophene–Pyridine–DPP Molecules for Bulk-Heterojunction Solar Cells. *Advanced Functional Materials* **27** (2017).
397. Perdigón-Toro, L. *et al.:* Excitons Dominate the Emission from PM6:Y6 Solar Cells, but This Does Not Help the Open-Circuit Voltage of the Device. *ACS Energy Letters* **6**, 557–564 (2021).
398. Strobel, N. *et al.:* Color-Selective Printed Organic Photodiodes for Filterless Multichannel Visible Light Communication. *Advanced Materials* **32**, 1908258 (2020).
399. Yang, W. *et al.:* Mitigating Dark Current for High-Performance Near-Infrared Organic Photodiodes via Charge Blocking and Defect Passivation. *ACS Appl. Mater. Interfaces* **13**, 16766–16774 (Apr. 2021).
400. Wang, R. *et al.:* Charge Separation from an Intra-Moiety Intermediate State in the High-Performance PM6:Y6 Organic Photovoltaic Blend. *Journal of the American Chemical Society* **142**, 12751–12759 (July 2020).
401. Lee, T. H. *et al.:* Planar Organic Bilayer Heterojunctions Fabricated on Water with Ultrafast Donor-to-Acceptor Charge Transfer. *Solar RRL* **5**, 2100326 (2021).
402. Marin-Beloqui, J. *et al.:* Insight into the Origin of Trapping in Polymer/Fullerene Blends with a Systematic Alteration of the Fullerene to Higher Adducts. *J. Phys. Chem. C* **126**, 2708–2719 (Feb. 2022).
403. Miao, J., Du, M., Fang, Y. & Zhang, F.: Acceptor-Free Photomultiplication-Type Organic Photodetectors. *Nanoscale* **11**, 16406–16413 (Sept. 2019).
404. Zhao, Z. *et al.:* Photomultiplication Type Broad Response Organic Photodetectors with One Absorber Layer and One Multiplication Layer. *J. Phys. Chem. Lett.* **11**, 366–373 (Jan. 2020).
405. Natsuda, S.-i. *et al.:* Cascaded Energy Landscape as a Key Driver for Slow yet Efficient Charge Separation with Small Energy Offset in Organic Solar Cells. *Energy Environ. Sci.* **15**, 1545–1555 (Apr. 2022).
406. Kaienburg, P. *et al.:* Assessing the Photovoltaic Quality of Vacuum-Thermal Evaporated Organic Semiconductor Blends. *Advanced Materials* **34**, 2107584 (2022).
407. Zhang, Z. & Lin, Y.: Organic Semiconductors for Vacuum-Deposited Planar Heterojunction Solar Cells. *ACS Omega* **5**, 24994–24999 (Oct. 2020).

408. Leung, L. M., Lo, W. Y., So, S. K., Lee, K. M. & Choi, W. K.: A High-Efficiency Blue Emitter for Small Molecule-Based Organic Light-Emitting Diode. *J. Am. Chem. Soc.* **122**, 5640–5641 (June 2000).
409. Terao, Y., Sasabe, H. & Adachi, C.: Correlation of Hole Mobility, Exciton Diffusion Length, and Solar Cell Characteristics in Phthalocyanine/Fullerene Organic Solar Cells. *Appl. Phys. Lett.* **90**, 103515 (Mar. 2007).
410. Sauvé, G. & Fernando, R.: Beyond Fullerenes: Designing Alternative Molecular Electron Acceptors for Solution-Processable Bulk Heterojunction Organic Photovoltaics. *J. Phys. Chem. Lett.* **6**, 3770–3780 (Sept. 2015).
411. Dupont, S. R., Oliver, M., Krebs, F. C. & Dauskardt, R. H.: Interlayer Adhesion in Roll-to-Roll Processed Flexible Inverted Polymer Solar Cells. *Solar Energy Materials and Solar Cells. Dedicated to the Global Organic Photovoltaics (GOPV) Conference in Hangzhou, China* **97**, 171–175 (Feb. 2012).
412. Pont, S., Foglia, F., Higgins, A. M., Durrant, J. R. & Cabral, J. T.: Stability of Polymer:PCBM Thin Films under Competitive Illumination and Thermal Stress. *Advanced Functional Materials* **28**, 1802520 (2018).
413. Heumueller, T. *et al.:* Morphological and Electrical Control of Fullerene Dimerization Determines Organic Photovoltaic Stability. *Energy and Environmental Science* **9**, 247–256 (2016).
414. Cnops, K. *et al.:* 8.4% Efficient Fullerene-Free Organic Solar Cells Exploiting Long-Range Exciton Energy Transfer. *Nat Commun* **5**, 3406 (Mar. 2014).
415. Verreet, B. *et al.:* A 4% Efficient Organic Solar Cell Using a Fluorinated Fused Subphthalocyanine Dimer as an Electron Acceptor. *Advanced Energy Materials* **1**, 565–568 (2011).
416. Lee, K.-H. *et al.:* Green-Sensitive Organic Photodetectors with High Sensitivity and Spectral Selectivity Using Subphthalocyanine Derivatives. *ACS Appl. Mater. Interfaces* **5**, 13089–13095 (Dec. 2013).
417. Claessens, C. G., González-Rodríguez, D., Rodríguez-Morgade, M. S., Medina, A. & Torres, T.: Subphthalocyanines, Subporphyrazines, and Subporphyrins: Singular Nonplanar Aromatic Systems. *Chem. Rev.* **114**, 2192–2277 (Feb. 2014).
418. Claessens, C. G., González-Rodríguez, D. & Torres, T.: Subphthalocyanines: Singular Nonplanar Aromatic CompoundsSynthesis, Reactivity, and Physical Properties. *Chem. Rev.* **102**, 835–854 (Mar. 2002).
419. Cnops, K. *et al.:* Energy Level Tuning of Non-Fullerene Acceptors in Organic Solar Cells. *J. Am. Chem. Soc.* **137**, 8991–8997 (July 2015).
420. Lee, K. H. *et al.:* Dynamic Characterization of Green-Sensitive Organic Photodetectors Using Nonfullerene Small Molecules: Frequency Response Based on the Molecular Structure. *Journal of Physical Chemistry C* **118**, 13424–13431 (2014).

421. Lim, S. J. *et al.:* Organic-on-Silicon Complementary Metal-Oxide-Semiconductor Colour Image Sensors. *Scientific Reports* **5**, 1–7 (Jan. 2015).
422. Keivanidis, P. E., Ho, P. K. H., Friend, R. H. & Greenham, N. C.: The Dependence of Device Dark Current on the Active-Layer Morphology of Solution-Processed Organic Photodetectors. *Advanced Functional Materials* **20**, 3895–3903 (2010).
423. Lee, C.-C. *et al.:* Vacuum-Processed Small Molecule Organic Photodetectors with Low Dark Current Density and Strong Response to Near-Infrared Wavelength. *Advanced Optical Materials* **8**, 2000519 (2020).
424. Armin, A., Jansen-van Vuuren, R. D., Kopidakis, N., Burn, P. L. & Meredith, P.: Narrowband Light Detection via Internal Quantum Efficiency Manipulation of Organic Photodiodes. *Nature Communications* **6**, 6343 (May 2015).
425. Park, J. B. *et al.:* Visible-Light-Responsive High-Detectivity Organic Photodetectors with a 1 Mm Thick Active Layer. *ACS Appl. Mater. Interfaces* **10**, 38294–38301 (Nov. 2018).
426. Kublitski, J. *Organic Semiconductor Devices for Light Detection* (ed Kublitski, J.) 117–149 (Springer International Publishing, Cham, 2022).
427. Nikolis, V. C. *et al.:* Field Effect versus Driving Force: Charge Generation in Small-Molecule Organic Solar Cells. *Advanced Energy Materials* **10**, 2002124 (2020).
428. Park, S. Y. *et al.:* Alkoxybenzothiadiazole-Based Fullerene and Nonfullerene Polymer Solar Cells with High Shunt Resistance for Indoor Photovoltaic Applications. *ACS Appl. Mater. Interfaces* **10**, 3885–3894 (Jan. 2018).
429. Park, S. Y. *et al.:* Non-Halogenated Diphenyl-Chalcogenide Solvent Processing Additives for High-Performance Polymer Bulk-Heterojunction Solar Cells. *RSC Adv.* **8**, 39777–39783 (Nov. 2018).
430. Brus, V. V.: Light Dependent Open-Circuit Voltage of Organic Bulk Heterojunction Solar Cells in the Presence of Surface Recombination. *Organic Electronics* **29**, 1–6 (Feb. 2016).
431. Wang, Y. *et al.:* The Critical Role of the Donor Polymer in the Stability of High-Performance Non-Fullerene Acceptor Organic Solar Cells. *Joule* **7**, 810–829 (Apr. 2023).
432. Zhang, X. *et al.:* A Potential Perylene Diimide Dimer-Based Acceptor Material for Highly Efficient Solution-Processed Non-Fullerene Organic Solar Cells with 4.03% Efficiency. *Advanced Materials* **25**, 5791–5797 (2013).
433. Holliday, S. *et al.:* A Rhodanine Flanked Nonfullerene Acceptor for Solution-Processed Organic Photovoltaics. *Journal of the American Chemical Society* **137**, 898–904 (2015).
434. Bai, H. *et al.:* An Electron Acceptor Based on Indacenodithiophene and 1,1-Dicyanomethylene-3-Indanone for Fullerene-Free Organic Solar Cells. *J. Mater. Chem. A* **3**, 1910–1914 (Jan. 2015).

435. Li, Y. *et al.:* A Fused-Ring Based Electron Acceptor for Efficient Non-Fullerene Polymer Solar Cells with Small HOMO Offset. *Nano Energy* **27**, 430–438 (Sept. 2016).
436. Liu, F. *et al.:* Efficient Semitransparent Solar Cells with High NIR Responsiveness Enabled by a Small-Bandgap Electron Acceptor. *Advanced Materials* **29** (2017).
437. Yao, H. *et al.:* Design, Synthesis, and Photovoltaic Characterization of a Small Molecular Acceptor with an Ultra-Narrow Band Gap. *Angewandte Chemie - International Edition* **56**, 3045–3049 (2017).
438. Yao, H. *et al.:* Achieving Highly Efficient Nonfullerene Organic Solar Cells with Improved Intermolecular Interaction and Open-Circuit Voltage. *Advanced Materials* **29**, 1700254 (2017).
439. Lu, B. *et al.:* Enhancing Performance of Fused-Ring Electron Acceptor Using Pyrrole Instead of Thiophene. *ACS Appl. Mater. Interfaces* **12**, 14029–14036 (Mar. 2020).
440. Huang, C. *et al.:* Highly Efficient Organic Solar Cells Based on S,N-Heteroacene Non-Fullerene Acceptors. *Chemistry of Materials* **30**, 5429–5434 (2018).
441. Zhou, Z. *et al.:* Subtle Molecular Tailoring Induces Significant Morphology Optimization Enabling over 16% Efficiency Organic Solar Cells with Efficient Charge Generation. *Advanced Materials* **32**, 1906324 (2020).
442. Zhang, Z. *et al.:* Selenium Heterocyclic Electron Acceptor with Small Urbach Energy for As-Cast High-Performance Organic Solar Cells. *J. Am. Chem. Soc.* **142**, 18741–18745 (Nov. 2020).
443. Lin, F., Jiang, K., Kaminsky, W., Zhu, Z. & Jen, A. K.-Y.: A Non-fullerene Acceptor with Enhanced Intermolecular π-Core Interaction for High-Performance Organic Solar Cells. *J. Am. Chem. Soc.* **142**, 15246–15251 (Sept. 2020).
444. Chai, G. *et al.:* Deciphering the Role of Chalcogen-Containing Heterocycles in Nonfullerene Acceptors for Organic Solar Cells. *ACS Energy Lett.* **5**, 3415–3425 (Nov. 2020).
445. Luo, M. *et al.:* A New Non-Fullerene Acceptor Based on the Heptacyclic Benzotriazole Unit for Efficient Organic Solar Cells. *Journal of Energy Chemistry* **42**, 169–173 (Mar. 2020).
446. Cui, Y. *et al.:* Single-Junction Organic Photovoltaic Cells with Approaching 18% Efficiency. *Advanced Materials* **32**, 1908205 (2020).
447. Zhang, Y. *et al.:* A New Non-Fullerene Acceptor Based on the Combination of a Heptacyclic Benzothiadiazole Unit and a Thiophene-Fused End Group Achieving over 13% Efficiency. *Phys. Chem. Chem. Phys.* **21**, 26557–26563 (Dec. 2019).
448. Yang, W. *et al.:* Simultaneous Enhanced Efficiency and Thermal Stability in Organic Solar Cells from a Polymer Acceptor Additive. *Nat Commun* **11**, 1218 (Mar. 2020).

449. Xu, X. *et al.:* Subtle Polymer Donor and Molecular Acceptor Design Enable Efficient Polymer Solar Cells with a Very Small Energy Loss. *Advanced Functional Materials* **30**, 1907570 (2020).

450. Luo, Z. *et al.:* Altering the Positions of Chlorine and Bromine Substitution on the End Group Enables High-Performance Acceptor and Efficient Organic Solar Cells. *Advanced Energy Materials* **10**, 2002649 (2020).

451. Lai, H. *et al.:* Trifluoromethylation Enables a 3D Interpenetrated Low-Band-Gap Acceptor for Efficient Organic Solar Cells. *Joule* **4**, 688–700 (Mar. 2020).

452. Qin, R. *et al.:* Tuning Terminal Aromatics of Electron Acceptors to Achieve High-Efficiency Organic Solar Cells. *J. Mater. Chem. A* **7**, 27632–27639 (Dec. 2019).

APPENDIX

A | Full Chemical Names

Short Chemical Name	Full Chemical Name
PCBM	[6,6]-phenyl-C_{61}-butyric acid methyl ester
ICMA	indene-C_{60} monoadduct
ICBA	indene-C_{60} bisadduct
PDI	perylene diimide
PBDTTT-C-T	poly[(2,6-(4,8-bis(5-(2-ethylhexyl)thiophen-2-yl)benzo[1,2-*b*:4,5-*b*′]dithiophene)-co-alkylcarbonyl-substituted-thieno[3,4-*b*]thiophene
P3TEA	poly[bis(2-octyldodecyl)5,5″-(5,6-difluorobenzo[*c*][1,2,5]thiadiazole-4,7-diyl)bis(4'-(2-hexylnonyl)-[2,2'-bithiophene]-3-carboxylate)]
FEHIDT	2,2′-((5,5′-(9,9-bis(2-ethylhexyl)-9H-fluorene-2,7-diyl)bis(thiophene-5,2-diyl))bis(methanylylidene))bis(1H-indene-1,3(2H)-dione)
P3HT	poly(3-hexylthiophene)
BT	benzothiadiazole
IDT	indacenodithiophene
IDTT	indacenodithieno[3,2-*b*]thiophene
DCI	(1,1-dicyanomethylene-3-indanone)
DC-IDT2T	1,1-dicyanomethylene-3-indanone-(1,3-di-(5-thiophene-2-yl))-indaceno[2,1-*b*:6,5-*b*′]dithiophene
ITIC	3,9-bis(2-methylene-(3-(1,1-dicyanomethylene)-indanone))-5,5,11,11-tetrakis(4-hexylphenyl)-dithieno[2,3-*d*:2′,3′-*d*′]-s-indaceno[1,2-*b*:5,6-*b*′]dithiophene
IDTIDT-IC	indacenodithiopheno-indacenodithiophene-3-(dicyanomethylidene)indan-1-one
IDTIDSe-IC	indacenodithiopheno-indacenodiselenophene-3-(dicyanomethylidene)indan-1-one

Short Chemical Name	Full Chemical Name
J51	poly[(5,6-difluoro-2-octyl-2H-benzotriazole-4,7-diyl)-2,5-thiophenediyl[4,8-bis[5-(2-hexyldecyl)-2-thienyl]benzo[1,2-*b*:4,5-*b*′]dithiophene-2,6-diyl]-2,5-thiophenediyl]
FBR	5,5′-[(9,9-dioctyl-9H-fluorene-2,7-diyl)bis(2,1,3-benzothiadiazole-7,4-diylmethylidyne)]bis[3-ethyl-2-thioxo-4-thiazolidinone]
IDT-2BR	indacenodithiophene-5-(benzo[*c*][1,2,5]thiadiazol-4-ylmethylene)-3-ethyl-2-thioxothiazo-lidin-4-one
O-IDTBR	rhodanine-benzothiadiazole-coupled indacenodithiophene, *n*-octyl side chains
O-IDFBR	(5Z,5′Z)-5,5′-((7,7′-(6,6,12,12-tetraoctyl-6,12-dihydroindeno[1,2-*b*]fluorene-2,8-diyl)bis(benzo[*c*][1,2,5]thiadiazole-7,4-diyl))bis(methanylylidene))bis(3-ethyl-2-thioxothiazolidin-4-one), *n*-octyl side chains
IDIC	2,2′-((2Z,2′Z)-((4,4,9,9-tetrahexyl-4,9-dihydro-s-indaceno[1,2-*b*:5,6-*b*′]dithiophene-2,7-diyl)bis(methanylylidene))bis(3-oxo-2,3-dihydro-1H-indene-2,1-diylidene))dimalononitrile
PDBT-T1	poly[[5,10-bis(5-octyl-2-thienyl)dithieno[2,3-*d*:2′,3′-*d*′]benzo[1,2-*b*:4,5-*b*′]dithiophene-2,7-diyl]-2,5-thiophenediyl[5,7-bis(2-ethylhexyl)-4,8-dioxo-4H,8H-benzo[1,2-*c*:4,5-*c*′]dithiophene-1,3-diyl]-2,5-thiophenediyl]
ITIC-Th	3,9-bis(2-methylene-(3-(1,1-dicyanomethylene)-indanone))-5,5,11,11-tetrakis(5-hexylthienyl)-dithieno[2,3-*d*:2′,3′-*d*′]-s-indaceno[1,2-*b*:5,6-*b*′]dithiophene
m-ITIC	3,9-bis(2-methylene-(3-(1,1-dicyanomethylene)-indanone))-5,5,11,11-tetrakis(4-*meta*-hexylphenyl)-dithieno[2,3-*d*:2′,3′-*d*′]-s-indaceno[1,2-*b*:5,6-*b*′]dithiophene
J61	poly[[5,6-difluoro-2-(2-hexyldecyl)-2H-benzotriazole-4,7-diyl]-2,5-thiophenediyl[4,8-bis[5-(dodecylthio)-2-thienyl]benzo[1,2-*b*:4,5-*b*′]dithiophene-2,6-diyl]-2,5-thiophenediyl]
IEICO	2,2′-[[4,4,9,9-tetrakis(4-hexylphenyl)-4,9-dihydro-s-indaceno[1,2-*b*:5,6-*b*′]dithiophene-2,7-diyl]bis[[4-[(2-ethylhexyl)oxy]-5,2-thiophenediyl]methylidyne(3-oxo-1H-indene-2,1(3H)-diylidene)]]bis[propanedinitrile]

Short Chemical Name	Full Chemical Name
PBDTTT-E-T	poly[(2,6-(4,8-bis(5-(2-ethylhexyl)thiophen-2-yl)benzo[1,2-*b*:4,5-*b*′]dithiophene)-co-alkoxycarbonyl-substituted thieno[3,4-*b*]thiophene
IDT-BOC6	2,2′-((2Z,2′Z)-((4,4,9,9-tetrakis(4-hexylphenyl)-4,9-dihydro-s-indaceno[1,2-*b*:5,6-*b*′]dithiophene-2,7-diyl)-bis(alkoxy)benzene-bis(methanylylidene))bis(3-oxo-2,3-dihydro-1H-indene-2,1-diylidene))dimalononitrile
PBDB-T	poly[(2,6-(4,8-bis(5-(2-ethylhexyl)thiophen-2-yl)benzo[1,2-*b*:4,5-*b*′]dithiophene)-co-(1,3-di(5-thiophene-2-yl)-5,7-bis(2-ethylhexyl)benzo[1,2-*c*:4,5-*c*′]dithiophene-4,8-dione)]
ATT-2	3,9-bis(2-methylene-(3-(1,1-dicyanomethylene)-indanone))-Z-dioctyl-6,6′-(4,4,9,9-tetrakis(4-hexylphenyl)-4,9-dihydro-s-indaceno[1,2-*b*:5,6-*b*′]dithiophene-2,7-diyl)-bis-thieno[3,4-b]thiophene-2-carboxylate
PTB7-Th	poly([2,6′-4,8-di(5-ethylhexylthienyl)benzo[1,2-*b*;3,3-*b*]dithiophene]3-fluoro-2[(2-ethylhexyl)carbonyl]thieno[3,4-*b*]thiophenediyl)
IT-M	3,9-bis(2-methylene-((3-(1,1-dicyanomethylene)-6/7-methyl)indanone))-5,5,11,11-tetrakis(4-hexylphenyl)-dithieno[2,3-*d*:2′,3′-*d*′]-s-indaceno[1,2-*b*:5,6-*b*′]dithiophene
IT-DM	3,9-bis(2-methylene-((3-(1,1-dicyanomethylene)-6,7-dimethyl)indanone))-5,5,11,11-tetrakis(4-hexylphenyl)-dithieno[2,3-*d*:2′,3′-*d*′]-s-indaceno[1,2-*b*:5,6-*b*′]dithiophene
ITIC-Th1	3,9-bis(2-methylene-((3-(1,1-dicyanomethylene)-6,7-difluoro)indanone))-5,5,11,11-tetrakis(5-hexylthienyl)-dithieno[2,3-*d*:2′,3′-*d*′]-s-indaceno[1,2-*b*:5,6-*b*′]dithiophene
IT-4F	3,9-bis(2-methylene-((3-(1,1-dicyanomethylene)-6,7-difluoro)indanone))-5,5,11,11-tetrakis(4-hexylphenyl)-dithieno[2,3-*d*:2′,3′-*d*′]-s-indaceno[1,2-*b*:5,6-*b*′]dithiophene
IEICO-4F	2,2′-[[4,4,9,9-tetrakis(4-hexylphenyl)-4,9-dihydro-s-indaceno[1,2-*b*:5,6-*b*′]dithiophene-2,7-diyl]bis[[4-[(2-ethylhexyl)oxy]-5,2-thiophenediyl]methylidyne(5,6-difluoro-3-oxo-1H-indene-2,1(3H)-diylidene)]]bis[propanedinitrile]
ITCC	3,9-bis(4-(1,1-dicyanomethylene)-3-methylene-2-oxo-cyclopenta[*b*]thiophen)-5,5,11,11-tetrakis(4-hexylphenyl)-dithieno[2,3-*d*′:2,3-*d*′]-s-indaceno[1,2-*b*:5,6-*b*′]-dithiophene

Short Chemical Name	Full Chemical Name
BZIC	1,1-dicyanomethylene-3-indanone-dithieno[3,2-*b*]pyrrolobenzotriazole
BTZ	benzotriazole
HFQx-T	poly[2,6-(4,8-bis(5-(2-ethylhexyl)thiophen-2-yl)benzo[1,2-*b*:4,5-*b*′]dithiophene)-co-(1,3-di(5-thiophene-2-yl)-hexafluoroquinoxaline)]
Y1	2,2′-((2Z,2′Z)-((6,12,13-tris(2-ethylhexyl)-12,13-dihydro-6H-thieno-[2″,3″:4′,5′]thieno[2′,3′:4,5]pyrrolo[3,2-*g*]thieno[2′,3′:4,5]thieno[3,2-*b*][1,2,3]triazolo-[4,5-*e*]indole-2,10-diyl)bis(methanylylidene))bis(3-oxo-2,3-dihydro-1H-indene-2,1-diylidene))dimalononitrile
Y2	2,2′-((5Z,5′Z)-((6,12,13-tris(2-ethylhexyl)-12,13-dihydro-6H-thieno-[2″,3″:4′,5′]thieno[2′,3′:4,5]pyrrolo[3,2-*g*]thieno[2′,3′:4,5]thieno[3,2-*b*][1,2,3]triazolo[4,5-*e*]indole-2,10-diyl)bis(methanylylidene))bis(6-oxo-5,6-dihydro-4H-cyclopenta[*c*]thiophene-5,4-diylidene))dimalononitrile
Y5	2,2′-((2Z,2′Z)-((12,13-bis(2-ethylhexyl)-3,9-diundecyl-12,13-dihydro-[1,2,5]thiadiazolo[3,4-*e*]thieno[2″,3″:4′,5′]thieno[2′,3′:4,5]pyrrolo[3,2-*g*]thieno[2′,3′:4,5]thieno[3,2-b]indole-2,10-diyl)bis(methanylylidene))bis(3-oxo-2,3-dihydro-1H-indene-2,1-diylidene))dimalononitrile
Y6	2,2′-((2Z,2′Z)-((12,13-bis(2-ethylhexyl)-3,9-diundecyl-12,13-dihydro-[1,2,5]thiadiazolo[3,4-*e*]thieno[2″,3″:4′,5′]thieno[2′,3′:4,5]pyrrolo[3,2-*g*]thieno[2′,3′:4,5]thieno[3,2-b]indole-2,10-diyl)bis(methanylylidene))bis(5,6-difluoro-3-oxo-2,3-dihydro-1H-indene-2,1-diylidene))dimalononitrile
PM6	poly[(2,6-(4,8-bis(5-(2-ethylhexyl-3-fluoro)thiophen-2-yl)-benzo[1,2-*b*:4,5-*b*′]dithiophene))-alt-(5,5-(1′,3′-di-2-thienyl-5′,7′-bis(2-ethylhexyl)benzo[1′,2′-*c*:4′,5′ -*c*′]dithiophene-4,8-dione))]
D18	poly[(2,6-(4,8-bis(5-(2-ethylhexyl-3-fluoro)thiophen-2-yl)-benzo[1,2-*b*:4,5-b′]dithiophene))-alt-5,5′-(5,8-bis(4-(2-butyloctyl)thiophen-2-yl)dithieno[3′,2′:3,4;2″,3″:5,6]benzo[1,2-*c*][1,2,5]thiadiazole)]

Short Chemical Name	Full Chemical Name
L8-BO	2,2′-((2Z,2′Z)-((12,13-bis(2-ethylhexyl)-3,9-dibutyloctyl-12,13-dihydro-[1,2,5]thiadiazolo[3,4-*e*]thieno[2″,3″:4′,5′]thieno[2′,3′:4,5]pyrrolo[3,2-*g*]thieno[2′,3′:4,5]thieno[3,2-b]indole-2,10-diyl)bis(methanylylidene))bis(5,6-difluoro-3-oxo-2,3-dihydro-1H-indene-2,1-diylidene))dimalononitrile
AQx-2	2,2′-((2Z,2′Z)-((13,14-bis(2-ethylhexyl)-3,10-diundecyl-13,14-dihydrothieno[2″,3″:4′,5′]thieno[2′,3′:4,5]pyrrolo[3,2-*f*]thieno[2″,3″:4′,5′]thieno[2′,3′:4,5]pyrrolo[2,3-*h*]quinoxaline-2,11-diyl)bis(methaneylylidene))bis(5,6-difluoro-3-oxo-2,3-dihydro-1H-indene-2,1-diylidene))dimalononitrile
Y6Se	2,2′-((2Z,2′Z)-((12,13-bis(2-ethylhexyl)-3,9-diundecyl-12,13-dihydro-[1,2,5]selenadiazolo[3,4-*e*]thieno[2″,3″:4′,5′]thieno[2′,3′:4,5]pyrrolo[3,2-*g*]thieno[2′,3′:4,5]thieno[3,2-b]indole-2,10-diyl)bis(methanylylidene))bis(5,6-difluoro-3-oxo-2,3-dihydro-1H-indene-2,1-diylidene))dimalononitrile
CH1007	2,10-bis(2-methylene-(3-(1,1-dicyanomethylene)-5,6-difluoroindanone))-12,13-bis(2-butyloctyl)-3,9-diundecyl-diselenopheno[2″,3″:4′,5′]thieno[2′,3′:4,5]pyrrolo[3,2-*e*:2′,3′-*g*][2,1,3]benzothiadiazole
BPF-4F	2,2′-((2Z,2′Z)-((12,13-bis(2-hexyldecyl)-12,13-dihydro-[1,2,5]thiadiazolo[3,4-*e*]thieno[2″,3″:4′,5′]furan[2′,3′:4,5]pyrrolo[3,2-*g*]thieno[2′,3′:4,5]furan[3,2-b]indole-2,10-diyl)bis(methanylylidene))bis(5,6-difluoro-3-oxo-2,3-dihydro-1H-indene-2,1-diylidene))dimalononitrile
BPT-4F	2,2′-((2Z,2′Z)-((12,13-bis(2-hexyldecyl)-12,13-dihydro-[1,2,5]thiadiazolo[3,4-*e*]thieno[2″,3″:4′,5′]thieno[2′,3′:4,5]pyrrolo[3,2-*g*]thieno[2′,3′:4,5]thieno[3,2-b]indole-2,10-diyl)bis(methanylylidene))bis(5,6-difluoro-3-oxo-2,3-dihydro-1H-indene-2,1-diylidene))dimalononitrile

Short Chemical Name	**Full Chemical Name**
BPS-4F	2,2′-((2Z,2′Z)-((12,13-bis(2-hexyldecyl)-12,13-dihydro-[1,2,5]thiadiazolo[3,4-*e*]selenopheno[2″,3″:4′,5′]thieno[2′,3′:4,5]pyrrolo[3,2-*g*]selenopheno[2′,3′:4,5]thieno[3,2-b]indole-2,10-diyl)bis(methanylylidene))bis(5,6-difluoro-3-oxo-2,3-dihydro-1H-indene-2,1-diylidene))dimalononitrile
SZ5	random copolymerised (2,6-(4,8-bis(5-(2-ethylhexyl-3-chloro)thiophen-2-yl)-benzo[1,2-*b*:4,5-*b*′]dithiophene))-1,3-bis(4-(2-ethylhexyl)thiophen-2-yl)-5,7-bis(2-alkyl)benzo[1,2-*c*:4,5-*c*′]dithiophene-4,8-dione-2-ethylhexyl-thiophene-thiazolo[5,4-*d*]thiazole
BTIC-CF_3-γ	2,2′-((2Z,2′Z)-((12,13-bis(2-ethylhexyl)-3,9-diundecyl-12,13-dihydro-[1,2,5]thiadiazolo[3,4-*e*]thieno[2″,3″:4′,5′]thieno[2′,3′:4,5]pyrrolo[3,2-*g*]thieno[2′,3′:4,5]thieno[3,2-b]indole-2,10-diyl)bis(methanylylidene))bis(γ-trifluoromethyl-3-oxo-2,3-dihydro-1H-indene-2,1-diylidene))dimalononitrile
BTIC-CF_3-*m*	2,2′-((2Z,2′Z)-((12,13-bis(2-ethylhexyl)-3,9-diundecyl-12,13-dihydro-[1,2,5]thiadiazolo[3,4-*e*]thieno[2″,3″:4′,5′]thieno[2′,3′:4,5]pyrrolo[3,2-*g*]thieno[2′,3′:4,5]thieno[3,2-b]indole-2,10-diyl)bis(methanylylidene))bis(γ/δ-trifluoromethyl-3-oxo-2,3-dihydro-1H-indene-2,1-diylidene))dimalononitrile
BTTPC	2,2′-((2Z,2′Z)-((12,13-bis(2-butyloctyl)-3,9-diundecyl-12,13-dihydro-[1,2,5]thiadiazolo[3,4-*e*]thieno[2″,3″:4′,5′]thieno[2′,3′:4,5]pyrrolo[3,2-*g*]thieno[2′,3′:4,5]thieno[3,2-b]indole-2,10-diyl)bis(methanylylidene))bis(2-(5-oxo-5,6-dihydro-7H-indeno[5,6-*b*]thiophen-7-ylidene)))malononitrile
BTTPC-Br	2,2′-((2Z,2′Z)-((12,13-bis(2-butyloctyl)-3,9-diundecyl-12,13-dihydro-[1,2,5]thiadiazolo[3,4-*e*]thieno[2″,3″:4′,5′]thieno[2′,3′:4,5]pyrrolo[3,2-*g*]thieno[2′,3′:4,5]thieno[3,2-b]indole-2,10-diyl)bis(methanylylidene))bis(2-(2-bromo-5-oxo-5,6-dihydro-7H-indeno[5,6-*b*]thiophen-7-ylidene)))malononitrile

Short Chemical Name	Full Chemical Name
BTP-H2	2,2′-((2Z,2′Z)-((12,13-bis(2-ethylhexyl)-3,9-dibutyloctyl-12,13-dihydro-[1,2,5]thiadiazolo[3,4-*e*]thieno[2″,3″:4′,5′]thieno[2′,3′:4,5]pyrrolo[3,2-*g*]thieno[2′,3′:4,5]thieno[3,2-b]indole-2,10-diyl)bis(methanylylidene))bis(5/6-bromo-3-oxo-2,3-dihydro-1H-indene-2,1-diylidene))dimalononitrile
PM1	4:1 random copolymerised (2,6-(4,8-bis(5-(2-ethylhexyl-3-fluoro)thiophen-2-yl)-benzo[1,2-*b*:4,5-*b*′]dithiophene))-1,3-bis(4-(2-ethylhexyl)thiophen-2-yl)-5,7-bis(2-alkyl)benzo[1,2-*c*:4,5-*c*′]dithiophene-4,8-dione-2-ethylhexyl-thiophene-thiazolo[5,4-*d*]thiazole
BTP-2F2Cl	2,2′-((2Z,2′Z)-((12,13-bis(2-butyloctyl)-3,9-dinonyl-12,13-dihydro-[1,2,5]thiadiazolo[3,4-*e*]thieno[2″,3″:4′,5′]thieno[2′,3′:4,5]pyrrolo[3,2-*g*]thieno[2′,3′:4,5]thieno[3,2-b]indole-2,10-diyl)bis(methanylylidene))-(5,6-difluoro-3-oxo-2,3-dihydro-1H-indene-2,1-diylidene))dimalononitrile-(5,6-dichloro-3-oxo-2,3-dihydro-1H-indene-2,1-diylidene))dimalononitrile
PM7	poly[(2,6-(4,8-bis(5-(2-ethylhexyl-3-chloro)thiophen-2-yl)-benzo][1,2-*b*:4,5-*b*′]dithiophene))-alt-(5,5-(1′,3′-di-2-thienyl-5′,7′-bis(2-ethylhexyl)benzo[1′,2′-*c*:4′,5′ - *c*′]dithiophene-4,8-dione)
ITO	indium tin oxide
PEDOT:PSS	poly(3,4-ethylenedioxythiophene) polystyrene sulfonate
ZnO	zinc oxide
MoO_3	molybdenum oxide
EH-IDT	rhodanine-benzothiadiazole-coupled indacenodithiophene with branched 2-ethylhexyl side chains
IHIC	fused-6-ring end-capped with 2-(3-oxo-2,3-dihydro-1H-inden-1-ylidene)malononitrile
F8IC	fused-8-ring end-capped with 2-(5,6-difluoro-3-oxo-2,3-dihydro-1H-inden-1-ylidene)malononitrile
C8IC	fused-8-ring end-capped with 2-(5,6-dichloro-3-oxo-2,3-dihydro-1H-inden-1-ylidene)malononitrile

Short Chemical Name	Full Chemical Name
PffBT4T-2OD	poly[(5,6-difluoro-2,1,3-benzothiadiazol-4,7-diyl)-alt-(3,3‴-di(2-octyldodecyl)-2,2′;5′,″;5″2‴-quaterthiophen-5,5‴-diyl)]
EH-IDTBR	rhodanine-benzothiadiazole-coupled indacenodithiophene, ethylhexyl side chains
N2200	(poly[N,N′-bis(2-octyldodecyl)-naphthalene-1,4,5,8-bis(dicarboximide)-2,6-diyl]-alt-5,5′-(2,2′-bithiophene))
DPP	diketopyrrolopyrrole
BDT	benzodithiophene
TQ	thiadiazoloquinoxaline
EDOT	3,4-ethylenedioxythiophene
P6T	α,ω-diphenyl *sexi*-thiophene
BP3T	α,ω-bis(biphenyl-4-yl)*ter*-thiophene
LBPP-1	poly(dialkoxy-phenylene-thiophene-*para*-alkoxyphenyl-thiadiazoloquinoxaline), phenylene end-capped
TQ-T	poly(*para*-alkoxyphenyl-thiadiazoloquinoxaline-thiophene)
DTBTT	dithienobenzotrithiophene
DPPB-3Se	diketopyrrolopyrrole with branched hexyloctyl side chains, polymerised with three selenophene units
DPPTTT	thieno[3,2-b]thiophene-diketopyrrolopyrrole
SeIn	3,9-bis(2-methylene-(3-(1,1-dicyanomethylene)indanone))-4,4,9,9-tetrakis(3-((2-ethylhexyl)oxy)phenyl)-diseleno[2,3-*d*:2′,3′- *d*′]-s-indaceno[1,2-*b*:5,6-*b*′]dithiophene
SeInMe	9-bis(2-methylene-((3-(1,1-dicyanomethylene)-6/7-methyl)indanone))-4,4,9,9-tetrakis-(3-((2-ethylhexyl)oxy)phenyl)diseleno[2,3-*d*:2′,3′-*d*′]-s-indaceno-[1,2-*b*:5,6-*b*′]dithiophene
SeOut	3,9-bis(2-methylene-(3-(1,1-dicyanomethylene)indanone))-4,4,9,9-tetrakis(3-((2-ethylhexyl)oxy)-phenyl)dithieno[2,3-*d*:2′,3′-*d*′]-s-indaceno[1,2-*b*:5,6-*b*′]- diselenophene
SeOutMe	3,9-bis(2-methylene-((3-(1,1-dicyanomethylene)-6/7-methyl)indanone))-4,4,9,9-tetrakis(3-((2-ethylhexyl)oxy)phenyl)dithieno[2,3-*d*:2′,3′-*d*′]-s-indaceno[1,2-*b*:5,6-*b*′]diselenophene
BDD	5,7-bis(2-ethylhexyl)benzo[1,2-*c*:4,5-c′]dithiophene-4,8-dione

Short Chemical Name	**Full Chemical Name**
NP-SA	2-((5-(naphthalen-1-yl(phenyl)amino)selenophen-2-yl)methylene)-1H-cyclopenta[*b*]naphthalene-1,3(2H)-dione
MPTA	2-((8-methyl-8H-thieno[2,3-*b*]indol-2-yl)methylene)-1H-cyclopenta[*b*]naphthalene-1,3(2H)-dione

B | Nonfullerene Acceptors: a Short Review of Molecular Design

Rylene diimide NFAs

The initial examples of NFAs were created by molecular engineering of the rylene diimide fused aromatic structure, offering beneficial properties such as straightforward functionalisation at different molecular sites, high electron mobility, low-lying LUMO, strong optical absorption, and excellent stability.[113–115] In particular, perylene diimide (**PDI**) is based on a fully fused polycyclic aromatic structure, with good rigidity and prone to self-assembly.[116–118] The strong tendency to aggregate causes large domain size in BHJ and extremely poor charge generation, so that chemical modification at different sites are required to prevent this. For example, functionalisation at imide,[119,120] α,[121] or bay[122] positions enhances device performances in BHJ with various donor polymers, although PCE remains limited to $<$4.5%. Another effective strategy to control aggregation is the twisting of PDI structure in dimeric molecules. PDI units can be connected *via* single bonds and spacer groups, resulting in significant increase in charge generation by morphology control,[123] and over 4% PCE can be achieved with PBDTTT-C-T donor.[432] Additional functionalisation can further twist the dimer NFA and boost performances, reaching $>$8% PCE by selenium capping in bay positions,[124] while spirobifluorene spacers can reduce domain size and achieve ultrafast charge separation, with a PCE record of 9.5% and 1.11 V of V_{OC} in conjunction with P3TEA donor.[125] However, perspectives of further efficiency increase for PDI derivatives are limited due to the delicate trade-off between molecular twisting for reduced aggregation and high rigidity and planarity for good transport and π-π stacking quality. In particular, the challenging morphology control often requires solvent additives, limiting stability and industrial scalability. Moreover, although energy level tuning can be achieved by functionalisation, PDI-derivative bandgaps remain typically large ($>$1.9 eV) and restrict the choice of matching donor polymers.

A-D-A calamitic NFAs

A powerful strategy to reduce NFA bandgap is by push-pull interaction in the so-called *calamitic* acceptors, which is extremely effective to extend absorption in the NIR range. These NFAs have a typical molecular structure with alternating electron accepting and electron donating building blocks (A-D-A), where HOMO/LUMO localisation on molecular units enhances ICT and extends absorption. These NFAs also offer facile FMO tunability for both V_{OC} and J_{SC} increase. Moreover, the molecular structure of the conjugated backbone is typically linear, offering good rigidity, high mobility, and promising stability, while different side chains can be attached to tune solubility and packing. The first example of A-D-A NFAs was reported in 2013, when Winzemberg *et al.*[126] synthesised a molecule called FEHIDT, based on indan-1,3-dione acceptor and fluorene donor units linked by thiophene spacers. FEHIDT has a large bandgap due to the significant thiophene-fluorene dihedral twisting, and only a limited $PCE \sim 2.5\%$ could be reached with P3HT. This was improved to 4% soon after with FBR,[433] using the same fluorene core and ethylrhodanine donor units, with BT spacers, showing similar strong twisting and suppressed morphological aggregation. A pivotal step was the synthesis of IDT and IDTT donor units, used respectively in DC-IDT2T[434] and ITIC,[127] where DCI is used as acceptor unit. In particular, **ITIC** molecular structure represents a model for later development of novel NFAs, and its optimum spectral coverage in the 600-800 nm range and favourable packing by end-group π-π stacking enabled to overcome the 10% PCE threshold. For example, a PCE of 11.21% with 16.81 mA/cm^2 of J_{SC} and a FF approaching 75% was reported with PBDB-T.[314] One of the strongest benefits of calamitic NFAs is the wide synthetic tunability of their chemical structure, where every functional unit can be finely engineered. For example, core elongation and heteroatom substitution have been trialled, such as in IDTIDT-IC[129] and IDTIDSe-IC,[435] both with a 10-fused ring backbone. Here, the increased conjugation length and strong quinoid resonance by large Se atoms help extend the absorption beyond 800 nm, and J51:IDTIDSe-IC OPVs achieve a PCE over 8%. Moreover, the central core (A unit) in FBR can be replaced by IDT in the so-called IDT-2BR,[133] with a planar backbone geometry and a strong electron mobility enhancement from 2.6x10^{-5} cm^{2}V^{-1}s^{-1}[1433] to 2.6x10^{-4} cm^{2}V^{-1}s^{-1} and >5% PCE with P3HT. The same molecular core is used in **O-IDTBR**,[128] while indacenodibenzene is introduced in O-IDFBR.[163] This has a highly twisted geometry due to the strong steric hindrance with the BT units, so that OPV performances are poor (only 4.5% of PCE with P3HT). However, when used in combination with well-packed O-IDTBR, the amorphous O-IDFBR can help morphology optimisation, and fine tuning of ternary

BHJs with P3HT is extremely beneficial for stable devices.[163]

Nonconjugated side chains also crucially affect BHJ formation and OPV performance, and extensive effort have been devoted to their design. While IDT and IDTT-based NFAs were originally synthesised with bulky hexylphenyl chains to control aggregation,[127,133] linear alkyl chains have also proved to yield good performances, with ordered crystalline packing and good NIR spectral coverage. Examples include O-IDTBR (IDT core, rhodanine end groups, BT spacers, with octyl side chains)[128] or IC-C6IDT-IC (also known as IDIC),[290] where the hexyl chains afford a $PCE > 8.5\%$ in blend with PDBT-T1. Side chain engineering has been especially fruitful on the ITIC molecular structure, like in ITIC-Th.[134] Here, the S-S noncovalent interactions between the alkylthienyl chains is beneficial for packing order, transport, and overall performances (67.1% FF, 9.6% PCE). Moreover, in m-ITIC[135] the alkyl chains are grafted onto the *meta*-position of the phenyl ring, allowing a better packing with no effect on HOMO/LUMO levels, and excellent efficiency in OPVs (11.5% PCE, $FF >70\%$, and 18.3 mA/cm^2 of J_{SC} with J61).

The role of spacer units along the A-D-A backbone have also been explored, to extend conjugation with a more straightforward synthesis of non-fused molecules, where rigidity can be controlled by noncovalent conformational lockers. For example, a thiophene with alkoxy side chains is used in IEICO,[288] with low-lying HOMO and extremely narrow bandgap (∼1.3 eV) due to the alkoxy group and low energy losses (∼0.5 eV in BHJ with PBDTTT-E-T). Diexyloxybenzene spacers are utilised in IDT-BOC6,[242] showing high μ_e, small bandgap and >9.6% of PCE with PBDB-T, while thieno-[3,4-b]-thiophenes are found in ATT-2,[436] extending the absorption beyond 900 nm and achieving ∼10% of PCE with PTB7-Th.

Finally, end-capping groups are also an extremely important site for tuning NFA properties, and end-group engineering is especially useful to control LUMO levels. This has been applied on the ITIC structure, with methylated (IT-M) and dimethylated (IT-DM) ITIC,[130] showing increased V_{OC} up to 0.94 V with PBDB-T and enhanced crystallinity, with over 12% PCE for IT-M. Fluorinated counterparts (ITIC-Th1[131] and IT-4F[132]) also show improved packing order thanks to stronger π-π interactions, with a deep LUMO and a narrow bandgap for increased spectral coverage and photocurrent generation. Notably, a record of 20.50 mA/cm^2 of J_{SC} and a $PCE >13\%$ has been reported for IT-4F, and photocurrent can be further boosted when fluorination is applied to the low bandgap IEICO (*i.e.*, IEICO-4F with PTB7-Th[437]), yielding a J_{SC} of almost 23 mA/cm^2. Other end-group units reported include fused thiophene-substituted DCI as in ITCC,[438] with high LUMO by strong electron-donating thiophene, good transport and weak recombination by

dense π-π stacking and pure domains, reaching a PCE of 11.4% with PBDB-T.

A-DA′D-A calamitic NFAs

Another design option for calamitic NFAs is the additional engineering of molecular core by introducing electron-deficient subunits, to further extend ICT and NIR absorption.[136,137] This is the design principle for the **Y-series** of acceptors, which has recently allowed to break all previous efficiency records. The first example of A-DA′D-A NFA was reported in 2017, when Zou *et al.* synthesised BZIC.[141] Here, the IDTT core typical of the ITIC family is substituted by a dithieno[3,2-*b*]pyrrolobenzotriazole six-ring unit, where the electron-withdrawing BTZ and the electron-donating pyrrole increase ICT and enhance electron mobility.[439,440] However, FF and J_{SC} of HFQx-T:BZIC OPVs were not promising, and the PCE was limited to 6.3%. Later on, improvements were shown with Y1 and Y2, where the extended eight-ring core increases J_{SC} over 20 mA/cm^2 with PBDB-T.[140] The greatest breakthroughs were achieved replacing the BTZ with BT unit as central A′ building block, as in Y5[138] and Y6.[139] The stronger electron-withdrawing nature of BT affords a narrow bandgap <1.40 eV, while the alkyl side chains on the outer core thiophene are important for structural control and rigidity.[212] Therefore, over 22.5 mA/cm^2 of J_{SC} and a FF >70% could be reached in Y5, for a PCE >14% with PBDB-T, while Y6 with fluorinated end groups touched 15.7% PCE with PM6 (fluorinated PBDB-T). By further optimisation and polymer matching, Y6 and its derivatives can afford a PCE >18%, as recently reported by Liu *et al.* with D18 donor[10] or for the branched-alkyl-chain-containing L8-BO (PCE>18.3%).[11]

The articulated molecular design of Y-family NFAs is also promising for engineering of different building blocks, especially in the elongated core region. Here, the D and A′ units are connected by pyrrole π-bridges, and each of these moieties can be carefully selected. For example, in addition to BTZ[140–142] and BT units,[138,139] other groups like quinoxaline or benzoselenadiazole can be utilised, as in AQx-2[441] and Y6Se,[442] respectively. A′ engineering has a significant impact on LUMO levels, with a 30 meV shallower LUMO for AQx-2 compared to Y6 or Y6Se, while the molecular rigidity by large selenium orbitals in Y6Se affords low energy disorder and efficient charge extraction ($J_{SC}\sim$ 28 mA/cm^2 with D18 polymer).

Core donor units can also be engineered. In CH1007,[443] outer thiophenes are replaced with selenophene for increased planarity and narrower bandgap, reaching >27 mA/cm^2 of J_{SC} and a FF of 72% with PM6. Noncovalent conformational lockers with end-group oxygen were also explored by H. Yan and colleagues,[444] us-

ing thieno[3,2-*b*]furan, thieno[3,2-*b*]thiophene, and selenopheno[3,2-*b*]thiophene, in BPF-4F, BPT-4F and BPS-4F, respectively. The O-O hindrance in BPF-4F results in excessive molecular twist and poor OPV performances, while optimum packing and best PCE is found for BPT-4F with SZ5 donor.

To control molecular structure and BHJ morphology, side chain design is also a key factor. This is especially true for Y-family NFAs, where the four nonconjugated side chains are grafted onto different core positions (*i.e.*, β-position of outer thiophenes and central pyrrole) and can be separately selected. Different studies on pyrrole-unit side chains[148–150] show that branched alkyls are preferable to linear ones for solubility, and chain length tuning is crucial for optimum domain size and packing orientation. Chains on outer thiophenes (β-position) have a specific impact on molecular conformation, controlling packing and morphological stability.[11,147] For example, undecyl moiety in many Y-series NFAs[139,142,445] is deemed to be the origin of molecular rigidity,[212] while reducing its length can result in too closer *d*-spacing in the crystalline packing and excessive phase segregation.[446] Here, branched alkyl chains help create a more condensed packing structure by strong intermolecular interactions, and acceptors such as L8-BO (with butyloctyl chains) exhibit a 18.32% PCE with record FF of 81.5%.[11]

Finally, end-group design is also the focus of synthetic chemists' effort, although the typical building blocks do not differ from the DCI units used in other calamitic NFAs. Electron-withdrawing properties and π-π stacking can be tuned by halogen[143–146] or thiophene[447–449] substitution, and combinations of different heteroatoms can determine dipole character, crystallinity, and carrier mobility.[450] The position of end-group substituents is also important to control molecular twisting, as shown in BTIC-CF_3-γ, where a small dihedral angle affords high ICT and superior J_{SC} and FF compared to BTIC-CF_3-*m*.[451] Moreover, elongated end groups such as in BTTPC and BTTPC-Br[452] result in shallower HOMO for more efficient hole transfer. Here, a promising strategy is to combine two Y-family NFAs with different end groups to fine-tune intermolecular interactions and D/A energetics in ternary BHJs, resulting in the highest OPV performances reported to date. For example, brominated BTP-H2 shows strong crystallinity and negligible HOMO offset with PM6, achieving optimum charge separation with $V_{OC}^{non-rad}$<200 meV.[146] Here, exceptional PCE of *circa* 18.5% is shown for PM6:BTP-H2-based devices, while values of 19.2% can be touched for ternary PM6:BTP-H2:L8-BO ternary BHJs. Similar performances (*i.e.*, PCE = 19.17%) are also reported for PM1:L8-BO:BTP-2F2Cl systems,[12] where the asymmetric end groups of the BTP-2F2Cl guest is utilised to extend absorption range and optimise the packing order in the host blend.

C | Improving Stability in Bulk Heterojunction Organic Photovoltaics *via* Selenium-Substituted Nonfullerene Acceptors - Supporting Material

Peak	Unit	Description
1	T, BDD	C=C, C-C in T and C-C between T and BDD
2,3	BDT, BDD, T	C-C
4	BDT	C-C antisymmetric
5	BDT, T	C-C antisymmetric
6	BDD	Carbonyl

Tab. C.1: Description of PBDB-T Raman modes assigned in Figure C.3.

Peak	Unit	Description
1	Core	Core C=C symmetric stretch outer thiophene/selenophene
2	Multiple	C-C outer core, H-wagging in flank or interunit H
3	Core	Phenyl – symmetric, minor H-wagging in end phenyl and alkene
4	Multiple	C=C and C-C outer thiophene/selenophene, alkene H-wagging
5	Multiple	C=C and C-C outer thiophene/selenophene, alkene and flank H-wagging
6	Core	C-C inner thiophene/selenophene
7	Multiple	C=C outer thiophene/selenophene, alkene and flank H-wagging
8	Multiple	Alkenes
9	Core	Phenyl – antisymmetric
10	Flank	Carbonyl

Tab. C.2: Description of NFA Raman modes assigned in Figure C.4.

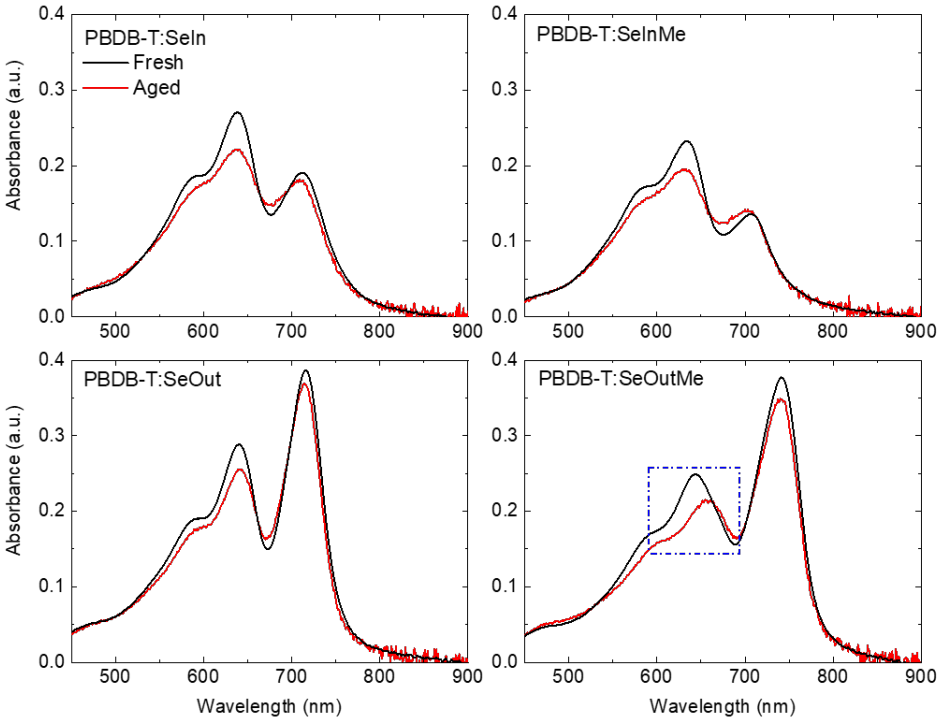


Fig. C.1: Absorption spectra of fresh and aged PBDB-T:NFA blends exposed to a white LED light source. The dashed square on SeOutMe spectra highlights the red shift of PBDB-T peak.

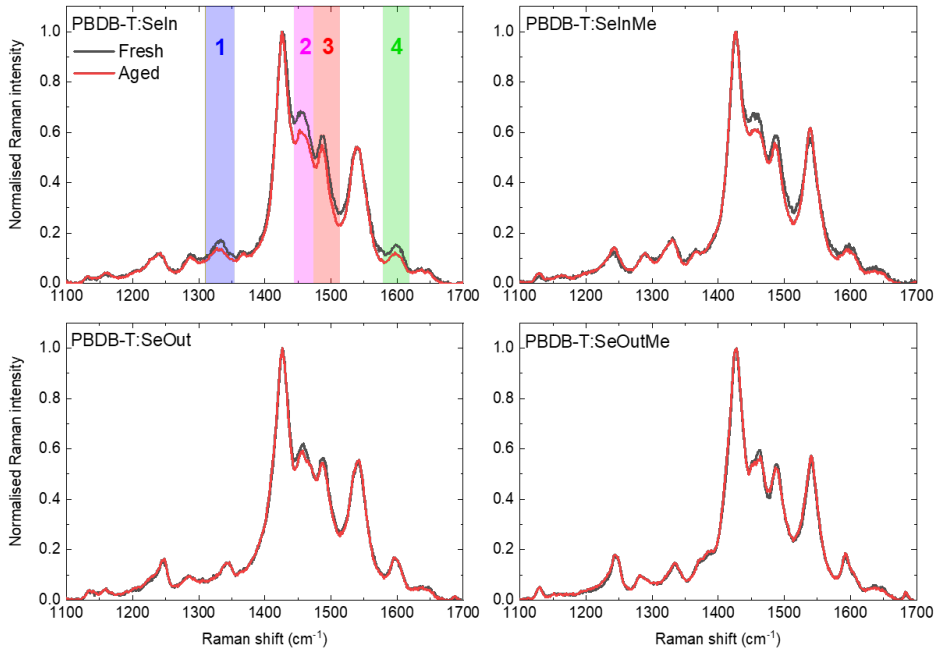


Fig. C.2: Raman spectra of fresh and aged PBDB-T:NFA blend films. The top left graph relative to SeIn blend shows the peak assignment to the relevant vibrational modes as detailed in Figure 4.7.

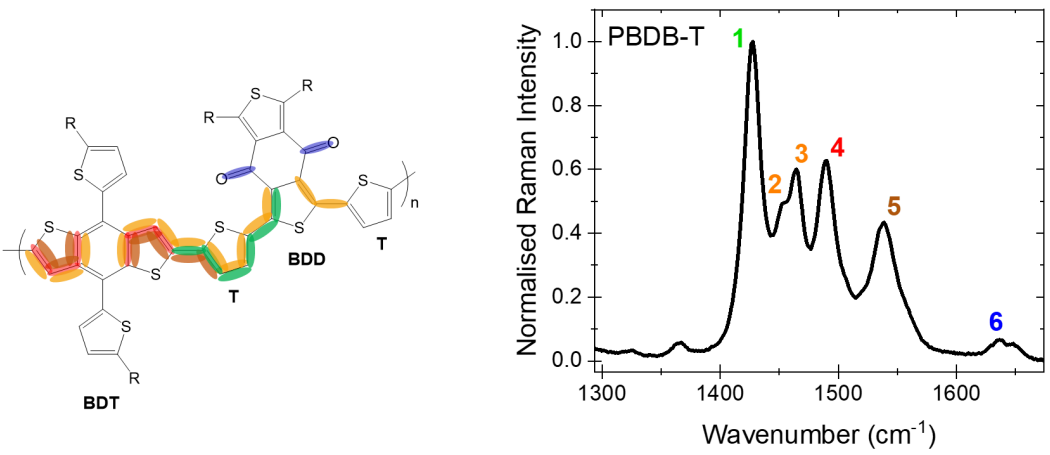


Fig. C.3: Assignment of Raman modes of PBDB-T, indicated on its chemical structure, with R = 2-ethylhexyl.

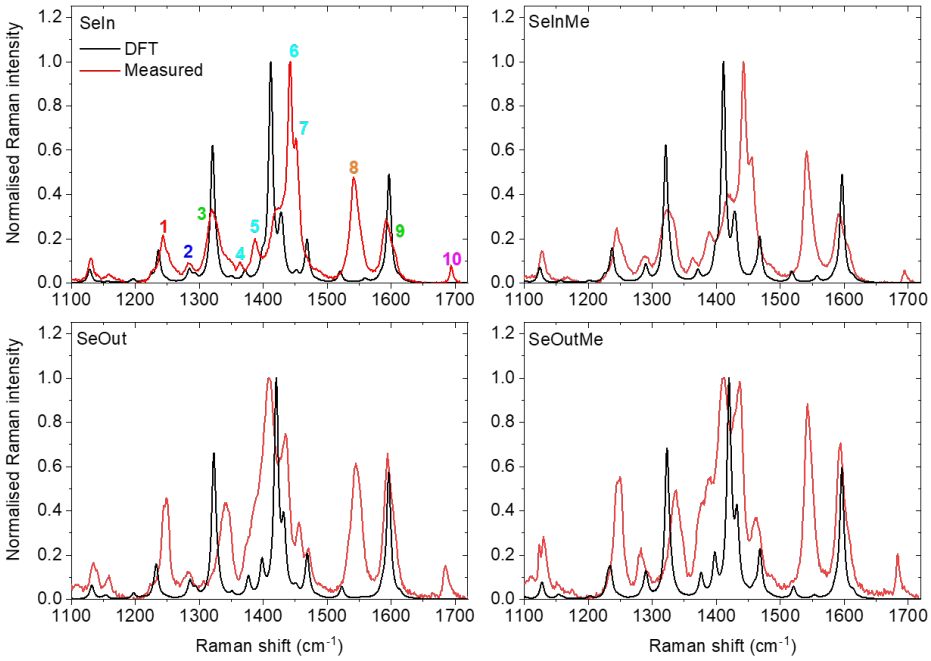


Fig. C.4: Assignment of the NFA Raman modes, comparing experimental data with DFT simulations. The labels are referred to the detailed description provided in Table C.2. The same colour is used for peaks involving the same molecular bonds.

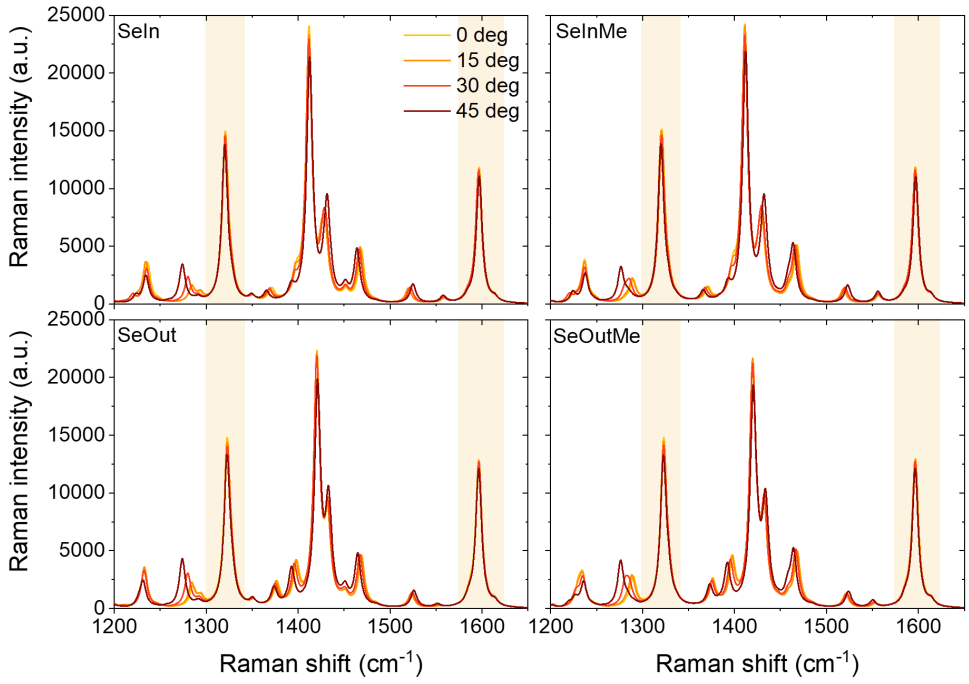


Fig. C.5: DFT-simulated Raman spectra of the four NFAs with different core-end dihedrals. The peaks at ∼1325 and ∼1600 cm^{-1} are highlighted and show decreasing intensity with increasing twisting angle.

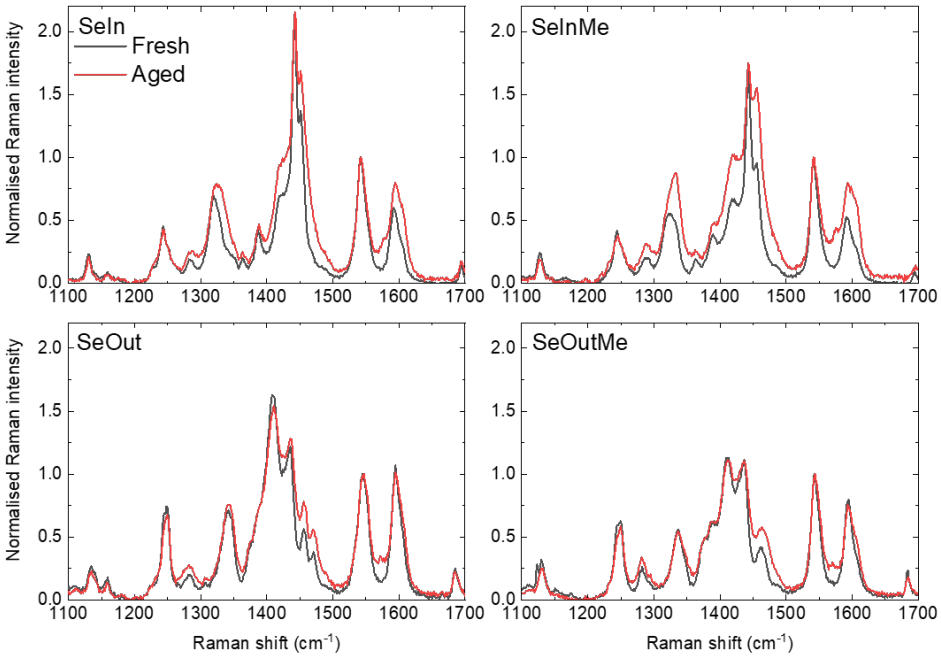


Fig. C.6: Raman spectra of fresh and aged neat NFAs exposed to a white LED light source, probed by 514 nm laser, normalised with respect to the alkene peak (∼1550 cm^{-1}).

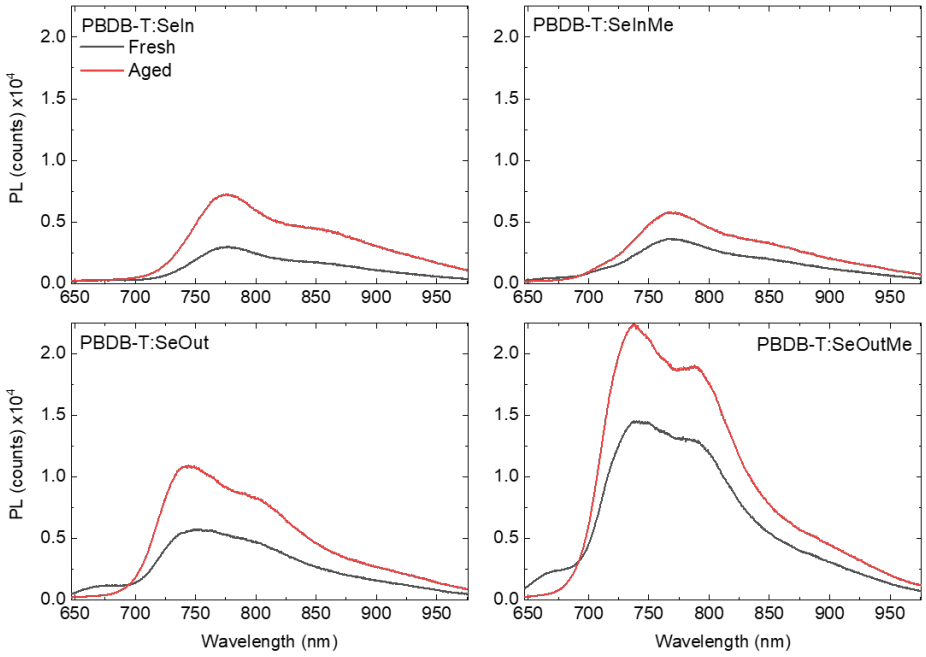


Fig. C.7: PL spectra of fresh and aged PBDB-T:NFA blends exposed to a white LED light source.

D Light-Intensity-Dependent Photoresponse Time of Organic Photodetectors and its Molecular Origin - Supporting Material

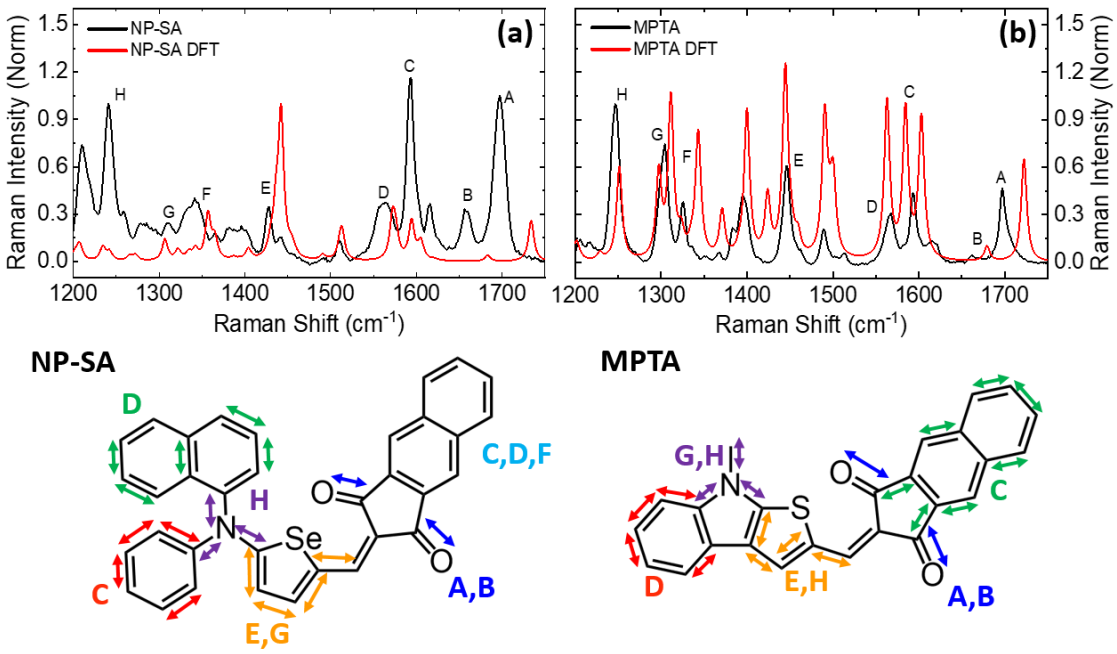


Fig. D.1: Comparison of experimental and DFT simulated Raman spectra for NP-SA (a) and MPTA (b), with the peak assignment illustrated in the respective molecular structures.

Peaks (± 1 cm^{-1})	**NP-SA** - Vibrational Assignments
H (1240)	C-N stretch; selenophene C=C stretch
Core Group	
G (1310)	Selenophene C=C; C-N and alkene stretch
F (1341)	H-wagging of selenophene and alkene stretch
E (1428)	Selenophene C-C intraunit; neighbouring C-N and C-C interunit
End Group	
D (1563)	Naphthalene intraunit stretch; strong alkene stretch
C (1594)	Phenyl intraunit stretch, interunit C-N; C-C stretch in A unit
B (1656)	C=O, antisymmetric stretch
A (1697)	C=O, symmetric stretch
Peaks (± 1 cm^{-1})	**MPTA** - Vibrational Assignments
H (1246)	C-N stretch; selenophene C=C and neighbouring C-C, C-N
Core Group	
G (1304)	C-N stretch; H-wagging of thiophene, D unit and alkene
F (1325)	H-wagging of thiophene and alkene; D unit C-C
E (1445)	Thiophene C=C; D unit C=C and alkene stretch
End Group	
D (1567)	D unit phenyl stretch; alkene and A unit C-C, C=C stretch
C (1594)	A unit C-C, C=C stretch; alkene and D unit phenyl stretch
B (1662)	C=O, antisymmetric stretch
A (1697)	C=O, symmetric stretch

Tab. D.1: Detailed assignment of Raman vibrational modes of NP-SA and MPTA, referred to Figure D.1.

E | Nonfullerene Acceptor Dilution as a Facile Strategy for Device Optimisation towards High-Efficiency Solution-Processed Bulk Heterojunction Organic Photodetectors - Supporting Material

Supplementary Note - Calculation of CT-State Binding Energy in PM6:Y6 Bulk Heterojunctions

For the calculation of CT state binding energies, the efficiency of CT dissociation at room temperature and null applied bias is expressed as

$$\frac{k_{d0}}{k_0 + k_{d0}} = EQE_{0V,RT}, \tag{E.1}$$

Where k_{d0} is the room temperature CT dissociation rate, k_0 the CT-to-ground recombination rate, and the 0 V EQE is obtained from the peak assigned to Y6 in Figure 6.5. The total CT decay rate $k_0 + k_{d0}$ is extracted from transient absorption data as half-life of low energy species (Figure 6.14c,d, at $12\,\mu J\,cm^{-2}$), so that k_0 can be calculated from Equation E.1.

Considering a thermally-activated CT dissociation, PL is measured during a heating cycle up to 200 °C (Figure E.1a,b) and temperature-dependent PL quenching efficiency $PLQE_T$ is calculated as (PL_{RT}-PL_T)/PL_{RT}, where PL_{RT} is the room

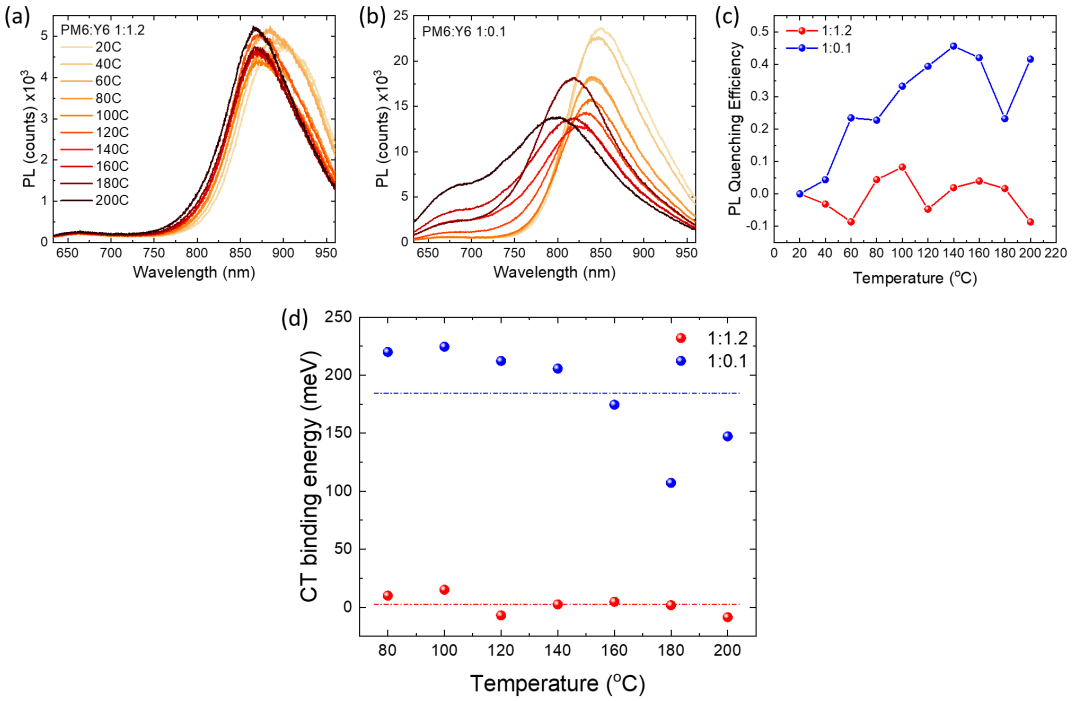


Fig. E.1: Temperature-dependent absolute PL for (a) 1:1.2 and (b) 1:0.1 PM6:Y6 blends. (c) Temperature-dependent PL quenching efficiency. (d) CT state binding energy of PM6:Y6 blends calculated at different temperatures, with average values indicated as dashed lines.

temperature PL and PL_{RT} the PL at a temperature T (see Figure E.1c). As such, the temperature-dependent CT dissociation yield a can be expressed as

$$a = 1 - [(1 - EQE_{0V,RT})(1 - PLQE_T)] = \frac{k_d}{k_0 + k_d}, \tag{E.2}$$

So that the CT dissociation rate at a specific temperature k_d can be calculated from Equation E.1 and Equation E.2. Finally, the CT binding energy E_B is the activation energy of CT dissociation with rate k_d, modelled by the Arrhenius equation

$$k_d = Ae^{-\frac{E_B}{k_B T}}, \tag{E.3}$$

With A a pre-exponential frequency factor. Therefore, the ratio k_d/k_{d0} allows to extract E_B by Equation E.3. Values of E_B for different temperatures are shown in Figure E.1d, from where an average value and its statistical error can be calculated. In particular, $E_B = 3\pm8$ meV for PM6:Y6 1:1.2 blends and $E_B = 180\pm40$ meV for the 1:0.1 case.

Supplementary Data

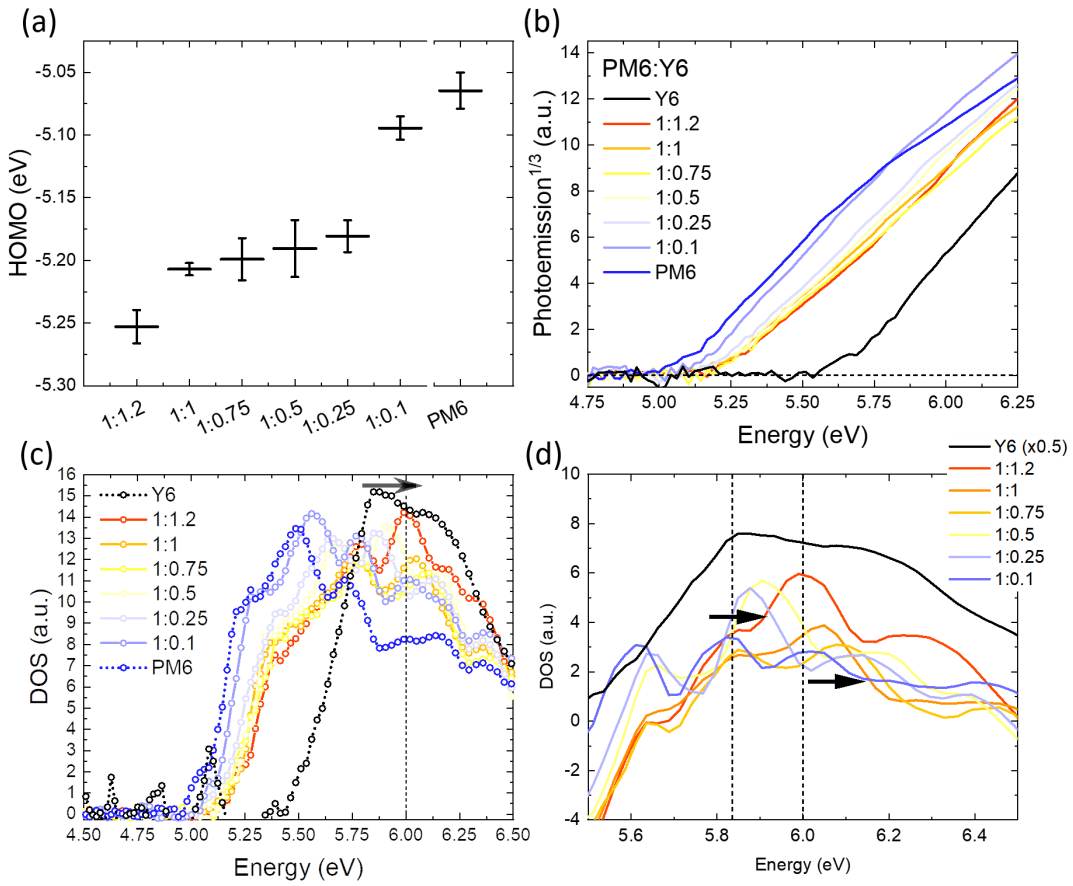


Fig. E.2: Energetic characterisation of PM6:Y6 BHJ thin films with different blend ratios by APS analysis. (a) HOMO levels of blended PM6 from photoemission cutoff, (b) photoemission spectra, (c) original and (d) deconvoluted DOS spectra with indicated the shift in the Y6 region. For deconvolution, the PM6 DOS is subtracted from the original spectra, and the result compared with neat Y6 data.